TU UB
Die approbierte Originalversion dieser Dissertation ist in der Hauptbibliothek der Technischen Universität Wien aufgestellt und zugänglich.
http://www.ub.tuwien.ac.at
TU WIEN UB Universitätsbibliothek
The approved original version of this thesis is available at the main library of the Vienna University of Technology.
http://www.ub.tuwien.ac.at/eng

TECHNISCHE
UNIVERSITÄT
WIEN

Prüfung der optischen Qualität von Intraokularlinsen hinsichtlich postoperativen Verschiebungen und Verkippungen

DISSERTATION

zur Erlangung des akademischen Grades

Doktor der Technischen Wissenschaften

eingereicht von

Dipl.-Ing. Lukas Traxler, BSc.
Matrikelnummer 1028999

an der Fakultät für Physik
der Technischen Universität Wien

Betreuung: ao.Univ.-Prof. Dipl.-Ing. Dr.techn. Wolfgang Husinsky
Zweitbetreuung: FH-Prof. Dr. Andreas Drauschke

Diese Dissertation haben begutachtet:

Prim. Univ. Prof. Dr. Oliver Findl
Prof. Dr. rer. nat. Wilhelm Stork

Wien, 24. August 2018

Lukas Traxler
Lukas Traxler

Technische Universität Wien
A-1040 Wien ▪ Karlsplatz 13 ▪ Tel. +43-1-58801-0 ▪ www.tuwien.ac.at

TECHNISCHE
UNIVERSITÄT
WIEN

Testing the Optical Quality of Intraocular Lenses Regarding Postoperative Tilt and Decentration

DISSERTATION

submitted in partial fulfillment of the requirements for the degree of

Doktor der Technischen Wissenschaften

by

Dipl.-Ing. Lukas Traxler, BSc.
Registration Number 1028999

to the Faculty of Physics

at the TU Wien

Advisor: ao.Univ.-Prof. Dipl.-Ing. Dr.techn. Wolfgang Husinsky
Second advisor: FH-Prof. Dr. Andreas Drauschke

The dissertation has been reviewed by:

Prim. Univ. Prof. Dr. Oliver Findl

Prof. Dr. rer. nat. Wilhelm Stork

Vienna, 24th August, 2018

Lukas Traxler

Lukas Traxler

Technische Universität Wien
A-1040 Wien ▪ Karlsplatz 13 ▪ Tel. +43-1-58801-0 ▪ www.tuwien.ac.at

Erklärung zur Verfassung der Arbeit

Dipl.-Ing. Lukas Traxler, BSc.
Schirnes 3, 3842 Thaya

Hiermit erkläre ich, dass ich diese Arbeit selbständig verfasst habe, dass ich die verwendeten Quellen und Hilfsmittel vollständig angegeben habe und dass ich die Stellen der Arbeit – einschließlich Tabellen, Karten und Abbildungen –, die anderen Werken oder dem Internet im Wortlaut oder dem Sinn nach entnommen sind, auf jeden Fall unter Angabe der Quelle als Entlehnung kenntlich gemacht habe.

Wien, 24. August 2018

Lukas Traxler

Lukas Traxler

Acknowledgements

I want to thank ao.Univ.-Prof. Dipl.-Ing. Dr.techn. Wolfgang Husinsky for the supervision of my thesis, for his advice and support.

I gratefully appreciate the financial support by the City of Vienna (Magistratsabteilung 23 – Wirtschaft, Arbeit und Statistik) for funding the project LOALiS (Laser and Optics in Applied Life Sciences) at the FH Technikum Wien – Institute for Biomedical, Health and Sports Engineering, which enabled me to do research on this topic. Many thanks to FH-Prof. Dr. Andreas Drauschke for setting up the project application and thus raising the funds, as well as for doing the second supervision of the thesis.

Thanks to the FH Technikum Wien for providing the necessary infrastructure which allowed building up a photonics laboratory for performing the experiments for this thesis.

I would like to offer my special thanks to my colleges from the LOALiS-research team for insightful discussions, great company on conference visits and a wonderful time through the period of this research project.

I also extend my thanks to my family and friends who gave me their warmth and responsiveness during the time I carried out my work.

Kurzfassung

Katarakt ist die Trübung der Augenlinse, was unbehandelt bis zur Erblindung führen kann. Bei der Katarakt–Operation, der häufigsten Operation in der westlichen Welt, wird die getrübte Linse entfernt und durch eine künstliche, eine sogenannte „Intraokularlinse“ (IOL), ersetzt. Das optische Design dieser Linsen wird ständig verbessert, u.a. durch Beseitigung von Abbildungsfehlern der IOL selbst, oder durch IOLs, die Abbildungsfehler des Auges korrigieren können. Postoperativ kann es durch den Heilungsprozess zu einer Verschiebung oder Verkippung der IOL im Auge kommen. Untersuchungen zeigten, dass hochentwickeltere Linsen in zentrierter Position bessere Ergebnisse zeigen, aber die Bildqualität bei Dezentrierung unter der von einfachen Linsen liegen kann. Um die postoperativen Eigenschaften von IOLs besser charakterisieren zu können, wird in dieser Arbeit untersucht, welche Abbildungsfehler durch bestimmte Dezentrierungen herbeigeführt werden und wie diese experimentell erfasst werden können.

Theoretische Analysen sind in der wissenschaftlichen Literatur selten, da Hersteller die optischen Linsendesigns meist nicht veröffentlichen. Experimentell verlangt der aktuelle Standard zur Linsenprüfung (ISO 11979–2) keine Tests zur Überprüfung von dezentrierungsbedingten Abbildungsfehlern. Aktuelle wissenschaftliche, nicht standardisierte Testmethoden beruhen oft auf Vereinfachungen des ISO–Teststandards und entsprechen nicht exakt der Physiologie des menschlichen Auges.

Diese Arbeit präsentiert ein neuartiges mechanisches Augenmodell, welches die optischen Eigenschaften des menschlichen Auges genau nachbildet. Zwei feinmechanische Stellmotoren ermöglichen automatisches Testen von IOLs bei simulierten postoperativen Dezentrierungen. Unter Verwendung eines Hartmann–Shack Wellenfront–Sensors und Zerlegung der Wellenfront in Zernike Polynome, kann die optische Qualität sowie die Art der Abbildungsfehler für den statistisch relevanten Bereich postoperativer IOL Positionen gemessen werden. Die Herstellung der künstlichen Kornea für das Augenmodell ist technologisch äußerst anspruchsvoll. Trotz dieser Schwierigkeit zeigen die bei dezentrierter IOL gemessenen Abbildungsfehler eine gute Übereinstimmung mit den Resultaten numerischer Simulationen, die für drei verschiedene, typische Linsen–Designs sowie zwei Irisdurchmesser durchgeführt wurden. Die Ergebnisse dieser Arbeit können ein wesentlicher Beitrag für die Verbesserung des aktuellen ISO-Teststandards sein, indem IOLs unter physiologischen Bedingungen und unter Berücksichtigung von postoperativer Fehlplatzierungen im Auge untersucht werden.

Abstract

Cataract, the clouding of the human eye lens, leads to blindness if it is not treated. But it can effectively be treated by surgery, this is the most frequent surgical intervention in western countries. During cataract surgery the clouded natural lens is replaced by an artificial lens, called "intraocular lens" (IOL). The optical design of IOLs is constantly improving. Some advances were the removal of the IOL's own optical aberration, or IOLs can be designed to correct optical aberrations of the eye. Postoperative healing processes can cause a change of the IOL's position within the eye. Research showed that advanced lens designs show increased performance in the centered position, but image quality can drop below the performance of simple lens designs if the IOL displaces postsurgically. To improve IOL characterization for better postsurgical outcome, this thesis questions, which types of aberrations are induced at specific IOL decentrations, and how they can experimentally be measured.

Theoretical analysis are rare in literature, since IOL design data are not revealed by the manufacturers. Experimentally, the current test standard for testing the optical performance of IOLs (ISO 11979–2) does not require an investigation of the aberration effects of IOL decentrations. Current non–standardized tests often rely on simplifications of the test standard, which do not accurately represent the physiology of the human eye.

This thesis presents a novel mechanical model eye, which closely represents the eye's optical properties. Two micro actuators allow for an automated test of the optical performance in presence of postoperative IOL displacements. Using a Hartmann–Shack wavefront sensor and wavefront decomposition into Zernike polynomials, the optical quality and types of aberrations can be assessed for the full parameter space that is possible for postoperative IOL positions. Technologically the manufacturing of the artificial cornea lens, required for the model eye, is very challenging. Apart from this, the measured decentration induced types of image aberrations show good agreement with results from a numerical simulation for three different typical lens designs under two different illumination conditions. Findings from this thesis can be a major contribution to further improve the current test standard, in order to test IOLs under physiological conditions and considering postsurgical lens displacements.

Contents

Kurzfassung **ix**

Abstract **xi**

Contents **xiii**

1 Introduction **1**
- 1.1 Motivation and Aim of the Work . . . 1
- 1.2 Problem Statement . . . 2
- 1.3 Methodological Approach . . . 2
- 1.4 Mathematical Notation . . . 3
- 1.5 Structure of the Thesis . . . 4

2 Medical Background **5**
- 2.1 The Human Eye . . . 5
- 2.2 Cataract and Cataract Surgery . . . 10

3 Physical Background **21**
- 3.1 Ideal Imaging Systems . . . 21
- 3.2 Ray Optics of an Imaging System . . . 23
- 3.3 Geometric Errors . . . 26
- 3.4 Wave Optics and Diffraction Errors . . . 32
- 3.5 Polychromatic Errors . . . 36
- 3.6 Characterization of Image Aberrations . . . 39
- 3.7 Summary Physical Image Formation . . . 47

4 Experimental Setup **49**
- 4.1 Numerical Simulations . . . 49
- 4.2 Optomechanical Model of the Human Eye . . . 54
- 4.3 Setup for Measuring the Modulation Transfer Function . . . 60
- 4.4 Setup for Measuring the Wavefront Aberrations . . . 65
- 4.5 Demonstrator for Visual Impression . . . 71
- 4.6 Summary on the Experimental Setup . . . 73

5 Results **75**
5.1 Numerical Simulations 75
5.2 Measurement Results 90
5.3 Characterisation of the Optical Projection Device 111
5.4 Summary: Cumulative Optical Performance 112

6 Discussion & Outlook **113**
6.1 Modifications on the ISO Model Eye 113
6.2 Aberrations Induced by Post–Surgical Intraocular Lens Displacements 114
6.3 Remarks on the Methodological Approach and Experimental Setup . . 118
6.4 Conclusion – Contribution to the Field 122
6.5 Outlook 123

A Conversion Error in the ISO 11979–2:2014 **125**

B Cornea 2 Surface Measurements **131**

List of Figures **135**

List of Tables **147**

List of Acronyms **149**

Bibliography **151**

CHAPTER 1

Introduction

This chapter describes the motivation for testing the optical quality of intraocular lenses regarding their tolerance to postsurgical tilt and decentration within the human eye. In the problem statement, the technical difficulties to be solved are defined. The methodological approach briefly describes how these difficulties are addressed. An explanation of the mathematical notation, coordinate systems and sign conventions for all mathematical considerations which are used throughout this thesis is given. The chapter closes with a general description of the structure of this thesis.

1.1 Motivation and Aim of the Work

Cataract is a clouding of the eye lens. In its early stage vision is deteriorated due to a reduced contrast sensitivity, progressed cataract can result in blindness [1]. Worldwide 39 million people are estimated to be blind, where cataract is responsible for approximately half of all blindnesses [2, 3]. The effects of this disease can effectively be treated by a surgery, where the clouded natural lens is removed and replaced by an artificial lens, a so called Intraocular Lens (IOL) [4]. In Austria this intervention was performed 102.973 times in the year 2015[5]. As explained in detail in section 2.2 IOLs are commonly inserted through a small incision, where the IOL is folded to fit the dimensions of this small incision. Inside the eye the IOL unfolds and small side structures on the IOLs, called haptics, should hold the lens centered in place within the eye. It is well known that IOLs can slightly move within the eye. It is well known that these decentrations can induce aberrations and thus can decrease vision quality [6, 7, 8, 9]. It is reported that this may even occur after a complication free surgery [10, 11].

The International Standards Organization (ISO) 11979–2 defines how IOLs have to be tested[12]. According to the standard, the IOL is tested within a model eye. Originally this model eye uses an aberration free model cornea. Since the human cornea is not free of Spherical Aberration (SA), the analysis with the ISO model has the limitation that the interaction between IOL aberrations and corneal aberrations cannot be correctly investigated [13]. The standard has been extended by adding a model cornea with a physiological amount of corneal SA [14, 15]. But still well known asymmetries in the normal human eye [16] and simulation of postoperative IOL tilt and decentration are still not included in the current standard.

These findings highlight the need for a novel well-engineered test method, which enables to test modern IOL design under physiological conditions by taking into account the effects of postoperative lens tilt and decentration.

1.2 Problem Statement

To eliminate the issues addressed above, a new test procedure for IOLs has to be devised. This thesis provides answers to the following questions:

- What are the necessary modifications to the ISO model eye, to test IOLs in an optical configuration, which is in agreement with the physiology of the human eye?
- Which image aberrations are induced by post–surgical IOL-displacements.
- How can post–surgical IOL displacements be reproduced with in a model eye under conditions close to those in the natural human eye?
- How can these post-surgical IOL displacements be characterized, regarding their influence on optical quality criteria regarding the quality of vision?

Providing solutions to these problems, this thesis contributes to the field of IOL–testing: It delivers a novel test procedure for IOLs, which is more informative than the current standard. By an automatic image characterization of systematically tilted and decentered IOLs within a model eye with physiological optical properties, it is more realistic than similar approaches currently found in literature.

1.3 Methodological Approach

Literature research was conducted to find the optical properties best describing the normal human eye. These properties were modeled using an optical ray-tracing software (ZEMAX OpticStudio). IOLs with known optical design can be included in this numeric computer model. Using Mathworks MATLAB and the Application Programming Interface (API) of OpticStudio, parameters like lens position within the model eye can systematically be manipulated. Various measures to analyze and quantify the quality of the produced image were obtained from the numeric simulation.

An optomechanical model of the human eye was constructed. This model incorporates a holder for IOLs, which can automatically and precisely be controlled by two miniature actuators. With this setup IOLs can be tested regarding their imaging quality, which they would produce in a physiologic environment. Where the two actuators enable to simulate specific lens displacements with two degrees of freedom. To evaluate the optical performance a measurement setup, in accordance to the current ISO standard, was built around the model eye to quantify the image quality. In addition, two measurement setups were developed, which allow for a more detailed characterization of the produced images. In detail, the individual image aberrations were extracted from the wave-front deformation, which is measured by a Harmann-Shack Wavefront Sensor (WFS). With a last setup, the image of the model eye can be projected onto the retina of a healthy subject, this setup allows for future investigation of the visual performance by including the human visual perception.

1.4 Mathematical Notation

In all equations of this thesis a coherent nomenclature is used. Different font types are used to distinguish the variable types:

- **Scalar values and constants** are noted in the default math font (e.g. a, A)
- **Vectors** are noted in lower case bold letters (e.g. $\mathbf{a}$)
- **Matrices, scalar fields, vector fields and complex numbers** are noted in capital letters (e.g. $\mathbf{A}$)

Different symbols are found in literature for some constants and mathematical operators. In this thesis coherently the following notation is used:

- j is the imaginary unit $j = \sqrt{-1}$
- $\mathcal{F}$ is the Fourier transform
- $\mathcal{F}^{-1}$ is the inverse Fourier Transform
- $\otimes$ is a mathematical convolution
- $\odot$ calculates the autocorrelation

A coordinate definition which should be used for calculations in geometric optics is define in the standard DIN1335 "Geometrical optics – Nomenclature and definitions" [17]. These definitions and nomenclatures are also used in this thesis. These coordinate definitions, applied to the right eye, are depicted in Figure 1.1. Furthermore, the standard recommends to use an inverted comma to annotate parameters in image space; i.e. If P is an object point in an imaging system, the conjugated image point is noted as P'.

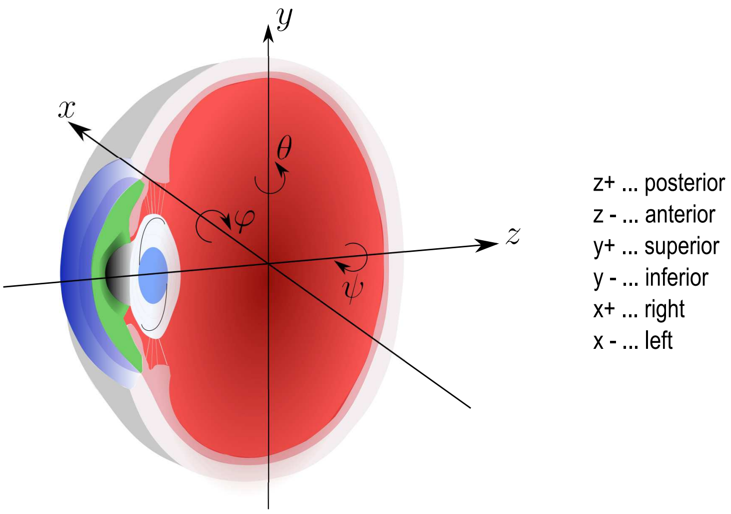

Figure 1.1: This graphic depicts the coordinate system for the eye, which is used throughout this thesis: All simulations, models and measurements describe a right eye. The z–axis corresponds to the OA, where the light propagation direction is the $z+$ as defined by DIN 1335 [17]. The x–axis is the left to right coordinate and the y–axis defines the inferior-superior coordinate. φ θ and ψ are the respective right–handed rotations around the $x-$, $y-$ and $z-$axis. Image adapted from [18]

1.5 Structure of the Thesis

After this introduction on the motivation and aim of this thesis in Chapter 2 the medical background will be illustrated - details on the structure of the human eye will be given here. An overview on the state of the art cataract treatment and recent development on IOL testing will be given. Based on that, detailed requirements for the proposed method are deduced, which are beyond the current state of the art. In Chapter 3 the underlying physical principles of optical image formation are discussed. The remarks in this chapter focus on the sources and characterization of image aberrations as these should be quantified by the experimental setups. In Chapter 4, based on three previous publications[19, 20, 21], the experimental setup, methodological approach and further developments beyond these publications are outlined in detail. Three IOLs were characterized with the proposed method. Results are given in Chapter 5 and compared with theoretical characteristics deduced from numerical simulations. Finally in Chapter 6 the results will be discussed in detail. Based on the findings from the results it will be deduced which modifications and further extensions to the proposed method would be useful e.g. to make the method applicable as an extension to the current test standard.

CHAPTER 2

Medical Background

This chapter provides the medical background necessary to understand the methodological approach for a novel test setup for IOLs. First the anatomy and physiology of the human eye will be explained in detail. The focus in this consideration lies on the optical properties of the human eye, as they have to be precisely reproduced by the model eye. In the second part of this chapter the fundamentals of cataract treatment are described, to clarify the requirements on IOLs to be used for cataract treatment.

2.1 The Human Eye

Vision is commonly seen as the most important sensory organ of humans. From a physical point of view the eye is responsible for generating and capturing the image. While the retina is responsible for capturing the image, the optical parts of the eye are responsible for imaging objects onto the retina. For the scope of this thesis the imaging part of the eye is of fundamental interest and explained here in detail. A cross section of the human eye is shown in Figure 2.1.

In the direction of light propagation, the **cornea** is the first refractive component of the human eye. With approximately 43 dpt it has the highest contribution of the total eye's refractive power of approximately 58,8 dpt [22]. Behind the cornea, a transparent fluid - the **aqueous humor** - fills up the space and maintains the eye's inner pressure. The **iris** acts as an aperture for the eye and is thus often referred to as pupil. There are mainly two mechanisms which control the pupil diameter: the first mechanism is to adjust to the correct amount of light, the second mechanism is responsible for increasing the depth of focus for the near accommodated eye by reducing the pupil diameter[22]. Behind the iris, the **crystalline lens** is located. With a varying refractive power it enables the human eye to accommodate to objects in varying distances. While the adolescent lens is able to change its refractive power by 14 dpt, the elasticity of the lens drops dramatically with age, and thus can typically only change its power by 3 dpt in the age of 45 years[22].

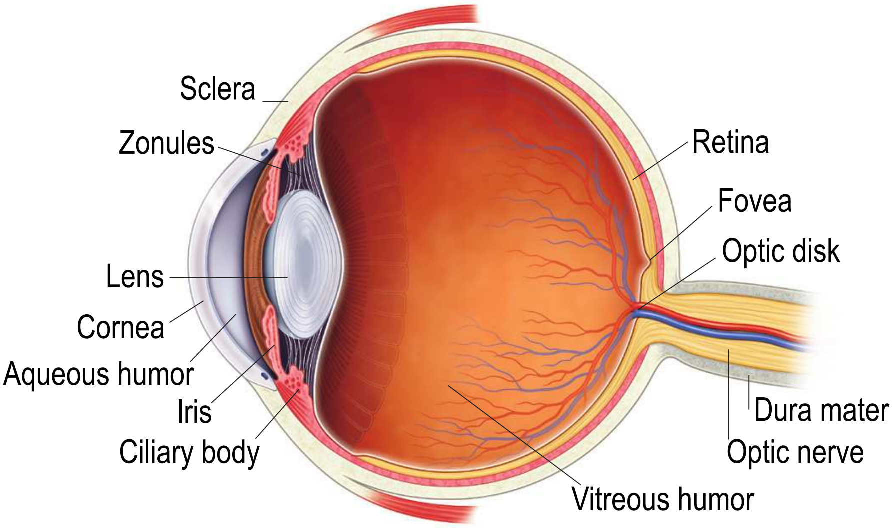

Figure 2.1: Anatomical structure of the human eye. Image used with permission from [1]

The lens is embedded within a capsule, which is suspended by microfibers, the zonules, within the ciliary body. The contraction of the ciliary body mussel, relax the tension in the zonules, which causes the eye lens adopt to a shape with a higher curvature (causing a higher refractive power) by it's own elasticity. Between the retina and lens a clear gel, the **vitreous humor**, is located. The **retina** is responsible for capturing the image, projected onto the rear end of the eye. The retina is a complex neuronal network, there are four types of sensory cells which are responsible for capturing the image:

- three types of cones: They are responsible for vision with bright illumination (photopic vision), colors and brightness can be perceptive by these cell types [1]
    - L–type: red-sensitive with an adoption maximum at 563 nm
    - M–type: green-sensitive with an adoption maximum at 532 nm
    - S–type: blue-sensitive with an adoption maximum at 414 nm
- rods: Rods have a higher light sensitivity than cones, but no color sensitivity. Thus they are responsible for vision in dark environments (scotopic vision). Rods are most sensitive at green light with an absorption maximum around 498 nm [23].

The highest density of cones can be found on the **fovea**. The fovea is the center of the field of view and provides the area of sharpest sight. The image shapes, and accordingly the density of cones, dramatically drops with increasing field of view. Figure 2.2 depicts the accurateness of vision vs. the visual field angle. Cone density in the fovea is approximately 2μm. This high density leaves no room for rods at the fovea, resulting in a maximal

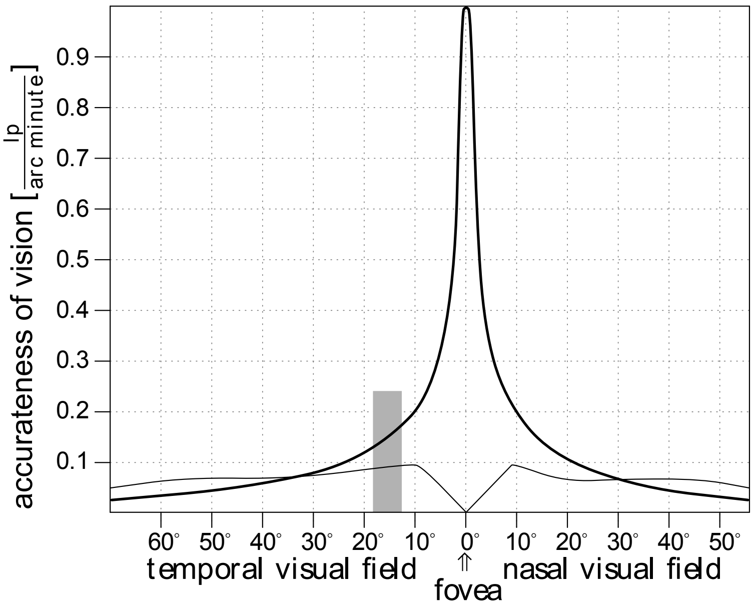

Figure 2.2: Accurateness of human vision. Thick line depicts the accurateness of vision for photopic vision with respect to the visual field angle. Thin line represents the accurateness for scotopic vision. The plot reveals that the maximal visual accurateness is only possible in bright illumination (photopic view) and in the fovea, the spot on the retina with the highest density of cones. The accuracy quickly drops down in the peripheral field of view. The gray bar represents the location of the blind spot. Data source for image: [22]

accurateness of vision around 10° off center. Considering the assessment of quality of vision, this information is crucial to identify the required visual accuracy vs. field position to restore normal human vision.

2.1.1 Generic Models of the Human Eye

Countless scientific work has been conducted in the past to describe the optics of the human eye [16, 24, 25, 26, 27, 28, 29, 30, 31, 32]. Such schematic models can be generated by obtaining biometric data from healthy human eyes e.g. by extensive literature review. These biometric data can include Axial Length (AL), Anterior Chamber Depth (ACD), radii of surface curvatures, asphericities, refractive and dispersion data of ocular media. Data with lacking empirical results or accuracy can be modeled to produce optical aberrations which match experimental data.

Liou and Brennan found that the SA predicted by available model eyes does not accurately resemble what is measured in living eyes[33]. Following this analysis they proposed a more accurate schematic model [16]. This model is, up to the present day, still used in the current standard for testing IOLs[12] and for optical design and design verification of

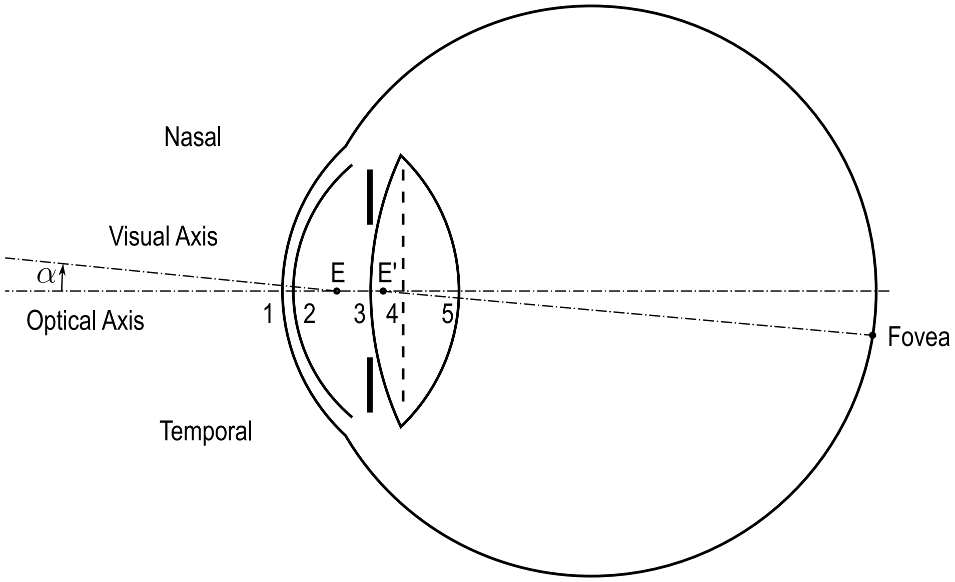

Figure 2.3: Schematic drawing of the model eye according to Liou and Brennan (see Table 2.1 for parameter values) [16]. E is the virtual image of the pupil center through the cornea; E' is the virtual image of the pupil center through the crystalline lens. Note: In contrast to all other simulations and models in this thesis this figure depicts a left eye

IOLs [9, 34, 35, 36, 37, 38]. Based on this wide use and recognizing that it accurately models the optic physiology of the human eye, all investigations in this thesis are based on the Liou and Brennan model eye. All necessary details are given in the following section.

2.1.2 Schematic of the Liou and Brennan Eye

Figure 2.3 depicts a cross-section through the optical components of the Liou and Brennan eye. Thicknesses and optical properties are given in Table 2.1.

A radius of curvature for the retina is not given in the Liou and Brennan paper [16]. As it will be outlined in Section 4.1 the exact values for the AL and the radius of curvature of the retina are not critical for the purpose of this thesis, as these values have to be adapted anyway to obtain meaningful results with a specific IOL.

Dispersion Models within the Liou and Brennan Eye

Typical optical media have in common, that they have wavelength dependent refractive indices, this causes wavelength dependent properties which go along with polychromatic aberrations which will be discussed in Section 3.5. To mimic these properties, the model

---

[1] Surface number corresponds to the numbering in Figure 2.3

[2] This surface coincides with the pupil position.)

Table 2.1: Structural parameters for the model eye in Figure 2.3. Source: [16]
Gradient refractive indices are calculated with $n(w, z) = n_{00} + n_{01}z + n_{02}z^2 + n_{10}r_{xy}^2$
z ... distance along the OA, r_{xy} ... radius normal to z
Grad A: $n_{00} = 1.368$, $n_{01} = 0.049057$, $n_{02} = -0.015427$, $n_{10} = -0.001978$
Grad B: $n_{00} = 1.407$, $n_{01} = 0.000000$, $n_{02} = -0.006605$, $n_{10} = -0.001978$
r ... radius of surface curvature, c ... asphericity, d ... thickness, n ... refractive index

Surface Name	#[1]	r [mm]	c	d [mm]	n at $\lambda = 555$ nm
Cornea anterior	1	7.77	-0.18	0.50	1.376
Cornea posterior	2	6.40	-0.60	3.16	1.336
Crystalline lens anterior[2]	3	12.40	-0.94	1.59	Grad A
Crystalline lens middle	4	∞	–	2.43	Grad B
Crystalline lens posterior	5	-8.10	+0.96	16.27	1.336

eye should be built close to the physiological dispersive properties of the human eye. Due to the fact that the tissue of all optical components of the human eye have a high water content, the dispersive properties of the ocular media are close to that of water; thus the Liou and Brennan model eye uses dispersion data from water for all optical components in the human eye [16]. As basis for calculating the wavelength dependent refractive index of water, Liou and Brennan used the measurements from Sivak and Mandelman [39]. The refractive index of water n_{water} can be calculated with:

$$n_{\text{water}}(\lambda) = 1.3847 - 0.1455\frac{\lambda}{1\ \mu\text{m}} + 0.0961\left(\frac{\lambda}{1\ \mu\text{m}}\right)^2 \tag{2.1}$$

Given that equation, the refractive index of water for $\lambda = 555$ nm can be calculated by $n_{\text{water}}(555\text{ nm}) = 1.3335$. With that, the wavelength independent constant 1.3847 can be rewritten as $1.3847 = n_{\text{water}} + 0.0512$. Therefore the wavelength dependent refractive index for any ocular media can be calculated by[16]:

$$n_{\text{media}}(\lambda) = n_{\text{media}}(555\text{ nm}) + 0.0512 - 0.1455\frac{\lambda}{1\ \mu\text{m}} + 0.0961\left(\frac{\lambda}{1\ \mu\text{m}}\right)^2 \tag{2.2}$$

where $n_{\text{media}}(555\text{ nm})$ is the refractive index of the ocular media as given in Table 2.1.

Asymmetries in the Liou and Brennan Eye

As outlined in Section 2.1, the fovea is the point of sharpest sight, and thus used as center point in various investigations. The axis connecting the virtual image of the intersection from pupil and OA (E') and fovea is referred to as visual axis, see Figure 2.3. As outlined in Figure 2.2, along the visual axis best color vision at photopic illumination is possible. This axis is the center of the field of view. The common line of all centers of curvatures is referred to as OA. According to the Liou and Brennan model eye, the visual axis is tilted with respect to the OA nasally [16]. For the angle α between optical and visual axis the Liou and Brennan eye uses 5°.

The pupil is usually slightly shifted nasally by 0.5 mm [40]. There are indications that the pupil decentration changes with pupil size, and thus with illumination brightness, but based on the investigated research, Liou and Brennan could not find specifications for a consistent change [16, 41, 42]. Therefore Liou and Brennan modeled the pupil decentration with a constant value of 0,5mm into nasal direction (= negative x direction for the right eye). Walsh and Charman [43] found that the pupil decentration has little effect on the ocular performance for small pupil sizes. Liou and Brennan provided the first schematic model eye which provided both asymmetries α angle and pupil decentration. The α angle decreases the Contrast Sensitivity (CS) compared to a centered system, but pupil decentration outbalances some of these errors [16].

Beside the OA and the visual axis, as depicted in Figure 2.3 many more axis are defined in literature: e.g. pupillary axis and line of sight are defined in addition to the optical and visual axis. Unfortunately across the relevant literature conflicting definitions can be found [44]. As the Liou and Brennan eye is chosen as reference model for the human eye, in this thesis only the visual axis and OA, as defined by their model, are used.

2.2 Cataract and Cataract Surgery

Cataract is a clouding of the crystalline lens. Aging is by far the most common cause, but also other factors as disease, trauma, medications and genetic disposition are known to influence cataract formation [45]. Due to an aging population a growth in need for cataract treatment can be predicted [46]. Cataract can effectively be treated via surgery. In Austria the cataract surgery is among the most performed surgical interventions by absolute numbers [5]. It is thought to be the most common and most effective surgical procedure in any field of medicine [47].

Until the 1960s and later, the clouded lens was simply removed without replacement [47]. With the missing refractive power of the lens, which approximately contributes for $\frac{1}{5}$ of the total refractive power, this resulted in a significant hyperopia. Thick glasses were required.

Mainly three techniques for extraction of the cataract exist. Intracapsular extraction, extracapsular extraction and phacoemulsification. Today by far the most common ($> 99\%$) surgical procedure is the phacoemulsification [47]. At phacoemulsification only a small incision 1.8 to 3.9 mm is needed, through which an ultrasonic tool is inserted. The lens' nucleus is emulsified by ultrasonic waves. With a suction tool emulsified pieces of the nucleus are aspirated. The capsule is left intact. Foldable IOLs can be inserted in the capsular bag without enlarging the small incision.

After the lens is removed from the capsular bag, the folded IOL is inserted with an syringe-like tool. Within the capsular bag the lens can unfold [48, 49]. Side structures, called haptics (see Figure 2.4), as well as mechanical properties like elasticity influence the unfolding procedure and lens placement within the remaining capsular bag. Therefore different materials and haptic designs will be discussed in the next section. It is known that many postoperative factors, e.g. wound healing, can lead to further displacement of the IOL within the eye after surgery [50, 51, 52, 53, 54]. Chang et al. [53] found that the surgical approach, e.g. location of the incision, influences the postoperative lens deceleration, which was measured by Scheimpflug imaging.

Scheimpflug imaging and Purkinje imaging are the main methods for assessing postoperative IOL displacements. Due to the dependence on many factors, a wide variety of values for mean postoperative decentration and tilt can be found. For the purpose of this thesis, the order of magnitude is of importance to test IOLs in a relevant range regarding their tolerance to postoperative displacements. Based on a literature research on Pubmed a common range of approximately 0.3mm ± 0.2mm for the mean decentration and 2° ± 1° for the mean postoperative lens tilt can be found. This is in accordance with many publications on this field [55, 56, 10, 9, 52, 57]. Not all of these publications give an information on the direction of these values and sometimes different axis are chosen as reference. As mentioned above, inconsistent definitions of these coordinates can be found in literature. Covering the full relevant range, the reported mean value plus 1.5 times the reported spread will be investigated. This results in a range of $x = \pm 0.6$mm for decentrations and $\theta = \pm$ 3.5° for tilts in the coordinate system defined in Figure 1.1.

2.2.1 Intraocular Lenses

Prior to the surgery, precise biometry of the patient's eye is performed. This step has become the most important in modern cataract surgery [58]. Based on these measurements, the best IOL suited for the patient's eye is chosen. The aim is, that after cataract surgery patients have sharp vision without the need for glasses. Biometric measurements cannot be done with perfect accuracy. Furthermore, the calculation formulae rely on a number of assumptions on the whole surgery process and the postoperative healing. Norrby [59] evaluated the effect of these variables and found that the biggest source for error (35,5%) is the prediction of the post-operative IOL position. From the biometric measurements the AL (17.0%)and keratometry measurements[3] (10.1%) are the biggest contributors to the error.

Dealing with these uncertainties in calculating the optimal IOL power is still a not completely solved problem, but formulae are constantly refined [60]. The newest formulae, which are currently used today, are called *theoretical formulae*. These formulae are based on regression models. Examples of modern formulae which can be found in today's clinical practice are e.g. Holladay 1[61], SRK/T[62], Hoffer Q[63], Holladay 2 [64], Olsen[65] and Haigis[66]. Theses formulae differ in the number of weightings and explanatory predictor variables; one factor these formulae have in common is the effective lens position – the effective distance between the anterior surface of the cornea and the IOL in *thin lens approximation*[4][60].

---

[3] Keratometry is the measurement of the shape of the cornea, from which the cornea's refractive power can be calculated

[4] See Section 3.2.1 for definition of the *thin lens approximation*

Optical Design of Intraocular Lenses

In the healthy human eye, the lens is responsible for accommodation, the ability to focus on different distances. Today the majority of implanted IOLs are monofocal IOLs, implantation of monofocal IOLs is still standard of care in the western world [67, 68]. This means that these lenses have a fixed focal length which is chosen preoperatively to provide best focus for a desired distance, either for spectacle free vision in the distance or for near work [69].

Monofocal IOLs are typically designed with a biconvex shape, where the back surface radius of curvature can be equal higher or lower than the front surface radius of curvature [70, 71]. Classical IOLs have *spheric* surfaces. It will be outlined in Section 3.3.2 that spherical surfaces introduce SA. Also the cornea itself produces SA. To counterbalance SA in the eye, aspheric surfaces can be included in the optical design [70]. In the category of aspheric IOLs there are two types: *"aberration– free"* IOLs have their intrinsic SA wholly corrected; *"aberration–correcting"* IOLs have a negative SA to partly or totally compensate for the – in average – positive SA of the human cornea [72]. In a study Pieh et al. [73] found that with ongoing tilt and decentration customized IOLs, which aim to correct the SA of the eye, loose their advantage compared to "aberration-free" lenses. It is concluded that "aberration-free" are the safest way.

Toric IOLs aim to reduce corneal astigmatism. Astigmatism will be discussed in detail in Section 3.3.3. In this case the eye exhibits a different refractive power, depending on the orientation perpendicular to the z–axis. In this case also the relative rotation around the z–axis (ψ) between IOL and eye is essential for proper function.

To overcome the limitation of a fixed focal length, **Multifocal IOLs** were developed. Multifocal IOLs are classified in refractive, diffractive or combined design. Refractive lenses have annular zones with different refractive power. Diffractive designs use concentric diffraction patterns which provide focus at different distances. Dividing the light in different distance focuses changes the physiology of vision – visual symptoms such as halos, glare, and lower contrast sensitivity may occur [74]. Greenstein and Pineda [75] reviewed the differences between multifocal IOLs and monovision for spectacle independence. *"Monovision uses traditional monofocal lens implants to treat the dominant eye for emmetropia , and the non-dominant eye for myopia."*[75]. They found no difference in patient satisfaction, complete spectacle independence was better achieved by the multifocal approach, but for effects like glare and halos, the possible need for IOL exchange and financial cost, the monovision approach is superior[75].

Addressing the problem of *"loss in contrast vision, halos and glare resulting in visual quality being imperfect at all distances"*[69] of multifocal IOLs, accommodating IOLs were developed in the last years. *"There is no accommodating IOL on the market that allows full restoration of accommodation and recent studies showed that the accommodative effect is weak to not existing[76]."*[69].

As it is known that the optical performance of more advanced lens designs, which aim to correct for more optical aberrations, are more sensitive to postoperative lens displacements

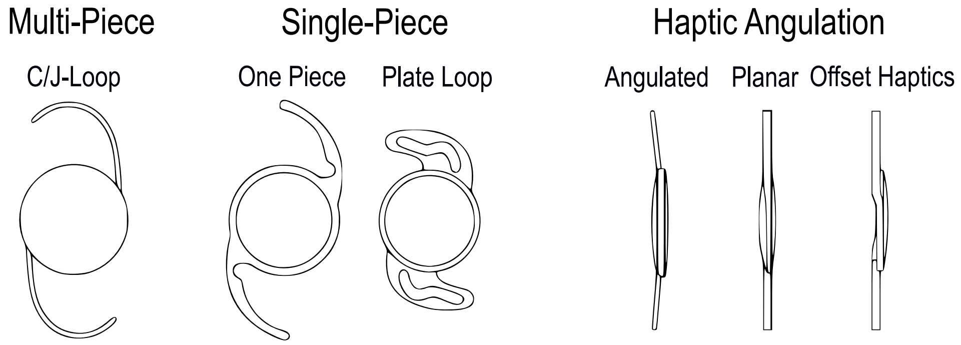

Figure 2.4: IOL haptic types: Three piece IOL are made of three pieces, where the material of the optics and the haptics can be different. Haptics can be L or C -shaped. One–piece IOLs are made of one material, haptics can have fingers. Graphics adapted from [70]

[14, 73], as well as the problem that the estimation of the post–operative lens position is the biggest contributor to errors in selecting the correct IOL [59], emphasizes the development of a test procedure, which takes into account post–operative lens displacements. Due to the fact that the monofocal design is the most widely used, only monofocal lenses will be evaluated in this theses. In Section 6.3.5 it will be discussed to which extend the setup can be used for other optical designs, described in this section.

Haptic Design and Lens Materials

The diameter of the optical part of an IOL is usually around 6mm in diameter [70]. This is sufficient for a proper optical function and allows a small incision in the surgical process. As the optical part of the IOL is much smaller than the human lens, additional structures have to be added to the lens to hold in place. Figure 2.4 depicts different haptic types.

The first material used for IOLs was Polymethylmethacrylate (PMMA). This material is rigid and thus requires large incisions, therefore it is no longer preferred today [71]. As mentioned above, foldable IOLs are preferred because they just require a small incision of about 2mm. These lenses are typically made from Hydrophobic Acrylic (HPoAC) or Hydrophilic Acrylic (HPiAC). Silicon was the first available material for foldable IOLs, a decline in use is reported in the past decades [70].

In multipiece IOLs the haptics and the optics are typically made of different materials, in contrast to that with new manufacturing methods single piece IOLs can be produced in one step[70]. Savini et al. [77] found that three-piece IOLs may yield better refractive outcomes than one-piece IOLs. This may be the case because the rigid haptics of 3-piece IOLs still exert more pressure against the capsular bag than in one–piece haptic designs. In contrast Chen et al. [78] tested a specific one–piece acrylic IOL, which showed clinically only not relevant displacements during the first three month.

As literature provides pros and cons for the different designs and haptic angulation, it was concluded that the test procedure developed in this thesis should permit testing of all types. This will be addressed in Section 4.2.5.

2.2.2 State of the Art in Intraocular Lens Testing

This section will outline the state of the art for IOL testing. This will be done from the normative point of view (tests accounting to current regulations), non standardized tests as done by research groups in this field and an overview on state of the art devices available on the market.

Intraocular Lens Testing according to ISO 11979-2

The ISO 11979 is a series of standards under the title "Ophthalmic implants – Intraocular lenses" which consists of 10 parts:

- Part 1: Vocabulary
- Part 2: Optical properties and test methods
- Part 3: Mechanical properties and test methods
- Part 4: Labeling and information
- Part 5: Biocompatibility
- Part 6: Shelf-life and transport stability testing
- Part 7: Clinical investigations
- Part 8: Fundamental requirements
- Part 9: Multifocal intraocular lenses
- Part 10: Phakic intraocular lenses

Since this thesis deals with the optical properties of IOLs, the relevant standard is the ISO 11979-2. To the date of this thesis the current latest version is the ISO 11979-2:2014.

MTF-Measurement according to ISO 11979-2:2014 Annex C: In annex C of the standard, a procedure for Modulation Transfer Function (MTF) measurement is defined. The physical background of the MTF can be found in this thesis in section 3.6.2. The IOL to be tested has to be placed within a model eye. The IOL has to be centered with the OA of the model eye, where a maximum decentration of 0,1 mm has to be guaranteed. Two model eyes are defined in the standard: 1) For a spherical IOL a model cornea with a minimal SA is used (Figure 2.5-a); 2) Aspheric IOLs are tested a with model cornea with a specified SA (Figure 2.5-b). Based on the SA of the IOL to be tested the standard defines the appropriate characteristics for the model cornea [12].

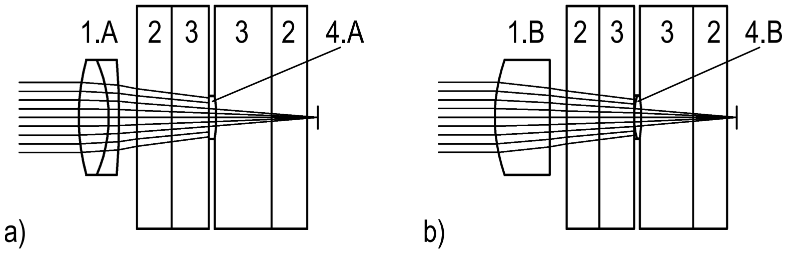

Figure 2.5: model eyes according to ISO 11979-2:2014 a) "model eye 1"; b) "model eye 2". 1.A model cornea: achromat with a minimal spherical aberration, 1.B model cornea with a known spherical aberration; 2: glass windows, 3: liquid medium in which the IOL is embedded. A refractive index of 1.2336 (refractive index of water) is specified, 4.A spherical IOL which is tested within the model eye. 4.B aspherical IOL which is tested within this model eye should counterbalance the aberrations of the model cornea 1.A, Image source: adapted from [12]

For lens assessment a light source with a wavelength of 546 nm ± 10 nm and Full Width at Half Maximum (FWHM) of 20 nm is required. An aperture diameter of 3 mm is used at the position of the IOL.

The test standard requires that the IOL, tested with the "model eye 1" (Figure 2.5-a), fulfills one of the following requirements:

- The modulation at 100 lp/mm is $\geqslant$ 0,43
- The modulation at 100 lp/mm is $\geqslant$ 70% of the maximal achievable modulation for the IOL–design, but at least $\geqslant$ 0,28

For a test with "model eye 2" the second criteria has to be fulfilled.

Before 2007 the "model eye 2" has not yet been included into the standard [15]. In 2008 Sverker Norrby, PhD, a main contributor to the current standard at that time[5], stated regarding the "MTF at 100 lp/mm is $\geqslant$ 0,43": *"For this particular part of the standard, the primary purpose is to ensure manufacturing quality, and not in vivo performance"*[15]. Furthermore he stated: *"The ISO eye model was conceived before the introduction of aspherical lenses. Because such lenses are designed to reduce or compensate for the spherical aberration of the human cornea, the ISO eye model is not suitable for assessing their performance in the human eye*[15].

Because of the aberration free model cornea in "model eye 1", this model is useful to assess spherical IOLs, since a deteriorated MTF arising from the SA of the IOL can be measured. If an IOL is designated with a negative SA to counter the positive SA of the normal human eye, the "model eye 1" is no longer useful since both, a negative and a positive SA of the IOL, deteriorate the MTF measured. Thus Norrby et al. [14] suggested a model eye with a physiologic amount of SA in the model cornea. Furthermore they found that only a lens, which is modeled close to physiological dimensions, provides correct results for objects at finite distance as well for objects at infinite distance; the ISO–model gives wrong results if the object is at finite distance [14].

---

[5] S. Norrby was leading involved in the development of the standard [79] and continued contributing and further developing test methods

Despite the introduction of the "model eye 2" the current standard ISO 11979-2:2014 [12] still mentions in Clause C.2: *“No inference should be made to performance in real eyes”*.

Not Standardized Intraocular Lens Testing

The high complexity of cataract treatment (postoperative lens displacements, different optical designs, physiology of the human eye), as already outlined in this thesis, is not sufficiently reproduced by the current ISO test standard. To account for these shortcomings, many researchers perform optical bench tests to mimic specific aspects. In this section, research which is closest to the aim of this thesis (investigation of the optical performances for tilted and decentered IOLs in a physiological environment) is reviewed. The research is put in order by appearance in literature.

Relevant interesting work has been conducted by **Pieh et al.** in 2009: In an in vitro optical bench setup spherical, aberration–free and aberration–correcting IOLs are tested with model corneas with different amounts of SAs. The effects on the optical performance when the IOL is shifted along the x–axis and tilted around the y–axis are tested. A decentration of the pupil as well as the tilt between the optical and the visual axis were not taken into account. The optical quality was assessed by directly measuring the Point Spread Function (PSF). The IOL is manually displaced within a wet cell by manipulating a goniometer holding the lens. Due to that fact, combined movements decentration and tilts are difficult to measure. Full parameter field for all possible combinations of decentrations and tilts were not tested.

In a 2011 study by **McKelvie et al.** [80] the influence of pupil size and IOL tilt and decentration was measured in an optical bench setup. A commercial Zywave aberrometer (Bausch & Lomb, Rochester, NY) in combination with a physical model eye was used. The physical model[81] which is used in this study does not incorporate the symmetries of the Liou and Brennan model eye. They used 4 levels of decentration (0.0 mm, 0.5 mm, 1.0 mm and 1.5 mm) along the x–axis and 4 levels of tilt (0 °, 2°, 4° and 6°) and three different pupil diameters (2 mm, 3 mm and 5 mm). The tilt and decentration levels appear to inadequately sample the relevant range of clinically observed postoperative tilt and decentrations as cited above.

Kim et al. [82] (2015) developed an optical bench methodology system to assess aspheric toric IOLs. They analyzed the influence on image quality of changing pupil diameters and lens tilt and decentrations. They assessed Wavefront (WF) aberrations with an Hartmann-Shack WFS (WFS150-5C, Thorlabs Inc.) in parallel with the MTF with a camera capturing the retinal image. As artificial cornea they used an IOL with high refractive power (40 dpt) and SA like a typical cornea. The artificial cornea was not embedded into an wet cell. The IOL to be tested was immersed into a wet cell. As IOL's optics are designed in water immersed environment and because information on the optical design like surface radii is lacking, it remains unclear from the publication how precisely this lens represents the physiological conditions of a natural cornea. Tilts and decentrations of the IOL to be tested were analyzed separately, but never combined tilts and decentrations were analyzed.

In a recent (2016) paper by **Bonaque-Gonzalez et al.** [83] a test setup for measuring optical power, MTF, PSF and WF aberrations in presence of IOL tilt and decentration was presented: The system consists of a wet cell, containing the IOL. The artificial cornea consists of a plano–convex lens with a spherical front surface and a focal length of 26.1 mm in air. The pupil is placed 3 mm behind this lens. An artificial retina, stainless steel with white acrylic paint, is used as diffuse reflector. A commercial aberrometer (irx3; Imagine Eyes, France) with an measurement wavelength of 780 nm is used. All other optical measurements (MTF, PSF) are not done directly, but deduced from the WF data. The IOL can be rotated around the y-axis (±4° in 1° steps) and shifted along the y-axis (from 0 to 0.4 mm in 0.1 mm steps). Compared to the work presented in this thesis the setup from Bonaque-Gonzalez et al.[83] supports only quite coarse steps (0.1 mm and 1°). As the IOL is tilted around the y-axis and shifted along the y-axis the tilt creates asymmetries about the y-z plane, where the shifts create asymmetries about the x-z plane. Thus counterbalance or amplification of image aberrations by the combination of the presence of tilts and decentrations at the same time cannot be exhibited as in a setup where the IOL is shifted along the x-axis. Also all other asymmetries, shift of the pupil and tilt of the visual axis with respect to the OA, are asymmetries about the y-z plane. These physiological asymmetries, as well as the real aspheric cornea shape, were not taken into account in their setup. As the measurements are not directly done with the standardized wavelength of 546 nm, the results must be corrected for the chromatic aberrations to be comparable with standardized tests. This is only possible if the dispersion data of the IOL to be tested is known.

In another recent (2016) work by **Ortiz et al.** [84] the effect of IOL decentration was evaluated in an optical bench setup. ISO 11979–2 compliant MTF measurements are performed with an ISO compliant artificial cornea. Due to the fact that the design is strictly consistent with the standard, it does not include the physiological parameters of the human eye, the setup simply adds the ability to assess lens decentrations.

The latest work in this field was conducted by **Perez-Merino and Marcos**[85]: IOLs were tested in a physical model eye, the IOL can be rotated within the model eye by a micron rotational–translational stage. The IOL–holder and the retina were manufactured with a 3D printer. Laser ray tracing is used to measure the total WF aberrations. MTF, PSF and Strehl Ratio are derived from the WF data. Three different artificial corneas with a different amount of SA were combined with 18 different IOLs. This leads to a considerable experimental complexity, conversely only three decentration levels 0 mm, 0.4 mm and 0.7 mm were tested. Only decentrations in one direction is reported in the paper. Thus asymmetric effects, which occur due to the human eye's asymmetry (see

Section 2.1.2), are not investigated. Also combined effects of decentered and tilted IOLs are not reported in the paper. For astigmatism they report increasing WF aberrations between 0.18 μm/mm and 0.26 μm/mm, coma increases with 0.19 to 0.39 /mm.

Commercial Devices for Intraocular Lens Testing

In addition to the experimental laboratory optical bench setups as discussed above, available commercial devices will be discussed here. This analysis is based on recent scientific work using such devices.

Fulan et al. [86] compares two commercial systems for testing IOLs. The authors outline the importance of such tests as, surprisingly, IOL producer are not required to report tolerance levels for the refractive power of their lenses. Due to several improvements in current state cataract surgery and lens design, near perfect refractive outcome is possible, so production tolerances are getting a significant influence factor [87]. The authors compare the test–devices **Kaleo-I** (Phasics S.A.Saint Aubin, France) and **IOLA Plus** (Rotlex, Omer, Israel). Both devices are designed to perform ISO 11979–2 compliant measurements. Over all a better performance is reported for the IOLA Plus. The obtained results were consistent for the assessing the MTF at 100 lp/mm quality criteria according to the ISO–Standard, but the authors report very unsatisfying results for the dioptic power measurements: *"For the reasons mentioned in the introduction on the relevance and importance of the subject, we believe that improvements are necessary in the manufacturing and calibration process to obtain more reliable commercial instruments for the characterization of IOLs and we encourage researchers to perform other studies like this one, comparing the performance of other instruments and techniques."*[86]. This further emphasizes that research in developing IOL test setups as done for this thesis is still highly relevant.

Trioptics, Germany provides devices for ISO compliant MTF measurement as well as optic power measurement (**OptiSpheric IOL**), for WF measurements of IOLs (**WaveMaster IOL**) and a wide variety of other parameters [88]. Such a device is used in current scientific studies e.g. [13].

The commercial devices clearly focus on ISO compliant MTF measurements and high reliability, this fact makes these devices inflexible to be used with experimental setups, like including physiological properties, IOL tilt and decentration. The large majority of current IOL testing methods does not take physiological conditions or postoperative lens displacements into account.

Requirements for a Novel Test Setup for Informative Test Results

It has to be mentioned that it can be difficult to draw conclusions on the clinical visual performance based on optical bench tests[89]. Recent studies [90, 89, 91, 92] conclude three major points which should be included into measurement procedures:

- The model eye should represent for spherical and chromatic aberrations.
- White light should be used. Since this represents normal viewing conditions.[6]
- Modeling the visual acuity should be done from data containing multiple spatial frequencies.

Additionally, in distinction to the most relevant work presented above, in this section the setup developed for this thesis features:

- The optical components of the model eye are designed as close as possible to the human anatomy and physiology as described by [16]. This includes a custom–made PMMA–cornea including an average SA at the cornea as suggested by Norrby et al., as well as all asymmetries like a decentered pupil and a tilt between the optical and the visual axis in combination with the possibility for modeling IOL tilt and decentrations, which could not be found in the work of other research groups.
- Tilts and shift can be automatically controlled by electromechanical stepper actuators. Finer steps in tilt and decentration can automatically be evaluated without the need for manual operation, which reduces error-prone manual adjustments, and increases repeatability of the measurements. As several levels of decentrations and tilts very soon lead to hundreds of individual configurations for each optical quality assessment. This might be the reason why other research groups only investigate pure tilts or pure decentrations or coarse steps for tilt and decentration to limit the experimental effort. With the presented setup only changing the pupil–size or the IOL to be tested requires manual manipulations. As the results will show, combined tilts and decentrations are relevant to be investigated.
- The model eye can be used within multiple measurement setups, thus different characterization methods can be compared to each other.
- The setups directly measure at a wavelength of 543 nm which corresponds to the ISO–standard and close to the peak sensitivity of the human eye. This is not done by all research groups. Directly measuring in the center of the visual spectrum requires no correction with dispersion data to make conclusions on the performance in the visual range. This is a major advantage as it avoids the problems if the dispersion data of the IOL to be tested is unknown.

---

[6] The model eye presented in this thesis correctly models dispersion, thus it permits measurements with white light, although measurements are done with monochromatic light. This fact is in detail discussed in Section 3.5.

CHAPTER 3

Physical Background

This chapter covers the necessary physical background of the proposed methods for testing the optical quality of IOLs. The physical principals of an imaging system such as the human eye, are discussed in this chapter. The first section covers the basic properties of an ideal imaging system. After the discussion of these ideal properties, causes of geometric and diffractive image aberrations are discussed in detail. In the end of this chapter the theory of quantifying these image aberrations are discussed.

3.1 Ideal Imaging Systems

In optics *an imaging system*, e.g. a simple lens, is a system where the light emitted from an object point P in any emission angle converges to a single image point P'. Such a system is depicted in Figure 3.1. This process can either be described in ray optics or in wave optics.

In **ray optics** or **geometric optics** the light is described in rays which propagate from the source to the detector. Ray optics is a correct approximation if the wavelength is small compared to spatial dimensions of the optical system. In **wave optics** the light propagation is described as the propagation of the electromagnetic wave. With that, phenomena such as interference and diffraction can be described correctly.

Both descriptions are useful to describe the image formation within the human eye. The two views on describing optical phenomena are closely linked to each other: In wave propagation, surfaces of constant phase are denoted as WF. Light rays describe the propagation direction of the light or, in other words, the propagation direction of the electromagnetic wave. Consequently the light rays are perpendicular to the WF. An ideal imaging system can equally be described in ray and wave optics as depicted in Figure 3.1: The object point P emits light. To fulfill the imaging condition, all light rays emerging from point P must geometrically intersect in the same point P' on the image

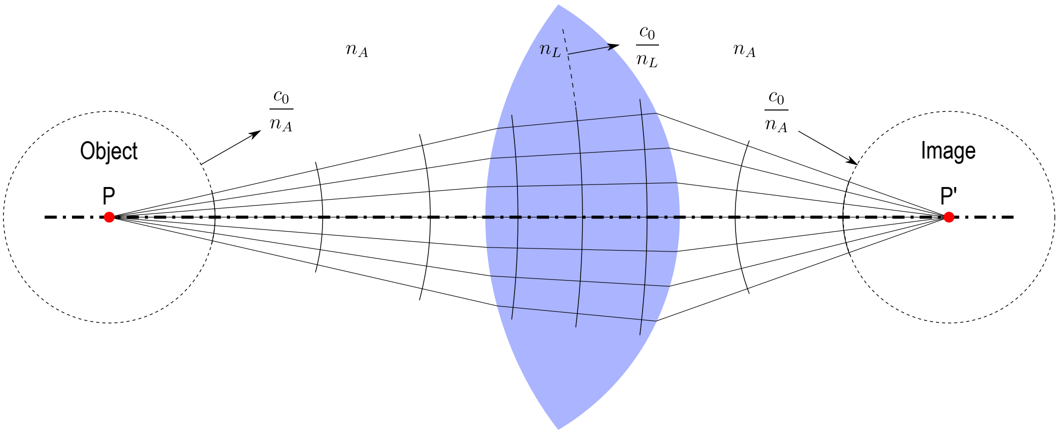

Figure 3.1: Analogy between ray and wave optics in a simple imaging system: Object point P emits light in all directions, drawn as straight light ray, since the light propagation in all directions in the homogeneous medium with the refractive index n_A is the same, the planes of constant phase (the WF) are concentric around P. When the light hits the lens, which has a higher refractive index n_L, the light rays are refracted. Light propagation is slower in the lens, thus the planes of constant phase are closer to each other. Behind the second lens surface light is refracted again. The rays converge to the image point P', as P' is the geometric intersection of all light rays emerging from the object point P.

plane. Assuming a homogeneous medium, light propagates equally fast in all directions, thus the WFs are spheres around the point P. To fulfill the imaging condition for the wave optical description, the imaging system has to manipulate this divergent spherical wave in such a way that the WF is converted to a convergent spherical wave, with the object point P' as center.

An alternative useful description of the imaging condition is the use of the Optical Path Length (OPL), which is defined by:

$$\mathrm{OPL} = \int_C n(s)ds \tag{3.1}$$

where $n(s)$ is the local refractive index as a function of the distance s along the optical path (e.g. a light ray) C. The Fermat's principle, named after the French mathematician Pierre de Fermat, states *"that the actual path between two points is the one for which the OPL is stationary with respect to variations of the path"*[93]. Applied to an imaging system, such as depicted in Figure 3.1, this means that all light emitted from P converges to the same point P', if all light rays have the same OPL. Light rays, which take geometrically the shortest path, have to be retarded by the optical system, compared to the rays which take a longer geometric path. This is a simple way of describing why a converging lens, with a higher refractive index n than the surrounding material, has to be thicker in the center than off center.

The WF is difficult to be described mathematically and is not necessary to describe the concept of image formation in the first place, but necessary to describe diffraction effects as shown in Section 3.4.1.

3.2 Ray Optics of an Imaging System

Linear matrix equations are a powerful tool to describe an ideal imaging system by means of light rays (geometric optics). In this formulation a ray is described by a two dimensional vector

$$\mathbf{b} = \begin{pmatrix} h \\ \sigma \end{pmatrix} \tag{3.2}$$

where h is the height of the beam with respect to the OA and σ is the ray angle with respect to the OA.

An optical system can manipulate both properties of a ray, where $\mathbf{b} = \begin{pmatrix} h \\ \sigma \end{pmatrix}$ are the ray properties at the input of the optical system and $\mathbf{b}' = \begin{pmatrix} h' \\ \sigma' \end{pmatrix}$ are the properties of the output ray. Mathematically this is modeled by a system matrix multiplication:

$$\mathbf{b}' = \mathbf{M_{Sys}}\mathbf{b} \tag{3.3}$$

with

$$\mathbf{M_{Sys}} = \begin{pmatrix} a_{11} & a_{12} \\ a_{21} & a_{22} \end{pmatrix} \tag{3.4}$$

the multiplication shows the result

$$\begin{pmatrix} h' \\ \sigma' \end{pmatrix} = \begin{pmatrix} ha_{11} + \sigma a_{12} \\ ha_{21} + \sigma a_{22} \end{pmatrix} \tag{3.5}$$

from that the matrix coefficients have the following meaning of the optical manipulating system $\mathbf{M_{Sys}}$:

- a_{11} describes how the output height depends on the input ray height
- a_{12} describes how the output height depends on the input ray angle
- a_{21} describes how the output angle depends on the input ray height[1]
- a_{22} describes how the output angle depends on the input ray angle

---

[1] these properties are commonly known as refractive power

With the imaging condition stated above, the ray propagation matrix $\mathbf{M_{SysImg}}$ has to have the following mathematical form:

$$\mathbf{M_{SysImg}} = \begin{pmatrix} \beta' & 0 \\ a_{21} & a_{22} \end{pmatrix} \tag{3.6}$$

The condition $a_{12} = 0$ implies that the ray height of the image does not depend on the ray angle of the object point. This means that all light rays emitted from P, regardless their direction end up at the same ray height h' in the object space, forming one object point P'. The coefficient $a_{11} = \frac{h'}{h}$ is the linear scaling object and image. This is also known as magnification and denoted as β'.

3.2.1 Thin Lens Approximation

In the *thin lens approximation* an imaging system is approximated by assuming that the whole refraction of the imaging system is done in one single plane. This approximation is useful for a lens which has a small thickness compared to its focal length, or if a system consists of a single refractive surface.

The system matrix (Equation 3.6) to describe the refraction at the single surface of a thin lens simplifies to:

$$\mathbf{M_{ThinLens}} = \begin{pmatrix} 1 & 0 \\ -D & \frac{n}{n'} \end{pmatrix} \tag{3.7}$$

$\beta' = 1$ implies that the ray height does not change at the refracting surface. If the refractive index for the object– and image–space is the same, the thin lens does not change the ray angle of the principal ray[2]. This property is described by $a_{22} = 1$. In general, e.g. for the image formation in the human eye, the object and image are in different optical media. Thus also the principal ray is refracted according to Snell's law. $a_{22} = \frac{n}{n'}$ is the paraxial approximation of Snell's law, with n the refractive index in object space and n' the refractive index in image space. D is the refractive power of the thin lens.

3.2.2 Principal Planes and Cardinal Points

In general, as in the human eye, the *thin lens approximation* cannot be used, since the refractions in an optical system can happen at multiple positions at distances which are not negligible compared to the focal length of the system. In general, any optical system can be reduced to a set of four points, the so called *cardinal points*[3]. These points are defined as the intersection of four planes with special optical properties, with the OA.

---

[2] the ray with ray height $h = 0$ at the refractive surface of the lens

[3] In Gaussian optics typically six cardinal points are defined. In addition to the explanation given above, also the *nodal points* can be defined[94], since four points are sufficient to describe the basic imaging properties of a system, only four points are defined here

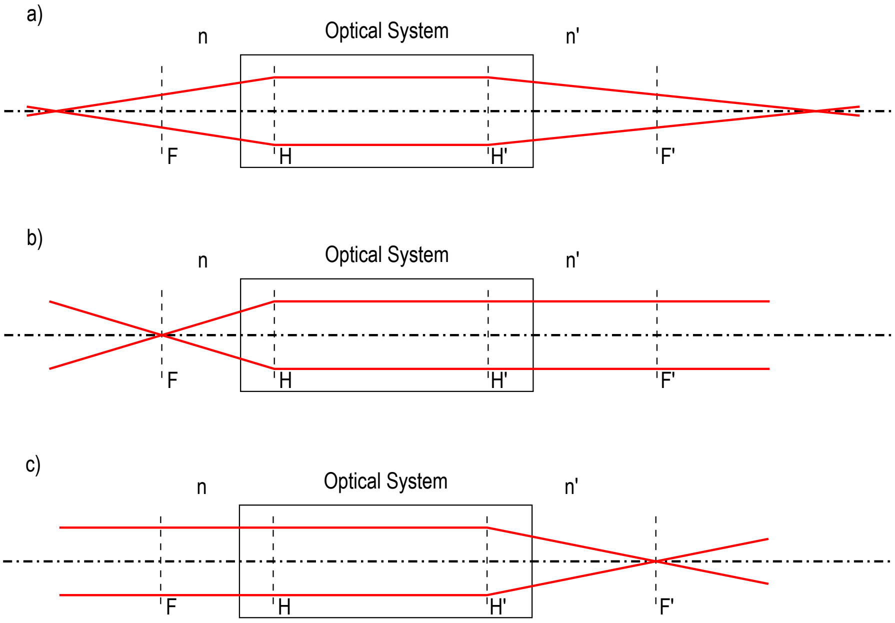

Figure 3.2: Definition of the cardinal points and planes: a) The principal planes H and H' are defined as the planes of effective refraction of an optical system. Between H and H' there is a horizontal ray propagation. b) A point source located in the object sided focal plane F produces parallel rays on the image side of the optical system. c) parallel rays entering the optical system on the object side intersect in a single point in the image sided focal plane F'.

By introducing new reference planes at certain locations, the so called ***principal planes*** H and H', the system matrix of any optical system between H and H' can be described with a matrix equivalent to the *thin lens approximation*:

$$\mathbf{M_{HH'}} = \begin{pmatrix} 1 & 0 \\ a_{21} & a_{22} \end{pmatrix} \tag{3.8}$$

In analogy to the refraction at a single plane in the *thin lens approximation* the *principal planes* H and H' can be understood as the planes of effective refraction for the optical system. The object rays entering the front principal plane H' are mapped parallel to the rear principal plane H', where they are then converted to the image point. The horizontal propagation of light rays between H and H' is described by the matrix elements $a_{11} = 1$ and $a_{12} = 0$ ($h' = a_{11} \cdot h + a_{12} \cdot \sigma \Rightarrow h' = h$).

The ***focal planes*** F and F' are planes in which parallel rays, entering or exiting the optical system, intersect on the opposite side of the optical system. The distance $\overline{HF}$ is defined as the object sided focal length f; whereas the distance $\overline{H'F'}$ is the image sided focal length f'. For an optical system with the same refractive index in the object and image space ($n = n'$), e.g. camera lens in air, it can be shown that $f = f'$. For the human eye the refractive index in the object space $n = 1$ (air) is different from the refractive index in the image space $n' = 1.336$ (aqueous humor, see Table 2.1). In such cases it can be shown that:

$$\frac{f}{n} = \frac{f'}{n'} \tag{3.9}$$

The definitions for H, H', F and F' are depicted in Figure 3.2.

3.3 Geometric Errors

As described above, the geometric condition of an imaging system $\mathbf{M_{Sys}}$ is given, if its matrix element a_{12} is zero. If an imaging system does not exactly fulfill this condition, rays do not geometrically intersect in one single image point P'. These violations of this geometric condition are called geometric errors. Typical types of geometric errors are discussed in this section. For simplicity the object is assumed to be in infinity, thus light rays entering the imaging system are parallel. This assumption is also used in ophthalmology, since the relaxed eye is accommodated to infinity; also the properties of the Liou and Brennan eye are for an eye accommodated to infinity. In the following sections typical geometric errors will be explained. A precise mathematical description is given in Section 3.6.

3.3.1 Defocus

Even for an optical system, free from geometric errors, where parallel light rays from the object intersect in a single point in the focal plane, the geometric imaging condition can be violated if the image is captured at another position than the focal plane, as depicted in Figure 3.3. Thus *defocus* can be approached analogue to the other geometric errors described in the following.

Later it will be shown that the wave optical consideration is more useful for characterization of image aberrations. This can be done by analyzing the OPL for a system with defocus. As mentioned above, for an aberration free system, the OPL must be equal for any light ray from the object point P to the conjugated image point P'. Figure 3.4 a) depicts a detail section from Figure 3.3. Within one WF (locations of equal phase) all rays have the same OPL. Depending on the direction and amount of defocus, the aberration can be described by the amount of phase difference $\Delta\Phi$ between the center and the peripheral rays. The phase difference depends on the distance to the OA, the shape is depicted in Figure 3.4 b).

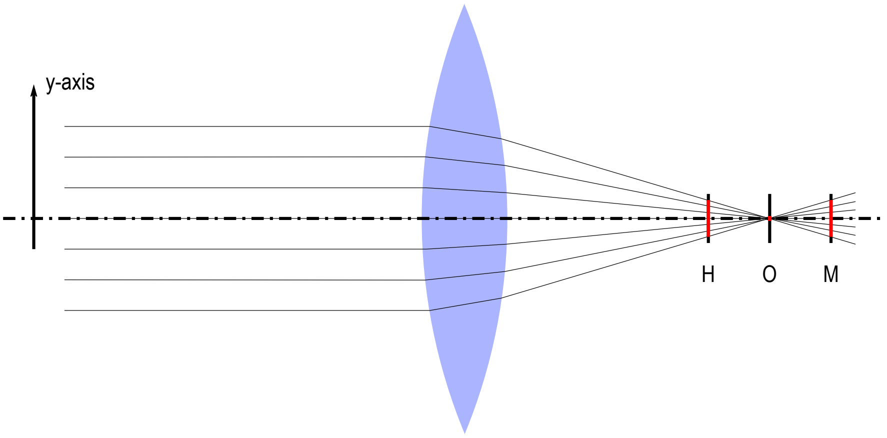

Figure 3.3: An ideal imaging system focuses incoming parallel rays to a single spot at (location O). If an imaging system is out of focus, the image is either captured too close at H or too far at M, the object point P is not projected to a single point P' but to a blurred spot. The size of the blurred spot is proportional to the amount of defocus and the aperture of the system, the y–axis extension of the light rays.

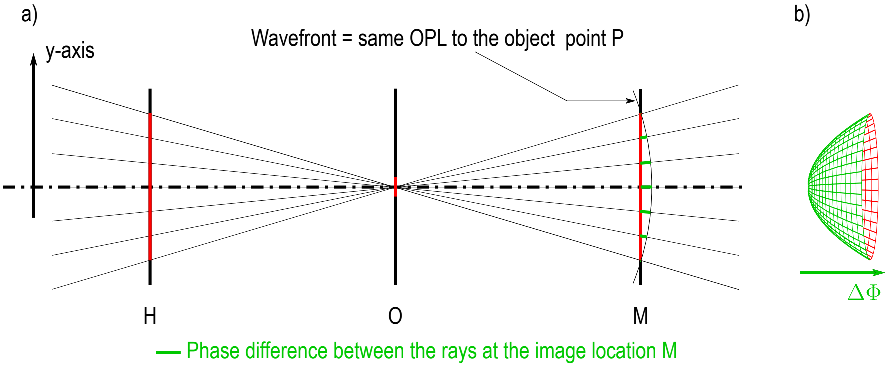
a)
b)
y-axis
Wavefront = same OPL to the object point P
H
O
M
ΔΦ
Phase difference between the rays at the image location M

Figure 3.4: a) Detail view from Figure 3.3: Light is focused to the point O, which can be seen as the source of a spherical wave. Thus WFs are spheres around O. Since WFs have a constant phase along the WF, theses spheres also have an equal OPL to the object P. At M (red line) the axial rays have not yet traveled the same OPL as the peripheral rays. Compared to the peripheral rays they have a negative phase difference $\Delta\Phi$. b) Phase difference $\Delta\Phi$ as a function of the distance from the OA

In general it is easier to reference the optical path difference to a plane WF. This is done by reversing the ray path. For the imaging condition the OPL between P and P' is equal for any ray, thus if a point-like light source would be placed in P', the emitted spherical wave has to have a planar WF in the object space. This planar wave would converge to a point in $-\infty$, since this is the location of the object P. This consideration is depicted in Figure 3.5.

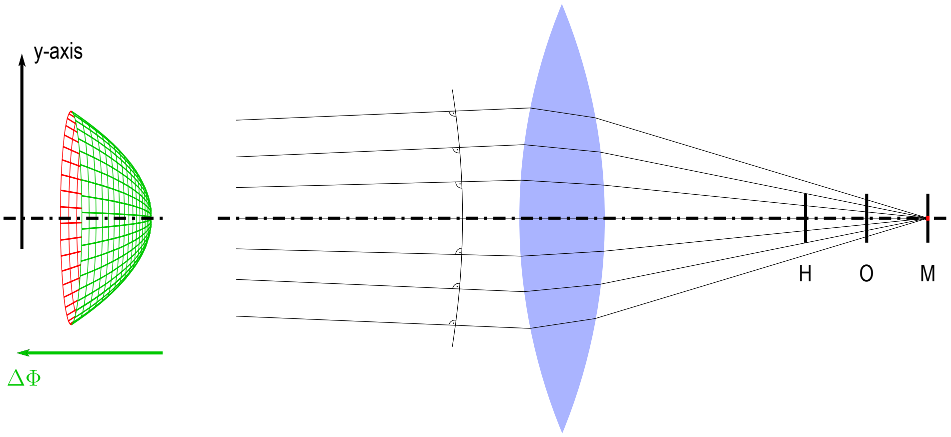

Figure 3.5: Defocused optical system under consideration of an inverse ray direction. In the optical system of Figure 3.3, a point source is placed in the off–focus location M. Compared to a point source in O the spherical WF around M has a bigger radius of curvature at the location of the lens than a spherical wave around O. Thus the wave is divergent in the object space. The WF in the object space (normals to the rays) reveals the same shape as the deliberations in Figure 3.4

In terms of classical ophthalmology, defocus corresponds to the phenomena of *Myopia* (Near Sightedness) – the focal length of the eye is shorter than the AL of the eye (point M in 3.3) and *Hyperopia* (Long Sightedness) – the focal length of the eye is longer, than the AL of the eye (point H in 3.3). In ophthalmology a defocus can be corrected by glasses with a concave or convex lens which adds a different amount of OPL to the central / peripheral rays to counterbalance $\Delta\Phi$ of the eye. For the IOL selection, the focal length of the eye with the new implanted IOL has to fit the individual eye's AL.

3.3.2 Spherical Aberration

SA can be defined as the variation of the focal length with respect to ray height h. This is for example the case for spherical surfaces if they are correctly treated without the paraxial approximation, the output ray angle is no longer linear proportional to the beam height $\sigma' = ha_{21} + \sigma a_{22}$. This case is depicted in Figure 3.6.

For a qualitative estimation of the magnitude of phase difference $\Delta\Phi$, it is again easier to reverse the ray path and compare the aberrated WF with the ideal plane WF. As shown in Figure 3.7 SA deforms the WF in a sombrero–like shape. This shape can also be interpreted as a combination of the defocus–shape (Figure 3.5) for peripheral rays and a negative defocus (inverted shape) for axial rays.

As outlined in Section 2.1.1, the human eye has a positive SA. Using glasses or IOLs with aspheric lens surfaces, the eye's SA can be compensated.

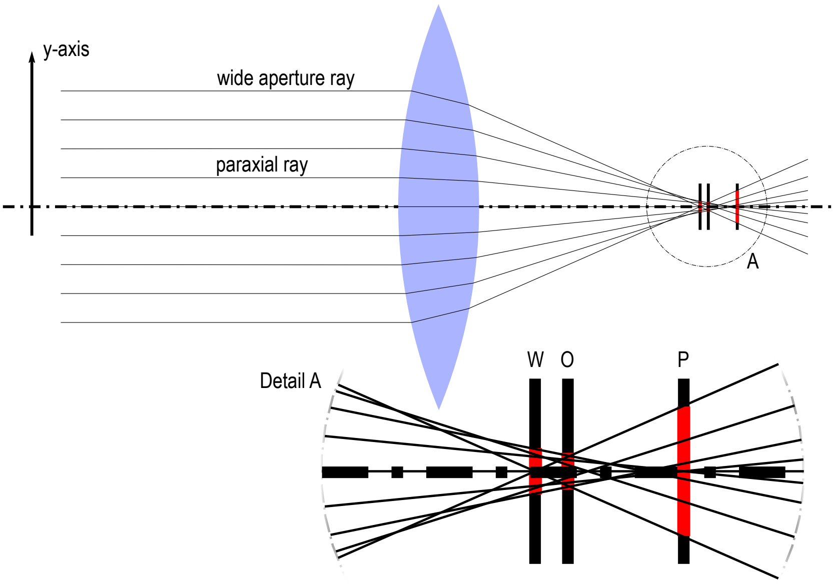

Figure 3.6: SA generated by a spherical lens: The focal length is shorter for rays with wide aperture (W), than for the paraxial rays (P). At an optimal distance, a minimal spot size can be obtained (O). The smaller the aperture the closer the position O is to the paraxial position P.

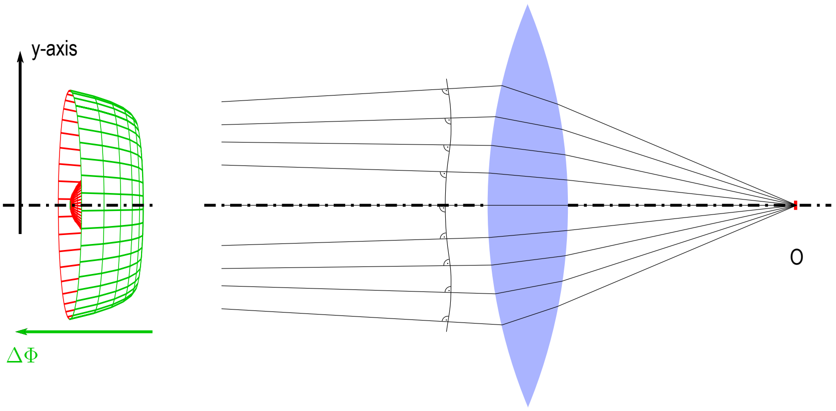

Figure 3.7: Positive SA shows a stronger refractive power for peripheral rays than for paraxial rays. If a point source is located in the optimal location O (see Figure 3.6 for explanation) intermediate rays are parallel in the object space. Wide aperture rays are refracted stronger than intermediate rays, resulting in divergent rays as in the case of a defocus. Axial rays are refracted weaker than intermediate rays, which results in convergent rays. The rotationally symmetric shape of the phase difference $\Delta\Phi$ to the ideal plane WF is depicted on the left.

3.3.3 Astigmatism

Astigmatism, literally translated "without a spot", is closely related to defocus. Astigmatism arises if the focal length of an imaging system is different for two orthogonal directions e.g. different focal length in the x-z–plan than in the y-z–plane. Thus the best focus in x– direction is at a different z locations than for the y–direction. This systematic is shown in Figure 3.8.

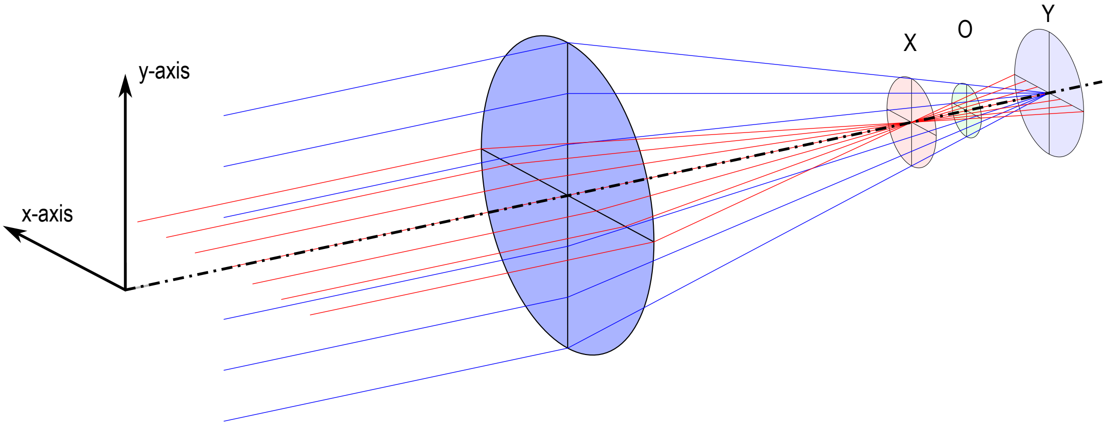

Figure 3.8: The object point P emits rays in all directions, exemplary a light bundle in the x-z–plane (red) and in the y-z–plane (blue) is drawn. The imaging system has different focal lengths for along the x and y direction. At the location X the x-z bundle is focused to a single spot. y-z ray bundle is defocused. Thus the image of P is a line elongated along the y–axis. At the location O the minimal spot size can be found, but both directions are out of focus. Y is the same systematic as in X but with flipped coordinates. There is no location where a single image point P' can be obtained.

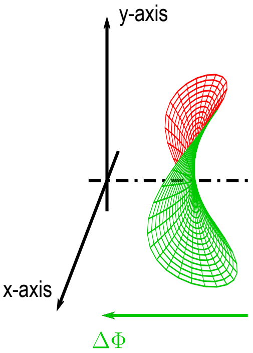

Figure 3.9: The WF deformation $\Delta\Phi$ is not rotationally symmetric for the astigmatism. It has the shape of a defocus in one direction, and the shape of an inverted (negative) defocus in the orthogonal direction.

From Figure 3.8 in combination with Figure 3.5 it is easy to deduce that for the astigmatic system a point source in location O would generate a convergent ray bundle in the x-z–plane and a divergent ray bundle in the y-z–plane in object space. Thus the shape of the aberrated WF ($\Delta\Phi$) is that of the defocus in x–direction and inverted defocus shape in y–direction. This shape is depicted in Figure 3.9.

Astigmatism can occur at various asymmetries: Astigmatic eyes for example do not have a rotationally symmetric cornea surface but a direction of steepest and flattest radius of curvature. For rotationally symmetric lenses astigmatism can occur if a ray bundle does not enter parallel to the OA. In this case the lenses surface curvature is different in tangential and sagittal direction.

3.3.4 Coma

The image aberration coma has its name from the fact that the image of a point object P has the shape of a comet. The image looks like a blurred point with a comet's tail.Coma occurs at spherical lenses for off axis point sources. As mentioned for the SA a spherical lens has a higher refractive power for peripheral rays. But contrary to SA coma is not rotationally symmetric. For comparability with the aberrations described above, Figure 3.10 depicts an optical system which induces coma for a ray bundle parallel to the OA.

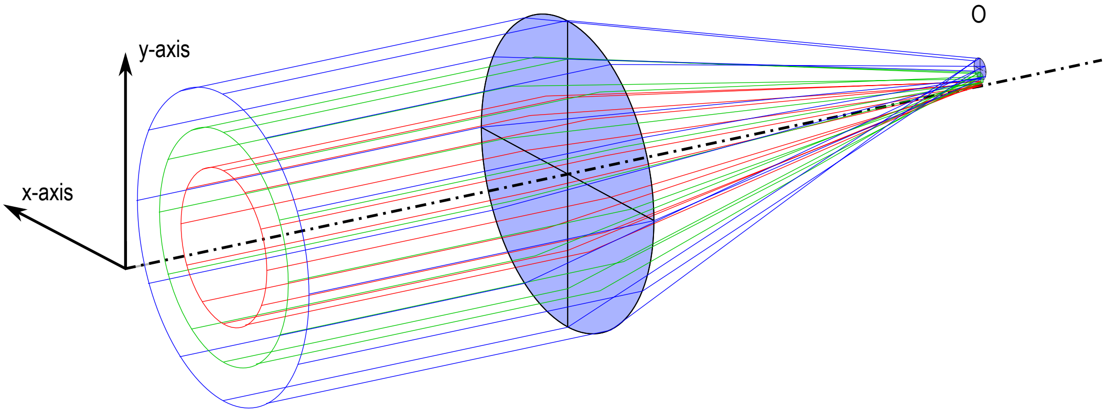

Figure 3.10: An optical system showing comatic aberration has, like a system with SA, different refractive power in the periphery than in the center of the lens. Additionally it induces a deflection of the ray bundle. The second effect also increases for peripheral rays. The figure depicts three parallel ray bundles, red green and blue with increasing distance to the center. The red bundle behaves nearly like an aberration free system. With increasing distance to the center (green and blue), the rays are not focused onto one spot but defocused across a circular area, additionally the blurred circles are shifted off center.

Again a qualitative estimation of the magnitude of phase difference $\Delta\Phi$ is done for the optical system with comatic aberration. The analysis of the reversed ray propagation is depicted in Figure 3.11.

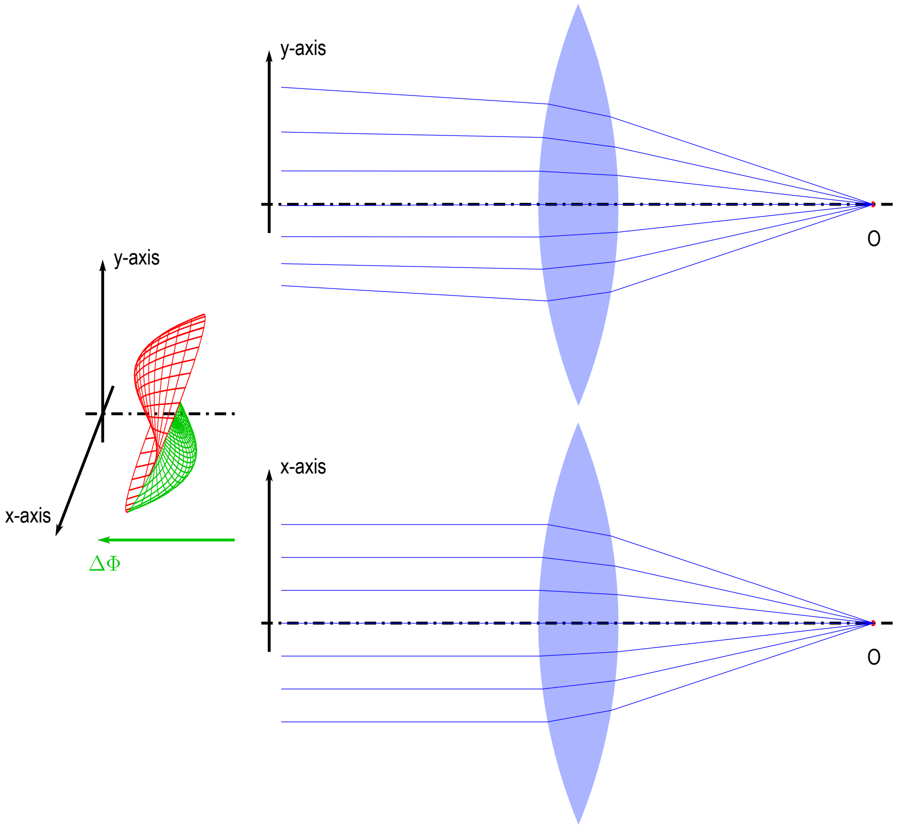

Figure 3.11: The WF deformation $\Delta\Phi$ is analyzed in in two separate directions for a point source in O. y–z ray fan: The paraxial rays are not aberrated (parallel rays to the OA on the left side). For the positive y–direction the rays show the divergent appearance of the a negative defocus, in the negative y–direction rays are convergent as for the defocus. x–z ray fan: For $y = 0$ the rays are not aberrated. This is the boundary between the segment with positive and the segment with negative defocus.

The so far described geometric aberrations are the most common ones. In general the idea of placing a point source in the location of the ideal image can be used for any aberration. Every deviation from the plane WF is associated with a geometric image aberration. A mathematic description to describe any WF–shape by a set of fundamental image aberrations will be presented in Section 3.6.3.

3.4 Wave Optics and Diffraction Errors

Geometric errors are deduced from geometric ray optical properties. They describe all deviations from the geometric condition that all light rays intersect in one single point. This approach neglects all effects arising from the wave nature of light. Due to diffraction of waves, even for an geometrical aberration free system it is impossible to focus light to a single spot, thus diffraction violates the ideal imaging condition. At ideal illumination conditions, when the pupil opening is very small, the healthy human eye is almost free from geometric errors and the Visual Acuity (VA) is just limited by diffraction. Therefore diffraction effects have to be considered in the IOL testing.

To describe image aberrations induced by wave diffraction, first some basics on wave optics are explained in the following:

3.4.1 Basics of Wave Optics

The wave characteristics of an optical system can be derived from the Maxwell Equations. For the considerations in this thesis dielectric material with an electric free charge density of $\varrho = 0$ and free of conductive current $\mathbf{j} = 0$ can be assumed.

$$\nabla \cdot \mathbf{E} = 0 \tag{3.10}$$

$$\nabla \cdot \mathbf{H} = 0 \tag{3.11}$$

$$\nabla \times \mathbf{E} = -\mu \frac{\partial \mathbf{H}}{\partial t} \tag{3.12}$$

$$\nabla \times \mathbf{H} = \varepsilon \frac{\partial \mathbf{E}}{\partial t} \tag{3.13}$$

E is the electric field, **H** the magnetic field intensity. Material constants are μ, the magnetic permeability, and ε, the electric permittivity. From these equations some algebraic manipulations lead to the wave equation:

$$\nabla^2 \mathbf{E} = \mu\varepsilon \frac{\partial^2 \mathbf{E}}{\partial t^2} \tag{3.14}$$

μ and ε can be linked to the vacuum permeability μ_0 and permittivity ε_0 via the relative permeability μ_r and the relative permittivity ε_r:

$$\mu = \mu_r \cdot \mu_0 \tag{3.15}$$

$$\varepsilon = \varepsilon_r \cdot \varepsilon_0 \tag{3.16}$$

For optical systems it is more convenient to replace the constants μ_r and ε_r by the refractive index:

$$n = \sqrt{\varepsilon_r \mu_r} \tag{3.17}$$

It can be shown that μ_0 and ε_0 are linked to the vacuum speed of light c_0[94, 95]:

$$c_0 = \frac{1}{\sqrt{\varepsilon_0 \mu_0}} \tag{3.18}$$

Therefore the phase velocity in a media is:

$$c = \frac{1}{\sqrt{\varepsilon\mu}} = \frac{c_0}{n} \tag{3.19}$$

Because of the linearity of the wave Equation 3.14 linear combinations of solutions of the wave Equation 3.14 are again solutions of the wave Equation 3.14. The decomposition in a linear combination cannot be done only in the time–domain but also in space. For the further investigations two fundamental solutions to the wave Equation 3.14 provide a useful and simple subset of functions: *Plane waves* and *spherical waves*.

Plane Waves are described by the function

$$\mathbf{E}(\mathbf{x},t) = \mathrm{Re}\left(E_0 e^{j(\mathbf{kx}-\omega t)}\right) = |E_0|\cos(\mathbf{kx}-\omega t+\phi) \tag{3.20}$$

E_0 is the the complex amplitude with the phase ϕ, j the imaginary unit, $\mathbf{k}$ is the wave vector, ω is the wave's angular frequency. In isotropic media, $\mathbf{k}$ is the direction of wave propagation, the WF is normal to $\mathbf{k}$. For Equation 3.20 being a solution to Equation 3.14, it can be shown:

$$|\mathbf{k}| = k = \frac{\omega}{c} = \frac{n\omega}{c_0} \tag{3.21}$$

wherewith $\mathbf{k}$ can be related to the above mentioned constants by the wave number k. The spatial distance between two WFs with a phase difference of $\Delta\Phi = 2\pi$ (wavelength) is

$$\lambda = \frac{2\pi}{k} \tag{3.22}$$

The exponential representation in Equation 3.20 is more convenient for further mathematical considerations. Another useful simplification is the time independent phasor representation [96]. The electric field phasor $\widetilde{\mathbf{E}}(\mathbf{x})$ is defined by:

$$\mathbf{E}(\mathbf{x},t) = \mathrm{Re}\left(\widetilde{\mathbf{E}}(\mathbf{x})e^{j\omega t}\right) \tag{3.23}$$

With that, the plane wave can be written as:

$$\widetilde{\mathbf{E}}(\mathbf{x}) = E_0 e^{-j\mathbf{kx}} \tag{3.24}$$

Spherical waves are described by the function

$$\mathbf{E}(\mathbf{x},t) = \mathrm{Re}\left(\frac{A_0}{r}e^{j(\omega t \mp kr)}\right) \tag{3.25}$$

A_0 is a complex amplitude, $r = |\mathbf{x}|$ the distance from the center O. The WFs are concentric spheres around O, with a negative sign the WFs travel away from O.

The spherical wave in phasor–representation is given by:

$$\widetilde{\mathbf{E}}(\mathbf{x}) = \frac{A_0}{r}e^{\mp jkr} \tag{3.26}$$

3.4.2 Diffractive Errors

An ideal thin lens, free from geometric errors, is assumed for the calculation of the pure diffraction effect. Furthermore, as in the investigations above, the object P is set in infinite distance to the lens, resulting in parallel rays at the location of the lens. The wave, having planar WF normal to the ray, can be depicted with the planar wave equation as given in Equation 3.20, where $\mathbf{k}$ is parallel to the z–axis.

If this wave hits an aperture, the field behind ($\widetilde{\mathbf{E}}_p$) and in front($\widetilde{\mathbf{E}}$) of the aperture are different:

$$\widetilde{\mathbf{E}}_p(x,y) = \mathbf{P}(x,y) \cdot \widetilde{\mathbf{E}}(x,y) \tag{3.27}$$

$\mathbf{P}(x,y)$ is the pupil function, where $P = 1$ for the transparent part of the aperture, and $P = 0$ for the locations (x,y) which permit the propagation of light.

It can be shown that a far-field intensity distribution of an aperture with the pupil function $\mathbf{P}$ is proportional to the 2D Fourier Transform of the pupil function[96, 95]. This is also true for the focal plane of an ideal (free from geometric errors) imaging lens [97, 96, 94]:

$$\widetilde{\mathbf{E}}(x',y',f) = e^{-j\frac{k}{2f}(x'^2+y'^2)} \int_{+\infty}^{-\infty}\int_{+\infty}^{-\infty} \widetilde{\mathbf{E}}(x,y,0)\mathbf{P}(x,y)e^{-j\frac{k}{f}(x'x+y'y)}dxdy \tag{3.28}$$

x and y are the integration variables and the coordinates in the pupil plane, x' and y' are the corresponding coordinates in the focal plane. $\widetilde{\mathbf{E}}(x',y',f)$ is the electric field phasor in the focal plane. $\widetilde{\mathbf{E}}(x,y,0)$ is the electric field phasor in the pupil plane.

In optics, usually circular apertures are used. Given that, and assuming an underrated plane wave[4]direction, Equation 3.28 results in a rotationally symmetric field distribution, which is known as the Bessel function of first kind $J1$. The observed light intensity is proportional to the squared Electric field amplitude:

$$I \propto E^2 \tag{3.29}$$

This results in the Airy–function depicted in Figure 3.12. For an aberration free lens with an opening of D and a focal length f the Airy–function has its first minimum at an radius of $1.22\frac{\lambda f}{D}$. This implies, that even if an optical system is free of geometric aberrations, it is not possible to direct the entire light from P to a single point P' due to the physical effects of wave diffraction.

This fundamental limit is inherent in any optical system. The characteristic fraction between focal length f and entrance pupil diameter D is defined as the *f–number*:

$$^{f}/_{\#} = \frac{f}{D} \tag{3.30}$$

As described above, geometric errors can be corrected by manipulating the mismatch in optical path length difference. For a given wavelength λ and f–number $^{f}/_{\#}$ the

---

[4] a plane wave according to Equation 3.24 with a $\mathbf{k}$–vector in z-

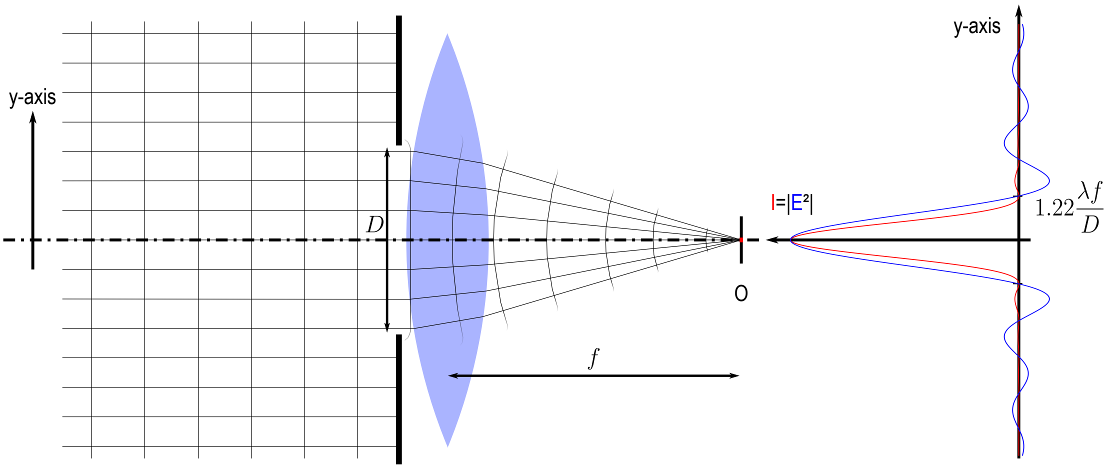

Figure 3.12: Diffraction limited image of an ideal lens: An ideal plane wave, which has an infinite extent in the x–y direction propagates towards an ideal lens, which is free from geometric image aberrations. The finite aperture, in this case a circular aperture with the diameter D, reduces the spatial extent of the plane wave – diffraction occurs. Diffraction, see text for the mathematical analysis, results in an electric field distribution which is proportional to the Fourier transform of the aperture (blue). The intensity is proportional to the square (red). The Point image extends over a circle with the radius of $1.22\frac{\lambda f}{D}$

diffractive spreading of the point image P' can't be compensated, this limit is referred to as *diffraction limit*.

3.5 Polychromatic Errors

Optical media typically have the property of dispersion. This means that the phase velocity – see Equation 3.19 – and thus the refractive index n depends on the wavelength of the light. As already shown in Section 2.1.2 this is also true for the optical media of the human eye, in particular the ocular media have dispersive properties similar to those of water. In context of geometric and diffractive image aberration this means:

- Since n depends on the wavelength λ, also the focal length f of the eye depends on λ. Thus the eye can only be in focus for one single wavelength. Any other wavelength has at least a geometric defocus.
- The diffraction limited minimal radius of a point source $1.22 \cdot {}^{f}/_{\#} = \frac{f}{D}\lambda$ is, just as geometric errors, dependent on the wavelength.

These errors occur in addition to mentioned geometric and diffraction errors, if the image is not produced by an monochromatic light. Thus these errors are called Chromatic

Aberration (CA). In technical optics combining glasses with high and low dispersion, CA can partly be compensated. Due to the similar dispersive properties of all optical media in the human eye, CA has to be taken into account.

The peak sensitivity of L-type cones is at a 36% longer wavelength than that of S-type cones and thus they have a 36% bigger diffraction limited minimal image point radius.

Geometric CA is described as Longitudinal Chromatic Aberration (LCA) and Transverse Chromatic Aberration (TCA) [94]:

- LCA is the effect, that the different focal lengths for different wavelengths cause different locations for the best focus. The focusses are shifted longitudinal along the OA. See Figure 3.13.
- TCA, sometimes also denoted as lateral CA, occurs for rays asymmetric to the OA. As the refractive power is different for different wavelengths, rays intersect at different transversal heights. This implies that different colors reveal different magnifications. See Figure 3.13.

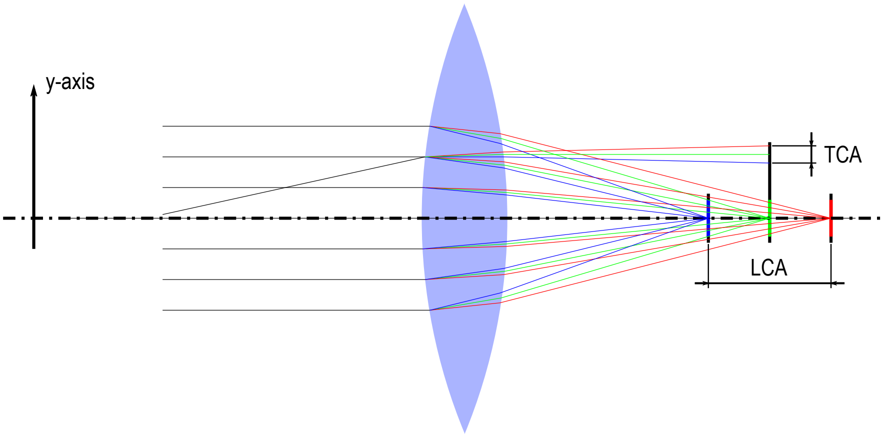

Figure 3.13: An ideal imaging system focuses incoming parallel rays to a single spot at (location O). If an imaging system is out of focus, the image is either captured too close at H or too far at M, the object point P is not projected to a single point P' but to a blurred spot. The size of the blurred spot is proportional to the amount of defocus and the aperture of the system, the y–axis extension of the light rays.

CA is a challenging topic to address, when one wants to assess the effects on VA. Furthermore there are inconsistencies in related publications on this topic. There also seem to be misconceptions on the principals of color vision [98].

LCA is uncorrected in the human eye [99]. It is around 2 diopters in the visual spectrum [100, 101].

From digital image processing it is well known that TCA can effectively be removed in post processing [102]: Commercial image sensors capture the visual spectrum by three separate color channels (red, green and blue), similar to the L–, M– and S– type cones. Having individual images, the magnification differences in the three images can be assessed and adjusted to the same level before the three channels are combined to a single image. It can be speculated that the human brain is capable of similar processing to counteract TCA.

Literature gives some evidence that the process of visual perception may counteract CA:

- Artal et al. [103] tested the effect on CS and VA if SA and LCA are fully corrected. Correcting both (SA and LCA) yielded significant improvements in CS and VA. The study showed that most of the benefit comes from SA correction. LCA did not show a large impact.

- Thibos et al. [104] found for the chromatic difference in focus only a "*moderate loss in CS and a minor loss in VA*"; for the chromatic difference in magnification "*no evidence which suggests chromatic difference in magnification has any bearing on monocular vision*"; the chromatic difference in position is found to be the "*mayor limiting factor*".

- Plainis et al. [105] found that binocular vision was superior to monocular vision when CA was present.

On a basic physiological level CA correction is achieved by the distribution of cones: L-type and M-type cones (having similar peak sensitivities and thus sense less chromatic aberrations) are by far more sensitive and S-type cones are not present in central fovea [22, 106].

For the reason that there is some evidence that much of CA is compensated on the sensory level and in neural processes, and in some conditions correcting CA even does not improve CS and VA, in this thesis only monochromatic measurements will be done. It is pointed out that this is against the recommendations outlined in Section 2.2.2, but also after careful research no dispersion data for commercial available IOLs could be found. Thus no validation between measurements and simulations would be possible. In addition, comparison with measurements according to the current test standard (monochromatic measurement at 546nm) would not be possible. The measurement setups are constructed to be used for measurements at different wavelengths. Ravikumar et al. [107] created a framework for calculating the retinal image quality for polychromatic light when only monochromatic aberrations are known/measured. Thus the presented method is in principal not limited to monochromatic investigations.

3.6 Characterization of Image Aberrations

In general, geometric errors (Section 3.3), Diffraction (Section 3.4.2) and CA (Section 3.5) altogether influence the quality of vision of an image. This section will point out the theory on how image aberrations can be characterized. This is again done by starting from the considerations done in 3.1: A perfect imaging system can be described as a system where each object point is projected onto one single point in the image.

3.6.1 The Point Spread Function

Contrary to an ideal imaging system, where the light from one object point converges to a single point in the image, in a real imaging system the light is spread across an extended area. This intensity distribution is defined as the PSF.

Mathematical Calculation of the Point Spread Function

To analyze the PSF of an imaging system, the image is assessed under the condition of a perfect point object and under presence of all types of image aberrations. Equation 3.28 cannot only be used to describe the diffraction limited electric field distribution and thus the intensity distribution, but also to describe the field distribution in combination with geometric errors: As outlined in Section 3.3, any geometric error is described by a deviation from the real WF–shape to the ideal plane WF. To assess the influence of both, diffraction and geometry, the deformed WF–shape at the aperture location $(x, y, 0)$ is plugged into the equation. This is done by adding a phase term (complex exponent) to the WF–phasor representation:

$$\widetilde{\mathbf{E}}(x, y, 0) = E_0 e^{-j\mathbf{k_z}z} e^{j2\pi\mathbf{\Phi}(x,y)} \tag{3.31}$$

$\mathbf{\Phi}(x, y)$ is the WF deformation in the pupil plane. $\mathbf{\Phi}(x, y)$ is scaled in λ[5]. Neglecting the quadratic phase term $e^{-j\frac{k}{2f}(x'^2+y'^2)}$ in Equation 3.28, which only changes the phasor's phase, but not the amplitude, and plugging in, Equation 3.28 can be rewritten as:

$$\widetilde{\mathbf{E}}' = \mathcal{F}\left\{\mathbf{P}(x, y)e^{j2\pi\mathbf{\Phi}(x,y)}\right\} \tag{3.32}$$

Further on the term $\mathbf{P}(x, y)e^{j2\pi\mathbf{\Phi}(x,y)}$ will be replaced by $\mathbf{P}_A(x, y)$, where $\mathbf{P}_A$ is a complex valued pupil function including geometric errors. With Equation 3.29 the intensity distribution in the image space, which is the PSF, can be expressed as[108]:

$$\mathbf{PSF} = \left|\mathcal{F}\left\{\mathbf{P}_A\right\}\right|^2 \tag{3.33}$$

Analogous to this calculation the PSF, only considering diffraction and no geometric errors, hence denoted *diffraction limited PSF*, can be expressed as:

$$\mathbf{PSF} = \left|\mathcal{F}\left\{\mathbf{P}\right\}\right|^2 \tag{3.34}$$

---

[5] In ophthalmology the WF deformation is sometimes measured in μm

Characterizing the Point Spread Function

Commonly the total intensity, which is the integral of the PSF, is normed to 1. If geometric aberrations in addition to the diffraction occur, the image gets spread (blurred) over a bigger area. Given the same total intensity, the PSF peak amplitude is always equal or less to the peak amplitude of the diffraction limited system $\mathbf{PSF}_{dl}$. From that, the so called Strehl ratio can be defined [69]:

$$SR = \frac{\max(\mathbf{PSF})}{\max(\mathbf{PSF}_{dl})} \tag{3.35}$$

The Strehl ratio SR is always between 1 (no geometric errors) and 0 (no image formation at all). The SR is simple to be understood but not sufficient to characterize the image quality. Optical systems with small apertures (small ${}^{f}/_{\#}$) can easily show SR close to 1, which comes from small WF deformations within a small aperture, but still have a very broad PSF due to diffraction. Thus for a meaningful interpretation of the image quality it has to be investigated how the PSF influences the image formation.

Image Formation with the Point Spread Function

Until now, only a single point object was considered. To analyze realistic objects, multiple point sources, forming the total object, have to be considered. For the image formation, the intensity is of interest, since optical detectors, equally to the receptors on the retina, are sensitive to the intensity, which can be calculated by[96]:

$$\mathbf{I}_{img}(x, y) = \left\langle |\mathbf{E}_{img}(x, y, t)|^2 \right\rangle \tag{3.36}$$

$\langle\rangle$ is the infinite time average, $\mathbf{E}_{img}$ is the electric field distribution in the image plane. When calculating $\mathbf{E}_{img}$ Equation 3.28 applies to the electric field from every object point. Mathematical analysis reveals that $\mathbf{E}_{img}$ is different, whether the object emits coherent or incoherent light[96]. For the purpose of this thesis, **incoherent light** sources have to be assumed, since they resemble usual illumination conditions. In the incoherent case no interference effects occur, thus the image intensities from each object point simply sum up to the total image intensity. This can mathematically be expressed by a convolution of the object with the PSF as the filter kernel:

$$\mathbf{I}_{img} = \mathbf{PSF} \otimes \mathbf{I}_{obj} \tag{3.37}$$

$\mathbf{I}_{obj}$ is the object's intensity distribution in the image space[6]. From this equation it is clear that the image is only equal to the object if the **PSF** is equal to the infinitely narrow Dirac–function (δ).

---

[6] In image space means that the distribution is scaled with the lateral magnification of the imaging system

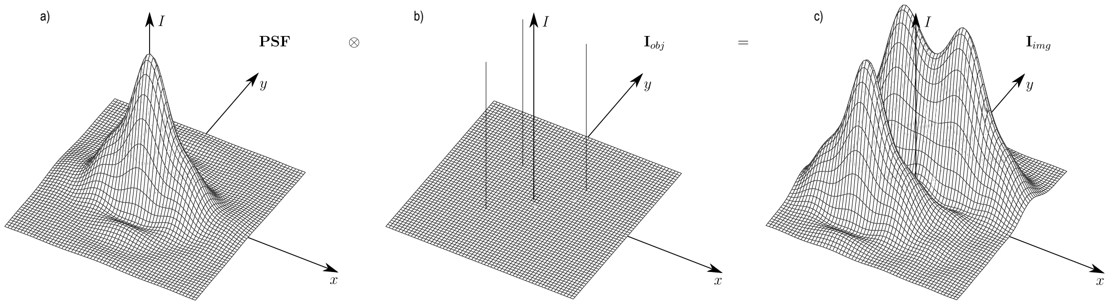

Figure 3.14: Example for an image formation from multiple points: a) Exemplary the PSF under presence of defocus and astigmatism is shown. Due to the astigmatism the PSF is broader in x–direction. b) The object consists of three prefect points, having the same distance in x– and y– direction. c) The convolution of PSF and the object results in this image. The points are clearly separable in the y–direction but badly in x–direction.

Line and Edge Spread Function

Analogue to the PSF the Line Spread Function (LSF) is defined as the intensity distribution of the image of a line object[109]. From the LSF only the spreading orthogonal to the line direction can be observed, thus it is not as informative as the PSF. Further the Edge Spread Function (ESF) is defined as the distribution of the image from an edge[109]. An edge object is experimentally easier to be constructed than a line or point object (see Section 4.3). The LSF is the derivative of the ESF [110]:

$$\mathbf{LSF} = \frac{\mathrm{d}}{\mathrm{d}\mathbf{x}}\mathbf{ESF} \tag{3.38}$$

where $\mathbf{x}$ must be orthogonal to the edge direction. The ESF will be of interest in Section 4.3 for measuring the MTF.

3.6.2 The Modulation Transfer Function

In Figure 3.14 it can be seen that if the distance between two points is small compared to the width of the PSF, the two points can hardly be resolved. To quantify the visibility, the *modulation* or *Michelson contrast* C is introduced [69]:

$$C = \frac{I_{max} - I_{min}}{I_{max} + I_{min}} \tag{3.39}$$

I_{min} and I_{max} represent the lowest and the highest intensity. From signal theory an imaging system, described by the convolution shown in Equation 3.37, can be interpreted as spatial low pass filter. This means that the modulation contrast of high spatial frequencies in the object are lowered in the image. The MTF describes the reduction in modulation for an object with sine-wave intensity grating of the spatial frequency ξ:

$$\mathbf{MTF}(\xi) = \frac{C_{img}(\xi)}{C_{obj}(\xi)} \tag{3.40}$$

where $C_{img}(\xi)$ is the contrast in the image and $C_{obj}(\xi)$ the object contrast, for an intensity distribution with the spatial frequency ξ. The spatial frequency describes spatial repetition of dark or bright lines in an image, hence the unit $\frac{\mathrm{lp}}{\mathrm{mm}}$ – line pairs per mm – is commonly used. The reduction of contrast due to the convolution with the PSF is depicted in Figure 3.15.

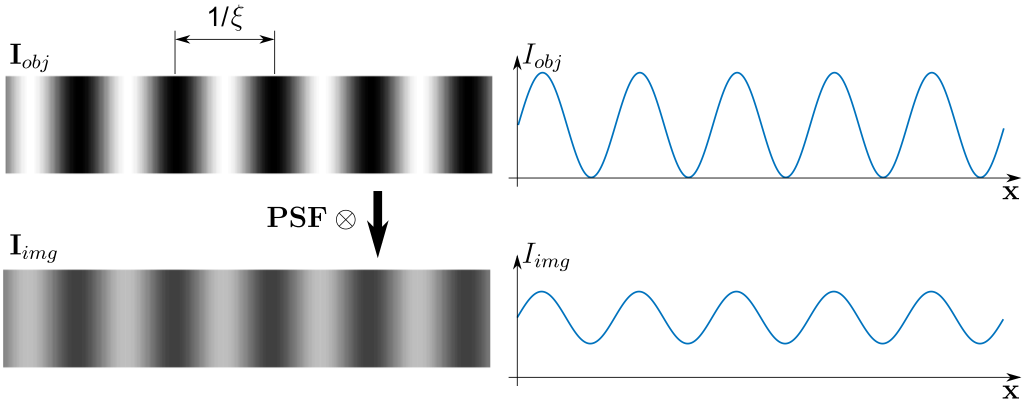

Figure 3.15: An object with a single spatial frequency of ξ is imaged with an optical system with the **PSF**, being the system's PSF. image formation can be described with a convolution with the **PSF**. This acts as a low–pass filter. Thus the modulation or contrast of the image is reduced compared to the object.

Relation between the Modulation Transfer Function and the Point Spread Function

The mathematical analysis can be done from Equation 3.37. The convolution theorem states that Fourier-Transform $\mathcal{F}$ of the convolution g and h is equal to the product of the individual functions.

$$\mathcal{F}\left\{g \otimes h\right\} = \mathcal{F}\left\{g\right\} \cdot \mathcal{F}\left\{h\right\} \tag{3.41}$$

With that, Equation 3.37 can be rewritten as:

$$\mathbf{I}_{img} = \mathcal{F}^{-1}\left\{\mathcal{F}\left\{\mathbf{PSF}\right\} \cdot \mathcal{F}\left\{g\right\}\right\} \tag{3.42}$$

For the MTF we are interested in the contrast at a specific spatial frequency ξ. A pure sine–wave intensity image has only a single peak in its Fourier spectrum. Thus the Fourier–transform of the object can be written as a shifted 2D $\delta(\xi_x, \xi_y)$ function:

$$\mathcal{F}\left\{\mathbf{I}_{obj\xi}\right\} = \delta(\xi_x - \xi_{x_{obj}}, \xi_{y_{obj}} - \xi_y) \tag{3.43}$$

where $\xi_{x_{obj}}$ and $\xi_{y_{obj}}$ are the object's spatial frequencies in x- and y–direction. The Fourier-Transform of the PSF will further on be denoted as Optical Transfer Function (OTF), which is also defined in an ISO standard [109]:

$$\mathbf{OTF} = \mathcal{F}\left\{\mathbf{PSF}\right\} \tag{3.44}$$

The $\mathbf{OTF}(\xi_x, \xi_y)$ is a complex function, where the modulus is normed to 1 for the spatial frequency of 0. Combining Equation 3.42 and Equation 3.43 we get:

$$\mathcal{F}\left\{\mathbf{I}_{img\xi}\right\} = \mathbf{OTF} \cdot \delta(\xi_x - \xi_{x_{obj}}, \xi_{y_{obj}} - \xi_y) \tag{3.45}$$

This means that the $\mathbf{OTF}$ at the spatial frequencies $\xi_{x_{obj}}$ and $\xi_{y_{obj}}$ is the Fourier–transform of the image intensity at these spatial frequencies. The modulus of this value can be interpreted as the amplitude of intensity modulation of the image at the spatial frequency of the object grating ($\xi_{x_{obj}}$ and $\xi_{y_{obj}}$), which is the same as the contrast C defined in Equation 3.39. With that, the continuous MTF for any arbitrary frequency (ξ_x, ξ_y) can be calculated as the modulus of the OTF; this is equal to the modulus of the Fourier–transform of the PSF [109]:

$$\mathbf{MTF}(\xi_x, \xi_y) = |\mathbf{OTF}(\xi_x, \xi_y)| = |\mathcal{F}\left\{\mathbf{PSF}\right\}| \tag{3.46}$$

Typically the MTF is depicted as a 2D plot, and thus only represented in certain directions. For the results in this thesis the MTF in x– and y–direction is used. The following definitions are used:

$$\mathbf{MTF}_x = \mathbf{MTF}(\xi_x, 0) \tag{3.47}$$

$$\mathbf{MTF}_y = \mathbf{MTF}(0, \xi_y) \tag{3.48}$$

And the mean value between $\mathbf{MTF}_x$ and $\mathbf{MTF}_y$

$$\mathbf{MTF}_{mean} = \frac{\mathbf{MTF}_x + \mathbf{MTF}_y}{2} \tag{3.49}$$

For a rotationally symmetric PSF all directions are equal ($\mathbf{MTF}_x = \mathbf{MTF}_y = \mathbf{MTF}_{mean}$).

Mathematical Calculation of the Modulation Transfer Function

Equation 3.33 together with Equation 3.46 results in:

$$\mathbf{OTF}(\xi_x, \xi_y) = \mathcal{F}\left\{|\mathcal{F}\left\{\mathbf{P}_A(x, y)\right\}|^2\right\} \tag{3.50}$$

In analogy to the frequency in the temporal Fourier–transformation, in Fourier–Optics the spatial frequency is defined as the Fourier pair to the transverse coordinates. This is expressed by the variable transforms[96]:

$$\xi_x = \frac{x}{\lambda f} \tag{3.51}$$

and

$$\xi_y = \frac{y}{\lambda f} \tag{3.52}$$

where x and y are the transverse coordinates, λ the wavelength and f the focal length of the imaging system[7].

---

[7] The Fourier–pair $\mathbf{x}$ and ξ used in Fourier–optics[96] is not to be confused with the Fourier pair in classical physics $\mathbf{x}$ and momentum $\mathbf{p}$

The *autocorrelation theorem* states that the Fourier–transform of the autocorrelation from a function h is equal to the absolute square of the Fourier–transform of h:

$$\mathcal{F}\left\{h \odot h\right\} = \left|\mathcal{F}\left\{h\right\}\right|^2 \tag{3.53}$$

Applying the *autocorrelation theorem* to Equation 3.50, the OTF (in the case of incoherent illumination) can be expressed as the autocorrelation of the complex pupil function:

$$\mathbf{OTF}(\xi_x, \xi_y) = \mathbf{P}_A(x, y) \odot \mathbf{P}_A(x, y) \tag{3.54}$$

To calculate the diffraction limited MTF, $\mathbf{P}_A(x, y)$ in Equation 3.54 is replaced by the real valued pupil function $\mathbf{P}(x, y)$. For a circular pupil with the diameter D, $\mathbf{P}(x, y)$ and $\mathbf{OTF}(\xi_x, \xi_y)$ are rotationally symmetric. Thus in the diffraction limited MTF only a single radial spatial frequency coordinate ξ is used. With Equation 3.46 and 3.54 the diffraction limited MTF can be expressed as:

$$\mathbf{MTF}_{dl}(\xi) = \left|\mathbf{P}_{\circ}(r) \odot \mathbf{P}_{\circ}(r)\right| \tag{3.55}$$

where $\mathbf{P}_{\circ}(r)$ is the pupil function of a circular aperture. Geometrically interpreting the autocorrelation it is vivid that the **MTF** drops to zero if $\mathbf{P}_{\circ}(r)$ is shifted beyond its diameter D in the autocorrelation function. This implies that the image contrast drops to zero at the corresponding spatial frequency. With the coordinate transforms from Equation 3.51 and 3.52 the cut of frequency of the diffraction limited MTF is:

$$\xi_{cut} = \frac{D}{\lambda f} \tag{3.56}$$

Using the definition of the *f–number* (Equation 3.30) this can be expressed as:

$$\xi_{cut} = \frac{1}{\lambda\, {}^{f}/_{\#}} \tag{3.57}$$

Analytical evaluation of Equation 3.55 results in[108]:

$$\mathbf{MTF}_{dl}(\xi/\xi_{cut}) = \frac{2}{\pi}\left(\cos^{-1}(\xi/\xi_{cut}) - \xi/\xi_{cut}\sqrt{1 - \xi/\xi_{cut}}\right) \tag{3.58}$$

3.6.3 Characterization of Geometric Wavefront Aberrations

For both, the PSF and the MTF it could be shown that both measures can be reduced to the description of the diffraction errors, induced by the pupil (pupil function $\mathbf{P}$) and geometric errors, described by the WF $\mathbf{\Phi}$. A phenomenological description of the WF is given in Section 3.3. There it could be shown that the WF–shape is characteristic for the type of image aberration. Thus describing the WF $\mathbf{\Phi}$ in the pupil of an imaging system is a powerful method to characterize image aberrations. Furthermore other parameters like the PSF and MTF can be derived from the WF (see Equation 3.50 and 3.33). In general $\mathbf{\Phi}(x, y)$ can have any shape.

Simple Wavefront Characterization

A very simple measure to assess to which extend the WF deviates from the ideal flat surface is the *Peak–to–Valley* value. It is defined as the difference between the maximum and minimum deviation to the flat WF [69]:

$$PV = \max(\mathbf{\Phi}) - \min(\mathbf{\Phi}) \tag{3.59}$$

As this value only depends on two values of the whole WF, this can be misleading, i.e. a system with a high PV can perform better than another system with a smaller PV–value.

All points of the of the WF can be considered if the*Root–Mean–Square* deviation to the ideal flat surface is calculated. It is defined as square–root of the arithmetic mean of the squared wave–front [69]:

$$RMS = \sqrt{\overline{\mathbf{\Phi}^2}} \tag{3.60}$$

For this calculation $\mathbf{\Phi}$ has to be normalized to zero mean. The RMS–value is generally more meaningful to specify the amount of WF–aberrations[69].

Zernike Polynomials

A powerful approach to characterize the WF $\mathbf{\Phi}$ is to decompose the $\mathbf{\Phi}$ in a linear combination of orthogonal Polynomials. Each polynomial represents a specific geometric image aberration. This set of orthogonal polynomials are called *Zernike polynomials*, named after Frederik Zernike who won the Nobel Prize in Physics in 1953 *"for his demonstration of the phase contrast method, especially for his invention of the phase contrast microscope"*[111]. As in optics usually circular pupils are used, the polynomials are usually expressed in the unit cycle in polar coordinates (ϱ,ψ). The WF linear combination is then given by:

$$\mathbf{\Phi}(\varrho, \psi) = \sum_{n,\pm m} Z_n^{\pm m} \cdot \mathbf{Z}_n^{\pm m}(\varrho, \psi) \tag{3.61}$$

$\varrho = \frac{r}{D/2}$, with $0 \leq \varrho \leq 1$ is the normalized radius, ψ the angular coordinate over the pupil, $Z_n^{\pm m}$ is the aberration coefficient and $\mathbf{Z}_n^{\pm m}(\varrho, \psi)$ the Zernike polynomial. $n \in \mathbb{N}$ is defined as the order of aberration, $m \in \mathbb{N}$ is the angular frequency of the aberration [69]. There are even and odd Zernike polynomials. The even polynomials are defined as[112]:

$$\mathbf{Z}_n^{+m}(\varrho, \psi) = R_n^m(\varrho)\cos(m, \psi) \tag{3.62}$$

the odd polynomials are defined as:

$$\mathbf{Z}_n^{-m}(\varrho, \psi) = R_n^m(\varrho)\sin(m, \psi) \tag{3.63}$$

where $n \geq m$. If $n - m$ is even, $R_n^m(\varrho)$ are the radial polynomials. For $n - m$ is odd, the polynomial $R_n^m(\varrho) = 0$ – which means that these polynomials do not exist. $R_n^m(\varrho)$ is defined as:

$$R_n^m(\varrho) = \sum_{k=0}^{\frac{n-m}{2}} \frac{(-1)^k (n-k)!}{k!(\frac{n+m}{2} - k)!(\frac{n-m}{2} - k)!} \varrho^{n-2k} \tag{3.64}$$

The polynomial can be expanded to any order, increasing the order decreases the error in fitting the polynomial (Equation 3.61) to the true WF. In ophthalmology polynomials up to the 4th order are usually considered[113], as they are sufficient to describe most common aberrations found in the human eye[114]. Dealing with the two indices m and n is sometimes unhandy, thus Noll[115] came up with an alternative indexing. The single Noll index is j. The graphical representation of the Zernike polynomials with j indexing as well as n,m indexing and their common aberration name are given in Figure 3.16 up to the 4th order.

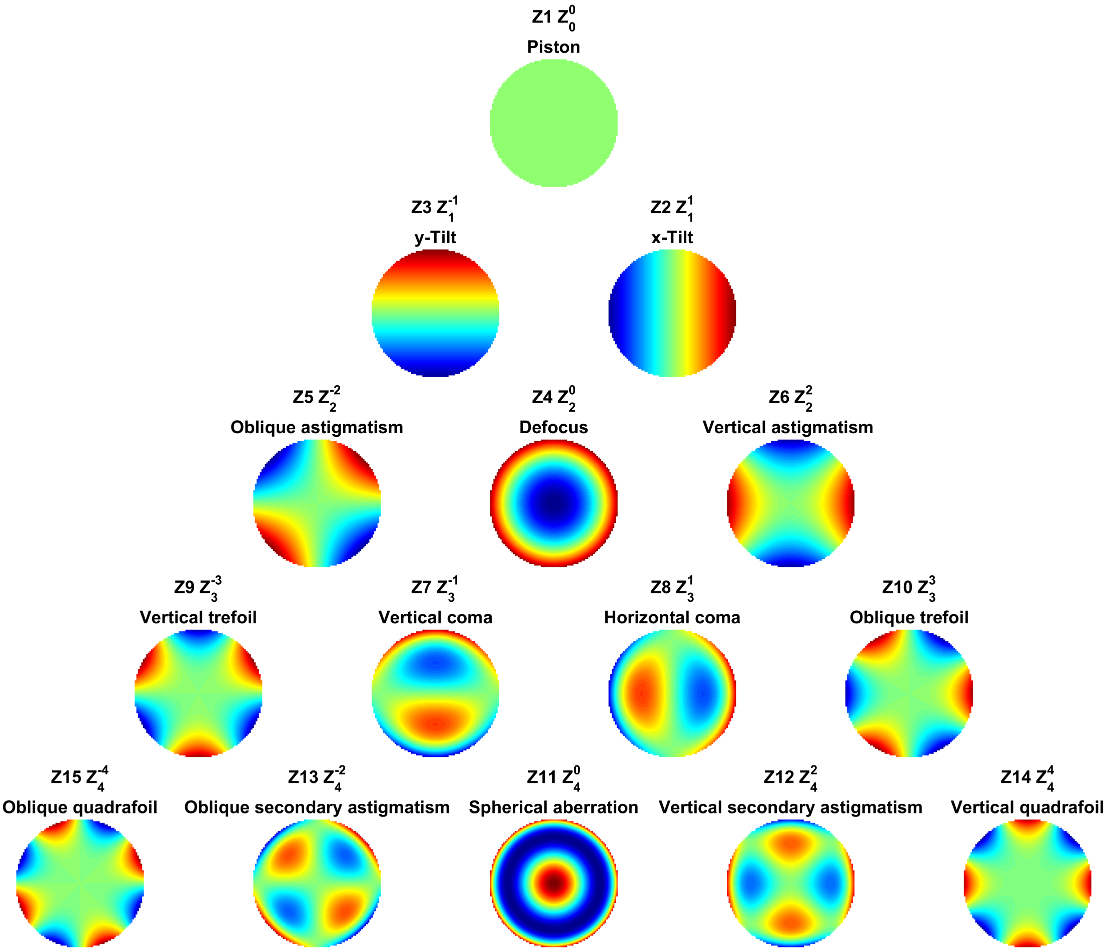
Z1 Z_0^0
Piston
Z3 Z_1^{-1}
y-Tilt
Z2 Z_1^1
x-Tilt
Z5 Z_2^{-2}
Oblique astigmatism
Z4 Z_2^0
Defocus
Z6 Z_2^2
Vertical astigmatism
Z9 Z_3^{-3}
Vertical trefoil
Z7 Z_3^{-1}
Vertical coma
Z8 Z_3^1
Horizontal coma
Z10 Z_3^3
Oblique trefoil
Z15 Z_4^{-4}
Oblique quadrafoil
Z13 Z_4^{-2}
Oblique secondary astigmatism
Z11 Z_4^0
Spherical aberration
Z12 Z_4^2
Vertical secondary astigmatism
Z14 Z_4^4
Vertical quadrafoil

Figure 3.16: Graphical representation of the Zernike polynomials on the unit cycle. m, n in $\mathbf{Z}_n^{\pm m}$ are the angular frequency and the order of the Polynomial; j in $\mathbf{Z}j$ is the Noll index. Detailed explanations on the aberrations Defocus, Astigmatism and Coma and SA are given in Section 3.3.

From Figure 3.16 it can be seen that the first three polynomials ($\mathbf{Z}_0^0$, $\mathbf{Z}_1^{-1}$ and $\mathbf{Z}_1^1$) and their linear combinations still preserve a flat WF, thus they do not violate the geometric imaging condition, and thus they do not describe geometric image aberrations. $\mathbf{Z}_0^0$ is a constant phase offset. $\mathbf{Z}_1^{-1}$ and $\mathbf{Z}_1^{1}$ cause that the image point P' is shifted from its center in x– and y–direction. These three coefficients will not further be analyzed, as the aim of this thesis is the investigation of image aberrations.

3.7 Summary Physical Image Formation

For a clear overview, the physical image formation under consideration of geometric errors and diffractive errors is summarized in Figure 3.17. The depiction is valid for incoherent illumination, as this is useful for the aim of this thesis. A focus is set on the mathematical connections between the mentioned characteristics for image aberrations, as they are later used for the experimental setup.

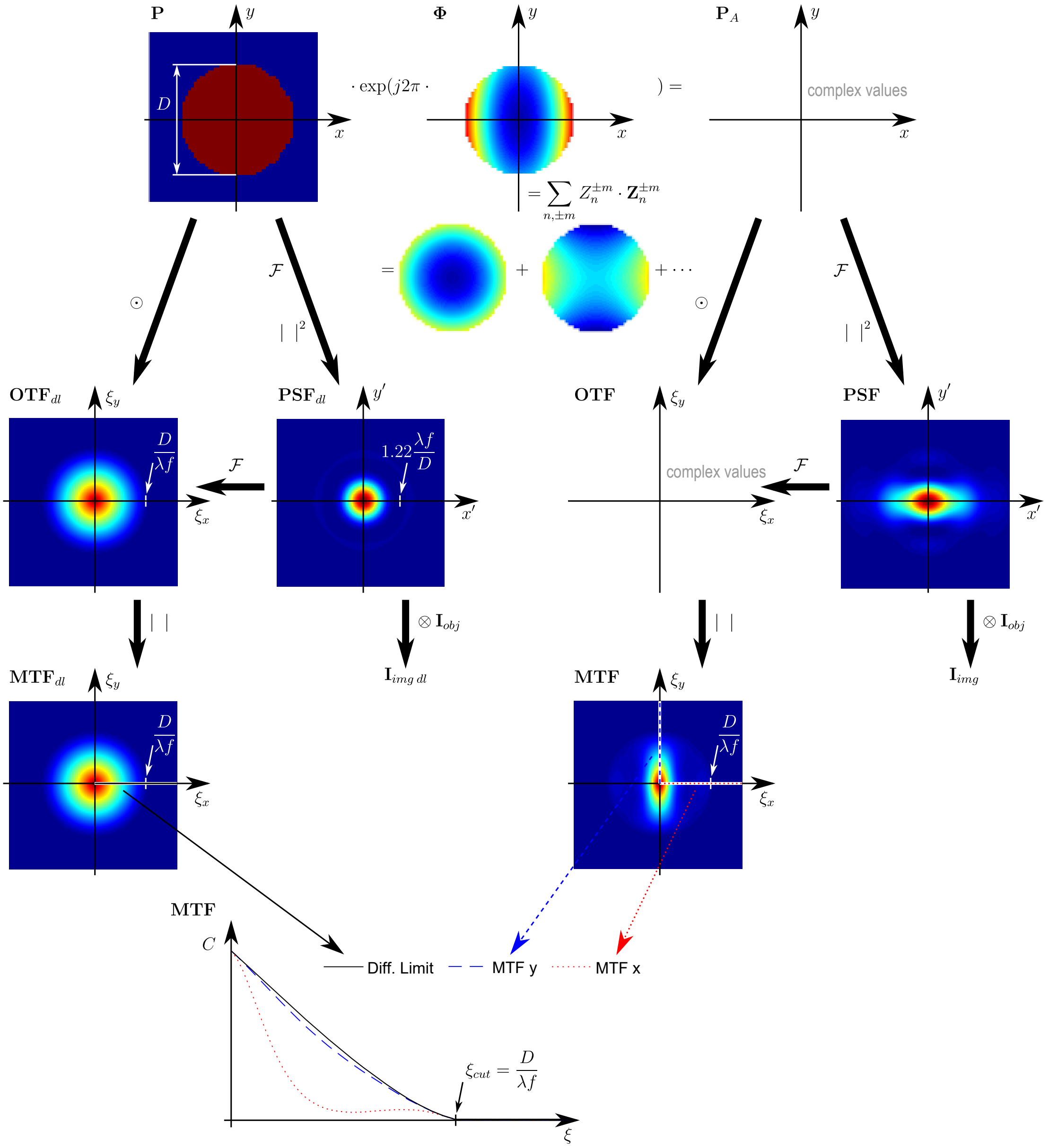
P
y
D
x
$\cdot \exp(j2\pi \cdot$
Φ
y
x
$) =$
P_A
y
complex values
x
$= \sum_{n,\pm m} Z_n^{\pm m} \cdot \mathbf{Z}_n^{\pm m}$
$=$
$+$
$+ \cdots$
$\odot$
$\mathcal{F}$
$| \, |^2$
$\odot$
$\mathcal{F}$
$| \, |^2$
OTF_{dl}
ξ_y
$\frac{D}{\lambda f}$
ξ_x
$\mathcal{F}$
PSF_{dl}
y'
$1.22\frac{\lambda f}{D}$
x'
OTF
ξ_y
complex values
ξ_x
$\mathcal{F}$
PSF
y'
x'
$| \, |$
$\otimes \mathbf{I}_{obj}$
$\mathbf{I}_{img\ dl}$
$| \, |$
$\otimes \mathbf{I}_{obj}$
$\mathbf{I}_{img}$
MTF_{dl}
ξ_y
$\frac{D}{\lambda f}$
ξ_x
MTF
ξ_y
$\frac{D}{\lambda f}$
ξ_x
MTF
C
Diff. Limit
MTF y
MTF x
$\xi_{cut} = \frac{D}{\lambda f}$
ξ

Figure 3.17: Summery on the mathematical connections in physical image formation. Left half: describes the diffraction limited image formation; Right half: consideration of diffractive and geometric errors; Top middle: WF decomposition into Zernike polynomials. Incoherent illumination with the wavelength λ is assumed, f is the focal length of the system. Mathematical operations along the errors are the transformations between the different image characterizations. $\odot$ is the autocorrelation, $\otimes$ the convolution, and $\mathcal{F}$ the Fourier Transform (all operations are 2D operations). Fields of complex values are not displayed, as this is impossible in a 2D graph. See text in Chapter 3 for the definitions of the other variables.

CHAPTER 4

Experimental Setup

This chapter outlines the precise configurations for all experiments and analysis done by numerical simulations. A detailed description of the optomechanical model eye and the working principle and construction of the measurement setups are presented in this section.

4.1 Numerical Simulations

As reference and for validation of the measurement results the optical ray tracing software ZEMAX OpticStudio is used to simulate the optical properties of the normal human eye and to assess the tilt and shift tolerance of IOLs with known data. If not noted otherwise all simulations are performed for a monochromatic illumination wavelength of $\lambda = 543$ nm. All WFs are corrected for tilt. For the iris diameter 3 mm and 4.5 mm were chosen, which are suitable values to mimic photopic vision and mesopic vision [9].

4.1.1 Optical Properties of the Normal Human Eye

The eye is modeled and simulated as depicted in Figure 4.1 the optical properties are in accordance with Table 2.1.

According to Liou and Brennan the nominal AL is 23.95 mm [16]. Simulations show, that the optimal AL for best focus depends on the iris diameter. Thus in all simulations the AL is optimized for best focus, this optimization results in slight differences to the nominal AL. This optimization can also be seen in other publications e.g. [9] and thus ensures that results can be compared with related scientific work. As focusing criterion the modulation at 100 lp/mm was chosen. The curvature of the retina (surface 6 in Figure 4.1) is not specified by Liou and Brennan. In the simulations the retina is modeled with a radius of $R = -12$ mm, which is in accordance with many of the model eyes mentioned in Section 2.1.1 e.g. [24]. Only the image on the central spot – image at

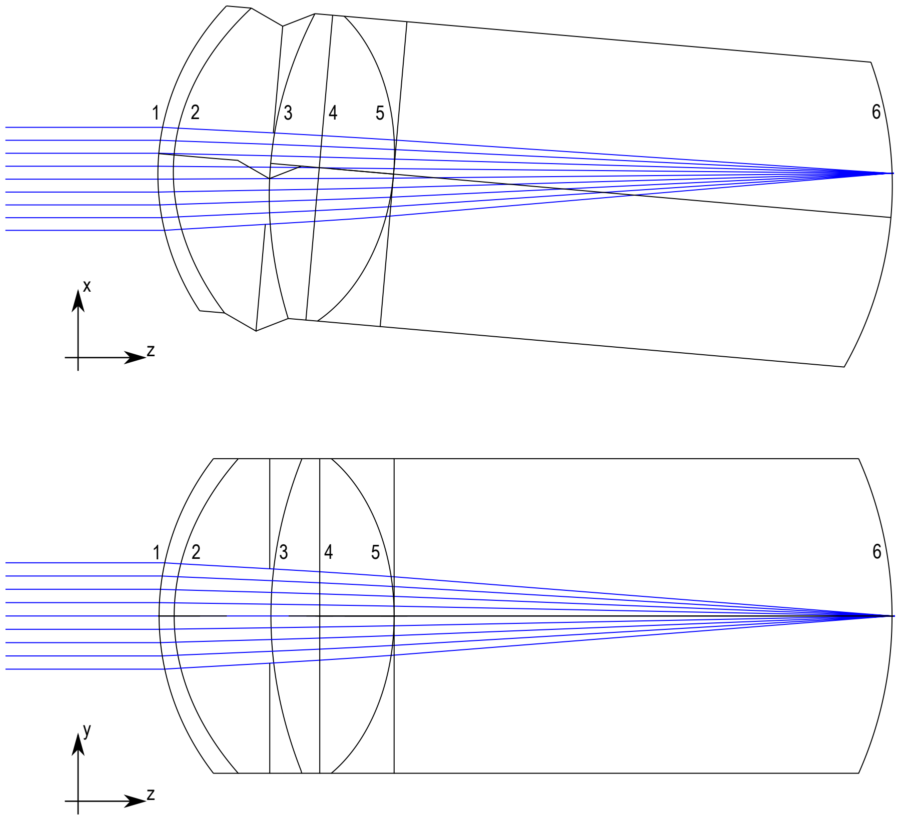

Figure 4.1: Layout for the numerical simulation of the Liou and Brennan Eye. The layout is depicted for a 3 mm iris diameter. In the x–z cross section the 5° tilt between the OA and the visual axis can be seen. Furthermore the iris is shifted 0.5 mm nasally (negative x-direction) corresponding to the Liou and Brennan Model. The eye is symmetric in the y–z cross section.

the fovea, the location of sharpest vision – is investigated. This, in combination with the optimization of the AL, causes that the radius of the retina barely influences the simulation results.

Comments on Correct Dispersion Simulation

Liou and Brennan[16] give detailed information to the construction of their model eye. Surprisingly, when reviewing results based on the Liou and Brennan eye one finds inconsistent data. One possible issue for this observation is a slightly wrong ZEMAX OpticStudio Knowledgebase resource[116], which seems to be used by many scientists: In this article the optical media are modeled with the ZEMAX material type "Model Glass". This model requires the refractive index n_d at the d-line ($\lambda_d = 587.5618$ nm), and the Abbe number V_d which is a measure for the dispersion of an optical media. ZEMAX uses the definition

$$V_d = \frac{n_d - 1}{n_F - n_C} \tag{4.1}$$

where n_F and n_C are the refractive indices at the F-line ($\lambda_F = 486.1327$ nm) and the C-line($\lambda_C = 656.2725$ nm) respectively. For the n_d value the article suggests to input the data as given in Table 2.1[116]. This is wrong, as the these values are the refractive indices for λ=555 nm and not for $\lambda_d = 587.5618$ nm. For all surfaces the article uses an Abbe number of $V_d = 50.23$[116]. Again this is wrong. The dispersion according to Liou and Brennan is given by Equation 2.2. Evaluating this equation for the wavelength λ_d, λ_F and λ_C and plugging the results into Equation 4.1 the correct values to be used as input for the ZEMAX model can be calculated. Results are shown in Table 4.1. There is a relevant difference between $n(\lambda_d)$, the correct input for the ZEMAX model, and the value $n(555\text{ nm})$. The differences get even more severe for the Abbe number V_d.

Table 4.1: Refractive indices for two optical media from the Liou and Brennan eye for four different wavelength and the corresponding Abbe Number V_d.

Material	$n(555\text{ nm})$[16]	$n(\lambda_d)$	$n(\lambda_F)$	$n(\lambda_C)$	V_d
Cornea	1.376	1.374886	1.379179	1.373102	61.6942
Ocular media	1.336	1.334886	1.339179	1.333102	55.1115

4.1.2 Assessing the Tilt and Shift Tolerance via Numerical Simulation

In Section 2.2.2 recent scientific work, which aims to test the optical performance of tilted and decentered IOLs in optical bench has been reviewed. To learn more about the tolerance regarding displacements of specific IOL designs, numerical computer simulations can be done. Unfortunately IOL manufacturers are not required to publish their optical design data. Also production tolerances are unknown. These facts underline the experimental optical bench setup approach chosen for this thesis. Nevertheless a new test procedure has to be validated. This validation will be done by comparing the measurement results with results from numerical simulation.

Scientists rarely get IOL design data for the purpose of publishing simulations based on these data. Two known papers with IOL design data are known. Altmann et al. [117] simulated the optical performance of three IOLs (SofPort AO, Bausch & Lomb; LI61U, Bausch & Lomb Inc. and Tecnis Z9000, Advanced Medical Optics) in the presence of decentration. The study was carried out at the Optics Center, Bausch & Lomb, Rochester, New York, USA. Eppig et al. [9] (Institute of Medical Physics, University of Erlangen-Nuremberg, Erlangen, Germany) analyzed six IOLs (Tecnis Z9000, Advanced Medical Optics; Invent ZO, Carl Zeiss Meditec AG; Aspira-aXA, Human Optics AG; MC6125AS, Dr. Schmidt Intraocularlinsen; SofPort AO, Bausch & Lomb Inc. and MC5812AS, Dr. Schmidt Intraocularlinsen[1]) in the presence of tilt and decentration. These publications are valuable as they provide the optical design data of the tested lenses. Altmann et al. [117] only tested for pure decentration and the model of the eye does not follow the findings for Liou and Brennan. Eppig et al. [9] carried out their simulations based on the Liou and Brennan model eye and thus is in accordance to the model used in this thesis. As recommended by the ISO standard, the MTF is evaluated at 30 cycles/degree, which corresponds with the 100 lp/mm of the test standard.

---

[1] Dr. Schmidt Intraocularlinsen are currently sold by Human Optics AG

Despite this publication being the most profound work which could be found regarding systematic simulation of tilt and shift tolerance of various IOL designs, there are some concerns about this work:

- Only the MTF is evaluated, which corresponds to the ISO standard – the WF would reveal more details on the type of image aberration generated by the lenses misalignments.
- Only pure shifts and pure tilts are tested, not the combination of both effects, which in reality occur.
- The modulation values at 100 lp/mm tends to be sensitive to displacements for some lenses, especially for decentrations exceeding 0.5 mm, where the tangential modulation values for the Aspira-aXA oscillate with decentration, see Figure 4.2. The 0.25 mm and 1° increments chosen by the authors are sometimes too rough. This under-sampling leads to the fact that the oscillation frequency could be higher, which is just not detectable by the chosen sampling.

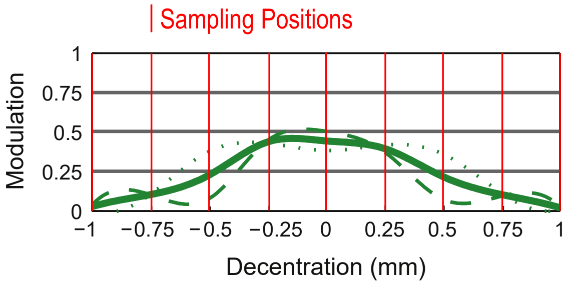

Figure 4.2: Modulation values at 100 lp/mm for the Aspira-aXA IOL at the 4.5 mm pupil diameter. The plot depicts the mean modulation (solid line), sagittal modulation (dotted lines) and tangential modulation (dashed lines). The sampling points chosen by the authors of the publication (Eppig et al. [9]) are marked with red lines. The interpolation for the tangential modulation is questionable for the amount of sampling points. Figure is adapted from [9]

For the simulations with IOLs the surface 3, 4 and 5 (see Figure 4.1 and Table 2.1 for surface definition) are replaced by two surfaces with the IOL design data as given in Table 4.2. The location of the iris is kept equal to the original position within the Liou and Brennan eye. The IOL is positioned in a way, that the object–sided principal plane of the IOL coincides with the object sided principal plane of the natural crystalline lens.

With the cardinal point analysis in ZEMAX OpticStudio the location of the natural crystalline lens can be found to be 2.06 mm behind the iris plane.

The simulation procedure is controlled by a MATLAB–function, which manipulates the geometry in the ZEMAX model via an API. The procedure comprises the following steps:

1. Modification of the IOL data for the lens to be simulated given in Table 4.2
2. IOL is shifted along the z–axis so that the IOL's principal plane H is located 2.06 mm behind the iris.
3. An optimization is started which finds the optimal AL, which maximizes the modulation at 100 lp/mm (mean value between the modulation x- and y–direction)
4. Tilting the IOL around the θ axis and shifting along the x–axis to simulate a certain position in the 2D (θ,x)–parameter field
5. WF–data (Zernike coefficients) and MTF in x and y direction are stored for each position (θ,x)
6. Continue with step (4.) until all positions in the parameter field (θ,x) are analyzed

Table 4.2: Data of the lenses which were used for simulations and measurements for this thesis. For the CT LUCIA 611PY only basic information is given, since the detailed lens data were provided under a non disclosure agreement.

Product	MC5812AS	MC6125AS	CT LUCIA 611PY
Supplier	Human Optics	Human Optics	Carl Zeiss Meditec
Design concept	Spherical	Aberration free	Aberration correction
Power [dpt]	22.0	22.0	21.0
Anterior surface	Sphere	Conic asphere	Aspheric
Radius R [mm]	13.0	12.0	–
Conic constant c	0	-7.8	–
Posterior surface	Sphere	Sphere	–
Radius R [mm]	-10.0	-10.733	–
Conic constant c	0	0	–
Center thickness [mm]	1.057	1.014	–
Material	HPiAC	HPiAC	HPoAC
Refractive index	1.461	1.461	1.49
Optic size [mm]	5.8	6.0	6.0
Overall size [mm]	12.0	12.5	13.0
Haptic angulation	0°	0°	–
Type	Single-piece	Single-piece	Single-piece
Data source	[9]	[9]	[118, 119]

Intraocular Lenses to be Tested

Of the lenses with known data [117, 9] not all lenses were currently available on the market, the publications are of 2005 and 2009. In other cases manufacturers did not sell the lenses for non–medical use. Finally three different lenses could be used for comparing simulation and measurement results within this thesis:

- MC5812AS, directly purchased from Human Optics AG, design data are known from Eppig et al. [9]
- MC6125AS, directly purchased from Human Optics AG, design data are known from Eppig et al. [9]
- CT LUCIA 611PY, supplied by Carl Zeiss Meditec AG, design data were supplied by the company but cannot be published in this thesis due to a non–disclosure agreement.

Lens data are listed in Table 4.2 as far as they are made publicly available.

4.2 Optomechanical Model of the Human Eye

Section 2.2 outlines the requirements for such a test setup based on findings from clinical application of IOLs for cataract treatment. Furthermore, features in distinction to already existing approaches are described there. An optomechanical model eye fulfilling all these requirements is described here.

Of the problems stated in section 1.2, the first two have to be considered in the design of the model eye. Resulting from these problems, two main requirements for the design can be deduced:

- The model eye has to precisely mimic the physiology of the human eye. Therefore the model eye is designed according to the Liou and Brennan eye as explained in detail in Section 2.1.2
- To simulate post surgical lense displacements the holder for the IOL is implemented in a way that it can automatically be tilted and shifted.

The construction is already published [19], as some recent changes were done a detailed description of the construction is given here:

4.2.1 Overall construction

To mimic a physiologic environment for the IOL to be tested, the optics have to be embedded into a liquid of the same refractive index as the aqueous humor. Water has an refractive index of 1.333[120] which is lightly less than the refractive index of 1.336 of the

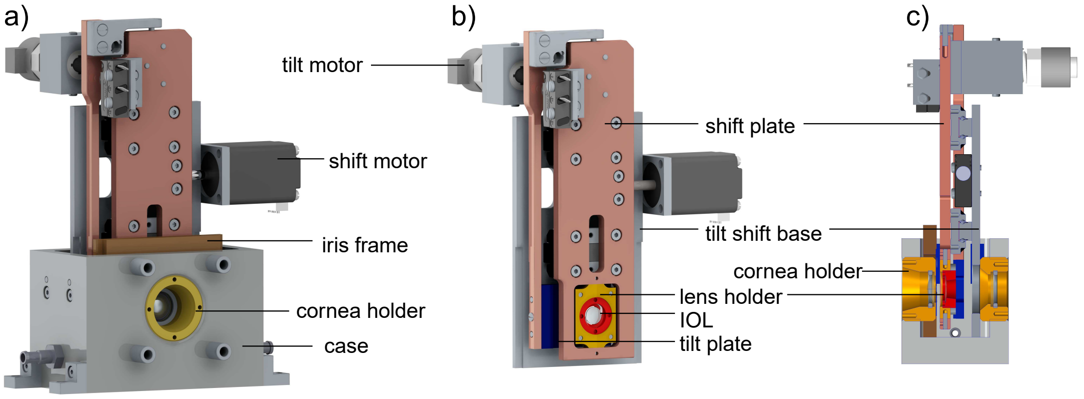

Figure 4.3: 3D renderings from the CAD model a) the overall assembly of the mechanical model eye b) tilt and shift unit of the mechanical eye model c) cross section of the mechanical eye model

aqueous humor. Some researches claim that the difference is negligible [14]. Nevertheless for the relevant components materials were chosen in a way that a saline solution with a concentration of 1.6% salt per mass unit can be used without damage on the model due to corrosion. With that, the exact refractive index of the aqueous humor can be simulated by the model eye.

The overall construction can be seen in Figure 4.3 a). The saline solution is kept in a case housing which is open on top. Precision threads on the front and the back of the case provide space for mounting a cornea lens and a retina window. The opening for cornea and retina are drilled in one production stage and minimize the inaccuracy of the misalignment on the individual components' OA.

The iris and a holder for the IOL are constructed as slide in modules. The precise position is guaranteed by register pins in the bottom of the case. Guide blocks on the left and right side walls of the case ensure a parallel alignment to the x-y–plane.

Due to the fact that saline solution is used, all components, which are in contact with the solution, are made of plastic or stainless steel.

A study by Walker et al. [121] suggests that the difference between room temperature and body temperature could influence the optical properties. Therefore the saline solution and the IOL can be heated for physiological measurements at body temperature. The test standard recommends to measure the IOL at ambient room temperature, except the dimensions of the lens change significantly at in situ temperatures [12]. Literature reports that the dimensions of the IOL do not change appreciably between ambient and in situ temperature[13]. From own experience measurements at in situ temperatures, cause additional experimental uncertainties, e.g. cornea– and retina– window can get fogged due to the temperature gradient, no significant change on the lens properties could be observed. This is consistent with the findings by Walker et al. [121], where

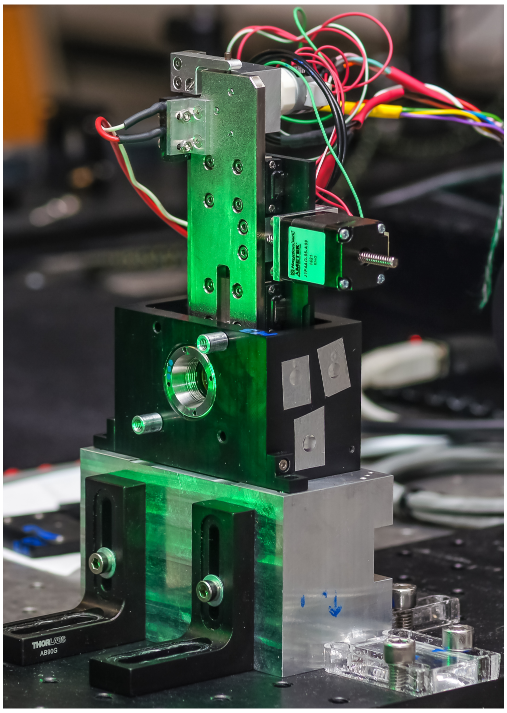

Figure 4.4: Photography of the assembled eye model during its use in a measurement.

significant changes can only be seen in the total refractive power[2]. Thus the heating mechanism was not used for the results presented in this thesis.

Within the measurement setups, which are described in Section 4.3 – 4.5, the case is held by two registration pins on the bottom of the case. As shown in Figure 2.3 the visual axis is tilted at five degrees with respect to the OA. To account for this deviation the measurement setup provides two sets of drill holes for the registration pins: one for a straight alignment (visual axis is aligned with the OA) and one for the physiological configuration, where the case is tilted at $\theta = -5°$ around the center of the entrance pupil E, as depicted in Figure 2.3.

Scattered light can decrease the optical performance, to minimize internal reflections all parts were made of black Polyoxymethylene (POM). Some parts required higher mechanical strength, these parts were made of stainless steel. Tight manufacturing tolerances are necessary to ensure a precise relative aliment of all components. The manufacturing was done with precision CNC machines by the Fraunhofer Institute for Applied Optics and Precision Engineering, Jena, Germany[3]. A photograph of the fully assembled eye model is shown in Figure 4.4.

---

[2] In this thesis the absolute refractive power is not measured, just the change in refraction due to lens displacements

[3] `https://www.iof.fraunhofer.de`

4.2.2 Design of the Model Cornea

No technical materials with the same refractive index as the human cornea lens are available. Thus an appropriate model–cornea has to be designed. PMMA can be precision diamond turned and thus is a suitable material for custom lenses. As its refractive index $n = 1.4921$ at $\lambda = 555$ nm[122] differs from that of the human cornea $n = 1.376$, the shape has to be modified. Manufacturers [4] recommended a minimum center thickness of 0.7 mm for manufacturing purposes. The anterior cornea surface was kept equal to the topography of the human cornea. The shape of the posterior surface was optimized to retain the same refractive power and equal image aberrations as the human lens. Calculations were done with ZEMAX OpticStudio. Optical parameters are given in Table 4.3. Note: In comparison to the original cornea (see Table2.1) the model cornea has slightly shifted locations of the principal planes. Thus the thickness of surface 2 (distance between posterior cornea surface and iris) has to be changed.

Table 4.3: Parameters for the model cornea.
r ... radius of surface curvature, c ... asphericity, d ... thickness

Surface Name	#	r [mm]	c	d [mm]	Material
Cornea anterior	1	7.77	-0.18	0.70	PMMA
Cornea posterior	2	7.186631	-0.346048	2.770	–

In literature it is recommended that artificial corneas are manufactured with a tolerance of ±0.025 mm in radii and ±0.001 for the conic constants[14]. Thus lenses were measured with a surface profiler after the manufacturing process. See Appendix B and Section 6.1.1 for a discussion on the measurement results.

The lens is held by a stainless steel lens holder and sealed with an O–ring.

4.2.3 Iris Aperture

The pupils are made of a 0.3 mm thick stainless steel plate. The pupils are placed with a plug–in–holder, which can easily be exchanged and precisely aligned without disassembling the model eye. A set of pupils with the diameters 2 mm, 3 mm, 4 mm, 4.5 mm and 5 mm are available. For the 0.5 mm nasal shift of the pupil according to Liou and Brennan a second set of pupils is available. The shape permits only an insertion of the pupils in one direction, thus unintended flip of the aperture blades is not possible.

4.2.4 Tilt–Shift Unit to Simulate Post–Surgical Lens Displacements

For the purpose of simulating post operative tilts and decentrations of the IOL, the model eye is equipped with a mechanism, which allows to automatically and precisely shift and tilt the IOL within the model. This unit, further referred to as "Tilt–Shift Unit" is depicted in Figure 4.3 b). Via the base plate the whole unit is placed in the eye model via plug-in system. The base plate does not move within the eye model, register pins ensure a precise and correct position.

---

[4] Sumipro Submicron Lathing, Almelo, Netherlands `http://www.sumipro.nl` manufactured the lenses for this project.

The shift plate is mounted on the base plate via miniature linear ball bearings. For an automatic shift movement a linear stepper motor is used to drive the shift plate with respect to the base plate along the x–axis of the optical system. The range of motion for the mechanism is ± 1.5 mm with respect to the centered position. This exceeds the range of displacement of IOLs in the human eye as outlined in Section 2.2. During the measurement procedures only a clinical relevant range of ± 0.6 mm is used.

The lens holder can pivot within the shift–plate, where the axis of rotation is parallel to the y–axis. Via a connection rod the tilt movement is transmitted to the top of the tilt and shift unit. A second linear stepper motor pushes against a lever, which converts the linear motor movement to a rotational movement. A tension spring, exerts a constant force against the tilt motor to guarantee a backlash free operation. The motion range with respect to the center position is $\pm 5°$. Again this exceeds the tilt range reported in literature. For the measurements again only a clinical relevant range of $\pm 3.5°$ was used.

Both actuators have a step width of 20 μm, which is electronically operated in a $\frac{1}{8}$ micro stepping mode. Thus linear shifts as small as 2.5 μm can be done. With an effective leaver length of 20.5 mm, the tilt mechanics has an angular resolution down to 2.13 $\mu°$. By combining both mechanisms, the IOL can be positioned automatically in a two dimensional parameter field x, θ.

Both mechanisms (shift and tilt) are equipped with a micro switch. With that, for each axis a reference position can be detected with an accuracy <20 μm. Prior and after each measurement sequence the centered position is checked within an optical measurement system, see Figure 4.5 a.).

4.2.5 Holder for the Intraocular Lens

The IOLs are mounted within 3D printed holders, which have a groove against which the elastic haptics can spread. As outlined in Section2.2.1 there is a vast variety of haptic designs, thus the holder has to be individually designed for each lens. The holder has a metric fine thread (M14x1) on its outside diameter with which it is screwed into the tilt and shift unit. Prior to the installation in the model eye, the IOL is inserted into the lens holder and examined under a stereo microscope for a centered position within the holder, see Figure 4.5 b).

In the human eye the object sided principal plane is located 2.06 mm behind the iris. To ensure the correct distance between IOL and iris, the holder is designed with the correct thickness in a way that the holder cannot be screwed into the tilt–shift–unit deeper than the desired distance.

Because most IOL data sheets deliver insufficient data on the mechanical properties, e.g. elasticity of the IOL–haptics and unknown haptic geometry, the precise position along

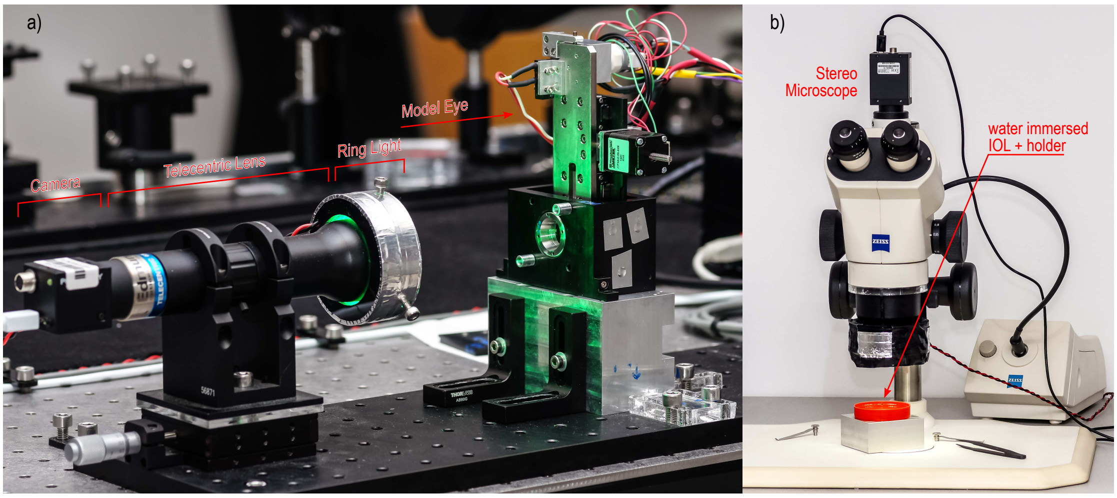

Figure 4.5: a) A machine vision setup (telecentric lens and a camera) with an optical resolution of 10 μm per pixel is used to perform absolute measurements of tilt and shift unit's position. b) With a stereo microscope the IOL is observed within the lens holder to check for a correct centered lens placement.

the OA (z–axis) is unknown. Extensive experiments have been performed to evaluate the best properties for an IOL–holder[123]. With the experience of designing several IOL–holders for different lenses, the tolerance is expected to be below ±0.3 mm within the desired axial position. The effect of a shift ±0.3 mm along the OA was evaluated for the numeric simulations as described in Section 4.1.2, it could be seen that the axial displacement has no or a negligible influence on the simulation results[5]. This observation also corresponds to the finding of other researchers e.g. Norrby at al. [14]. The shift along the OA changes the total refractive power of the eye, but since measurement setups are set to the optimal focus, this defocus effect is compensated by the measurement procedure.

The mechanical axis of rotation of the tilt-shift unit is installed 3.35 mm behind the iris diaphragm (red spot in Figure 4.6). As the lens position is determined by optical properties, see above, rotating the tilt unit induces a lateral shift in x–direction, if the lens center does not coincide with the axis of rotation. This can be compensated by a movement of the decenter mechanism. Thus, by combining the θ–tilt and the x–shift movement, the IOL can be rotated virtually about any axis of rotation along the z–axis (OA). It allows to reproduce a rotation about the same optical point (e.g. lenses' principal plane or lens center) for each IOL, even if they require different distances to the iris.

---

[5] Results are not shown in this thesis, since now differences can't be seen

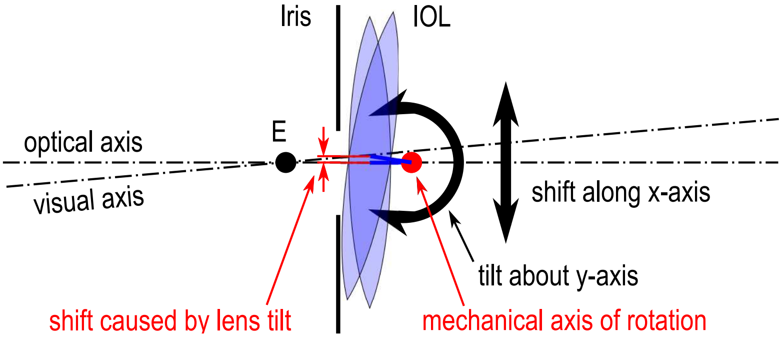

Figure 4.6: If the IOL is not rotated about its own center, each θ tilt induces a small x shift. This movement is outbalanced by a counter shift with the x–axis shift mechanism.

4.2.6 Retina

The retina is implemented as a 1 mm thick optical BK7 glass plate. The glass is mounted in a stainless steel holder similar to that holding the cornea lens.

The window, which optically connects the model eye to the measurement setups could be replaced by a reflective element. If the reflective properties are similar to those of the human retina, model eyes can be examined with devices from clinical ophthalmology, this was e.g. demonstrated by Norrby at al. [14].

4.3 Setup for Measuring the Modulation Transfer Function

The mathematical fundamentals of the MTF are given in Section 3.6.2. The purpose of this setup is to deliver ISO 11979-2 compliant MTF–measurements, but the ISO model is replaced by the physiological accurate model eye. With that, results can directly be compared with the current test standard. For MTF–measurements the ISO 11979-2 [12] refers to the ISO 9335 "Optics and photonics – Optical transfer function – Principles and procedures of measurement". The ISO 9335 basically defines an optical bench setup where the optical system to be tested ("test specimen") images a known test target; An image analyzer captures the image produced by the system [124]. The test target to be used is not defined: *"Depending on the characteristics of the test specimen, several different types of test target may be used. Circular apertures, slits, edges, gratings and self-luminous test targets such as incandescent wires are commonly used."[124]*. The direct measurement can be done by observing the image of objects with known spacial frequencies. For this procedure a standard test chart, the United States Air Force (USAF)–target (see Figure 4.7 a)), is available. Only discrete frequencies, available on the chart, can be evaluated. The Siemens star (see Figure 4.7 b)) provides continuously increasing spacial frequencies towards the center, but the evaluation is tedious, since each frequency can only be found at a specific field point.

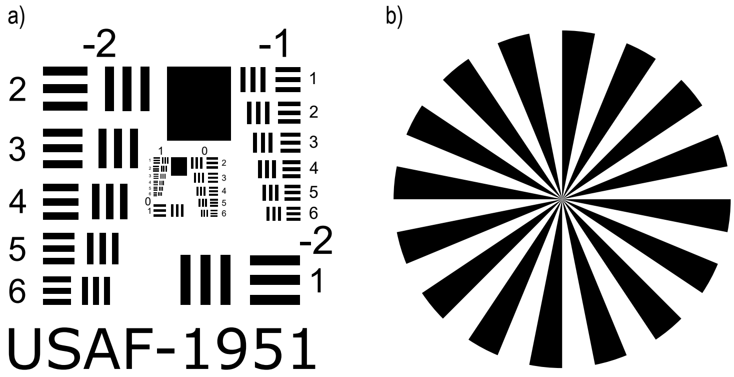

Figure 4.7: a)The USAF–target provides patterns of specific spatial frequencies. b) The Siemens star has continuously increasing spacial frequencies from the outer border to center. Both targets can be produced with a sinusoidal intensity pattern which does not include harmonics of the fundamental spatial frequency.

As outlined in Section 3.6.2, the MTF can be calculated from the PSF, LSF and ESF. The so called "Slanted–Edge" method is a very popular approach [125]. It relies on an indirect MTF–calculation from an ESF–measurement. The calculation requires the derivative of the edge function (see Equation 3.38). This calculation is prone to errors due to image–noise and ultimately limited by the spatial frequency of the Nyquist limit ξ_{Nyq}:

$$\xi_{\mathrm{Nyq}} = \frac{1}{2p} \tag{4.2}$$

where p is the pixel pitch of the image acquisition sensor. By slightly tilting the edge (e.g. by 5°) sub–pixels can be interpolated from the adjacent sensor lines (see Figure 4.8). An algorithm for the slanted edge–method is defined in the ISO 12233 "Photography – Electronic still picture imaging – Resolution and spatial frequency responses" [126]. Changes in the standard were made in 2014, major change was the reduction of the image contrast[125]. Too high image contrasts can cause clipping on the whites or blacks of the image, which often caused wrong results.

The slanted edge method was also used for this setup. The schematic concept for MTF–measurement with the model eye is depicted in Figure 4.9. In detail, the following components were used:

- The **slanted edge target** is mounted on a white LED illumination panel (Edmund Optics # 83–873). The slanted edge is a high resolution print on a transparent film, the edge is aligned slanted by 5° to the y–axis

- The **model eye** is tilted by 5° to simulate the physiologic antisymmetry between optical– and visual axis.

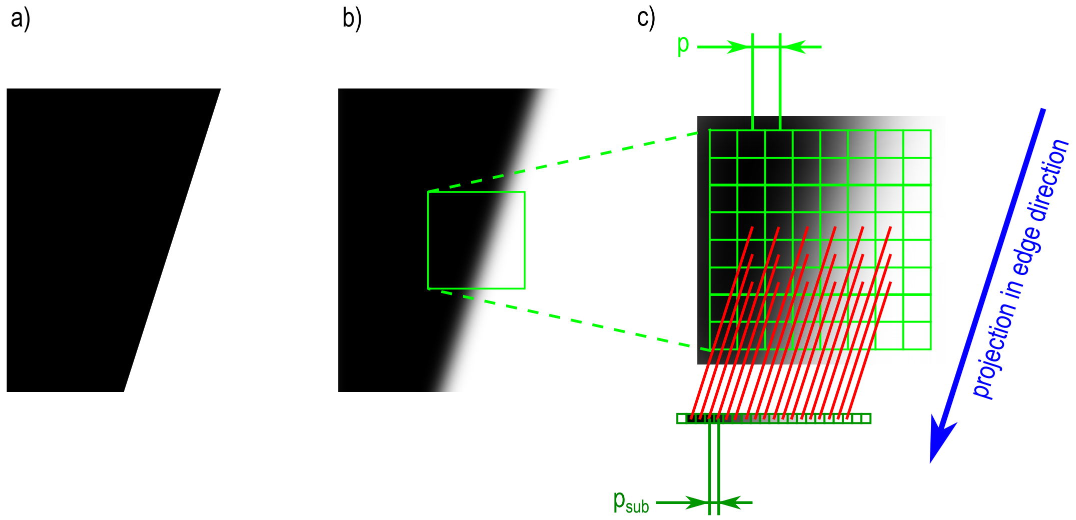

Figure 4.8: a) A slanted edge target image. b) Due to image aberrations the image of the target is blurred. c) Detail view of b); The green grid depicts the pixel grid from the image acquisition camera sensor with the pixel pitch p. If the pixel intensities are projected along the edge direction, adjacent sensor lines can be used to generate interpolated sub–pixels with higher spatial sampling p_{sub}.

- For the measurements a **narrow band** 543.5 nm, FWHM 10 nm **filter** (Thorlabs FL543.5–10) was used for measurement at the wavelength specified by the ISO 11979–2. See Figure 4.10.

- The retina image is captured with an **5x magnification objective** lens (Edmund Optics # 88–353) with Numerical Aperture (NA) 0.15 and a working distance of 16.2 mm.

- A monochrome 5 Mega Pixel (MP) **camera** (FLIR Blackfly BFLY-U3-50H5M-C) with 2448 × 2048 pixel size 3.45 μm × 3.45 μm and 7.5 Frames Per Second (FPS). Exposure values were adjusted in a way that the dynamic range of the sensor was fully used but no intensity clipping below black and above white occurs at any time.

- A **MATLAB software** was written, which controls the stepper motors via a Data Acquisition (DAQ)–board (National Instruments USB–6211) and electronics, as described in an earlier publication[19], reads out the camera images, performs the MTF evaluation and data management. The algorithm for the slanted edge MTF evaluation provided by Peter Burns is ISO 12233 compliant[127].

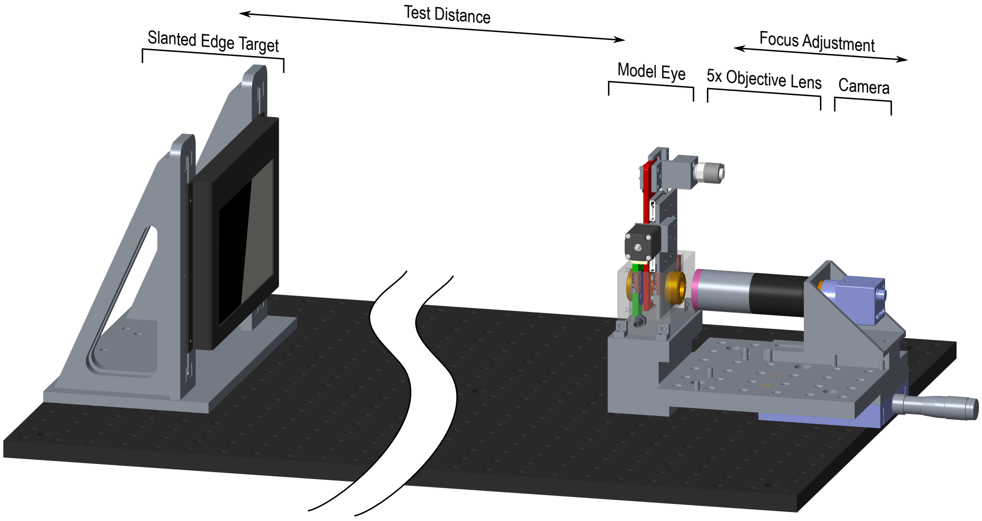

Figure 4.9: Schematic of the setup for measuring the MTF. A slanted edge target is observed by the model eye. The retina image of the model eye is captured by a camera with a 5x microscope objective. The camera with the microscope objective is mounted on a translation stage, with that the AL of the model eye can be adjusted to different target distances and to the refractive power of the IOL to be tested. Between Model Eye and target optionally color filters for monochromatic measurements can be inserted.

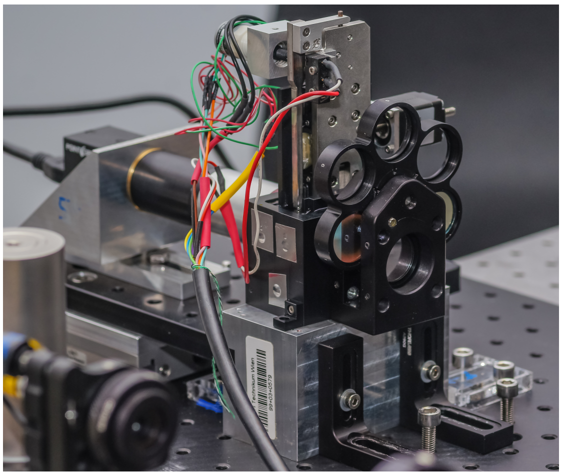

Figure 4.10: A filter wheel, equipped with three narrow bandpass filters 488 nm, 543.5 nm and 650 nm, all with FWHM 10 nm (Thorlabs FL488–10, FL543.5–10 and FB650–10), can be attached in the front of the eye to measure the optical properties at specific wavelengths.

4.3.1 Details on the Retina Image Sampling

To implement a proper MTF–measurement with the model eye, a sufficient sampling of the retina image has to be guaranteed. Thus a careful selection of the image capturing system is required. As mentioned in Section 2.1, the accurateness of vision under optimal conditions (photopic vision) is $1\frac{\text{lp}}{\text{arc minue}}$ – see also Figure 2.2. For the normal human eye it can be shown that the conversion between $\frac{\text{lp}}{\text{degree}}$ in the object space and $\frac{\text{lp}}{\text{mm}}$ on the retina is given by:

$$1\frac{\text{lp}}{\text{degree}} = 3.37\frac{\text{lp}}{\text{mm}} \tag{4.3}$$

This calculation is based on the normal focal length of the human eye[6] With Equation 4.3 the visual accuracy corresponds to 202.2 $\frac{\text{lp}}{\text{mm}}$ on the retina plane. This is consistent with the results of the Liou and Brennan Eye as shown in Figure 5.1 and 5.2, where it can be seen that these spatial frequencies can be observed with a modulation of approximately 0.3.

Furthermore the MTF–measurement should be compliant with the specifications of the current ISO–standard, which requires measurements at 100 $\frac{\text{lp}}{\text{mm}}$. Therefore the acquisition system for the retina image should be free of aberrations at 100 $\frac{\text{lp}}{\text{mm}}$ and must be able to capture spacial frequencies beyond 200 $\frac{\text{lp}}{\text{mm}}$.

The objective lens used with 5x magnification and the camera with 2448 x 2048 pixel size 3.45 μm x 3.45 μm results in a pixel size of p_{Retina} =690 nm in object space (Retina) and a field of view of 1.689 mm in x–direction and 1.413 mm in y–direction. Therefore the Nyquist limit for the retina sampling $\xi_{\text{Nyq Retina}}$ is given by

$$\xi_{\text{Nyq Retina}} = \frac{1}{2p_{\text{Retina}}} = \frac{1}{2 \cdot 690\text{nm}} = 724.4\frac{\text{lp}}{\text{mm}} \tag{4.4}$$

This spatial frequency is further increased by the sub—pixel interpolation of the slanted edge algorithm.

The optical resolution of the objective is limited by its diffraction limit. The lens has NA=0.15. This corresponds to ${}^{f}/_{\#} = 3.33$. With Equation 3.57 this results in:

$$\xi_{cut_{\text{Objective}}} = 552\frac{\text{lp}}{\text{mm}} \tag{4.5}$$

The Liou and Brennan eye has a ${}^{f}/_{\#} = 4.88$ for a 3 mm iris diameter and ${}^{f}/_{\#} = 3.25$ for 4.5 mm iris diameter (see Table 5.1). In an optical system, chaining up multiple optical image formations, the diffraction limit is determined by the smallest aperture. Thus in the case of a 3 mm aperture, the objective lens used does not induce additional diffractive errors. For the 4.5 mm aperture the diffraction limit is only slightly reduced by the objective. Thus the chosen NA of the objective lens is sufficient, but it has to be pointed out that geometric aberrations of the objective lens can interfere with the aberrations of the model eye. See Section 6.3.3 for a detailed discussion on that issue.

---

[6] In the standard ISO 11979-2:2014 section 4.3.1 [12] a wrong conversion factor of 1 cycle/degree = 0,297 lp/mm is given. During the research of this work this mistake was reported to the standardization organization, a correction will be done in the next revision of the standard, see Appendix A.

4.3.2 Measurement Procedure

All components as described above are set up on an active vibration isolating optical table to prevent coupling of surrounding vibrations on the measurement setup. The target is set to a distance of 1420 mm. Numerical simulations proved, that this finite distance, compared to the theoretically assumed infinite distance just changes the AL for an optimal focus but does not change the image aberrations significantly. Notable changes are only observable if distances closer to about 1 m are used. Each measurement followed this procedure:

- The IOL to be tested is mounted within the lens–holder and examined under a microscope. The lens–holder gets mounted into the tilt–shift–unit and assembled with the model eye and a iris aperture (3 mm or 4.5 mm).
- With a telecentric machine vision setup, as described above, the centered position is approved.
- The Model Eye is now put into the MTF–setup and equipped with a 543.5 nm color filter for monochromatic measurements.
- The linear translation stage (see Figure 4.9) is adjusted to retain the highest contrast at $(100 \,\frac{\mathrm{lp}}{\mathrm{mm}})$ for the $\mathbf{MTF}_x$.
- The MTF is stored (pre–measurement)
- A computer software automatically sequentially goes through all possible lens positions in the defined range and stores the MTF for each position (auto–measurement).
- The lens is set back to the centered position. The MTF is recorded again (post–measurement).
- The lens position is again checked with telecentric machine vision setup.
- If a mechanical lens displacement in the lens holder during the measurement sequence is observed in the machine vision setup the whole measurement is discarded and repeated. In this case a mismatch of the pre–, auto– and post–measurement MTF is visible.

4.4 Setup for Measuring the Wavefront Aberrations

There are many measurement principles to measure WF aberrations [69]. The so called Hartmann–Shack sensor is a frequently chosen principle in ophthalmology. This sensor's working principle is to measure the local gradient of the WF at many spots over the sensing area. The WF is then mathematically derived from the local gradients. The local gradient at many positions can be examined by an array of tiny lenses (lenslet array). The working principle is depicted in Figure 4.11

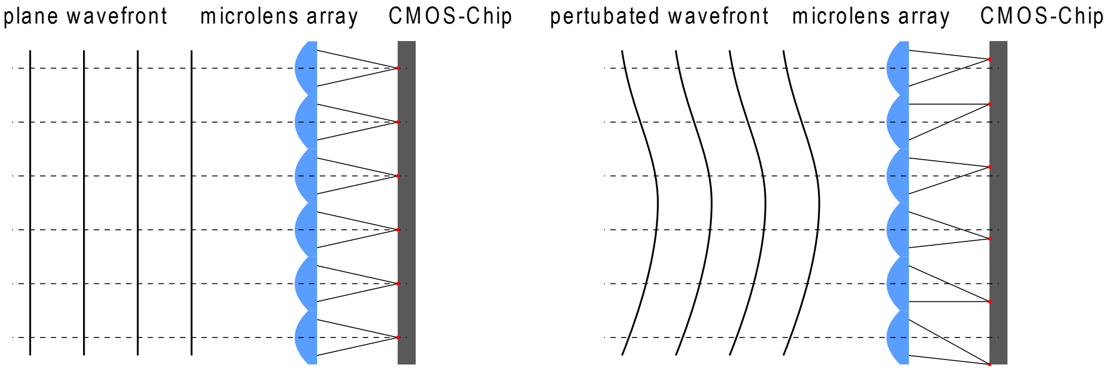

Figure 4.11: Working principle of a Hartmann–Shack WFS: The sensor consists of a lenslet array and a CMOS sensor. For a plane WF light focuses on the OA of the microlenses. For the perturbed WF the local WF gradient acts as a WF tilt at the location of a microlens. Thus the individual focuses shift proportional to the local gradient of the WF. By measuring all spot positions behind the lenslets, compared to the reference position the WF can be reconstructed. Image source: [19]

Hartmann–Shack sensor including software for calibration and calculation of the WF and Zernike coefficients are commercially available and typically measure the deviation from a plane WF. For an experimental setup, as presented in this thesis, the sensor has to be fitted to the application. The relay optics which has to be constructed to optically connect the WFS to the imaging system (model eye) has to fulfill these criteria:

- Wave from a point in the image plane (ideally a spherical wave) has to be converted into a plane wave. The sensor sits at the location of the plane wave.
- The lenslet array (plane in which the WF is measured) has to be in a conjugated plane to the pupil. This means, that the imaging condition has to be true between the pupil plane and the plane lenslet array.
- The magnification has to be chosen in a way that the sensor can fully capture the image of the pupil with a sufficient number of local gradient measurement points.

For the proposed model eye three different measurement setups were investigated and tested by the author of this thesis regarding their experimental complexity and reliability [21]. In principle, either so called dual–pass and single–pass setups can be used [128]. The working principle of the dual–pass, which is typically used in ophthalmology to characterize human eyes, is depicted in Figure 4.12. It could be seen that this setup is the most complicated to align and setup and thus not very reliable for an experimental setup [21].

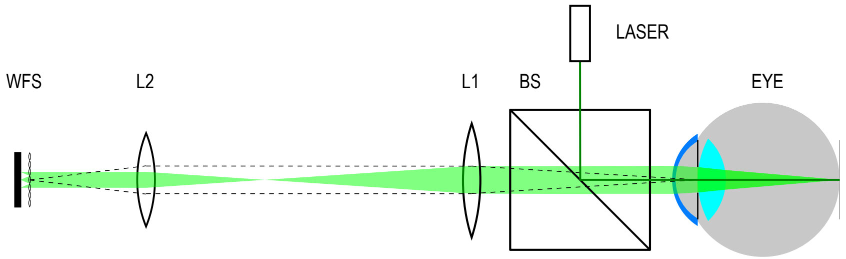

Figure 4.12: Simplified schematic for the double–pass setup: A laser illuminates the eye via a beam splitter (BS). The diffuse reflection of the illuminated point on the retina propagates through the eye. Telescope optics (L1 and L2) bring the sensor in a conjugate plane to the iris with an appropriate magnification. The deviations from a plane wave are measured by a WFS. Image source: [21]

Single–pass 1, see Figure 4.13, has many benefits as outlined in [21]. But it proved to be impractical because of the necessity to change the AL in the measurement procedure. Thus it was further developed by replacing the pin hole aperture by an open end of single–mode–fiber tip, which can conveniently be moved by miniature liner stages (see Figure 4.14 for an image of the developed prototype). Experiments showed, that this construction is handy to calibrate and would be the recommended choice. Unfortunately, despite best research until finishing this thesis, no fiber manufacturer could deliver a mono–mode fiber for 543 nm with an NA>0.17, which would be necessary to fully illuminate an iris aperture of 4.5 mm

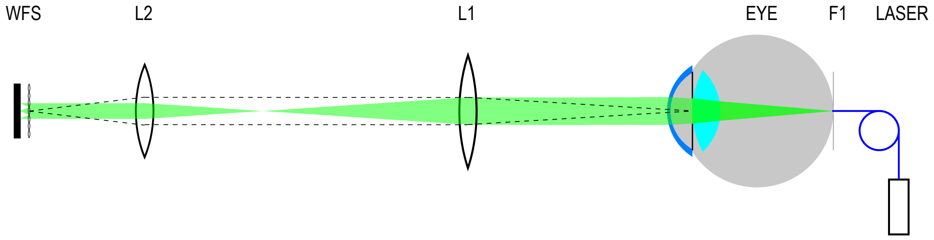

Figure 4.13: Simplified schematic for single–pass 1 setup: A laser with a tiny pinhole aperture or alternatively the tip of a mono mode fiber (F1) produces a point source at the location of the retina. The light from the illuminated point on the retina propagates through the eye. L1, L2 and WFS are the same as in Figure 4.12. Image source: adapted from [21]

Therefore finally single–pass 2, see Figure 4.15 for the schematic construction, was chosen for the final measurements. To retain the correct magnification, lens L1 has to have a small focal length ($f \approx 10$ mm) and again has to have NA higher >0.17. Commercially available CNC-polished aspheric lenses, as the Thorlabs AL1210M-A used in this setup,

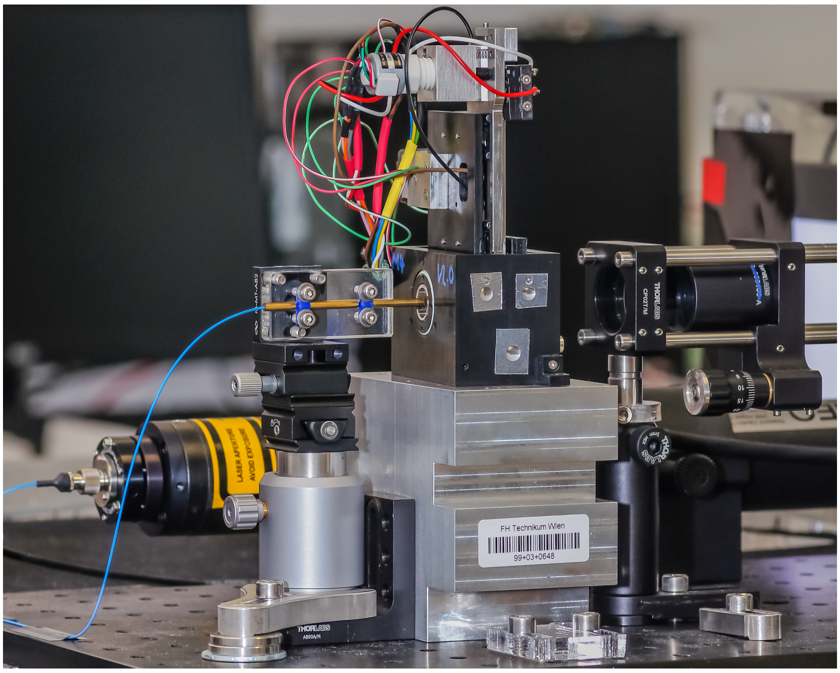

Figure 4.14: Photo of the prototype implementation of the single–pass 1 setup: The schematic construction follows Figure 4.13. The tip of a single mode fiber, which acts as a perfect emitter for a spherical wave, is inserted into a rigid brass canula. For a precise adjustment of the AL and point source location on the retina, the canula is mounted on miniature precision translation stages.

are specified with a RMS WF–error of <0.5 μm [129]. As it can be seen in the results, an RMS of 1λ is remarkable high compared to the WF–aberrations in the eye, but a typical specification for of–the–shelf lenses of this type.

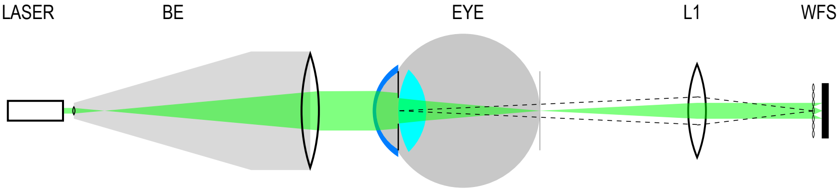

Figure 4.15: Simplified schematic for single–pass 2 setup: A laser is expanded with a beam expander (BE) to a parallel beam with >6 mm diameter having a plane WF to fully illuminate the iris aperture. The eye focuses the beam onto the retina. This aberrated spot image is converted to a parallel beam by lens L1. The WFS measures the deviation from a plane wave. Image source: [21]

A model of the complete setup is depicted in Figure 4.16. In detail the following components were used:

- The **laser source** is a REO R-39568 of 543 nm wavelength and laser class 3R (5.0 mW optical output power).
- A **beam expander** is used to expand the laser beam width over the full pupil. The output of the beam expander serves as plane wave reference. Imperfections can be compensated by a calibration with the WFS. A Thorlabs GBE15-A 15× expander is used.
- The **model eye** is tilted by 5° to simulate the physiologic antisymmetry between optical– and visual axis.
- **Relay optics** is a Thorlabs AL1210M-A "CNC Polished Mounted High-Precision Asphere", which converts the (ideally) spherical wave from the image point back to a (ideally) plane wave.
- The **Hartmann–Shack sensor** is a Thorlabs WFS150-7AR, with an active sensor area of 5.95 mm × 4.76 mm and a lenslet array with 150 μm pitch (max. active micorlenses 39 × 31) providing an RMS accuracy of 0.06λ.
- A **MATLAB Software** was developed to control the stepper motors of the model eye (as with the MTF–setup). Further, the software communicates with the software from the Thorlabs WFS150-7AR to continuously read out the first 15 Zernike coefficients. In real time the algorithms summarized in Figure 3.17 were calculated, to simultaneously display and record the MTF.

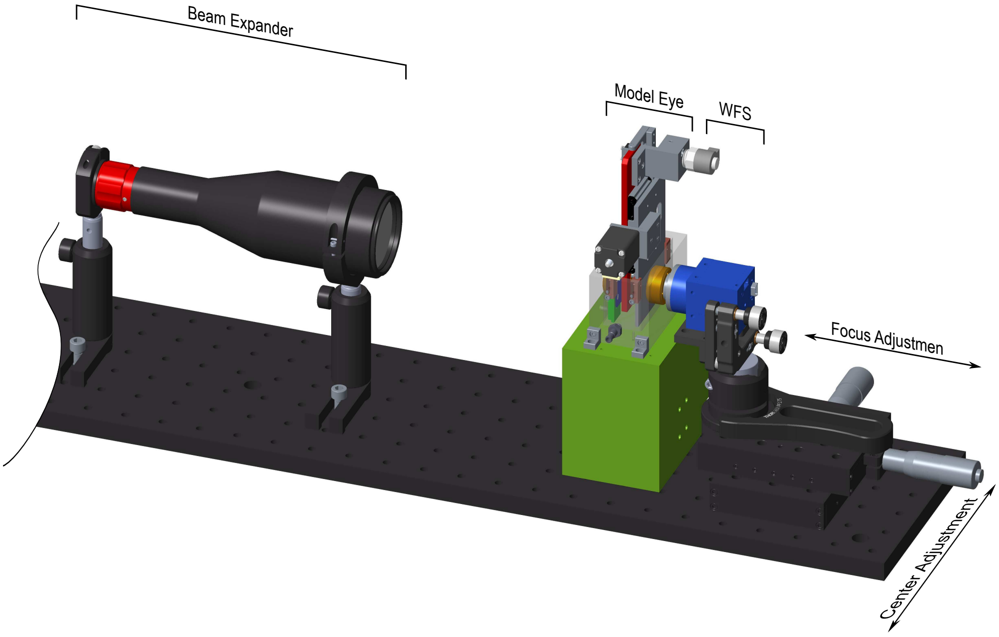

Figure 4.16: Schematic of the setup for measuring the WF. The system is illuminated by a HeNe laser source (not shown), expanded to a diameter bigger than the entrance pupil of the model eye. A compact assembly of a precision aspheric lens and a WFS is mounted on translation stages. With them, the focal point of the aspheric lens can be aligned with the focus of the model eye.

4.4.1 Measurement Procedure

All components as described above are set up on an active vibration isolating optical table to prevent coupling of surrounding vibrations on the measurement setup. Each measurement followed this procedure:

- Assembly and measurement of the IOL and aperture with the model eye (same as the first two steps for the MTF–setup)
- The model eye is now put into the WF–setup.
- The linear translation stage (see Figure 4.16) is adjusted to retain the highest contrast at ($100\ \frac{\mathrm{lp}}{\mathrm{mm}}$) for the $\mathbf{MTF}_{mean}$, which is calculated in real time from the WF–aberrations.
- The WF aberration coefficients are stored (pre–measurement)
- A computer software automatically sequentially goes through all possible lens positions in the defined range and stores the WF aberration coefficients (auto–measurement).

- The lens is set back to the centered position. The WF aberration coefficients are recorded again (post–measurement).
- The lens position is again checked with telecentric machine vision setup.
- If a mechanical lens displacement in the lens holder during the measurement sequence is observed in the machine vision setup, the whole measurement is discarded and repeated. As described for the MTF–setup (see Section 4.3.2) a lens displacement within the holder is also visible in a mismatch of the derived pre–, auto– and post–measurement MTF. High order aberrations ($n = 4$) can show high deviations between pre–, auto– and post–measurement, but do not have an impact on the MTF. Thus lens displacements in the lens holder during the measurement procedure can not be derived from these coefficients.

4.5 Demonstrator for Visual Impression

In the last point of the problem statement Section 1.2 it is questioned how these post–surgical IOL displacements influence the quality of vision. The effects on the physical imaging process can be quantified as outlined before. The physiological process of visual perception is very complex. Thus answering this question would require extensive clinical trials and is out of the scope of this thesis. Based on findings of this thesis together with clinical expertise of researchers at the clinic "Hanusch hospital", Vienna, it is planned to submit a proposal for conducting further research. Aim of this part of the thesis is to demonstrate the feasibility to perform such studies in conjunction with the proposed method.

One approach for such tests which can be found is using adaptive optics[130, 131]: Using adaptive optics, e.g. deformable mirrors, specific geometric aberrations can artificially be generated and presented to human probands. Another approach is to use an artificial model eye in which an IOL is embedded and the image from the model eye is projected onto a proband's retina [37]. This approach was chosen for this thesis, as the developed model eye can be used. For an efficient usage of the components the system was designed mostly with the components of the MTF–setups. Only the breadboard holding the digital retina image acquisition is replaced by a projection optic. The setup is depicted in Figure 4.17.

The projection optics is designed to fulfill the following requirements:

- The magnification between the image on the model eye's retina and the proband's retina must be 1:1.
- The image orientation must be equal.
- The projection optics should not include additional aberrations, as these would influence the visual perception. This is only critical for the image center, as the visual accuracy in the periphery of the human eye is very bad – see 2.2.

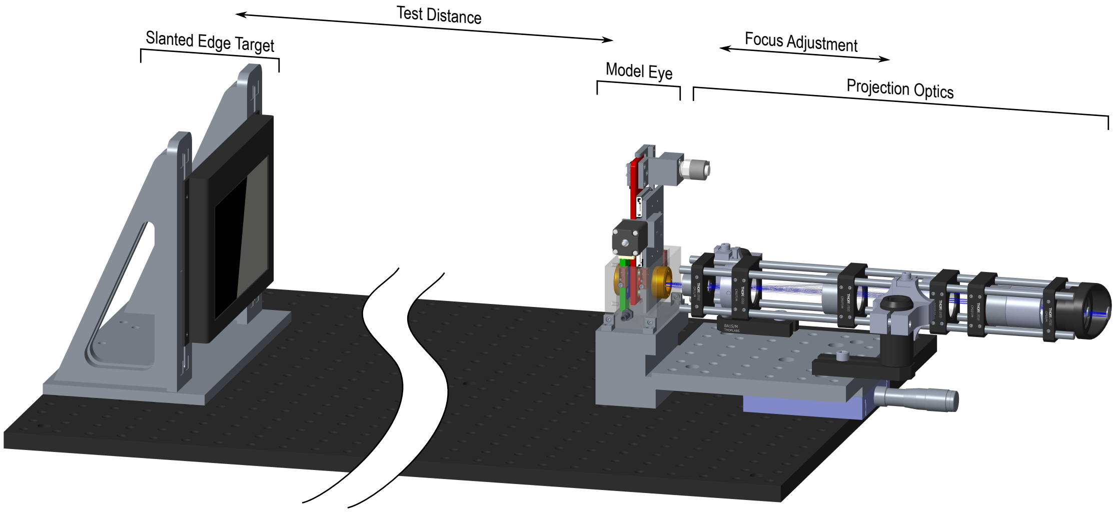

Figure 4.17: Schematic of the optical projection device. A slanted edge target, or any other object, is mounted on the target screen. The model eye produces an image of the object in the retina plane of the model eye. Compared to Figure 4.9 the retina image is not digitally captured but projected onto the retina of a human investigator by a projection optics.

To minimize CA and SA, the system was built from commercially available achromatic lens doublets. The correct position of the proband's eye is guaranteed by an eye–piece, in which the proband's eyecup can rest. Using ZEMAX OpticStudio, the distances between the optical components were optimized to optimally fulfill the stated requirements. The optical layout is depicted in Figure 4.18. The components assembled using an optical cage system on a breadboard as shown in Figure 4.19. Results from characterizing this construction are given in Section 5.3.

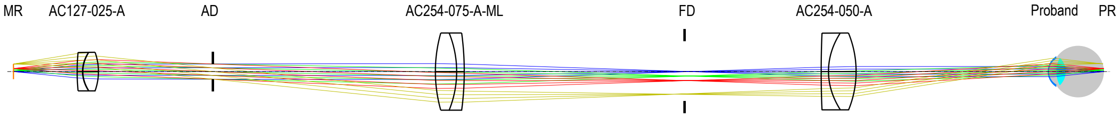

Figure 4.18: The optical system consists of three achromatic doublets with a focal length of 25 mm, 75 mm and 50 mm and two diaphragms, the aperture diaphragm (AD) and the field diaphragm (FD). Between the model eye's retina (MR) and the proband's retina (PR) a 1:1 magnification is set up. The ray colors depict four different field heights (0 mm, 0.5 mm, 1 mm and 2.5 mm)calculating the visual performance vs. field height for comparison with Figure 2.2

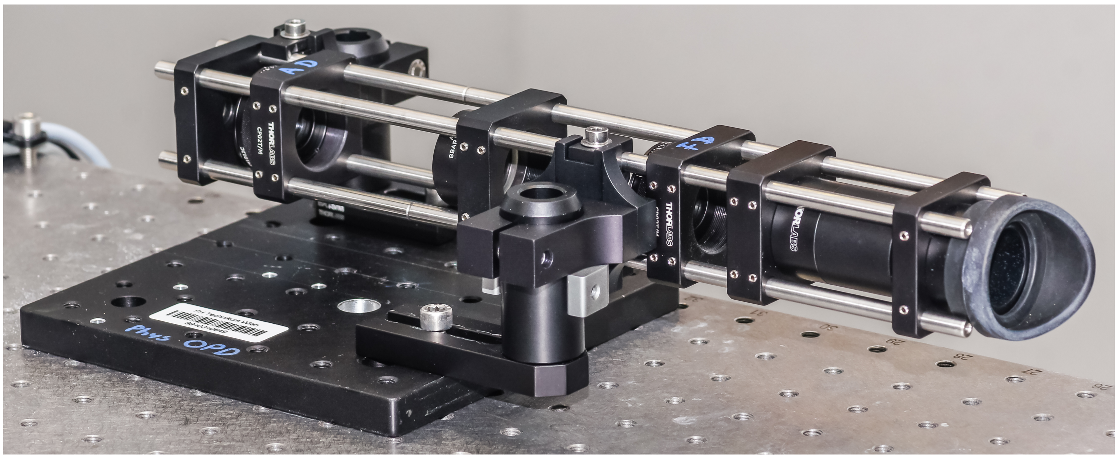

Figure 4.19: The breadboard with the projection optics is mechanically compatible to the breadboard of the MTF–setup. They can easily be exchanged by two mounting screws.

4.6 Summary on the Experimental Setup

All experiments were set up in the photonics laboratory at the University of Applied Sciences Technikum Wien. The laboratory was set up within the research project LOALiS (Laser and Optics in Applied Life Sciences), which is funded by the "Magistratsabteilung 23" (MA 23) of the City of Vienna[132]. The complete experimental arrangement is depicted in Figure 4.20.

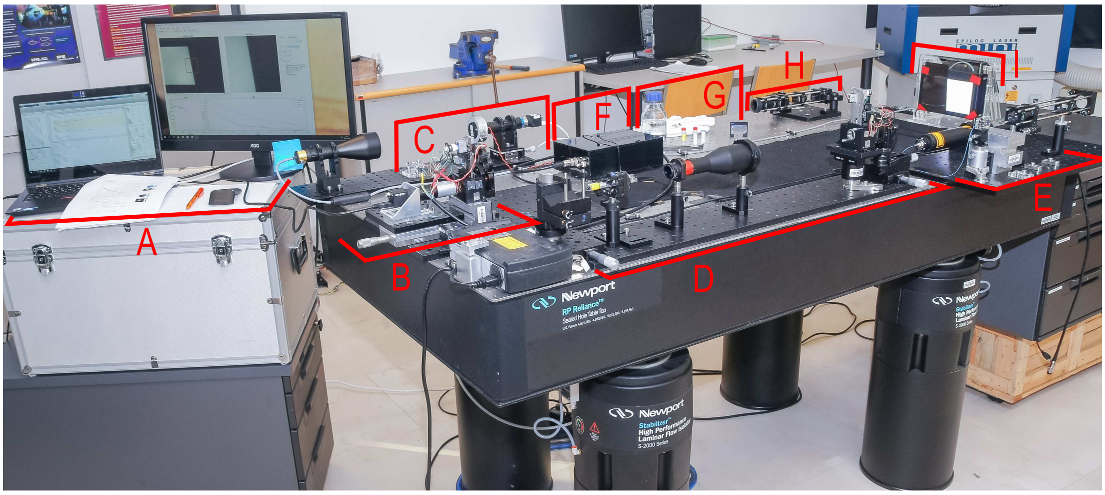
H
I
C
F
G
E
A
B
D
Newport
RP Reliance
Newport
Stabilizer
High Performance
Laminar Flow Isolator
S-2000 Series

Figure 4.20: Setup of the experiments for this thesis in the photonics laboratory at the UAS Technikum Wien. A) Computer with control and measurement software; B) MTF–setup; C) Camera with telecentric lens for checking the IOL position; D) WF–setup singe–pass 2; E) WF–setup single–pass 1; F) Control electronics for the model eye's stepper motors; G) Different IOLs, IOL–holder and iris holder; H) Optical projection device; I) Target screen of MTF–measurement and demonstration for the visual impression.

CHAPTER 5

Results

In this chapter at first the results of the numerical simulations are presented, these results serve as reference for validation of the measurement–results of the experimental setups. In addition, some analysis on the optical projection device are presented. To compare the lenses in a single value, the optical performance is summarized in a single value for each lens. If not noted otherwise, all simulations and measurements are done at an illumination of 543 nm.

5.1 Numerical Simulations

5.1.1 The Liou and Brennan Eye

The results of the Liou and Brennan Eye will serve as reference for all further simulations and show the optical performance of the normal healthy human eye. All results better than these would indicate an improvement of vision beyond the default situation; vice versa all results worse than these reveal a deteriorated visual performance.

Figure 5.1 depicts the optical performance of the Liou and Brennan Eye for a 3 mm iris diameter (photopic vision), Figure 5.2 is simulated at 4.5 mm iris diameter (scotopic vision). A detailed description on how to read the plots is given in Figure 5.1, this description also applies to all following figures of this format. When assessing the visual performance at 100 $\frac{\text{lp}}{\text{mm}}$, best vision contrast can be seen under photopic condition (3 mm iris diameter). Increasing the iris diameter increases the MTF cut–off frequency (better performance due to diffractive properties), but WF aberrations increase (higher geometric aberrations).

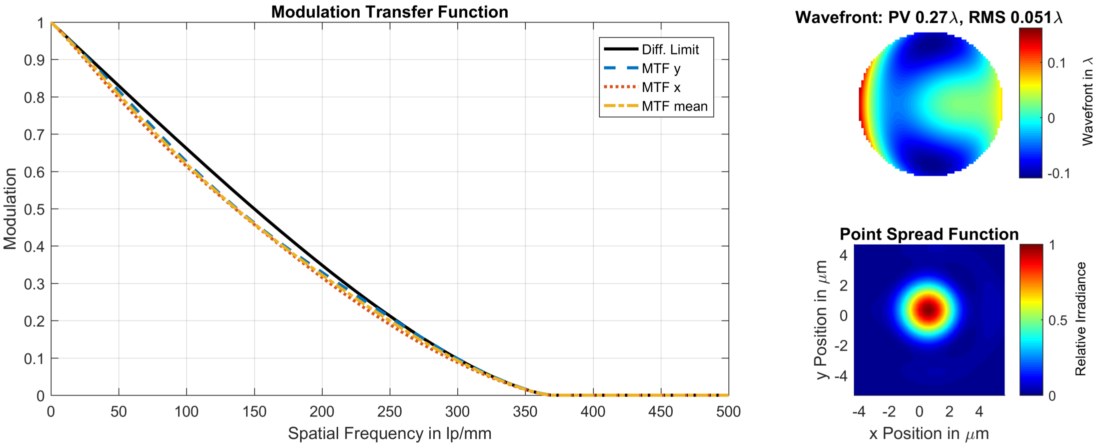

Figure 5.1: Numerical simulation results: Liou and Brennan eye with 3 mm iris diameter. $\mathbf{MTF}_{mean}(100\frac{\mathrm{lp}}{\mathrm{mm}})$=0.62. **Reading the plot:** The MTF depicts the *modulation* or *visibility* vs. spatial frequency ξ. The black line represents the *diffraction limited MTF*, due to diffraction the modulation can not be higher than this limit determined by the iris diameter. Due to additional geometric errors the true modulation of the optical system further drops. Since the WF is not rotational symmetric, the MTF is direction dependent. $\mathbf{MTF}_y$ (dashed blue) and $\mathbf{MTF}_x$ (dotted red) describe MTF in y and x direction. $\mathbf{MTF}_{mean}$ is the mean between those two functions. Corresponding to the ISO–standard the modulation at 100 $\frac{\mathrm{lp}}{\mathrm{mm}}$ is used to quantify the optical performance with a single value. The geometric errors are depicted as WF–map $\mathbf{\Phi}(x, y)$ on the circular pupil. A uniform color would indicate a undistorted WF. The PSF depicts the intensity distribution on the retina plane, when a point–like object is examined. The narrower this function the better the imaging condition is fulfilled.

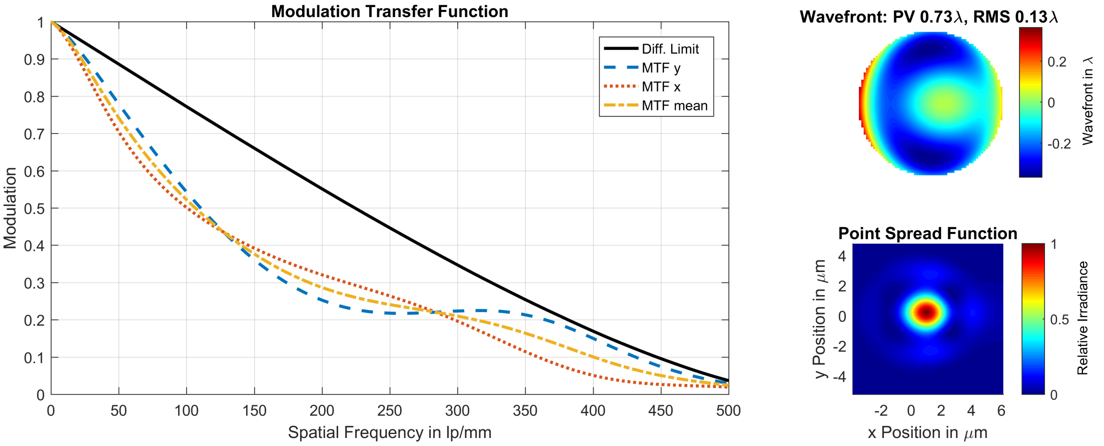

Figure 5.2: Numerical simulation results: Liou and Brennan eye with 4.5 mm iris diameter. $\mathbf{MTF}_{mean}(100\frac{\mathrm{lp}}{\mathrm{mm}})$=0.52

5.1.2 The Liou and Brennan Eye with Model Cornea

As outlined in Section 4.2.2, the cornea in the Liou and Brennan eye had to be replaced by an PMMA equivalent. Figures 5.3 and 5.4 depict the simulation results of the Liou and Brennan eye with the PMMA cornea. Comparing Figure 5.1 and 5.3 as well as Figure 5.2 and 5.4, it can be seen that the eye model with the PMMA cornea closely represents MTF and WF–aberrations of the Liou and Brennan eye independent of the iris diameter.

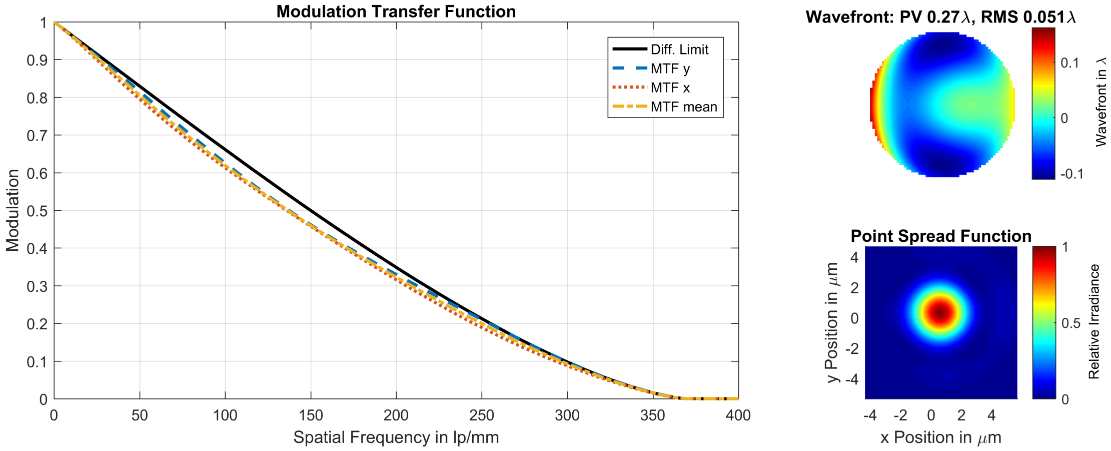

Figure 5.3: Numerical simulation results: Liou and Brennan eye with the PMMA model cornea 3 mm iris diameter. $\mathbf{MTF}_{mean}(100\frac{\mathrm{lp}}{\mathrm{mm}})$=0.62

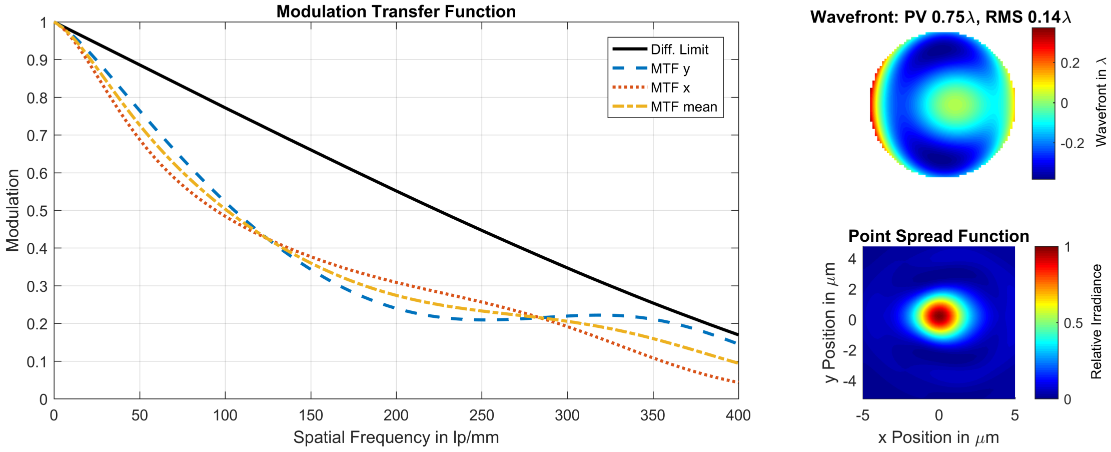

Figure 5.4: Numerical simulation results: Liou and Brennan eye with the PMMA model cornea 4.5 mm iris diameter. $\mathbf{MTF}_{mean}(100\frac{\mathrm{lp}}{\mathrm{mm}})$=0.50

5.1.3 Performance of the Model Eye without Eye Lens

It will be shown later on, that so far the manufacturing process of the PMMA–cornea is the most limiting factor of the method. For a better understanding of the obtained results, it is beneficial to quantify the aberrations from the imperfections of the cornea. Therefore the model eye was simulated without an eye lens at both iris diameters (Figure 5.5 and 5.6). Because of the missing refractive power of the eye lens, the $^f/_\#$ is lower – resulting in a lower cut–off frequency compared to the model with eye lens (Figure 5.3 and 5.4). The Zernike aberration coefficients for 3 mm and 4.5 mm iris diameter are given in Table 5.5 and 5.6 in comparison with the measurement results.

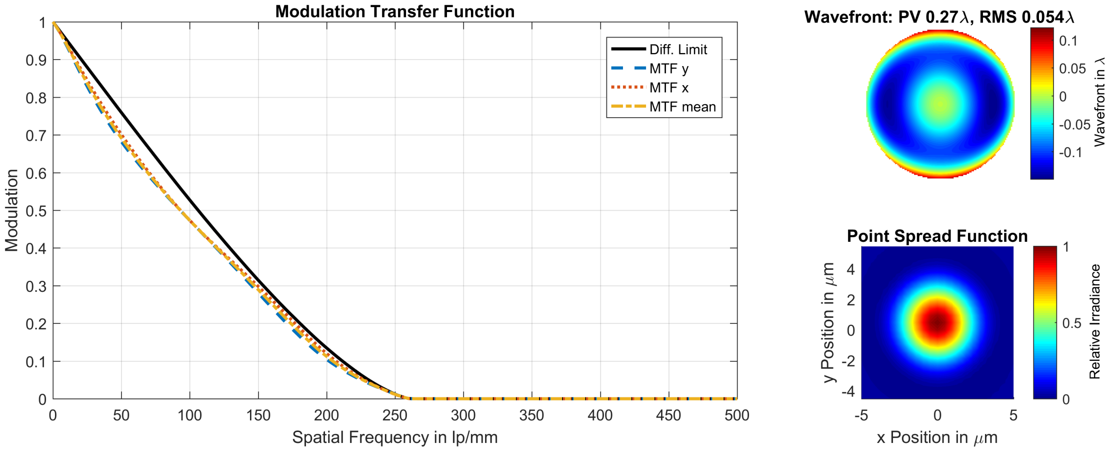

Figure 5.5: Only PMMA model cornea with 3 mm iris diameter. $\mathbf{MTF}_{mean}(100\frac{\mathrm{lp}}{\mathrm{mm}})$=0.47

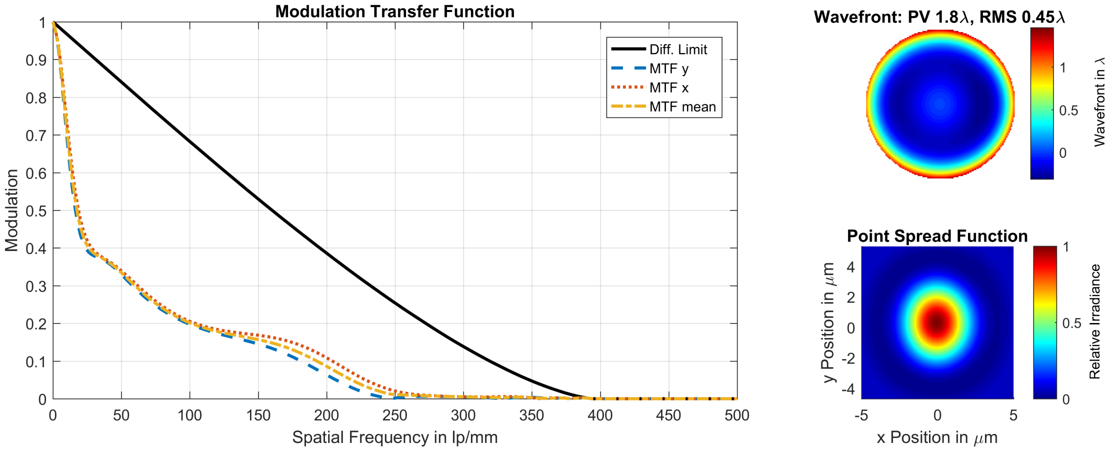

Figure 5.6: Numerical simulation results: Only PMMA model cornea with 4.5 mm iris diameter. $\mathbf{MTF}_{mean}(100\frac{\mathrm{lp}}{\mathrm{mm}})$=0.20

5.1.4 Tilt and Shift Tolerance of Intraocular Lenses

In this section, following the simulation procedure outlined in Section 4.1.2, three IOLs (spherical, aberration free and aberration correcting) are compared regarding their sensitivity to displacements within the eye. Full results (MTF, WF and PSF) are shown for the centered position. The effects on combined tilt (along θ–direction) and decentration (along x–axis) are shown for the modulation at a spatial frequency of $100\frac{\text{lp}}{\text{mm}}$; a detailed description on how to read the plots is given in Figure 5.10, this description also applies to all following figures of this format. The effects on the geometric image aberrations are depicted by the WF–coefficients $Z4$ to $Z15$. The parameters for the central position are compared with the Liou and Brennan Eye in Table 5.1.

General remarks on the figures in this chapter: For depicting the change of the MTF in dependence of the tilts end decentrations, the full MTFs have to be reduced to a single value. Corresponding to the test standard, the contrast at $100\frac{\text{lp}}{\text{mm}}$ is used to characterize the MTF with one value [12]. All plots depicting MTF vs. decentration use the same axis scaling and color map for better comparability. The color map for the modulation value at $100\frac{\text{lp}}{\text{mm}}$ is depicted in Figure 5.9. The WF–errors are decomposed into the Zernike coefficients and depicted split into twelve subplots, each subplot depicting the change of one coefficient vs. decentration. The same axis scaling and color map is used whenever a 3 mm iris was used, a different scaling and color map is used for an iris diameter of 4.5 mm.

Table 5.1: Comparison of the full Liou and Brennan eye (L&B) and the Liou and Brennan cornea with three different IOLs, when they are centered in the capsular bag. P = photopic vision with 3 mm iris; S = scotopic vision with 4.5 mm iris. Δ AL is the required shortening of the AL to regain optimal contrast at $100\frac{\text{lp}}{\text{mm}}$, when the iris is changed from 3 mm to 4.5 mm.

Model	L&B	MC5812AS	MC6125AS	CT LUCIA 611PY
Lens Power [dpt]	22.1	22.0	22.0	21.0
f [mm]	16.574	16.595	16.622	16.709
Image space $^f/_\#$ P	3.25	3.25	3.26	3.28
Image space $^f/_\#$ S	4.88	4.88	4.89	4.91
$\mathbf{MTF}_{mean}(100\frac{\text{lp}}{\text{mm}})$ P	0.62	0.37	0.50	0.59
$\mathbf{MTF}_{mean}(100\frac{\text{lp}}{\text{mm}})$ S	0.50	0.17	0.25	0.38
WF RMS [λ] P	0.0051	0.22	0.10	0.08
WF RMS [λ] S	0.14	1.1	0.57	0.73
Δ AL [μm]	28	46	24	3

Simulations with the MC5812AS

Centered Position

The image performance of the MC5812AS IOL in the centered position is depicted in Figure 5.7 for photopic vision and Figure 5.8 for scotopic vision. The Zernike coefficients from $Z4$ to $Z15$ in the centered position are summarized in Table 5.2. Due to the properties of symmetry the coefficients $Z5$, $Z7$, $Z9$, $Z13$ and $Z15$ must be zero.

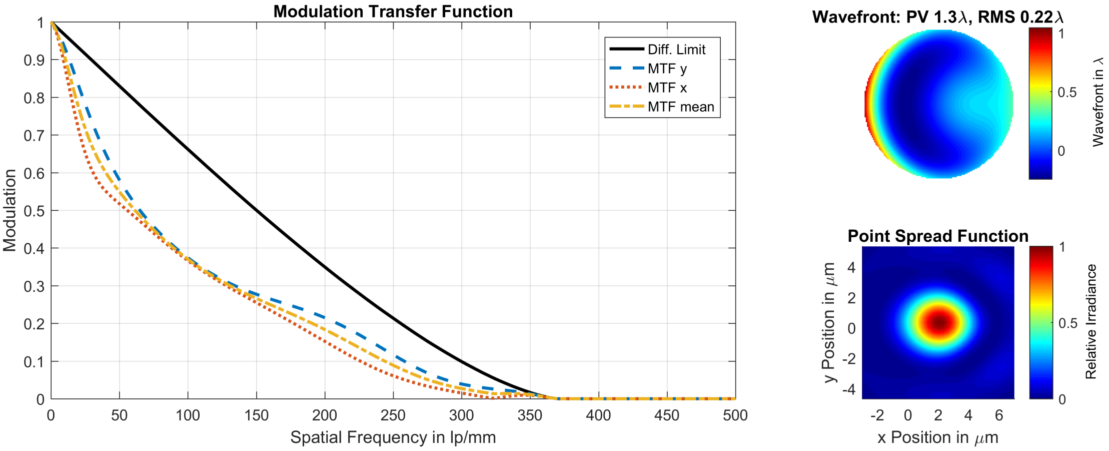

Figure 5.7: Numerical simulation results: Liou and Brennan eye with the MC5812AS IOL and 3 mm iris diameter. $\mathbf{MTF}_{mean}(100\frac{\text{lp}}{\text{mm}})$=0.37

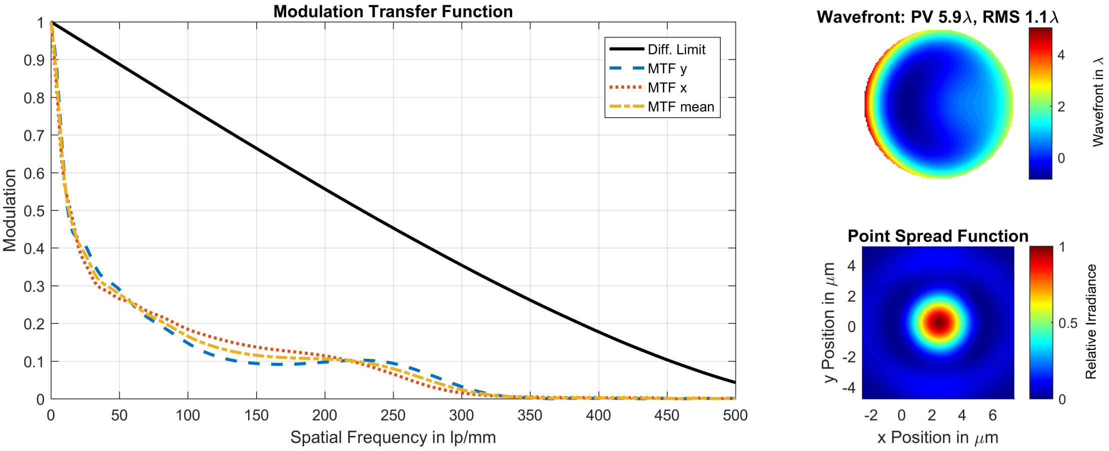

Figure 5.8: Numerical simulation results: Liou and Brennan eye with the MC5812AS IOL and 4.5 mm iris diameter. $\mathbf{MTF}_{mean}(100\frac{\text{lp}}{\text{mm}})$=0.17

Table 5.2: Zernike coefficients (scaled in λ): Liou and Brennan eye with the MC5812AS

Coefficient	Iris = 3 mm	Iris = 4.5 mm
$Z4$	0.1642	1.0722
$Z6$	0.1002	0.2243
$Z8$	-0.1219	-0.4125
$Z10$	0.0001	0.0001
$Z11$	0.0782	0.4022
$Z12$	-0.0002	-0.0009
$Z14$	0.0000	0.0000

Displacement effects on the MTF

The MTF values at $(100\frac{\mathrm{lp}}{\mathrm{mm}})$ are depicted in Figure 5.10 for photopic and in Figure 5.11 for scotopic vision.

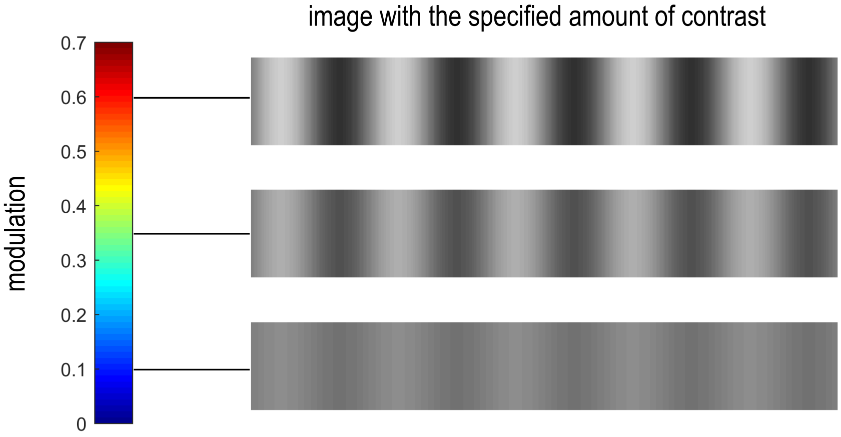

Figure 5.9: Color map for all plots describing the tilt and shift dependent modulation at $(100\frac{\mathrm{lp}}{\mathrm{mm}})$. On the right side of the figure exemplary images of a sine intensity grating with the modulation or contrast C of 0.6 (map color red), 0.35 (map color green) and 0.1 (map color blue) are depicted, where $C = 0.6$ results in a good visibility and the grating can hardly be resolved at a contrast of $C = 0.1$.

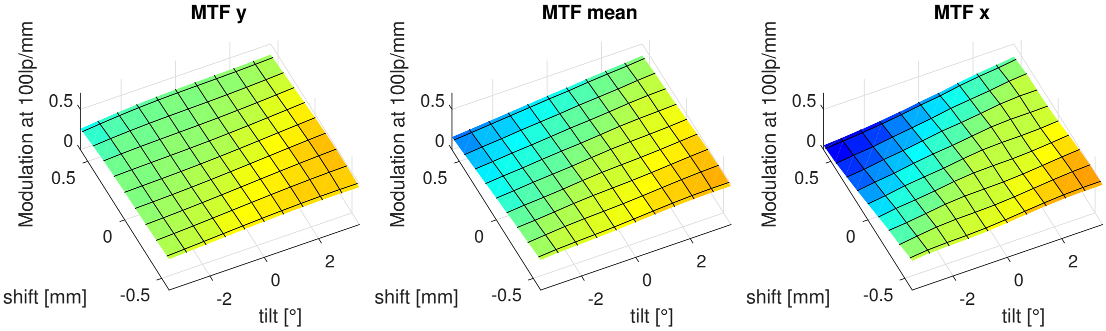

Figure 5.10: Numerical simulation results: Liou and Brennan eye with the MC5812AS IOL and 3 mm iris diameter. **Reading the plot:** The three subplots depict the modulation, which corresponds to the visibility, at $100\frac{\mathrm{lp}}{\mathrm{mm}}$ for each IOL–position (θ,x). The color map and illustrative examples for the corresponding image contrast is depicted in Figure 5.9. Due to the fact that the MTF is direction dependent, the modulation value is shown for the y–direction ($\mathbf{MTF}_y$), the x–direction ($\mathbf{MTF}_x$) and the mean value between y and x ($\mathbf{MTF}_{mean}$). In this particular example the visibility is best, if the lens is tilted by $\theta = +3.5°$ and shifted by $x = -0.6$ mm, with a mean contrast of approximately 0.5 at $100\frac{\mathrm{lp}}{\mathrm{mm}}$

.

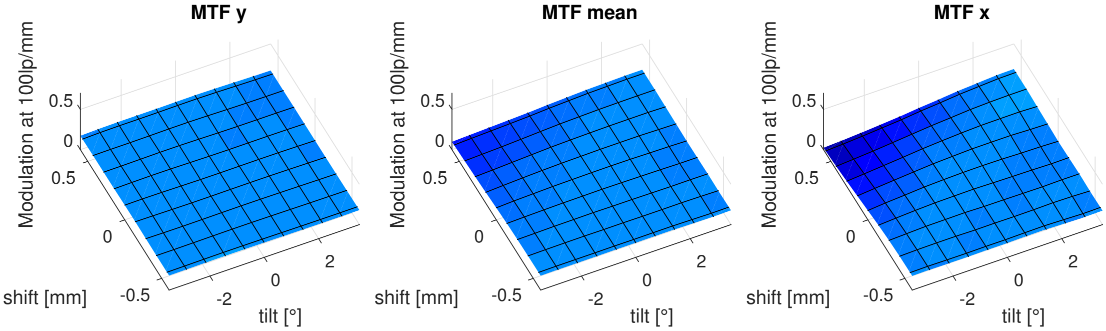

Figure 5.11: Numerical simulation results: Liou and Brennan eye with the MC5812AS IOL and 4.5 mm iris diameter. $\mathbf{MTF}_y$, $\mathbf{MTF}_{mean}$ and $\mathbf{MTF}_x$ at $100\frac{\mathrm{lp}}{\mathrm{mm}}$ is depicted for each IOL–position (θ,x)

Displacement effects on the WF

The WF's Zernike coefficients in dependence on tilt and shift are depicted in Figure 5.12 for photopic and in Figure 5.13 for scotopic vision.

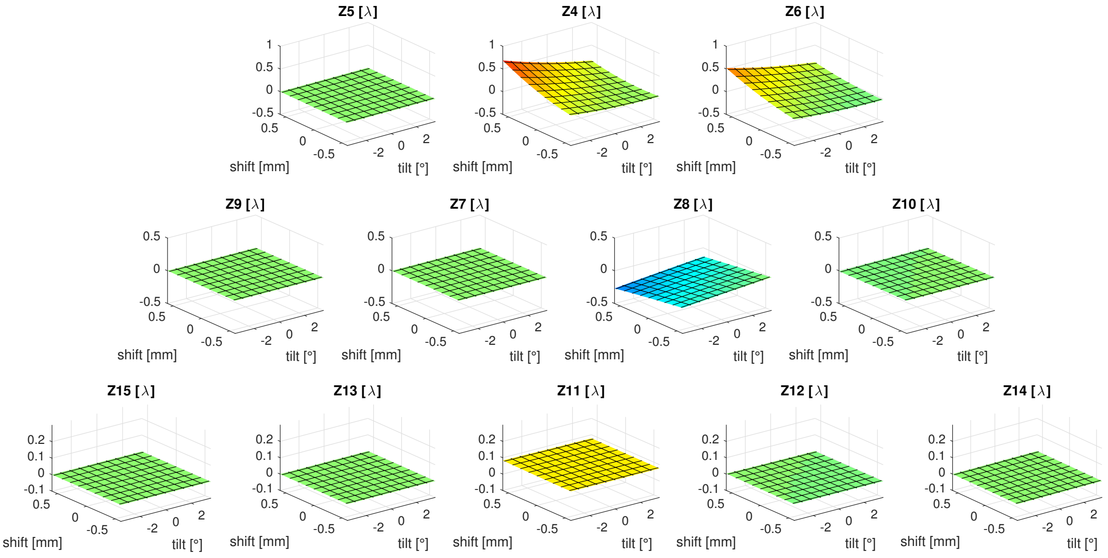

Figure 5.12: Numerical simulation results: Liou and Brennan eye with the MC5812AS IOL and 3 mm iris diameter. The Zernike Coefficients $Z4$ to $Z15$ are depicted for each IOL–position (θ,x)

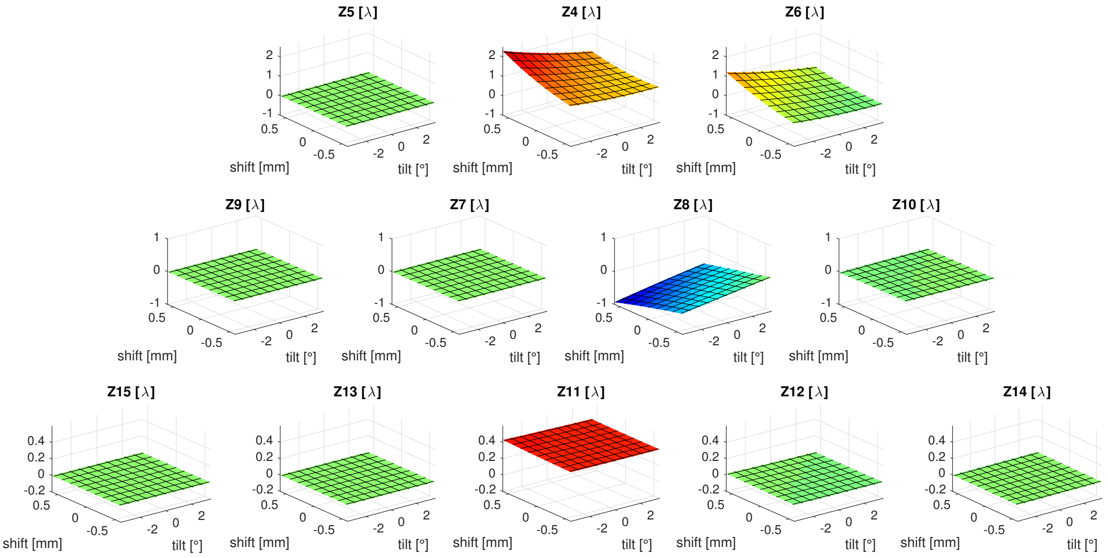

Figure 5.13: Numerical simulation results: Liou and Brennan eye with the MC5812AS IOL and 4.5 mm iris diameter. The Zernike Coefficients $Z4$ to $Z15$ are depicted for each IOL–position (θ,x)

Simulations with the MC6125AS

Centered Position

The image performance of the MC6125AS IOL in the centered position is depicted in Figure 5.14 for photopic vision and Figure 5.15 for scotopic vision. The Zernike coefficients from $Z4$ to $Z15$ in the centered position are summarized in Table 5.3. Due to the properties of symmetry the coefficients $Z5$, $Z7$, $Z9$, $Z13$ and $Z15$ must be zero.

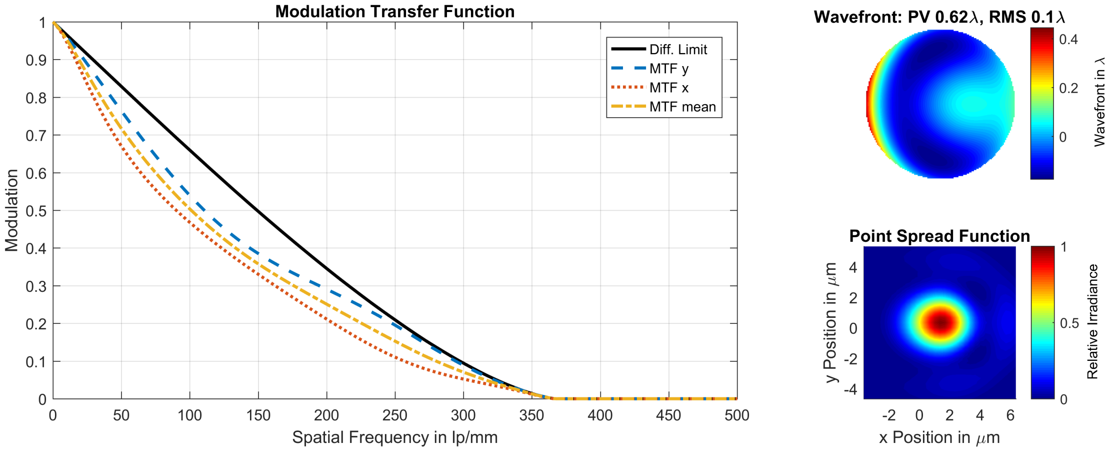

Figure 5.14: Numerical simulation results: Liou and Brennan eye with the MC6125AS IOL and 3 mm iris diameter. $\mathbf{MTF}_{mean}(100\frac{\mathrm{lp}}{\mathrm{mm}})$=0.50

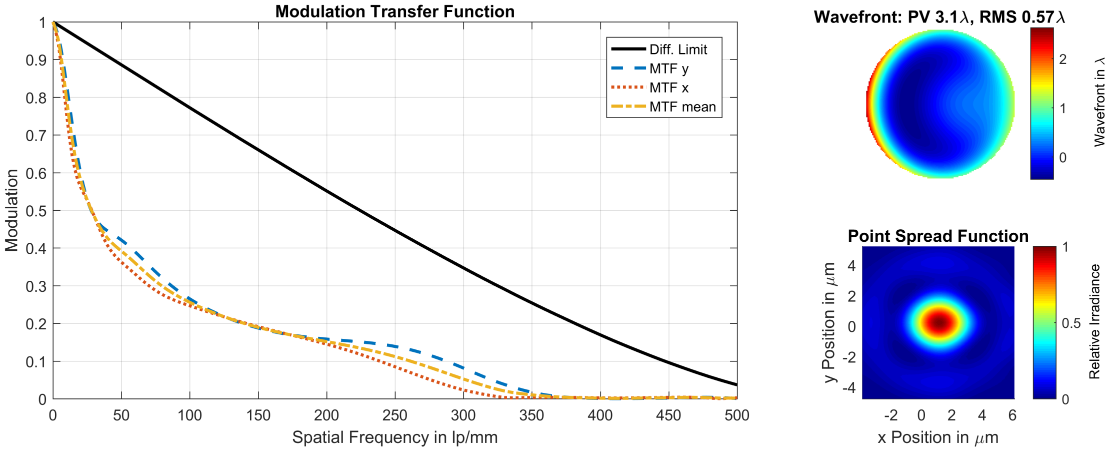

Figure 5.15: Numerical simulation results: Liou and Brennan eye with the MC6125AS IOL and 4.5 mm iris diameter. $\mathbf{MTF}_{mean}(100\frac{\mathrm{lp}}{\mathrm{mm}})$=0.25

Table 5.3: Zernike coefficients (scaled in λ): Liou and Brennan eye with the MC6125AS

Coefficient	Iris = 3 mm	Iris = 4.5 mm
$Z4$	0.0259	0.4327
$Z6$	0.0708	0.1661
$Z8$	-0.0565	-0.2131
$Z10$	-0.0003	-0.0008
$Z11$	0.0401	0.2232
$Z12$	0.0007	0.0028
$Z14$	-0.0000	-0.0001

Displacement effects on the MTF

The MTF values at $(100\frac{\text{lp}}{\text{mm}})$ are depicted in Figure 5.16 for photopic and in Figure 5.17 for scotopic vision.

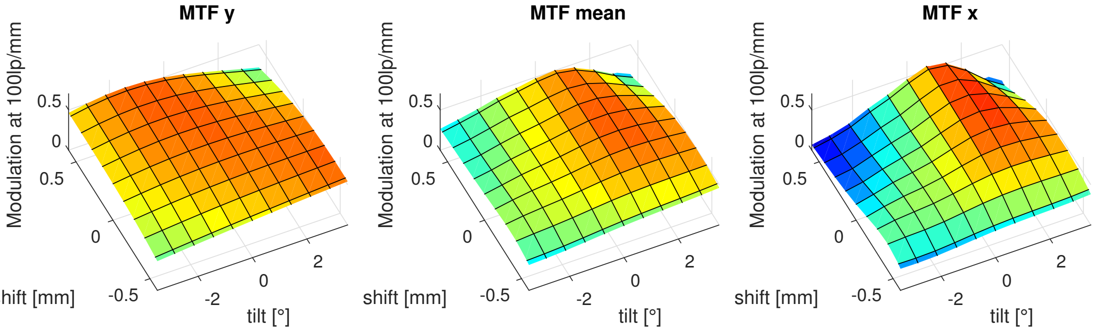

Figure 5.16: Numerical simulation results: Liou and Brennan eye with the MC6125AS IOL and 3 mm iris diameter. $\mathbf{MTF}_y$, $\mathbf{MTF}_{mean}$ and $\mathbf{MTF}_x$ at $100\frac{\text{lp}}{\text{mm}}$ is depicted for each IOL–position (θ,x)

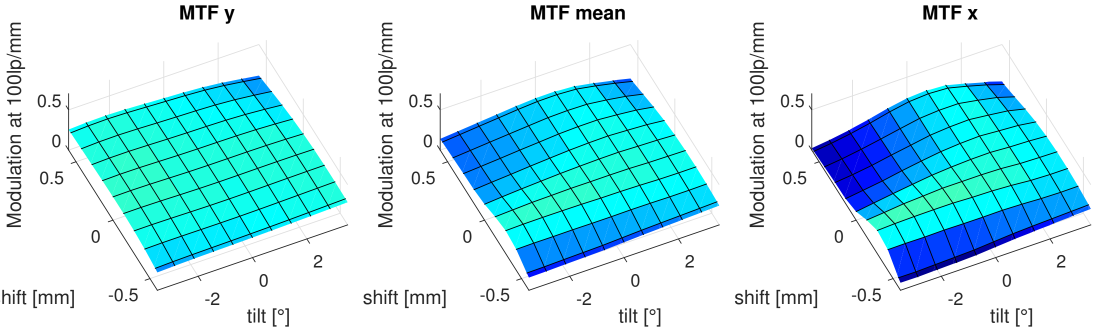

Figure 5.17: Numerical simulation results: Liou and Brennan eye with the MC6125AS IOL and 4.5 mm iris diameter. $\mathbf{MTF}_y$, $\mathbf{MTF}_{mean}$ and $\mathbf{MTF}_x$ at $100\frac{\text{lp}}{\text{mm}}$ is depicted for each IOL–position (θ,x)

Displacement effects on the WF

The WF's Zernike coefficients in dependence on tilt and shift are depicted in Figure 5.18 for photopic and in Figure 5.19 for scotopic vision.

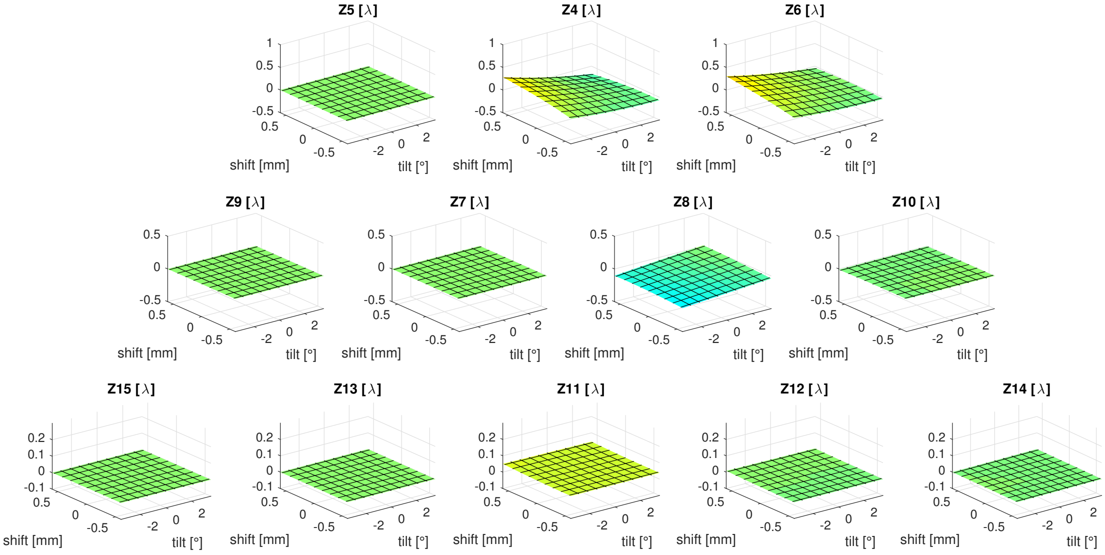

Figure 5.18: Numerical simulation results: Liou and Brennan eye with the MC6125AS IOL and 3 mm iris diameter. The Zernike Coefficients $Z4$ to $Z15$ are depicted for each IOL–position (θ,x)

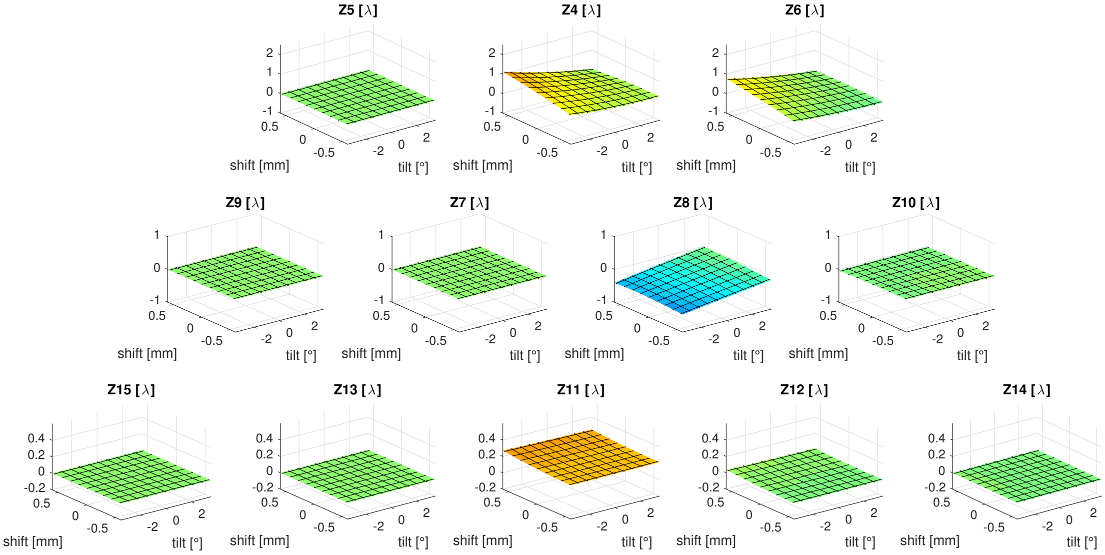

Figure 5.19: Numerical simulation results: Liou and Brennan eye with the MC6125AS IOL and 4.5 mm iris diameter. The Zernike Coefficients $Z4$ to $Z15$ are depicted for each IOL–position (θ,x)

Simulations with the CT LUCIA 611PY

Centered Position

The image performance of the CT LUCIA 611PY IOL in the centered position is depicted in Figure 5.20 for photopic vision and Figure 5.21 for scotopic vision. The Zernike coefficients from $Z4$ to $Z15$ in the centered position are summarized in Table 5.4. Due to the properties of symmetry the coefficients $Z5$, $Z7$, $Z9$, $Z13$ and $Z15$ must be zero.

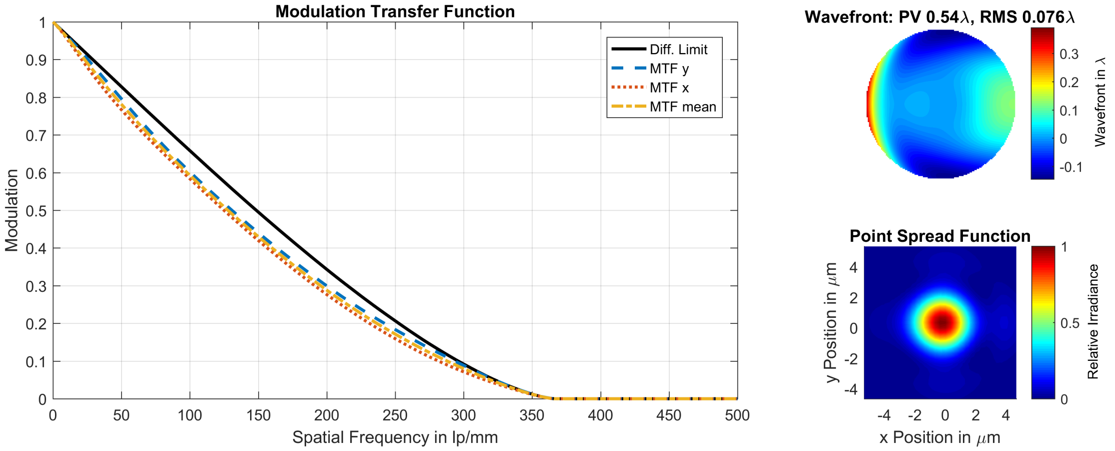

Figure 5.20: Numerical simulation results: Liou and Brennan eye with the CT LUCIA 611PY IOL and 3 mm iris diameter. $\mathbf{MTF}_{mean}(100\frac{\text{lp}}{\text{mm}})$=0.59

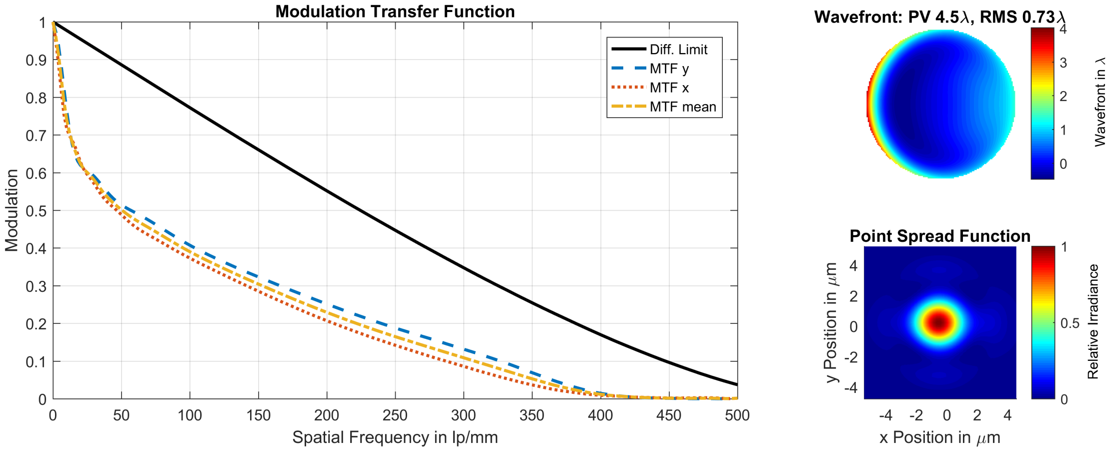

Figure 5.21: Numerical simulation results: Liou and Brennan eye with the CT LUCIA 611PY IOL and 4.5 mm iris diameter. $\mathbf{MTF}_{mean}(100\frac{\text{lp}}{\text{mm}})$=0.38

Table 5.4: Zernike coefficients (scaled in λ): Liou and Brennan eye with the CT LUCIA 611PY

Coefficient	Iris = 3 mm	Iris = 4.5 mm
$Z4$	0.0062	0.4487
$Z6$	0.0686	0.2366
$Z8$	-0.0245	-0.3510
$Z10$	-0.0033	-0.0052
$Z11$	0.0107	0.2840
$Z12$	0.0100	0.0331
$Z14$	-0.0002	-0.0015

Displacement effects on the MTF

The MTF values at $(100\frac{\text{lp}}{\text{mm}})$ are depicted in Figure 5.22 for photopic and in Figure 5.23 for scotopic vision.

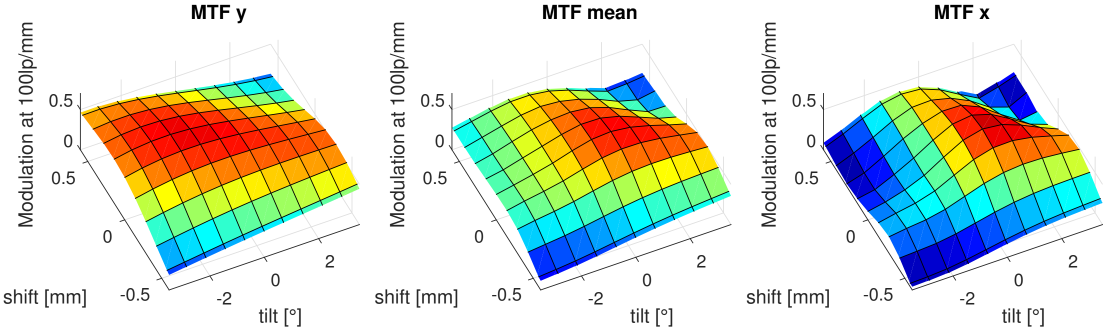

Figure 5.22: Numerical simulation results: Liou and Brennan eye with the CT LUCIA 611PY IOL and 3 mm iris diameter. $\mathbf{MTF}_y$, $\mathbf{MTF}_{mean}$ and $\mathbf{MTF}_x$ at $100\frac{\text{lp}}{\text{mm}}$ is depicted for each IOL–position (θ,x)

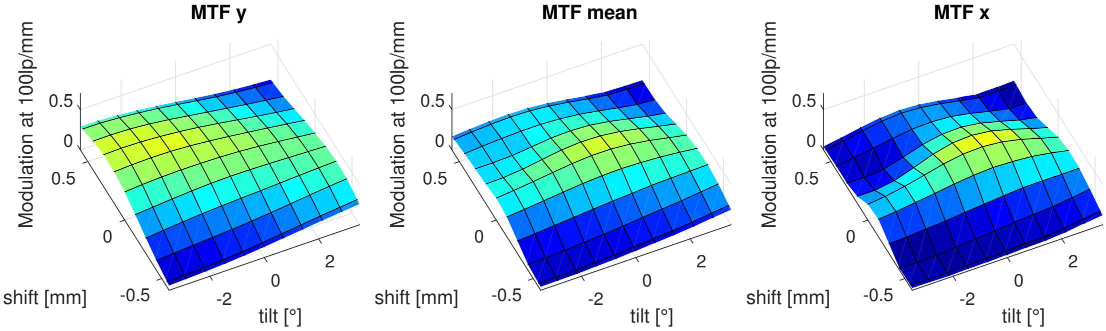

Figure 5.23: Numerical simulation results: Liou and Brennan eye with the CT LUCIA 611PY IOL and 4.5 mm iris diameter. $\mathbf{MTF}_y$, $\mathbf{MTF}_{mean}$ and $\mathbf{MTF}_x$ at $100\frac{\text{lp}}{\text{mm}}$ is depicted for each IOL–position (θ,x)

Displacement effects on the WF

The WF's Zernike coefficients in dependence on tilt and shift are depicted in Figure 5.24 for photopic and in Figure 5.25 for scotopic vision.

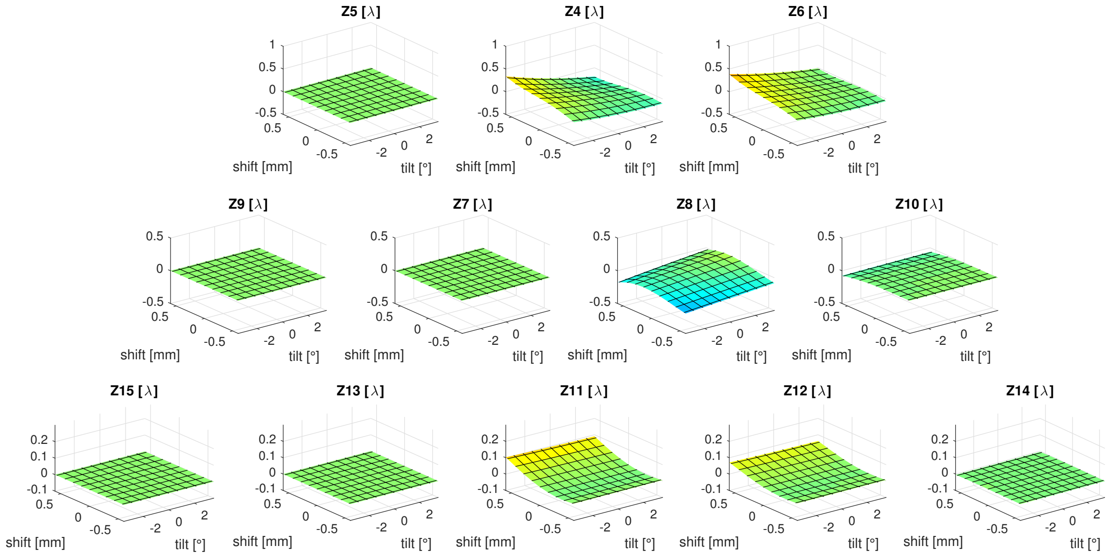
Z5 [λ]
Z4 [λ]
Z6 [λ]
Z9 [λ]
Z7 [λ]
Z8 [λ]
Z10 [λ]
Z15 [λ]
Z13 [λ]
Z11 [λ]
Z12 [λ]
Z14 [λ]

Figure 5.24: Numerical simulation results: Liou and Brennan eye with the CT LUCIA 611PY D3 IOL and 3 mm iris diameter. The Zernike Coefficients $Z4$ to $Z15$ are depicted for each IOL–position (θ, x)

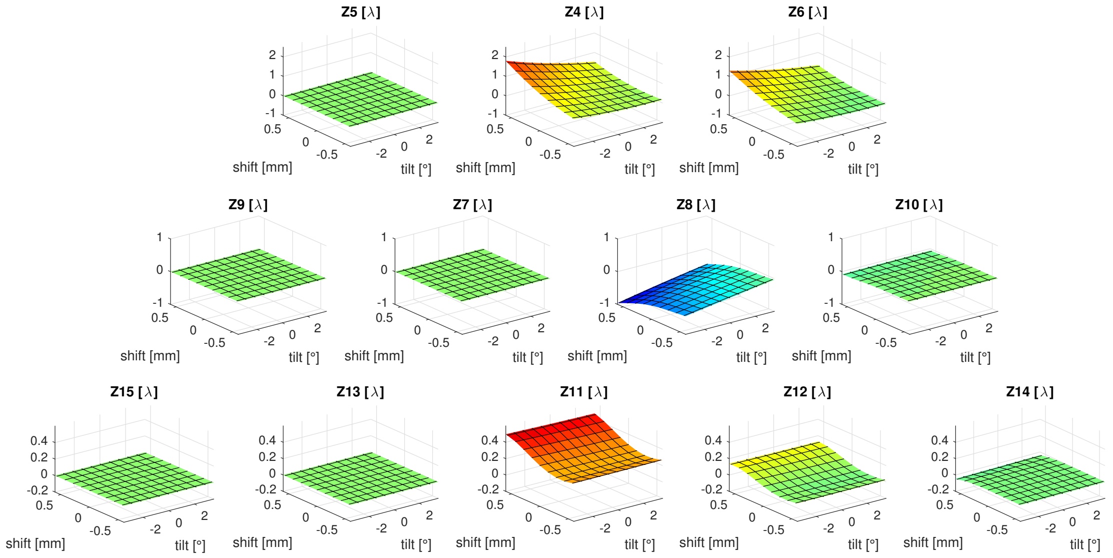
Z5 [λ]
Z4 [λ]
Z6 [λ]
Z9 [λ]
Z7 [λ]
Z8 [λ]
Z10 [λ]
Z15 [λ]
Z13 [λ]
Z11 [λ]
Z12 [λ]
Z14 [λ]

Figure 5.25: Numerical simulation results: Liou and Brennan eye with the CT LUCIA 611PY D3 IOL and 4.5 mm iris diameter. The Zernike Coefficients $Z4$ to $Z15$ are depicted for each IOL–position (θ, x)

5.2 Measurement Results

5.2.1 Model Eye without Intraocular Lens Measurement Results

From previous failed manufacturings it was known that the manufacturing process of the PMMA model cornea is challenging. The cornea lenses were manufactured in several lots. The last lot, which was used for this thesis, contained three pieces, from which the best one was selected. This was done by measuring all three lenses (C1, C2 and C3) without an IOL at the 4.5 mm iris diameter (Figure 5.27). 4.5 mm was chosen, as geometric errors are easier to be obtained at wide open apertures. Cornea 2 performed best, thus all further measurements (including Figure 5.26) were done with C2.

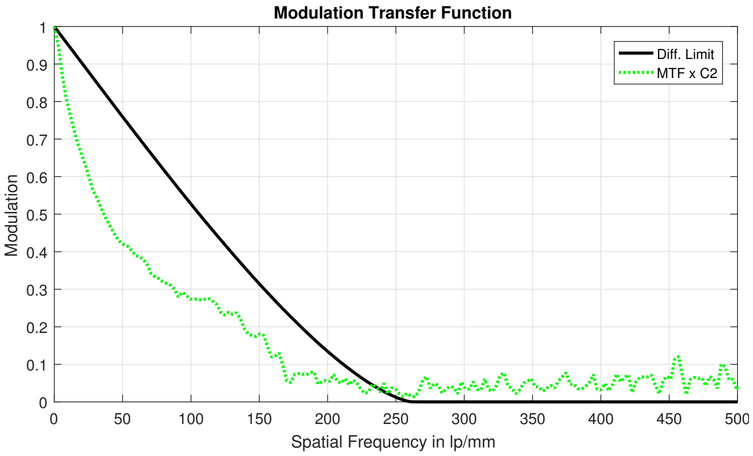

Figure 5.26: MTF–measurement of the model cornea C2 with 3 mm iris diameter. $\mathbf{MTF}_x(100\frac{\text{lp}}{\text{mm}})$=0.27

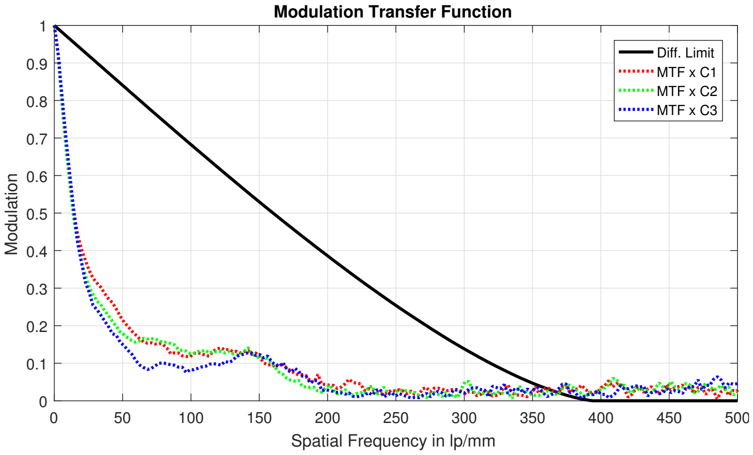

Figure 5.27: MTF–measurements of three model cornea C1, C2 and C3 with 4.5 mm iris diameter. $\mathbf{MTF}_x(100\frac{\text{lp}}{\text{mm}})$= 0.13 for cornea 2.

Cornea 2 has the best performance for the $\mathbf{MTF}_x(100\frac{\text{lp}}{\text{mm}})$. This is only 65% of the simulated modulation (Figure 5.6). As discussed in Section 6.1.1 it cannot be assumed that the cornea is rotationally symmetric. Thus the cornea was never disassembled from the model eye for all measurements of this thesis to ensure a consistent orientation of additional geometric aberrations of the cornea lens. For further analysis the WF–aberrations of cornea 2 were measured with the WF–measurement setup.

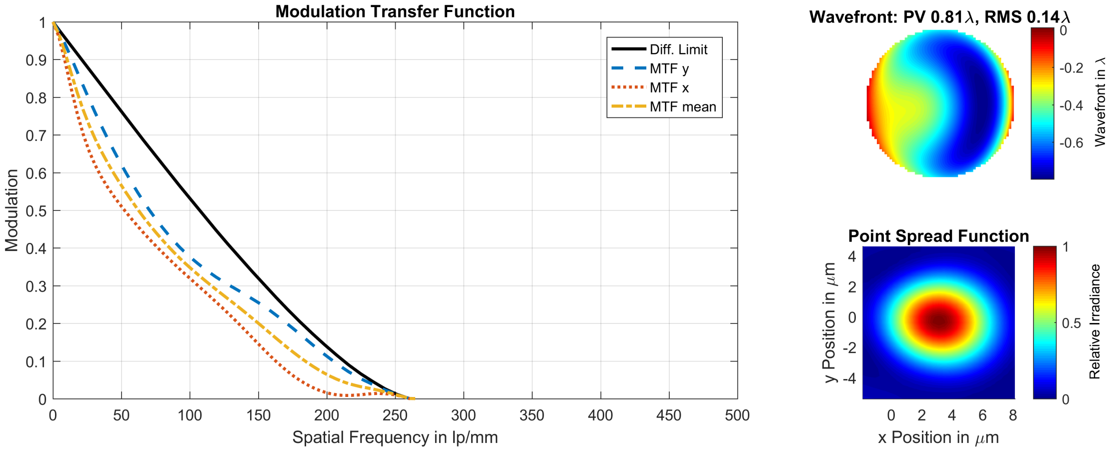

Figure 5.28: WF–measurement of the model cornea C2 with 3 mm iris diameter. The WF is reconstructed from coefficients $Z4$ to $Z15$. MTF and PSF are derived from the WF–data $\mathbf{MTF}_{mean}(100\frac{\text{lp}}{\text{mm}})$=0.35

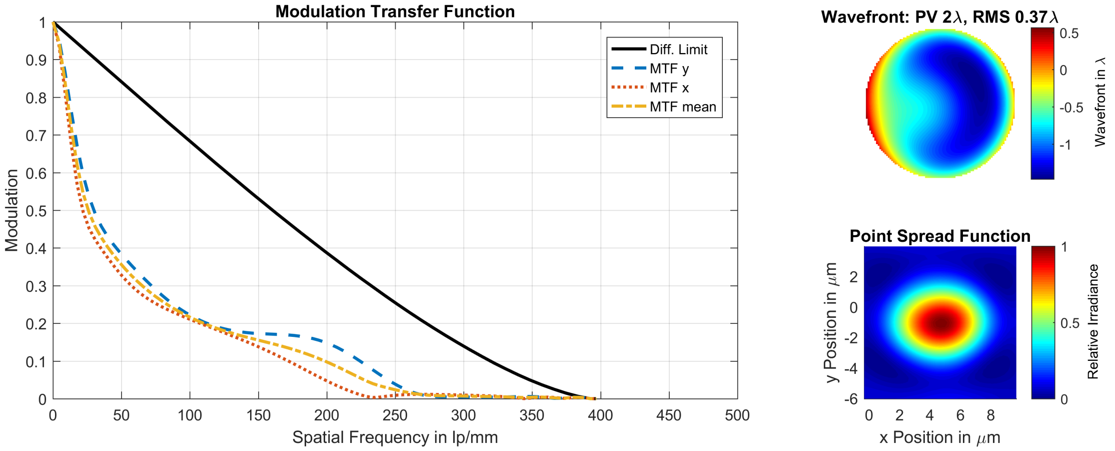

Figure 5.29: WF–measurement of the model cornea C2 with 4.5 mm iris diameter. The WF is reconstructed from coefficients $Z4$ to $Z15$. MTF and PSF are derived from the WF–data $\mathbf{MTF}_{mean}(100\frac{\text{lp}}{\text{mm}})$=0.21

Despite the fact that the cornea lens C2 is the best among all delivered lenses, Table 5.5 and 5.6 reveal,that in comparison with the simulation, the cornea lens has a significant amount of coma and also increased astigmatism.

Table 5.5: Zernike coefficients (scaled in λ) measured from the model PMMA-Cornea without an IOL are compared with the simulated data for 3 mm iris diameter. Bold marked values reveal that vertical astigmatism $Z6$ and horizontal coma $Z8$ are increased.

Coefficient	n	m	measurement	simulation
$Z4$	2	0	0.0570	0.2274
$Z5$	2	-2	-0.0250	0
$Z6$	2	2	**0.1090**	-0.0230
$Z7$	3	-1	-0.0160	0
$Z8$	3	1	**0.1110**	0.0020
$Z9$	3	-3	0.0080	0
$Z10$	3	3	0.0210	0.0000
$Z11$	4	0	0.0870	0.0443
$Z12$	4	2	0.0290	-0.0006
$Z13$	4	-2	0.0060	0
$Z14$	4	4	0.0090	0.0000
$Z15$	4	-4	0.0090	0

Table 5.6: Zernike coefficients (scaled in λ) measured from the model PMMA-Cornea without an IOL are compared with the simulated data for 4.5 mm iris diameter. Bold marked values reveal that vertical astigmatism $Z6$ and horizontal coma $Z8$ are increased.

Coefficient	n	m	measurement	simulation
$Z4$	2	0	0.2720	0.3731
$Z5$	2	-2	-0.0240	0
$Z6$	2	2	**0.1710**	-0.0544
$Z7$	3	-1	-0.0560	0
$Z8$	3	1	**0.1490**	0.0129
$Z9$	3	-3	0.0050	0
$Z10$	3	3	-0.0260	-0.0001
$Z11$	4	0	0.2210	0.2260
$Z12$	4	2	-0.0130	-0.0029
$Z13$	4	-2	-0.0050	0
$Z14$	4	4	-0.0030	0.0000
$Z15$	4	-4	-0.0070	0

5.2.2 Tilt and Shift Tolerance of Intraocular Lenses

Measurements with the MC5812AS

Centered Position

The image performance of the MC5812AS IOL in centered position is measured with the MTF and the WF–setup. Results for the $\mathbf{MTF}_x$ from the MTF–setup are depicted in Figure 5.30 for photopic vision (P) and in Figure 5.31 for scotopic vision (S). The WF is reconstructed from coefficients $Z4$ to $Z15$ measured with the WF-setup. From that, $\mathbf{MTF}_x$, $\mathbf{MTF}_y$ and PSF are derived mathematically. Results are depicted in Figure 5.32 (P) and Figure 5.33 (S).

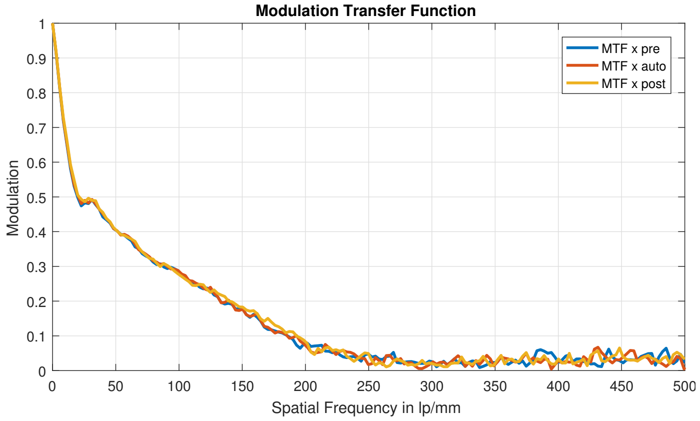

Figure 5.30: Direct $\mathbf{MTF}_x$ measurements: Liou and Brennan eye with MC5812AS IOL and 3 mm iris diameter depicted for a centered IOL. The three functions show the MTF before (pre), during (auto) and after (post) automatically doing all tilts and shifts.

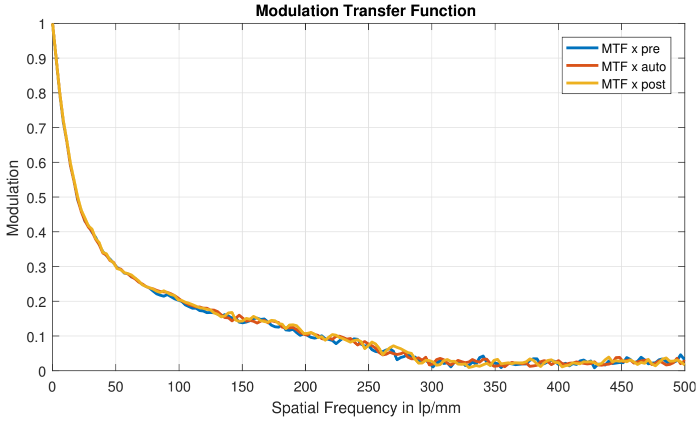

Figure 5.31: Direct $\mathbf{MTF}_x$ measurements: Liou and Brennan eye with MC6125AS IOL and 4.5 mm iris diameter depicted for a centered IOL. The three functions show the MTF before (pre), during (auto) and after (post) automatically doing all tilts and shifts.

Figure 5.30 and Figure 5.31 show the MTF measurements for the center position prior, during and after the measurement. The Zernike coefficients prior, during and after the measurement procedure are given in Table 5.7 and 5.8. Fail measurements as described in Section 4.3.2 and 4.4.1 were discarded.

Table 5.7: Zernike coefficients (scaled in λ): Liou and Brennan eye with the MC5812AS and 3 mm iris diameter at centered position prior (pre), during (auto) and after (post) the measurement procedure.

Coefficient	n	m	pre	auto	post
$Z4$	2	0	0.128	0.139	0.14
$Z5$	2	-2	-0.047	-0.04	-0.04
$Z6$	2	2	0.247	0.25	0.263
$Z7$	3	-1	-0.01	-0.011	-0.009
$Z8$	3	1	0.188	0.193	0.178
$Z9$	3	-3	0.006	-0.005	-0.002
$Z10$	3	3	-0.008	-0.013	-0.018
$Z11$	4	0	0.103	0.106	0.096
$Z12$	4	2	0.028	0.031	0.022
$Z13$	4	-2	0.005	0	0.006
$Z14$	4	4	0.018	0.023	0.017
$Z15$	4	-4	-0.007	-0.009	0.004

Table 5.8: Zernike coefficients (scaled in λ): Liou and Brennan eye with the MC5812AS and 4.5 mm iris diameter at centered position prior (pre), during (auto) and after (post) the measurement procedure.

Coefficient	n	m	pre	auto	post
$Z4$	2	0	0.647	0.663	0.546
$Z5$	2	-2	-0.062	-0.07	-0.065
$Z6$	2	2	0.488	0.493	0.424
$Z7$	3	-1	-0.07	-0.075	-0.074
$Z8$	3	1	0.44	0.457	0.408
$Z9$	3	-3	0.017	0.016	0.01
$Z10$	3	3	-0.027	-0.043	-0.024
$Z11$	4	0	0.38	0.385	0.378
$Z12$	4	2	-0.024	-0.028	-0.028
$Z13$	4	-2	-0.007	-0.011	-0.009
$Z14$	4	4	0	-0.004	0.002
$Z15$	4	-4	0.011	0.018	0.016

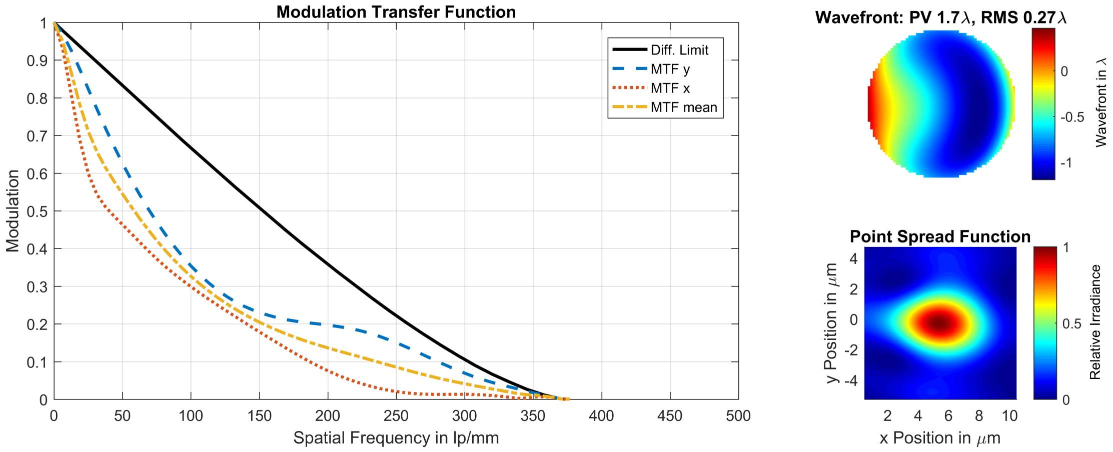

Figure 5.32: Derived from WF–measurements: Liou and Brennan eye with the MC5812AS IOL and 3 mm iris diameter. $\mathbf{MTF}_{mean}(100\frac{\text{lp}}{\text{mm}})$=0.32

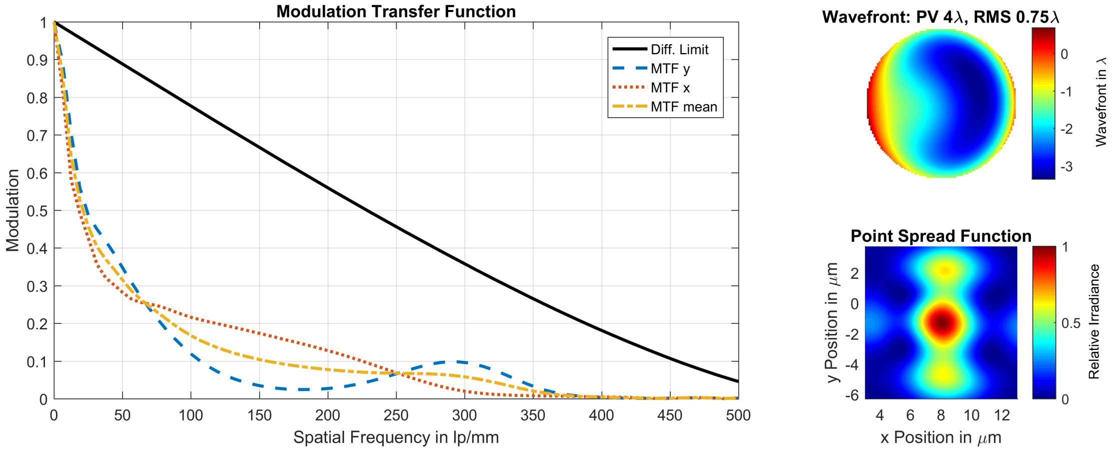

Figure 5.33: Derived from WF–measurements: Liou and Brennan eye with the MC5812AS IOL and 4.5 mm iris diameter. $\mathbf{MTF}_{mean}(100\frac{\text{lp}}{\text{mm}})$=0.17

Displacement effects on the MTF

The directly measured $\mathbf{MTF}_x$ values at $100\frac{\text{lp}}{\text{mm}}$ are depicted in Figure 5.34 for photopic (P) and in Figure 5.36 for scotopic (S) vision. The **MTF** data derived from the WF–measurements are depicted in Figure 5.35 (S) and Figure 5.37 (P)

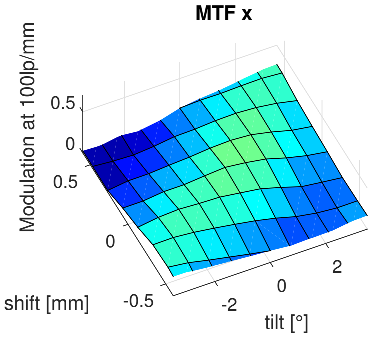

Figure 5.34: Direct $\mathbf{MTF}_x$ measurements: Liou and Brennan eye with the MC5812AS IOL and 3 mm iris diameter. The MTF at $100\frac{\text{lp}}{\text{mm}}$ is depicted for each IOL–position (θ,x)

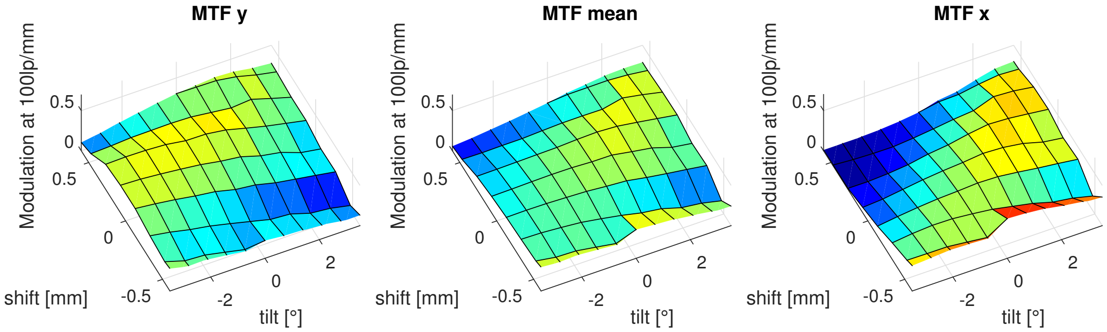

Figure 5.35: $\mathbf{MTF}_y$, $\mathbf{MTF}_{mean}$ and $\mathbf{MTF}_x$ derived from WF–measurements: Liou and Brennan eye with the MC5812AS IOL and 3 mm iris diameter. The MTF at $100\frac{\text{lp}}{\text{mm}}$ is depicted for each IOL–position (θ,x)

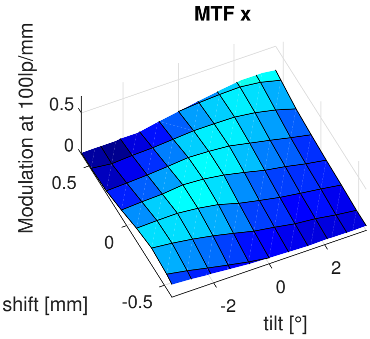

Figure 5.36: Direct $\mathbf{MTF}_x$ measurements: Liou and Brennan eye with the MC5812AS IOL and 4.5 mm iris diameter. The MTF at 100$\frac{\text{lp}}{\text{mm}}$ is depicted for each IOL–position (θ,x)

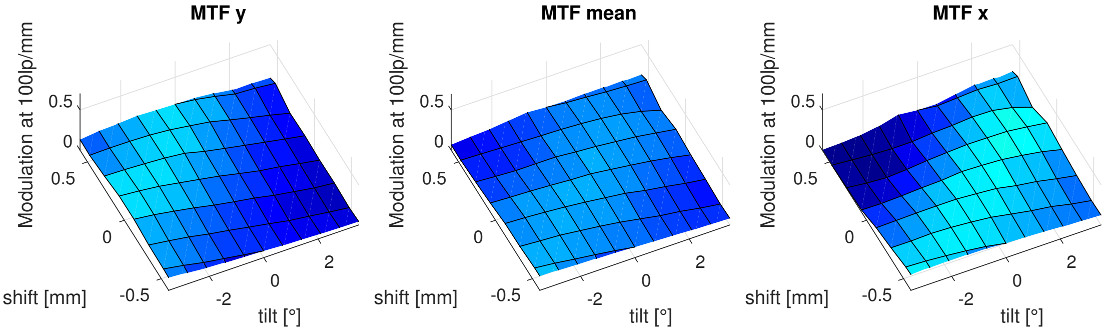

Figure 5.37: $\mathbf{MTF}_y$, $\mathbf{MTF}_{mean}$ and $\mathbf{MTF}_x$ derived from WF–measurements: Liou and Brennan eye with the MC5812AS IOL and 4.5 mm iris diameter. The MTF at 100$\frac{\text{lp}}{\text{mm}}$ is depicted for each IOL–position (θ,x)

Displacement effects on the WF

The measured WF's Zernike coefficients in dependence on tilt and shift are depicted in Figure 5.38 for photopic and in Figure 5.39 for scotopic vision.

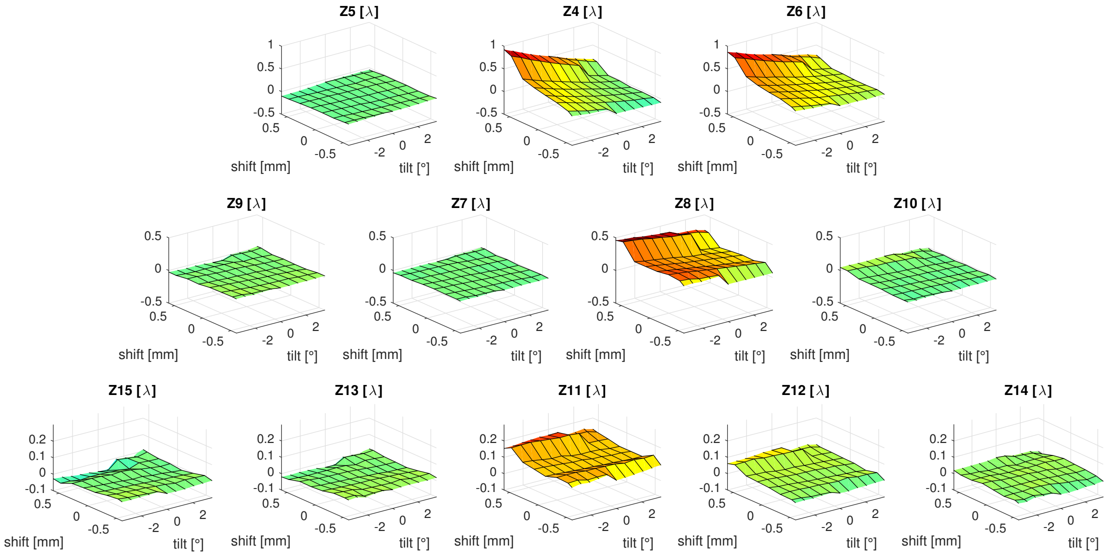

Figure 5.38: WF measurement results: Liou and Brennan eye with the MC5812AS IOL and 3 mm iris diameter. The Zernike Coefficients $Z4$ to $Z15$ are depicted for each IOL–position (θ,x)

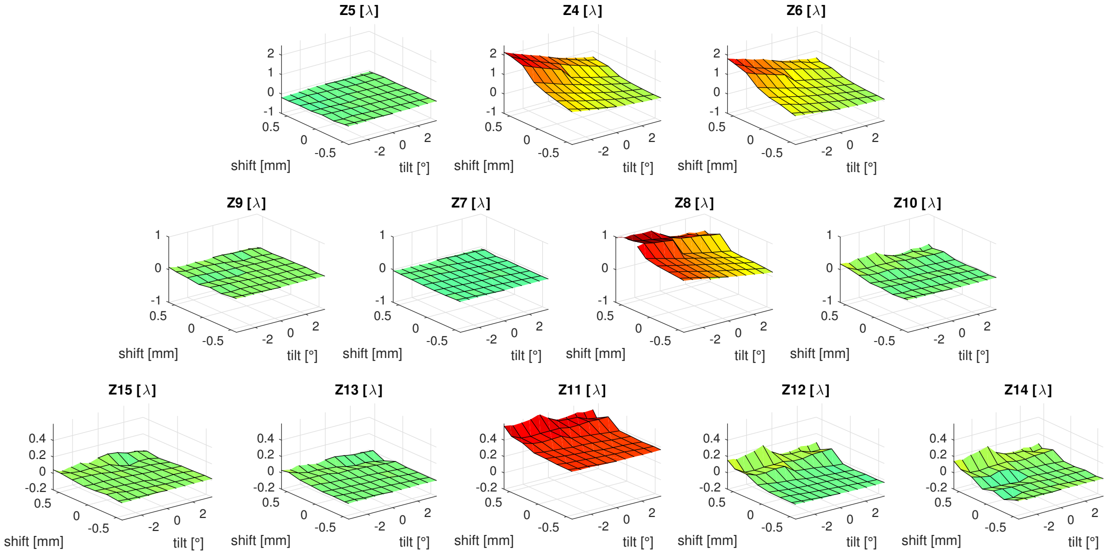

Figure 5.39: WF measurement results: Liou and Brennan eye with the MC5812AS IOL and 4.5 mm iris diameter. The Zernike Coefficients $Z4$ to $Z15$ are depicted for each IOL–position (θ,x)

Measurements with the MC6125AS

Centered Position

The image performance of the MC6125AS IOL in centered position is measured with the MTF and the WF–setup. Results for the $\mathbf{MTF}_x$ from the MTF–setup are depicted in Figure 5.40 for photopic vision (P) and in Figure 5.41 for scotopic vision (S). The WF is reconstructed from coefficients $Z4$ to $Z15$ measured with the WF-setup. From that, $\mathbf{MTF}_x$, $\mathbf{MTF}_y$ and PSF are derived mathematically. Results are depicted in Figure 5.42 (P) and Figure 5.43 (S).

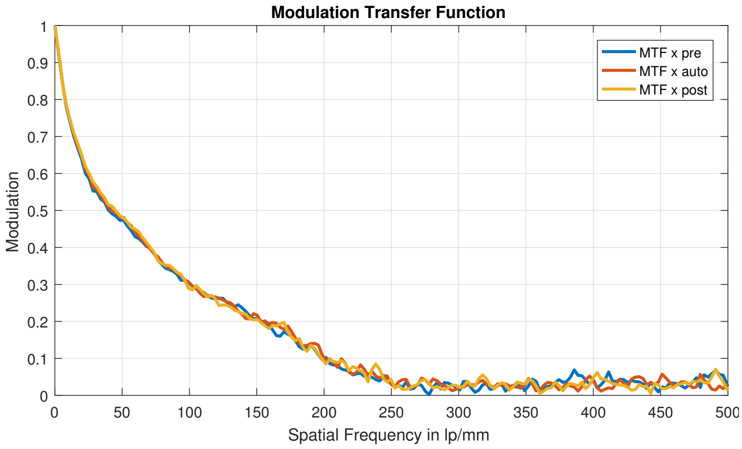

Figure 5.40: Direct $\mathbf{MTF}_x$ measurements: Liou and Brennan eye with MC6125AS IOL and 3 mm iris diameter depicted for a centered IOL. The three functions show the MTF before (pre), during (auto) and after (post) automatically doing all tilts and shifts.

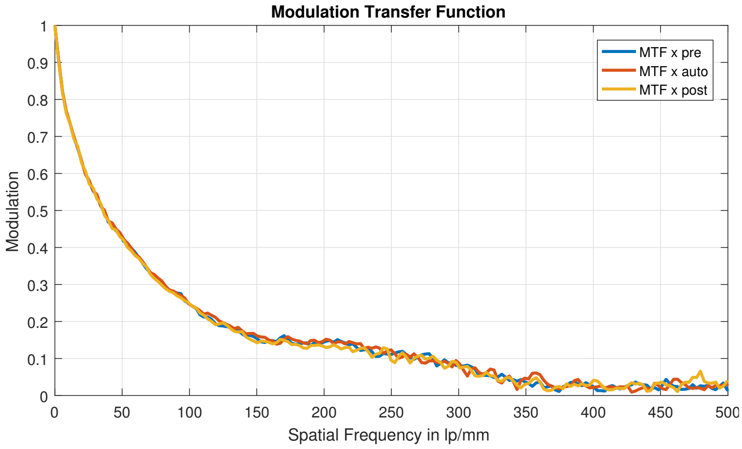

Figure 5.41: Direct $\mathbf{MTF}_x$ measurements: Liou and Brennan eye with MC6125AS IOL and 4.5 mm iris diameter depicted for a centered IOL. The three functions show the MTF before (pre), during (auto) and after (post) automatically doing all tilts and shifts.

Figure 5.40 and Figure 5.41 show the MTF measurements for the center position prior, during and after the measurement. The Zernike coefficients prior, during and after the measurement procedure are given in Table 5.9 and 5.10. Fail measurements as described in Section 4.3.2 and 4.4.1 were discarded.

Table 5.9: Zernike coefficients (scaled in λ): Liou and Brennan eye with the MC6125AS and 3 mm iris diameter at centered position prior (pre), during (auto) and after (post) the measurement procedure.

Coefficient	n	m	pre	auto	post
$Z4$	2	0	0.045	0.046	0.014
$Z5$	2	-2	0.024	0.018	0.017
$Z6$	2	2	0.066	0.083	0.078
$Z7$	3	-1	-0.019	-0.009	-0.015
$Z8$	3	1	0.105	0.117	0.096
$Z9$	3	-3	0.016	0.008	0.005
$Z10$	3	3	0.007	0.006	0.005
$Z11$	4	0	0.086	0.091	0.084
$Z12$	4	2	0.029	0.024	0.023
$Z13$	4	-2	0	0.002	-0.003
$Z14$	4	4	-0.003	-0.005	-0.005
$Z15$	4	-4	0.012	0.002	0.008

Table 5.10: Zernike coefficients (scaled in λ): Liou and Brennan eye with the MC6125AS and 4.5 mm iris diameter at centered position prior (pre), during (auto) and after (post) the measurement procedure.

Coefficient	n	m	pre	auto	post
$Z4$	2	0	0.375	0.613	0.4
$Z5$	2	-2	0.071	0.037	0.021
$Z6$	2	2	0.311	0.342	0.303
$Z7$	3	-1	0.032	0.01	-0.005
$Z8$	3	1	0.103	0.093	0.11
$Z9$	3	-3	-0.002	-0.024	-0.023
$Z10$	3	3	0.018	0.004	0.005
$Z11$	4	0	0.263	0.255	0.238
$Z12$	4	2	-0.012	-0.021	-0.026
$Z13$	4	-2	-0.007	-0.017	-0.012
$Z14$	4	4	-0.019	-0.031	-0.031
$Z15$	4	-4	0.012	0.004	0.013

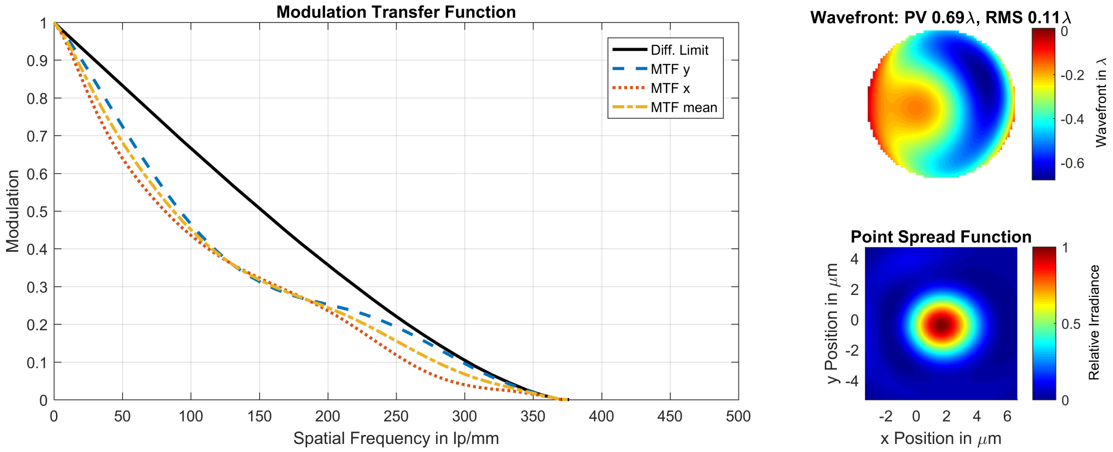

Figure 5.42: Derived from WF–measurements: Liou and Brennan eye with the MC6125AS IOL and 3 mm iris diameter. $\mathbf{MTF}_{mean}(100\frac{\text{lp}}{\text{mm}})$=0.45

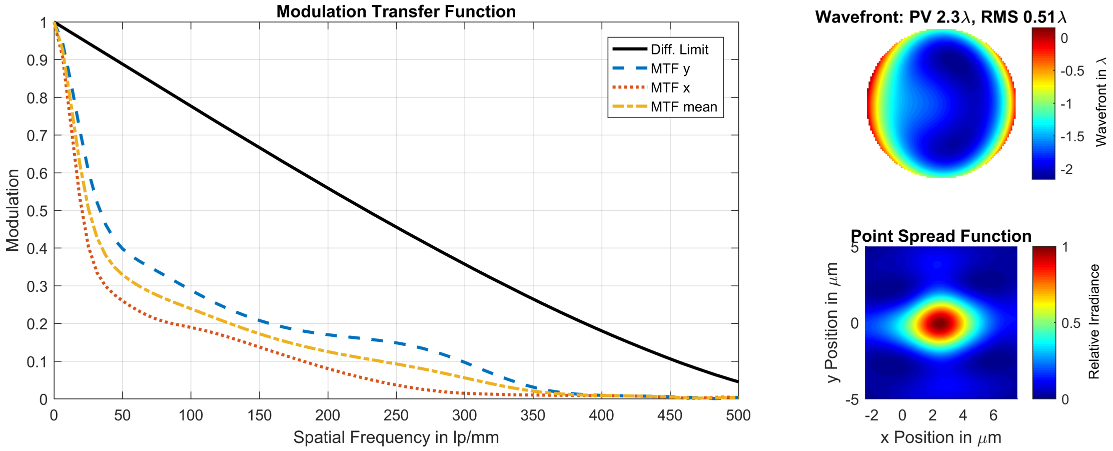

Figure 5.43: Derived from WF–measurements: Liou and Brennan eye with the MC6125AS IOL and 4.5 mm iris diameter. $\mathbf{MTF}_{mean}(100\frac{\text{lp}}{\text{mm}})$=0.24

Displacement effects on the MTF

The directly measured **MTF**$_x$ values at $100\frac{\text{lp}}{\text{mm}}$ are depicted in Figure 5.44 for photopic (P) and in Figure 5.46 for scotopic (S) vision. The **MTF** data derived from the WF–measurements are depicted in Figure 5.45 (S) and Figure 5.47 (P)

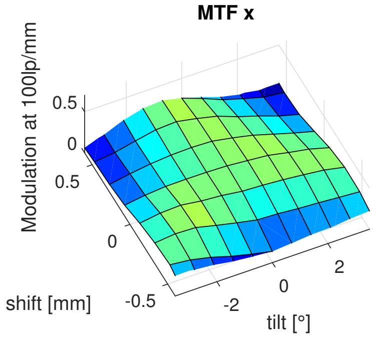

Figure 5.44: Direct **MTF**$_x$ measurements: Liou and Brennan eye with the MC6125AS IOL and 3 mm iris diameter. The MTF at $100\frac{\text{lp}}{\text{mm}}$ is depicted for each IOL–position (θ,x)

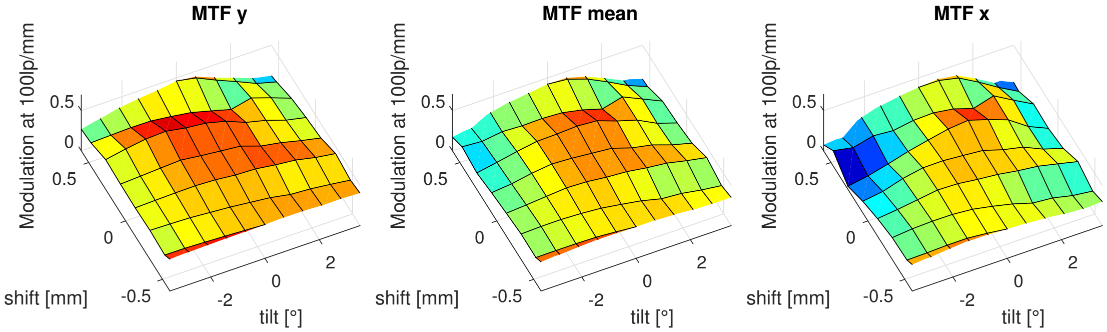

Figure 5.45: **MTF**$_y$, **MTF**$_{mean}$ and **MTF**$_x$ derived from WF–measurements: Liou and Brennan eye with the MC6125AS IOL and 3 mm iris diameter. The MTF at $100\frac{\text{lp}}{\text{mm}}$ is depicted for each IOL–position (θ,x)

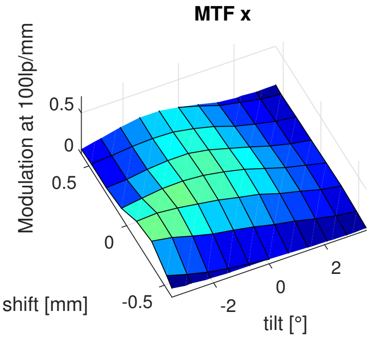

Figure 5.46: Direct $\mathbf{MTF}_x$ measurements: Liou and Brennan eye with the MC6125AS IOL and 4.5 mm iris diameter. The MTF at $100\frac{\text{lp}}{\text{mm}}$ is depicted for each IOL–position (θ,x)

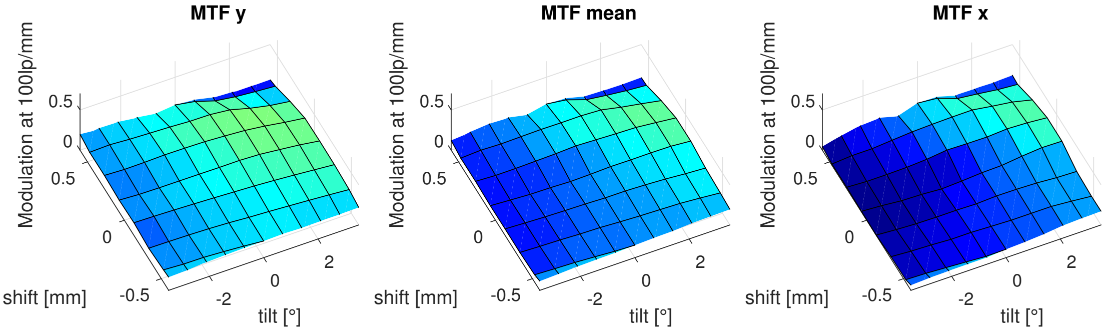

Figure 5.47: $\mathbf{MTF}_y$, $\mathbf{MTF}_{mean}$ and $\mathbf{MTF}_x$ derived from WF–measurements: Liou and Brennan eye with the MC6125AS IOL and 4.5 mm iris diameter. The MTF at $100\frac{\text{lp}}{\text{mm}}$ is depicted for each IOL–position (θ,x)

Displacement effects on the WF

The measured WF's Zernike coefficients in dependence on tilt and shift are depicted in Figure 5.48 for photopic and in Figure 5.49 for scotopic vision.

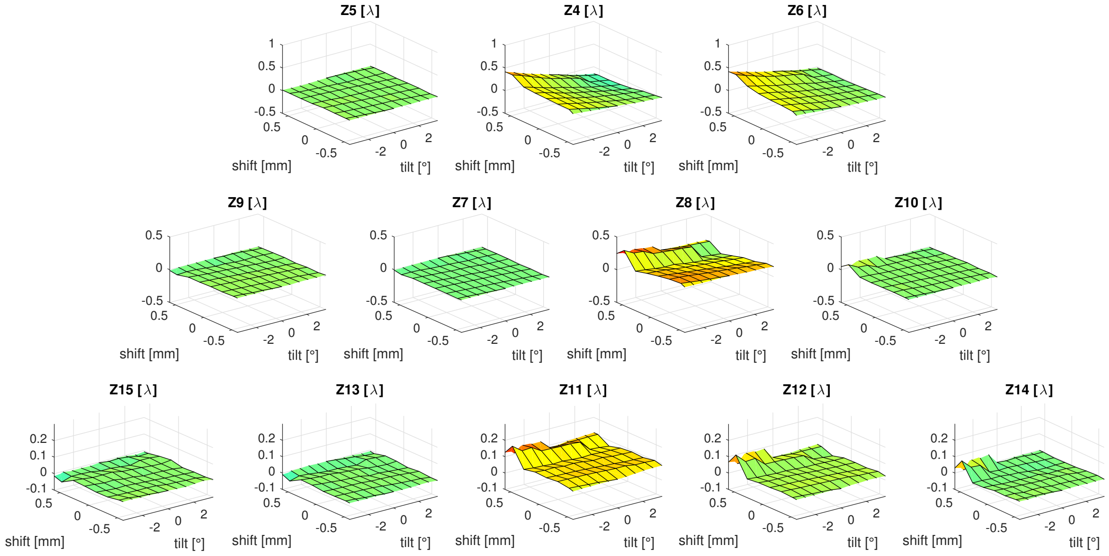

Figure 5.48: WF measurement results: Liou and Brennan eye with the MC6125AS IOL and 3 mm iris diameter. The Zernike Coefficients $Z4$ to $Z15$ are depicted for each IOL–position (θ,x)

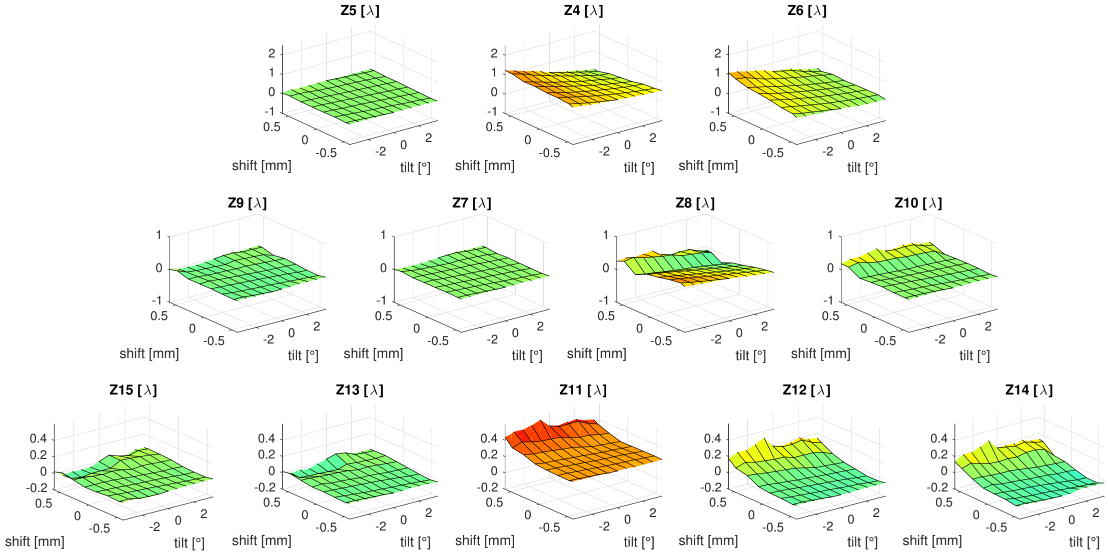

Figure 5.49: WF measurement results: Liou and Brennan eye with the MC6125AS IOL and 4.5 mm iris diameter. The Zernike Coefficients $Z4$ to $Z15$ are depicted for each IOL–position (θ,x)

Measurements with the CT611PY

The image performance of the CT611PY IOL in centered position is measured with the MTF and the WF–setup. Results for the $\mathbf{MTF}_x$ from the MTF–setup are depicted in Figure 5.50 for photopic vision (P) and in Figure 5.51 for scotopic vision (S). The WF is reconstructed from coefficients $Z4$ to $Z15$ measured with the WF-setup. From that, $\mathbf{MTF}_x$, $\mathbf{MTF}_y$ and PSF are derived mathematically. Results are depicted in Figure 5.52 (P) and Figure 5.53 (S).

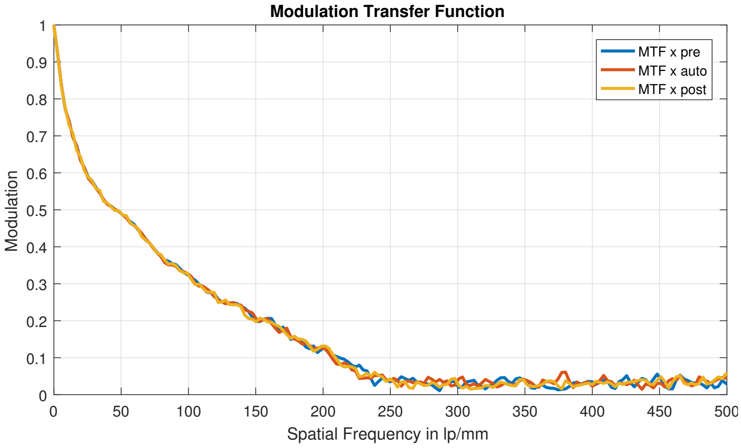

Figure 5.50: Direct $\mathbf{MTF}_x$ measurements: Liou and Brennan eye with CT611PY IOL and 3 mm iris diameter depicted for a centered IOL. The three functions show the MTF before (pre), during (auto) and after (post) automatically doing all tilts and shifts.

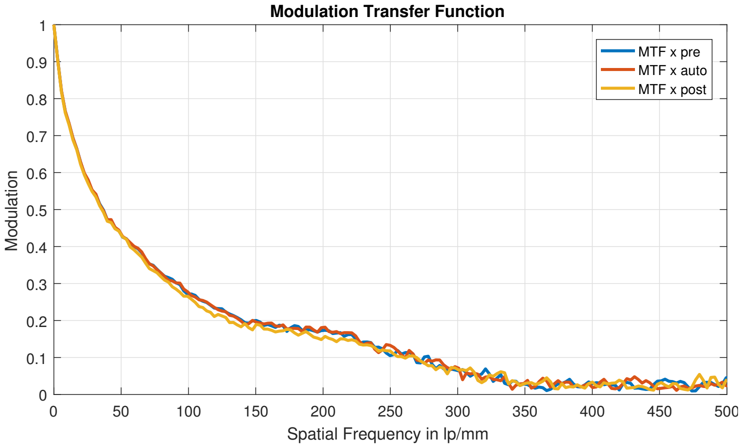

Figure 5.51: Direct $\mathbf{MTF}_x$ measurements: Liou and Brennan eye with CT611PY IOL and 4.5 mm iris diameter depicted for a centered IOL. The three functions show the MTF before (pre), during (auto) and after (post) automatically doing all tilts and shifts.

Figure 5.50 and Figure 5.51 show the MTF measurements for the center position prior, during and after the measurement. The Zernike coefficients prior, during and after the measurement procedure are given in Table 5.11 and 5.12. Fail measurements as described in Section 4.3.2 and 4.4.1 were discarded.

Table 5.11: Zernike coefficients (scaled in λ): Liou and Brennan eye with the CT611PY and 3 mm iris diameter at centered position prior (pre), during (auto) and after (post) the measurement procedure.

Coefficient	n	m	pre	auto	post
$Z4$	2	0	0.031	0.035	0.058
$Z5$	2	-2	0.013	0.012	0.01
$Z6$	2	2	0.11	0.111	0.12
$Z7$	3	-1	0	-0.001	-0.006
$Z8$	3	1	0.075	0.079	0.047
$Z9$	3	-3	0.014	0.018	0.014
$Z10$	3	3	0.003	0.007	-0.009
$Z11$	4	0	0.069	0.071	0.065
$Z12$	4	2	0.031	0.036	0.017
$Z13$	4	-2	0.009	0.01	0.015
$Z14$	4	4	0.026	0.031	0.013
$Z15$	4	-4	-0.004	-0.004	-0.001

Table 5.12: Zernike coefficients (scaled in λ): Liou and Brennan eye with the CT611PY and 4.5 mm iris diameter at centered position prior (pre), during (auto) and after (post) the measurement procedure.

Coefficient	n	m	pre	auto	post
$Z4$	2	0	0.727	0.731	0.77
$Z5$	2	-2	0.03	0.041	0.03
$Z6$	2	2	0.434	0.421	0.456
$Z7$	3	-1	-0.063	-0.038	-0.062
$Z8$	3	1	0.51	0.503	0.51
$Z9$	3	-3	0.016	0.011	0.014
$Z10$	3	3	0.03	0.011	0.025
$Z11$	4	0	0.39	0.396	0.395
$Z12$	4	2	0.046	0.041	0.047
$Z13$	4	-2	-0.013	-0.011	-0.015
$Z14$	4	4	-0.003	-0.003	-0.009
$Z15$	4	-4	-0.009	-0.018	-0.008

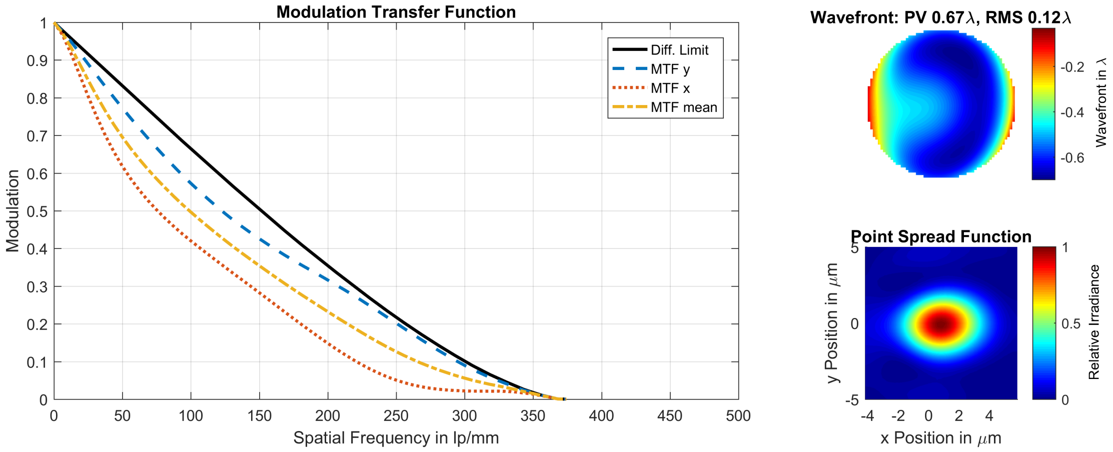

Figure 5.52: Derived from WF–measurements: Liou and Brennan eye with the CT611PY IOL and 3 mm iris diameter. $\mathbf{MTF}_{mean}(100\frac{\mathrm{lp}}{\mathrm{mm}})$=0.50

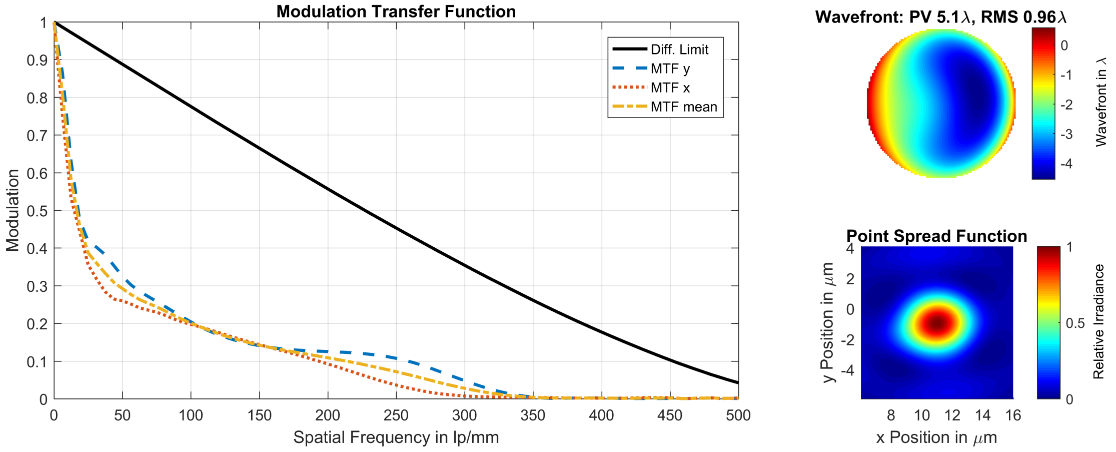

Figure 5.53: Derived from WF–measurements: Liou and Brennan eye with the CT611PY IOL and 4.5 mm iris diameter. $\mathbf{MTF}_{mean}(100\frac{\mathrm{lp}}{\mathrm{mm}})$=0.20

Displacement effects on the MTF

The directly measured **MTF**$_x$ values at $100\frac{\mathrm{lp}}{\mathrm{mm}}$ are depicted in Figure 5.54 for photopic (P) and in Figure 5.56 for scotopic (S) vision. The **MTF** data derived from the WF–measurements are depicted in Figure 5.55 (S) and Figure 5.57 (P)

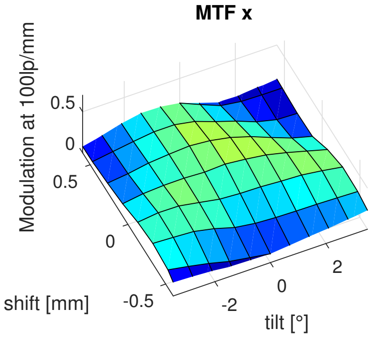

Figure 5.54: Direct **MTF**$_x$ measurements: Liou and Brennan eye with the CT611PY IOL and 3 mm iris diameter. The MTF at $100\frac{\mathrm{lp}}{\mathrm{mm}}$ is depicted for each IOL–position (θ,x)

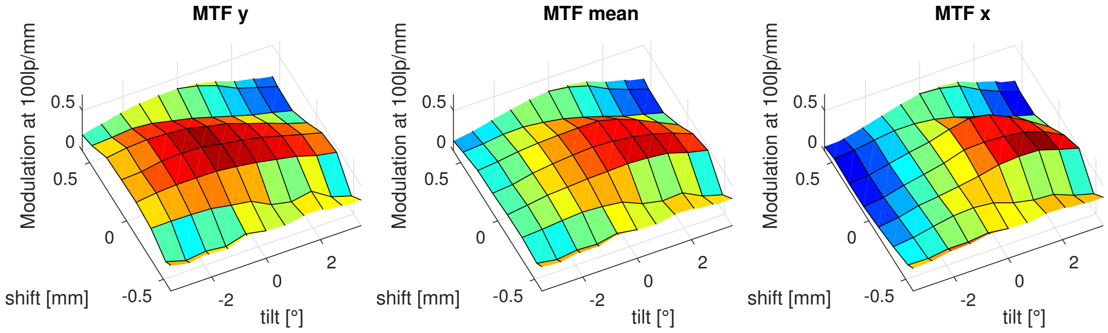

Figure 5.55: **MTF**$_y$, **MTF**$_{mean}$ and **MTF**$_x$ derived from WF–measurements: Liou and Brennan eye with the CT611PY IOL and 3 mm iris diameter. The MTF at $100\frac{\mathrm{lp}}{\mathrm{mm}}$ is depicted for each IOL–position (θ,x)

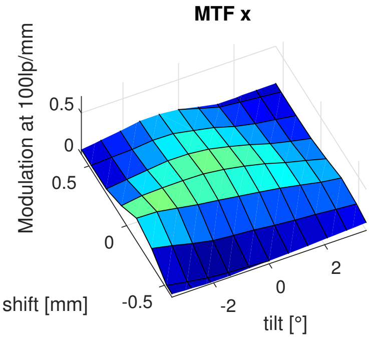

Figure 5.56: Direct $\mathbf{MTF}_x$ measurements: Liou and Brennan eye with the CT611PY IOL and 4.5 mm iris diameter. The MTF at $100\frac{\text{lp}}{\text{mm}}$ is depicted for each IOL–position (θ,x)

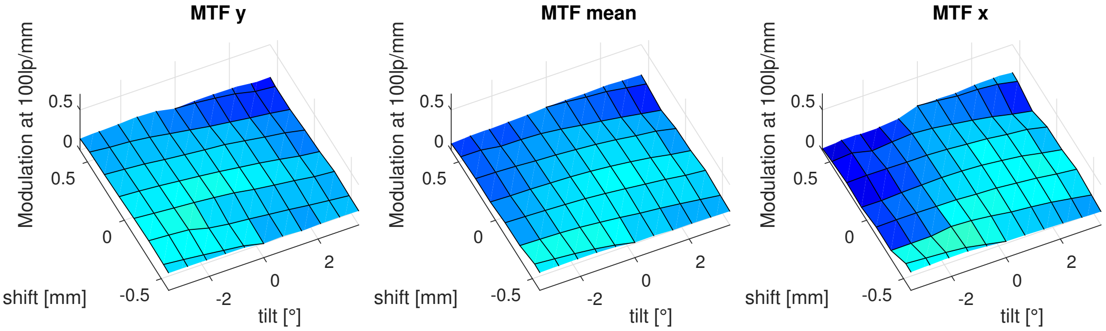

Figure 5.57: $\mathbf{MTF}_y$, $\mathbf{MTF}_{mean}$ and $\mathbf{MTF}_x$ derived from WF–measurements: Liou and Brennan eye with the CT611PY IOL and 4.5 mm iris diameter. The MTF at $100\frac{\text{lp}}{\text{mm}}$ is depicted for each IOL–position (θ,x)

Displacement effects on the WF

The measured WF's Zernike coefficients in dependence on tilt and shift are depicted in Figure 5.58 for photopic and in Figure 5.59 for scotopic vision.

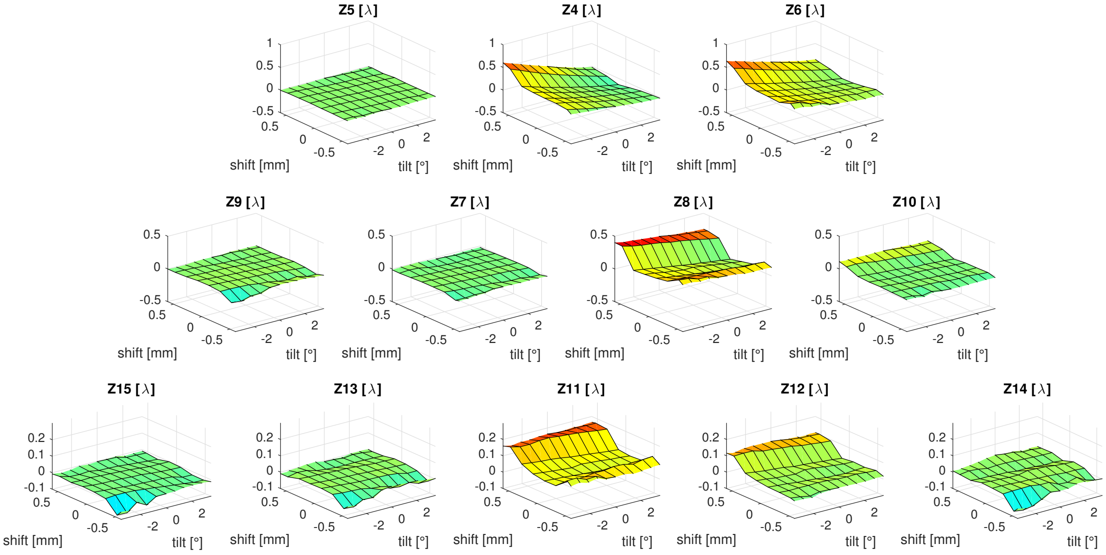

Figure 5.58: WF measurement results: Liou and Brennan eye with the CT611PY IOL and 3 mm iris diameter. The Zernike Coefficients $Z4$ to $Z15$ are depicted for each IOL–position (θ,x)

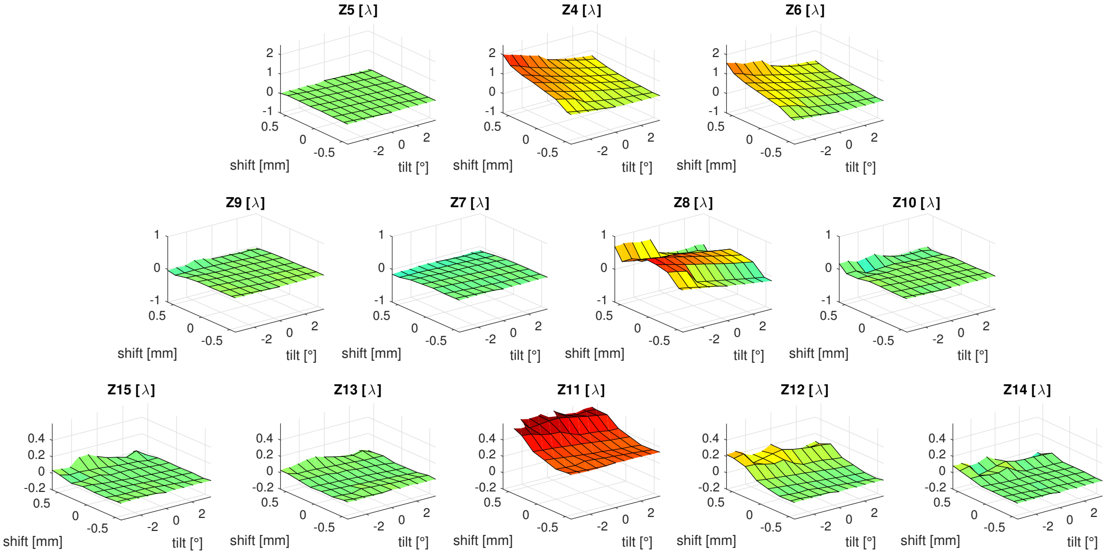

Figure 5.59: WF measurement results: Liou and Brennan eye with the CT611PY IOL and 4.5 mm iris diameter. The Zernike Coefficients $Z4$ to $Z15$ are depicted for each IOL–position (θ,x)

5.3 Characterisation of the Optical Projection Device

Numerical Analysis

An objective characterization was done with the optic design software ZEMAX OpticStudio. The system is characterized for four field points (center = 0 mm, 0.5 mm, 1 mm and 2.5 mm). In comparison with Figure 2.2 these field points correspond to a field angle of approximately 0°, 2.3°, 4.8° and 12°. With the conversion from Equation 4.3 it can be found out, that the human eye can resolve $200\frac{\text{lp}}{\text{mm}}$, $120\frac{\text{lp}}{\text{mm}}$, $70\frac{\text{lp}}{\text{mm}}$ and $30\frac{\text{lp}}{\text{mm}}$ at these field angles. Comparing with the numerical analysis (Figure 5.60) it can be seen, that the optics can resolve these spatial frequencies at least with a contrast of 30%.

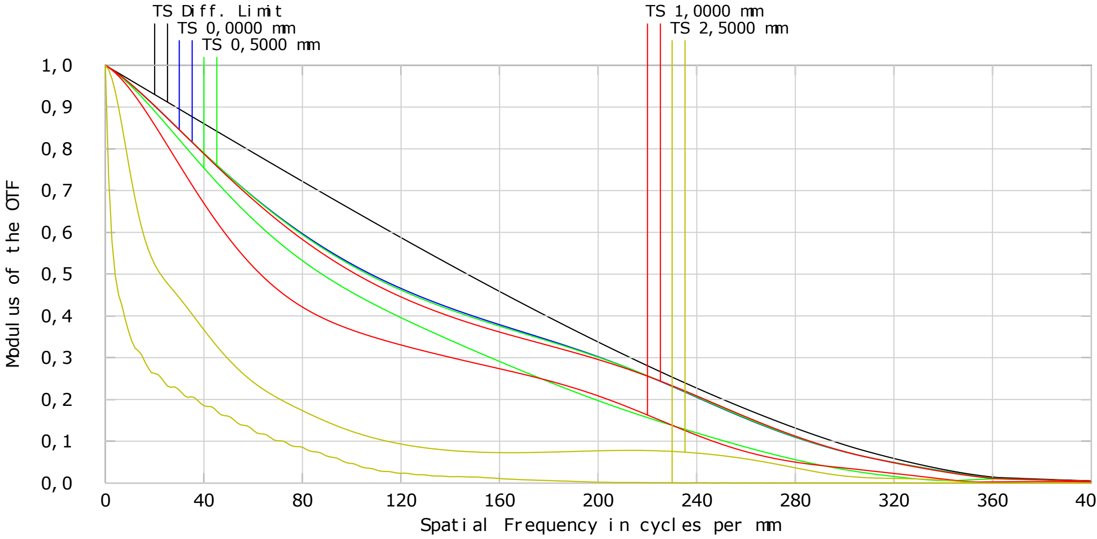

Figure 5.60: MTF from the projection optics at four different field heights: center = 0 mm (blue), 0.5 mm (green), 1 mm (red) and 2.5 mm (gold). "T" is the MTF in tangential direction "S" is in the sagittal direction. Comparison with Figure 2.2 shows that the optics do not impair the accurateness of vision.

Subjective Analysis

The projection device was used in combination with a microscope resolution test slide as object instead of the model eye. A test grating with $200\frac{\text{lp}}{\text{mm}}$ can be resolved clearly.

In combination with the model eye, it is possible to get the visual impression of the image projected on the model eye's retina.

5.4 Summary: Cumulative Optical Performance

As shown in Table 5.1, advanced lens designs are advantageous if the IOL is in the centered position. Analyzing the tilt and shift dependent optical performance brings along the problem of comparability, regarding the assessment of which lens is better than another lens: A lens with a better optical performance compared to another lens in one position (e.g. in the centered position), can on the other hand show inferior results at another location (e.g. at an extreme decentration).

To summarize the results of the optical performance of the investigated lenses in one comparable value, the cumulative optical performance for the whole parameter space (x and θ) weighted with location probability is presented in this section. The distribution of postoperative IOL–displacements depends on the IOL (see Section 2.2 for detailed information), normal distribution of the displacement is reported in these studies. Many publications only report values on the absolute displacement values (e.g. [55, 56]). Crnej et al. [133] report displacements with additional information on the direction. From these data normal distribution with approximately zero mean and a standard deviation of 0.2 mm for shifts along the x–axis and a standard deviation of 1.5° for tilts (θ) can be expected for the postoperative lens position[1]. The over all quality Q of an individual lens is estimated by weighting the optical performance ($\mathbf{MTF}_{mean}(100\frac{\text{lp}}{\text{mm}})$) with the probability of each specific location, integrated over the entire parameter space x and θ:

$$Q = \iint_{-\infty}^{\infty} \text{MTF}_{mean}(100\frac{\text{lp}}{\text{mm}}, x, \theta) \cdot \text{pdf}(x, \theta)\, dx\, d\theta \tag{5.1}$$

$\text{pdf}(x, \theta)$ is the probability density for a specific location x and θ[2], where the distribution for the shifts and tilts are assumed to be normal distributions with zero mean, standard deviations as mentioned above and independent from each other. In Table 5.13 the quality measure for all lenses investigated in this thesis is given.

Table 5.13: A weighted cumulative optical performance, see Equation 5.1, is given for all three lenses tested in this thesis. Values are calculated for photopic vision (3 mm iris) and scotopic vision (4.5 mm). The two values are simulation / measurement. Measurement values were deduced from the WF–setup

Model	MC5812AS	MC6125AS	CT LUCIA 611PY
Design concept	Spherical	Aberration free	Aberration correction
Q photopic	0.36 / 0.29	0.48 / 0.40	0.49 / 0.43
Q scotopic	0.17 / 0.15	0.26 / 0.18	0.31 / 0.19

---

[1] It is emphasized, that these values are only approximate general estimates, as the postoperative displacements depend on many factors, as e.g. the haptic design

[2] Practically only the range $x = \pm 0.6$ mm and $\theta = \pm\, 3.5°$ is considered, which accounts for 98% of the cumulative position probability and gives the correct value, as the MTF outside this range is very low.

CHAPTER 6

Discussion & Outlook

In this chapter the results and achievements will be analyzed from the perspective of the problem statement in Section 1.2. Based on that the methodological approach will be discussed. The chapter is summarized by outlining the contribution to the field by this work.

6.1 Modifications on the ISO Model Eye

The findings of Liou and Brennan and normative standards of the ISO 11979-2 could be combined in a novel optical bench setup. The automatic tilt and shift mechanism allows for a convenient analysis of effects on postoperative IOL displacements. To fulfill the requirement that the model eye should closely represent the optics of a normal human eye, the most challenging part is the cornea lens. First of all no technical materials with the same refractive and dispersive properties are available. To reasonable market prices custom lenses can be made of PMMA. By adapting the shape of the human cornea the differences in the optical properties between the real material and PMMA can be matched very closely (see Figure 5.1 and 5.2 in comparison with the model eye with the PMMA cornea Figure 5.3 and 5.4). Unfortunately a very thin lens thickness is required, due to which many manufacturers claimed that machining these lenses is impossible. They assumed that the lens would bend under the tooling pressure, which could deteriorate or even break the lens. Within extensive research two manufacturers could be found, who tried to manufacture these lenses. Only one of them (Sumipro Submicron Lathing, Almelo, Netherlands) could deliver lenses with a useable performance. But still these lenses did not perform as theoretically expected:

6.1.1 Performance of the artificial cornea lenses

The differences between the theoretical performance and the true experimental observation can be seen by comparing the WF aberrations of the model eye without an eye lens

(Table 5.5 and 5.5): vast deviations can be found in the coefficients $Z6$ and $Z8$, which correspond to vertical astigmatism and horizontal coma (see Figure 3.16 for the WF shape of these aberrations). Both are not rational symmetric which indicates that the manufactured cornea lenses are not rotational symmetric. Non rotational symmetries can also arise from imperfections of the mechanical components of the model eye e.g. OA of the optical sub components are not aligned, but measurements on the components and tolerance analysis in ZEMAX OpticStudio could not explain the observed deviations. The hypothesis that the asymmetries arise from the lens could further be strengthened by rotating the cornea lens within the lens holder: A clear change in the WF pattern could be observed, which would not be the case if the asymmetric aberrations would arise from asymmetries in the model eye itself (which keeps its orientations).

As it was known that the cornea lenses are a critical component, measurement protocols were requested from the manufacturer. For "cornea 2", which was used for the measurements in this thesis, the protocols are attached in Appendix B. The measurements were done with a Talysurf (Taylor Hobson, Leicester, England). This device, as it can also be seen in the protocols, only measures the front and back surfaces individually along one axis, assuming that the surfaces are rotational symmetric. This is most likely true for the surfaces itself due to the lathing process, but there is no information whether the OA of the back and front surface are aligned or tilted against each other.

6.2 Aberrations Induced by Post–Surgical Intraocular Lens Displacements

Within this work a convenient framework, based on ZEMAX OpticStudio and its API and MATLAB could be developed, to numerically investigate tilt and decentration effects of IOLs. In addition to analysis found in literature e.g. Eppig et al. [9], this thesis explores combined effects on tilts and decentration on all relevant WF aberration coefficients. The three selected IOLs are not representative to deduce general trends. The results are in consistence with the expectations outlined in section 2.2: In terms of performance in the central position the simple spherical lens is much worse than aspheric IOLs. The aberration correcting IOL slightly outperforms the aberration free IOL. Thus it can be summarized that more sophisticated lens designs are beneficial in the centered position. But investigating the results of lens position outside the central position, the more sophisticated designs reveal a higher dependency of image aberrations on a misalignment. In certain cases, at extreme tilts and decentrations, the simple spherical lens can outperform the other lenses. These general observations can be deducible form the simulations as well es from the measurements of the real IOLs. For a detailed analysis first the WF aberrations will be discussed, as some of the MTF analysis are based on the WF–aberrations.

6.2.1 Wavefront Aberrations induced by IOL–Displacements

Low order aberrations n=2
Negative tilt (θ) and positive decentration (x) increases defocus ($Z4$) and vertical astigmatism ($Z6$) in all lenses. The order of magnitude is the same for all three lenses. There is a good agreement between simulations and measurement. The PMMA cornea's astigmatism ($< 0.2\lambda$, see Table 5.5 and 5.6) is small compared to the astigmatism induced by lens tilt and shift (up to $> 2\lambda$, see e.g. Figure 5.13 for simulation and 5.39 for the corresponding measurement) and thus not negatively influencing the measurements.

Aberrations of order n=3
Due to the symmetry with respect the x–z–plane, $Z7$ and $Z9$ have to be zero, as these two coefficients are not symmetric with respect to the x–axis as it can be seen in Figure 3.16. This is the case in the simulations as well as in the measurement results. $Z10$ (oblique trefoil) is also zero in all lenses. $Z8$ (horizontal coma) is the only coefficient, were simulations and measurements deviate significantly for all IOLs, pupil diameters, tilts and decentrations. $Z8$ is increased in all measurements, which is in accordance to the positive coma of the PMMA cornea. This issue could be fixed by a properly fault free artificial cornea. Thus for analyzing the horizontal coma, only the simulations are meaningful: It can be seen that the aberration free IOL is more stable than the spherical and the aberration correcting IOL. Again a combination of positive shift and negative tilt is the most critical configuration.

High order aberrations n=4
Again, due to the symmetry, $Z13$ and $Z15$ have to be zero. This is also the case in the measurements, due to the fine scaling small deviations $< \frac{\lambda}{10}$ can be observed which is in the range of the sensor accuracy. $Z11$ (SA) is the most dominant high order aberration. The spherical lens has a constant high SA of 0.4λ at a 4.5 mm pupil. Here the aberration free lens with a constant SA of 0.2λ clearly shows the benefit of using aspheric lens surfaces. The SA is little increased for the aberration correcting lens at 4.5 mm iris diameter, but the eye with the aberration correcting IOL is by far the best corrected system at 3 mm iris diameter (see Table 5.4 in comparison to Table 5.2 and 5.3). Regarding the optical design of this lens, it makes sense to optimize for minimal SA at a pupil diameter of 3 mm, as humans experience best vision at photopic illumination (see Figure 2.2 and also Figure 5.1 vs. 5.2). Figure 5.24 and 5.25 reveal that with ongoing positive shift the aberration correcting IOL gains SA exceeding the aberration free IOL, but never gets worse than the constantly high SA of the spherical lens. The same systematic can also be found in the measurement results: For the centered position one finds $Z11 = 0.1\lambda$ for the spherical, $Z11 = 0.09\ \lambda$ for the aberration free and $Z11 = 0.07\ \lambda$ for aberration correcting IOL at photopic vision (Table 5.7, 5.9 and 5.11) and the similar characteristics for tilt and decentration (see Figure 5.48 for photopic and 5.49 for photopic vision for the aberration free IOL and Figure 5.58 and 5.58). In the simulations $Z12$ is only present at the aberration correcting IOL at extreme positive shifts, but only to a very moderate extent ($< 0.1\lambda$ at 3 mm iris diameter and $< 0.2\lambda$ at 4.5 mm iris diameter). In the measurements this systematic can be seen across all three lenses.

Conclusion and general observations

In general the aberration coefficients are approximately increased by factor 2 when the iris opens from 3 mm to 4.5 mm. Thus the bigger aperture, which in theory has the higher cut off frequency (Equation 3.56), has in total a worse optical imaging quality.

A systematic deviation between simulation and measurements can be seen for extreme shifts in positive directions at 4,5 mm iris diameter, especially for $n = 4$ where the coefficients start to increase for shifts approximately > 0.5 mm (see Figure 5.39, 5.49 and 5.59). This occurs due to the reason that the pupil is shifted by -0.5 mm and thus at extreme shifts the peripheral rays start to get vignetted as depicted in Figure 6.1. IOL stability in the lens holder requires that the IOL is supported on the outer 0.1 to 0.2 mm rim of the optics, thus this effect occurs at even smaller shifts than in the simulation. Vignetting, diffraction and scattering on the edge of the IOL–holder, cause high order aberration and decrease the accurateness of the Zernike polynomial fit.

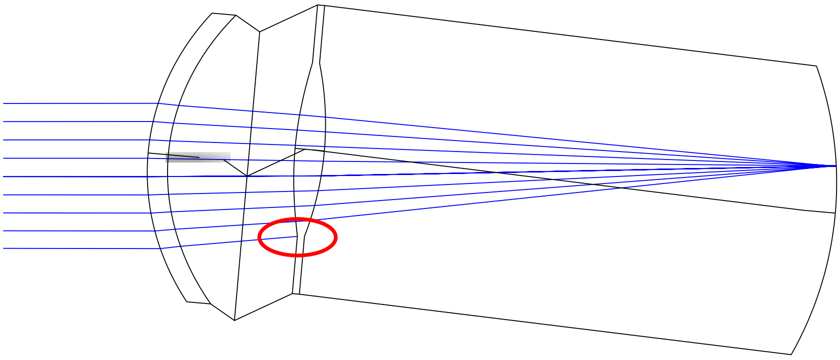

Figure 6.1: Simulated optical layout for the aberration free IOL at a shift of +0.6 mm. Red circle: The peripheral ray is outside optical diameter of the IOL, vignetting occurs.

In general the WF analysis reveals that in the centered position (especially at 3mm iris diameter) the aberration correcting IOL shows the best correction of geometric errors, but also has the most complex changes in the aberrations coefficients if the lens is not perfectly aligned. From that no direct conclusions on the visual performance can be drawn. Therefore the investigation of the MTF is useful, which considers all geometric errors in combination with diffraction effects.

6.2.2 Change in Vision Contrast induced by IOL–Displacements

As already discussed in Section 4.5, conclusions on the true visual impression can only be done by extensive clinical studies. To enable such work a device for demonstrating the visual impression by using the proposed model eye was developed and tested - see results in Section 5.3. This thesis' main goal is to present a new approach for characterizing IOLs by physical measures for better IOL–testing and possibly novel test standards. Which physical measure best represents the visual performance for the human is still an unanswered question. Thus for this investigation the contrast at $100\frac{\mathrm{lp}}{\mathrm{mm}}$ (as in the ISO 11979-2) is used for the analysis of the image contrast.

Central Position

In the simulations the contrast at $100\frac{\mathrm{lp}}{\mathrm{mm}}$ is 0.37 for photopic vision (P) and 0.17 for the scotopic vision (S) for the spherical IOL p. 80, 0.50 (P) / 0.25 (S) for the aberration free IOL p. 84 and 0.59 (P) / 0.38 (S) for the aberration correcting IOL p. 87, which reveals the clear benefit of an aberration correcting IOL in the central position.

This is in agreement with the observations derived from the WF measurements, which show: 0.32(P) 0.17 (S) for the spherical IOL p. 95, 0.45 (P) / 0.24 (S) for the aberration free IOL p. 101 and 0.50 (P) / 0.20 (S) for the aberration correcting IOL p. 107. At photopic vision the same trend for the contrast at the centered position with slightly worse values due to the additional aberrations from the PMMA–cornea can be observed. The trend is different for scotopic vision: The simulated configurations reveal negative coma for all lenses (Table 5.2, 5.3 and 5.4) which is partly compensated by the additional positive coma from the PMMA–cornea, but due to wide aperture all other additional aberrations deteriorate the total contrast.
A steady increase (from the spherical, the aberration free to the aberration correcting IOL) in the contrast values, for both photopic and scotopic vision, is visible in the MTF measurements from the MTF–setup (see results on p. 93, 5.41 and 5.51), but for photopic vision the absolute contrast values are below the results of simulation. This finding will be discussed in detail later on.

Another benefit of aberration correction can be seen in Table 5.1: In accordance to other literature[9, 14], the AL was adjusted to gain best focus. This can be criticized (see Section 6.3.1), as the eye would not change AL when the illumination changes from photopic to scotopic illumination. As depicted in Figure 3.6 SA causes a shift optimal focus when the aperture changes. Due to the almost full SA correction, the aberration correcting IOL would suffer the least if the AL would not be adapted, it only shows a focal shift of 3 μm. The spherical lens would suffer the most if the AL would not be adapted, as it shows the highest focal shift (46 μm).

Decentered Positions

For the spherical IOL the pattern is easy to analyze: Aberrations vanish with negative shifts and positive tilts (basically when the IOL aligns with the pupil center and the OA) only SA remains constant (see p. 83). Therefore, the contrast increases in the direction of negative shifts and positive tilts and exceeds the performance of the centered position (see Figure 5.10 and 5.11). As the horizontal coma effects the $\mathbf{MTF}_x$, this systematic is pronounced in the $\mathbf{MTF}_x$, whereas the $\mathbf{MTF}_y$ remains almost constant. As the coma is not represented correctly by the model eye, the measurements do not share this systematic (see p. 96-97). Again the direct MTF–measurements show a lower contrast than the contrast derived from the WF measurement.
The aberration free lens is closer to the diffraction limit, small geometric aberrations gain importance in the over all performance. The performance deteriorates in all directions with a maximum slightly off center (approximately at +1° and +0.15 mm) - see Figure

5.16. Only at the extreme positions, in combination of tilt and shift the contrast drops below the performance of the spherical lens. This can be also seen in the corresponding measurement (Figure 5.45). There is a rather poor match between simulation and measurements for scotopic vision. As outlined above a single coefficient ($Z8$) does not match. With the MTF the insight into the single aberrations get lost, thus (especially for wide open apertures) the MTF can severely change its shape only by changing a single aberration coefficient.
The increased optical performance of the aberration correcting IOL for photopic and scotopic illumination can be seen by comparing p. 85 and 88: Regardless of the tilt, the aberration correcting IOL is at least as good as the aberration free IOL; only for shifts beyond approximately ±0.3 mm the performance of aberration correcting lens drops below the other lenses. A shift of 0.3 mm is about the usual mean postoperative shift reported in literature as outlined in Section 2.2. Comparing the corresponding measurements for photopic vision (Figure 5.45 and 5.55) also reveals this systematic: equal or increased optimal performance of the aberration correcting lens compared to the aberration free lens, regardless of the tilt, but a decreased optical performance at extreme decentrations.

6.3 Remarks on the Methodological Approach and Experimental Setup

Remarks on the evaluation method and suggested improvements on the experimental setup were found during research for this project which will be discussed in this section:

6.3.1 Refocusing Between Changed Configurations

It has to be mentioned that in the measurement procedure, as mentioned before, the focus (AL of the eye) is only adapted once in the central position. This is also done in other work[9]. One problem with this procedure is, as it can be seen from the WF-results, that an IOL displacement can lead to a defocus ($Z4$). Since conventionally in clinical practice, the remaining refractive error is corrected by spectacles some weeks after the surgery, defocus induced by postoperative displacements will be corrected with the glasses. Regarding a study where a drop in optical performance was observed when the IOL is shifted within the eye, Norrby et al.[14] stated: *"This can be explained by the fact that they did not refocus the system for the defocus caused by decentration. In clinical practice the patient is refracted to find the best spectacle correction whether the IOL is decentered or not. To best mimic the clinical situation, calculations should be made at best focus."* Refocusing for each tilt end shift position is not done in this work, against the suggestion from Norrby et al. This can be argued since modern ophthalmology with steadily increasing methods for biometry [58] aims optimal refractive outcome after cataract surgery without the need for spectacles. Thus lenses robust against defocus when the lens is shifted are beneficial, and thus should be tested for that. This procedure is also chosen by others[9]. Consequently the eye should not be refocused between changing from photopic to scotopic illumination. In this work this had to be done, since changing the aperture requires removing and re-assembling the "tilt– and shift–unit". After such manipulations on the model eye refocusing is required to get reproducible results. Norrby et al. [14] also refocused between changing the illumination. They stated: *"It could perhaps be argued that refocusing for defocus caused by different pupil sizes, as we have done in this paper, should not be applied, because the refraction given to a patient is obtained with the pupil size induced by the illumination in the examination room. The focusing criterion used should at any rate be clearly stated. However, it remains an open question which focusing criterion best represents human visual preference."*[14].

6.3.2 Image Formation in the Fovea

Simulating the Liou and Brennan [16] eye reveals that the optical performance rapidly drops with the distance from the fovea along the retina plane, similar to the systematic shown in Figure 2.2. It is known, that also the retinal sampling (density of cones) rapidly drops with the distance from the fovea[22]. Postoperative shifts of the IOL causes a shift central ray on the fovea. A lens shift of 0.5 mm causes a shift of the image on the retina of approximately 0.2 mm. Therefore the image would be projected on a spot on the retina, which does not show the maximal cone density, and thus cause possible retinal undersampling. It can be speculated that the human eye would compensate for that by counter-rotating the eye ball, to focus to the image center back onto the the fovea. This would change the visual axis by about 1° at an IOL displacement of 0.5 mm. Despite the fact that the tilt between the visual and optical axis individually varies among individuals[16], the described effect could lead to a systematic change in the visual axis, but no reports on that specific issue could be found in literature. It is suggested that this effect should be considered in further analysis, and incorporated into further analysis, if evidence can be found for this effect.

6.3.3 Setup for Measurement of the Modulation Transfer Function

The measurements from the MTF–setup show a considerably lower MTF compared to the MTF reconstructed from WF measurements. Despite the fact that the same optical system is analyzed (same model eye + IOL), there are some facts which explain the divergence between MTF and WF measurements:

- Since only the $\mathbf{MTF}_x$ can be measured in the MTF–setup, the AL was adjusted by finding the maximal $\mathbf{MTF}_x$ at $100\frac{\text{lp}}{\text{mm}}$, for the simulations and WF–measurements the $\mathbf{MTF}_{mean}$ was optimized to prevent sacrificing the $\mathbf{MTF}_y$–contrast in preference to $\mathbf{MTF}_x$.

- The model eye is the same in both setups, but held on different pedestals in both setups. Production tolerances can lead to different alignments of the model eye within the setup.

- The slanted edge method uses the information from multiple image lines. Thus it does not strictly measure the aberrations from a single (central) image point as the WF–setup.
- The microscope objective for capturing the retinal image can include further aberrations.

Regarding the last point, the microscope objective with $NA = 0.15$ is sufficient not to add additional relevant diffraction, but further analysis, based on a black–box model which was requested from the manufacturer after the measurements, revealed that the lens is not corrected to its diffraction limit. Furthermore, due to the tilt of the visual axis of the model eye, the rear retina–window is tilted by 5° to the OA resulting in a tilted light cone exiting the model eye, which is beyond the lens' NA, and also further asymmetric geometric aberrations are induced – see Figure 6.2 for an illustration.

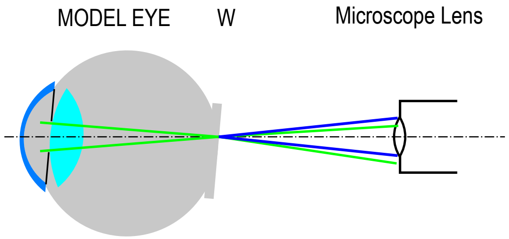

Figure 6.2: Light cone alignment in the MTF–setup. Green: Light cone of the model eye. For constructive reasons the window (W) is tilted with respect to the visual axis and the OA of the microscope lens, thus the output light cone is refracted off axis. Blue: The microscope lens in theory has a sufficient NA, but not aligned with the output light cone. As the output light cone angle changes with IOL tilt and shift, the microscope can not be aligned with the eye for the full measurement sequence. Thus image aberrations are induced by the microscope system.

Only microscope lenses with a high working distance can be used, to prevent mechanical interference with the model eye. As shown above, a slightly higher NA would be useful for the setup, but increasing the NA to 0.21 would dramatically increase the price to about 10 times the cost for the lens used. As the unidirectional slanted edge MTF measurement does not provide information on the type of aberration and directional dependency of the optical performance, the MTF characterization is not the preferential method.

6.3.4 Setup for Wavefront Characterization

The single–pass 2 setup delivers measurements which are in good agreement with the simulated data. The component L1 (Figure 4.15) is the most critical one, and the theoretical maximal production tolerance could severely influence the results. For the high order aberrations at some IOLs there is considerable noise visible in the polynomial fit. With a slightly higher focal length for L1, a larger fraction of the WFS sensor–area could be filled, resulting in a higher accuracy and more reliable fit of the Zernike polynomial. Unfortunately no better choice for the lens was available at the time of constructing the setup.

As already outlined in a previous publication [21] the single single–pass 1 setup would bring further improvements, if single mode fibers with a sufficient NA would be available.

Order of Zernike polynomials: As already outlined in Section 3.6.3, literature [114, 113] gives evidence, that coefficients up to the 4th order are sufficient to obtain an accurate description of common aberrations in the human eye. Thus this order was also used in the measurement procedure. Other references e.g. Carvalho [134] suggest that polynomials up to the 7th order can be necessary, whereby it has to be mentioned that this is reported for keratoconus, or after keratoplasty. As discussed in Section 6.2.1, the measured coefficients are getting noisy at the 4th order and are, in their magnitude, in the range of the sensor accuracy. Therefore a measurement of higher order coefficients is not possible with the current setup. Further divergence between the results from the MTF and the WF setup can thus arise from the possibility of imperfections of the cornea and IOL induce higher order aberrations which are not captured by the limited polynomial order of the measured WF coefficients. From a theoretical point of view the Zernike polynomial fit errors were simulated for the aberration correcting IOL in Table 6.1. It can be seen that the fitting only to the 3rd order is insufficient due to the high fit error compared to the absolute RMS error. The problem is not as severe for the other IOLs. This corresponds to the observation when comparing Table 5.2 and 5.4, which shows that simpler lens designs have higher low order aberrations values, but smaller aberration coefficients for high order aberrations.

Table 6.1: Zernike fit error for the aberration correcting IOL at isotopic illumination. The true RMS value is 0.73λ (see Figure 5.21).

Highest order	Number of coefficients	RMS fit error
3rd	10	0.30λ
4th	15	0.11λ
5th	21	0.06λ
6th	28	0.01λ

6.3.5 Applicability to other Lens Designs

In this thesis only monofocal IOLs were tested, as these are the majority of the implanted lenses. As discussed in Section 2.2, many lens design types exist. Testing toric IOLs would be possible without further modifications. But meaningful results could only be obtained if the cornea is replaced by an astigmatic cornea, which matches the astigmatism that should be corrected by the IOL. Due to the experience with manufacturing difficulties of the current lens, the lens manufacturing could prohibit the practical feasibility.

Regarding multifocal IOLs the WF–setup can not be used at all, as outlined above. The ability of measuring Zernike coefficients up to the order $n = 4$ is the lower limit to obtain meaningful results for current monofocal IOLs. WF–shapes of multifocal IOLs are much more complex[135], characterization seems to be difficult with current WF sensing technologies.

Calatayud et al. [136] used similar components, as used in this thesis for assessing the MTF (Camera + 5× microscope objective). Using this image forming approach is useful to characterize multifocal IOLs: *"Contrary to most of the commercially available setups, our system allows the measurement of diffractive MIOLs*[1] *because, instead of using Hartmann-Shack or interferometric principles, it is based on an image forming setup."*[136]. Also earlier studies show the characterization of multifocal IOLs by means of image forming approach[137]. Under consideration of the remarks on the MTF–setup mentioned above, the MTF–setup currently would be the most promising approach for characterization of multifocal IOLs, also because the classical aberration theory of geometric errors as outlined in Section 3.3 does not apply well to the working principle of multifocal IOLs.

6.4 Conclusion – Contribution to the Field

Concluding the following main findings could be achieved in this thesis which are a relevant contribution to the current state–of–the–art testing of the optical performance of monofocal IOLs regarding their tolerance to postoperative displacements.

- A model eye could be developed which closely represents the human physiology, with an automatic tilt and shiftable holder for the IOL postoperative lens tilts and decentrations can be simulated. Current literature does not provide similar solutions.
- In contrast to the cited papers which only simulate or only measure how postoperative displacements deteriorate the optical performance, in this thesis the same lenses are investigated by both methods. This give a unique insight on the difference between simulated and measured results.
- It could be demonstrated that the model eye is compatible to direct MTF–measurements as suggested by the current standard (ISO 11979-2); that WF–aberrations can be measured and that the model eye's retina could even be projected onto the retina of a healthy proband to investigate the full visual process (physical image formation plus the human perception)
- WF–aberration delivers insight into individual types of aberrations. The observed measurements are in good agreement with simulation, except for the coma–term, which is corrupted by a flaw in the model cornea.

---

[1] multifocal IOLs

- All investigations were done on three different design concepts for IOLs. The lenses showed unique characteristics which are difficult to compare. In Section 5.4 the results from each lens were summarized in a single quality measure, which incorporates the lenses tolerance to displacements. The proposed measurement method reveals the same ranking of the lenses quality measure as predicted from simulations.

With that, future cataract treatment can profit from this work, as lens designs cannot only be evaluated in simulations, but also can objectively be analyzed in a model eye. This enables tasks as quality assurance or can even contribute to enhance the current test standard.

6.5 Outlook

Results of this thesis suggest that monofocal lenses, which are currently the majority of implanted lenses, should be characterized by WF–aberrations. In contrast to the simpler MTF–measurement required by the test standard, the knowledge of the type of aberration provide a deeper insight on the proper function of an IOL. Using WF–characterizations, links the field of IOL–testing to other work conducting clinical trails to investigate the visual perception of different aberrations by humans. Especially if physiological asymmetrical and asymmetric IOL-tilts and shifts should be analyzed, the simple ISO-model and characterization by a single contrast-value is only an insufficient characterization. Though photopic illumination is the most important, findings of this thesis also suggest that scotopic illumination should be investigated, which is not the case in the current standard. Further work will include detailed research on optimizing the artificial cornea, to fit possibilities of small-batch custom lens manufacturing. This would eliminate the last disparities between simulated and measured results. With that, the proposed method is a useful enhancement to the current test standard for IOLs.

APPENDIX A

Conversion Error in the ISO 11979–2:2014

In the current version of the ISO 11979–2, a wrong conversion value between $\frac{\text{lp}}{\text{degree}}$ in the object space and $\frac{\text{lp}}{\text{mm}}$ on the retina for the normal human eye is given. This mistake was discovered during research for this thesis. The correspondence with the responsible authority is attached in the following pages. The responsible ISO–group approve it as a mathematical inaccuracy, the value will be adapted in the next version of the standard.

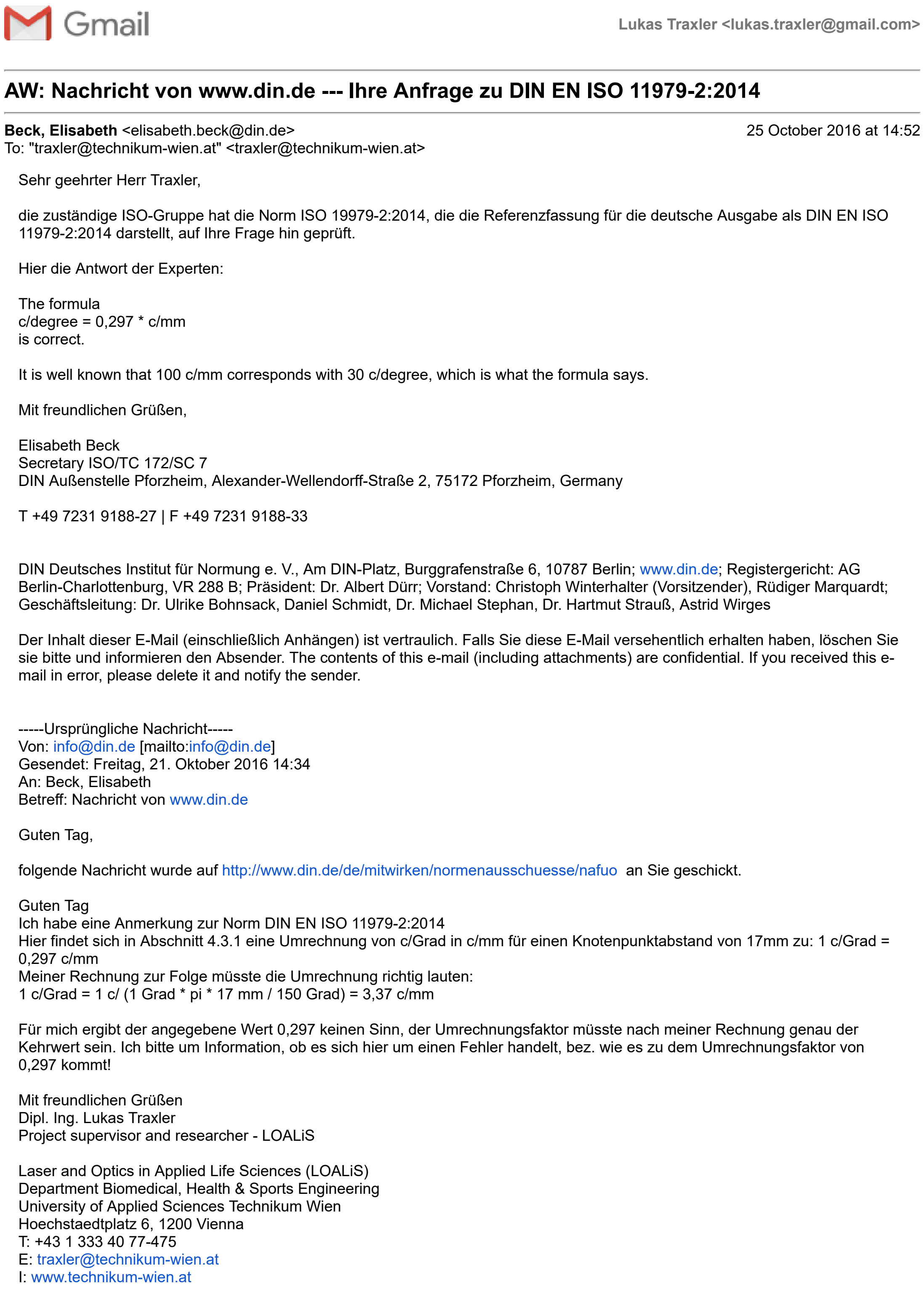

Gmail

Lukas Traxler <lukas.traxler@gmail.com>

AW: Nachricht von www.din.de --- Ihre Anfrage zu DIN EN ISO 11979-2:2014

Beck, Elisabeth <elisabeth.beck@din.de>
To: "traxler@technikum-wien.at" <traxler@technikum-wien.at>

25 October 2016 at 14:52

Sehr geehrter Herr Traxler,

die zuständige ISO-Gruppe hat die Norm ISO 19979-2:2014, die die Referenzfassung für die deutsche Ausgabe als DIN EN ISO 11979-2:2014 darstellt, auf Ihre Frage hin geprüft.

Hier die Antwort der Experten:

The formula
c/degree = 0,297 * c/mm
is correct.

It is well known that 100 c/mm corresponds with 30 c/degree, which is what the formula says.

Mit freundlichen Grüßen,

Elisabeth Beck
Secretary ISO/TC 172/SC 7
DIN Außenstelle Pforzheim, Alexander-Wellendorff-Straße 2, 75172 Pforzheim, Germany

T +49 7231 9188-27 | F +49 7231 9188-33

DIN Deutsches Institut für Normung e. V., Am DIN-Platz, Burggrafenstraße 6, 10787 Berlin; www.din.de; Registergericht: AG Berlin-Charlottenburg, VR 288 B; Präsident: Dr. Albert Dürr; Vorstand: Christoph Winterhalter (Vorsitzender), Rüdiger Marquardt; Geschäftsleitung: Dr. Ulrike Bohnsack, Daniel Schmidt, Dr. Michael Stephan, Dr. Hartmut Strauß, Astrid Wirges

Der Inhalt dieser E-Mail (einschließlich Anhängen) ist vertraulich. Falls Sie diese E-Mail versehentlich erhalten haben, löschen Sie sie bitte und informieren den Absender. The contents of this e-mail (including attachments) are confidential. If you received this e-mail in error, please delete it and notify the sender.

-----Ursprüngliche Nachricht-----
Von: info@din.de [mailto:info@din.de]
Gesendet: Freitag, 21. Oktober 2016 14:34
An: Beck, Elisabeth
Betreff: Nachricht von www.din.de

Guten Tag,

folgende Nachricht wurde auf http://www.din.de/de/mitwirken/normenausschuesse/nafuo an Sie geschickt.

Guten Tag
Ich habe eine Anmerkung zur Norm DIN EN ISO 11979-2:2014
Hier findet sich in Abschnitt 4.3.1 eine Umrechnung von c/Grad in c/mm für einen Knotenpunktabstand von 17mm zu: 1 c/Grad = 0,297 c/mm
Meiner Rechnung zur Folge müsste die Umrechnung richtig lauten:
1 c/Grad = 1 c/ (1 Grad * pi * 17 mm / 150 Grad) = 3,37 c/mm

Für mich ergibt der angegebene Wert 0,297 keinen Sinn, der Umrechnungsfaktor müsste nach meiner Rechnung genau der Kehrwert sein. Ich bitte um Information, ob es sich hier um einen Fehler handelt, bez. wie es zu dem Umrechnungsfaktor von 0,297 kommt!

Mit freundlichen Grüßen
Dipl. Ing. Lukas Traxler
Project supervisor and researcher - LOALiS

Laser and Optics in Applied Life Sciences (LOALiS)
Department Biomedical, Health & Sports Engineering
University of Applied Sciences Technikum Wien
Hoechstaedtplatz 6, 1200 Vienna
T: +43 1 333 40 77-475
E: traxler@technikum-wien.at
I: www.technikum-wien.at

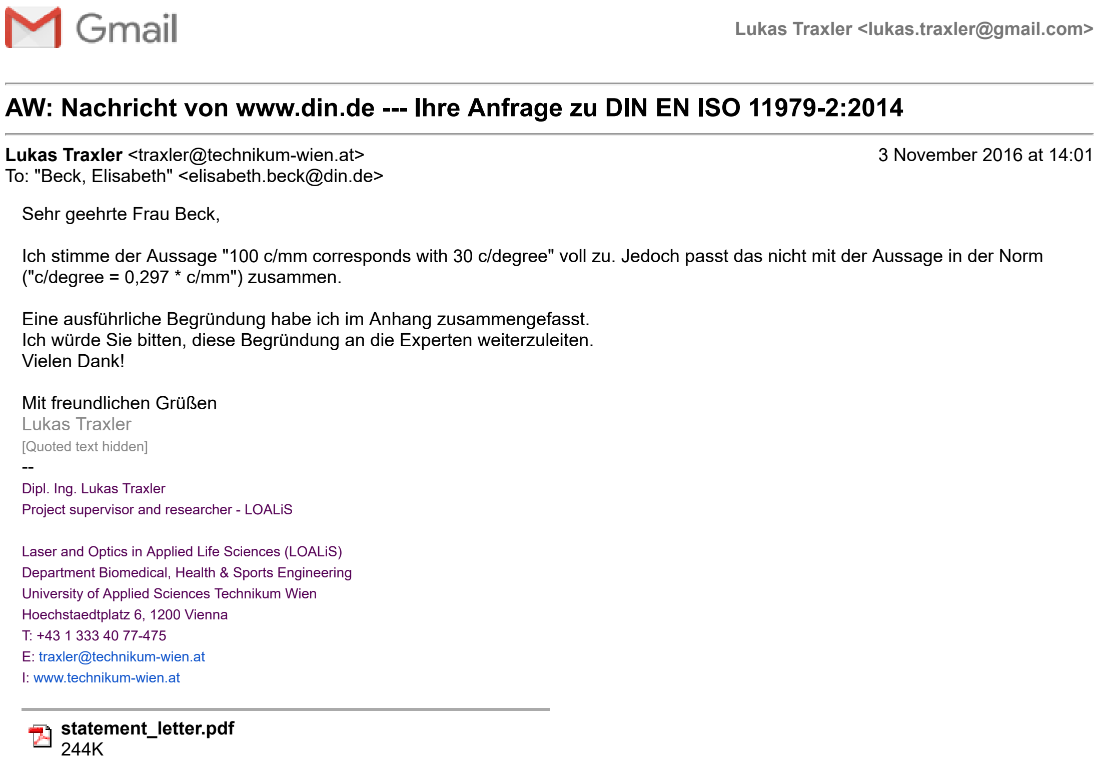

Gmail

Lukas Traxler <lukas.traxler@gmail.com>

AW: Nachricht von www.din.de --- Ihre Anfrage zu DIN EN ISO 11979-2:2014

Lukas Traxler <traxler@technikum-wien.at>
To: "Beck, Elisabeth" <elisabeth.beck@din.de>

3 November 2016 at 14:01

Sehr geehrte Frau Beck,

Ich stimme der Aussage "100 c/mm corresponds with 30 c/degree" voll zu. Jedoch passt das nicht mit der Aussage in der Norm ("c/degree = 0,297 * c/mm") zusammen.

Eine ausführliche Begründung habe ich im Anhang zusammengefasst.
Ich würde Sie bitten, diese Begründung an die Experten weiterzuleiten.
Vielen Dank!

Mit freundlichen Grüßen
Lukas Traxler
[Quoted text hidden]
--
Dipl. Ing. Lukas Traxler
Project supervisor and researcher - LOALiS

Laser and Optics in Applied Life Sciences (LOALiS)
Department Biomedical, Health & Sports Engineering
University of Applied Sciences Technikum Wien
Hoechstaedtplatz 6, 1200 Vienna
T: +43 1 333 40 77-475
E: traxler@technikum-wien.at
I: www.technikum-wien.at

statement_letter.pdf
244K

FH University of Applied Sciences
TECHNIKUM
WIEN

Subject:
Statement to the answer regarding conversion between c/degree and c/mm in ISO 19979-2:2014

Dear experts,

Via an e-mail from “DIN-Normenausschuss Feinmechanik und Optik (NAFuO)” on October 25th I received following answer regarding my question to the conversion between c/degree and c/mm in ISO 19979-2:2014:

> “The formula
> c/degree = 0,297 * c/mm
> is correct.
>
> It is well known that 100 c/mm corresponds with 30 c/degree, which is what the formula says.”

I totally agree with the statement: „100 c/mm corresponds with 30 c/degree“, but not with the statement: „which is what the formula says“.
If „corresponds with“ is replaced with a mathematical „is equal to“ the statement says:

100 c/mm = 30 c/degree

Dividing both sides of this formula by 30 we get:

1 c/degree = 3,33 * c/mm

This is not the formula of the standard.

Here I send again my calculation with the 17mm as given in the standard:

$$1\frac{c}{\circ} = 1\frac{c}{1^\circ\cdot\frac{\pi\, rad}{180^\circ}} = 57{,}3\frac{c}{rad} = 57{,}3\frac{c}{17\frac{mm}{rad}rad} = 3{,}37\frac{c}{mm}$$

$$0{,}297\frac{c}{\circ} = 1\frac{c}{mm}$$

This calculation is consistent with the statement „100 c/mm corresponds with 30 c/degree“ but not with the formula in the standard.

Another way of interpreting the formula in the standard: “c/degree = 0,297 * c/mm” is done here. If both sides of the equation are divided by 0,297 * c/mm we get:

$$1 = \frac{1\ c/degree}{0{,}297\ \mathrm{c/mm}}$$

When applied to 100 c/mm we get:

$$100\ c/mm = 100\ c/mm \cdot 1 = 100\cancel{c/mm}\cdot\frac{1\ c/degree}{0{,}297\ \cancel{\mathrm{c/mm}}} = 337\ c/degree$$

As demonstrated, the formula in the standard leads to a wrong result (30 c/degree would be correct).

I also looked up how unit-conversions are done in other standards, exemplary I took the ISO 80000-3 (see attachment on the next page). For conversion between mm and inch it is written:

$$1\, in\ \coloneqq\ 25{,}4\, mm$$

In analogy to this the unit conversion in ISO 19979-2:2014 should be:

$$1\frac{c}{degree} := 3{,}37\frac{c}{mm}$$

As stated above I am aware of the fact that „100 c/mm corresponds with 30 c/degree“ but I hope this explanations clarifies why I am convinced that the statement “c/degree = 0,297 * c/mm” in the ISO 19979-2:2014 is incorrect.

As I notice some inconsistences in MTF-plots in scientific publications, which may arise from wrong unit conversion, I think that a clarification in the standard would contribute to less confusion and better scientific work in this field of research.

Best Regards
Lukas Traxler
Project supervisor and researcher - LOALiS
Laser and Optics in Applied Life Sciences (LOALiS)
Department Biomedical, Health & Sports Engineering
University of Applied Sciences Technikum Wien
Hoechstaedtplatz 6, 1200 Vienna
T: +43 1 333 40 77-475
E: traxler@technikum-wien.at
I: www.technikum-wien.at

Attachment: excerpt from ISO 80000-3

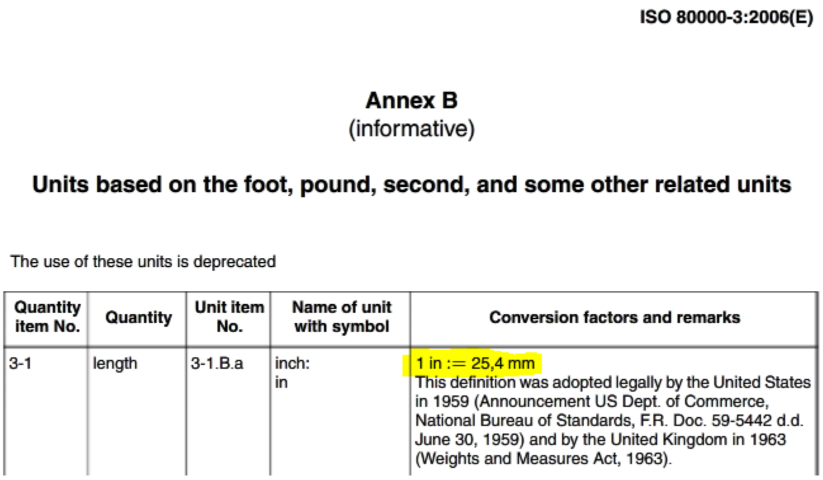

ISO 80000-3:2006(E)

Annex B
(informative)

Units based on the foot, pound, second, and some other related units

The use of these units is deprecated

Quantity item No.	Quantity	Unit item No.	Name of unit with symbol	Conversion factors and remarks
3-1	length	3-1.B.a	inch: in	1 in := 25,4 mm This definition was adopted legally by the United States in 1959 (Announcement US Dept. of Commerce, National Bureau of Standards, F.R. Doc. 59-5442 d.d. June 30, 1959) and by the United Kingdom in 1963 (Weights and Measures Act, 1963).

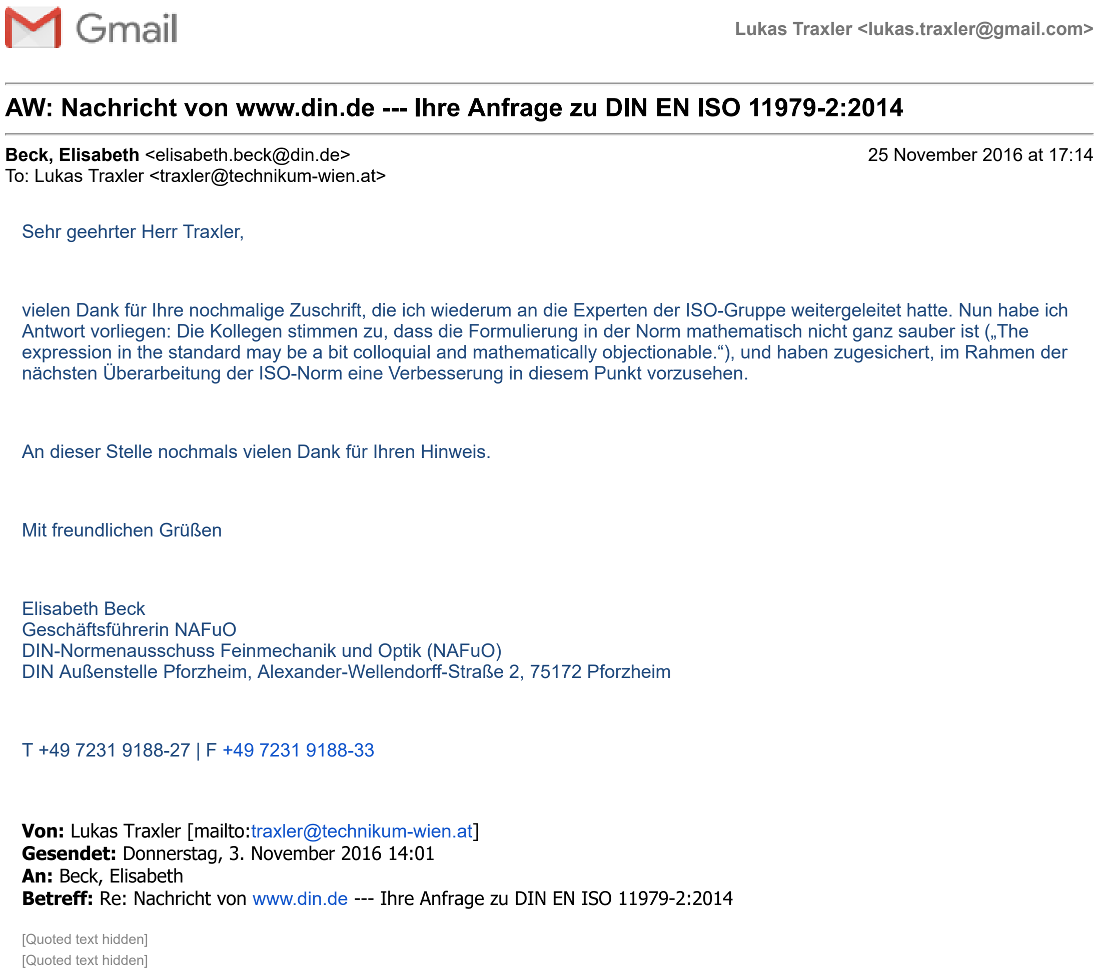

Gmail

Lukas Traxler <lukas.traxler@gmail.com>

AW: Nachricht von www.din.de --- Ihre Anfrage zu DIN EN ISO 11979-2:2014

Beck, Elisabeth <elisabeth.beck@din.de>
To: Lukas Traxler <traxler@technikum-wien.at>

25 November 2016 at 17:14

Sehr geehrter Herr Traxler,

vielen Dank für Ihre nochmalige Zuschrift, die ich wiederum an die Experten der ISO-Gruppe weitergeleitet hatte. Nun habe ich Antwort vorliegen: Die Kollegen stimmen zu, dass die Formulierung in der Norm mathematisch nicht ganz sauber ist („The expression in the standard may be a bit colloquial and mathematically objectionable.“), und haben zugesichert, im Rahmen der nächsten Überarbeitung der ISO-Norm eine Verbesserung in diesem Punkt vorzusehen.

An dieser Stelle nochmals vielen Dank für Ihren Hinweis.

Mit freundlichen Grüßen

Elisabeth Beck
Geschäftsführerin NAFuO
DIN-Normenausschuss Feinmechanik und Optik (NAFuO)
DIN Außenstelle Pforzheim, Alexander-Wellendorff-Straße 2, 75172 Pforzheim

T +49 7231 9188-27 | F +49 7231 9188-33

Von: Lukas Traxler [mailto:traxler@technikum-wien.at]
Gesendet: Donnerstag, 3. November 2016 14:01
An: Beck, Elisabeth
Betreff: Re: Nachricht von www.din.de --- Ihre Anfrage zu DIN EN ISO 11979-2:2014

[Quoted text hidden]
[Quoted text hidden]

APPENDIX B

Cornea 2 Surface Measurements

On the following two pages the measurement protocols of the artificial PMMA cornea, which was used for the experiments in this thesis, are given.

Form Error(Radius
Optimised)

②+

Cornea_PMMA R7.18 2

10:57 10 Nov 2017

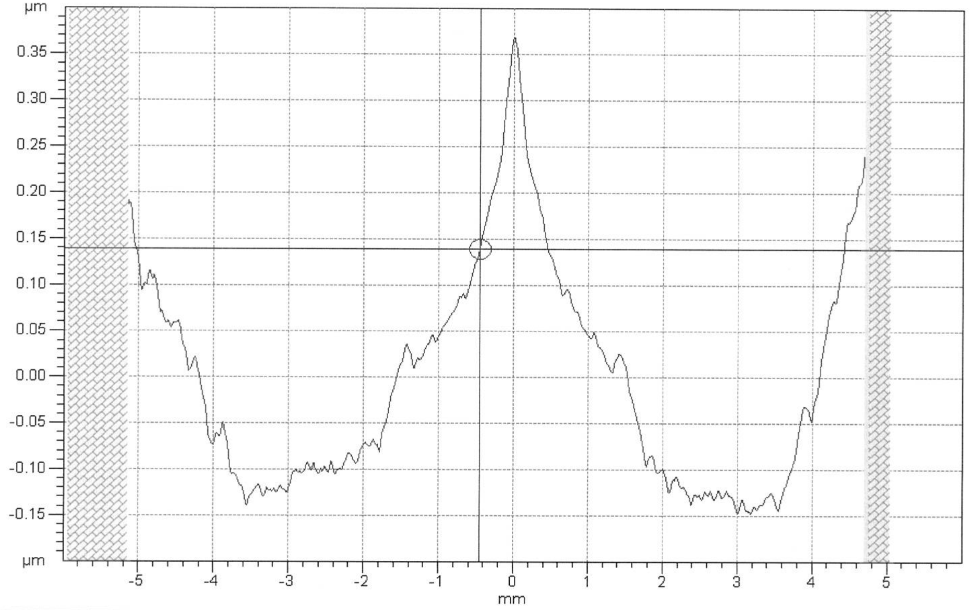

Fig	0.3669	µm	Pa	0.1016	µm	Pt	0.5159	µm
Smn	0.015	°	Smx	0.066	°	Tilt	-0.035	°
Xp	9.4104	µm	Xv	3.1800	mm	Xt	5.6649	mm
RMS	0.1201	µm						

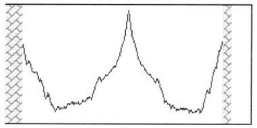

Coefficients	
A01	0.0000000
A02	0.0000000
A03	0.0000000
A04	0.0000000
A05	0.0000000
A06	0.0000000
A07	0.0000000
A08	0.0000000
A09	0.0000000
A10	0.0000000
A11	0.0000000
A12	0.0000000
A13	0.0000000
A14	0.0000000
A15	0.0000000
A16	0.0000000
A17	0.0000000
A18	0.0000000
A19	0.0000000
A20	0.0000000
Conic Form Settings	
Base Radius	7.19179mm
Conic Constant	-0.346048
Shape	Concave
Manual Scaling	
X-Clear Aperture	0.000mm
Lambda S Filter Settings	
Cut Off	0.08
Radius Optimisation Settings	
Original Radius	7.19179mm

Page 1

10 November 2017 : 10:57

Form Error(Radius Optimised)

②+

Cornea_PMMA R7.77 2

11:04 10 Nov 2017

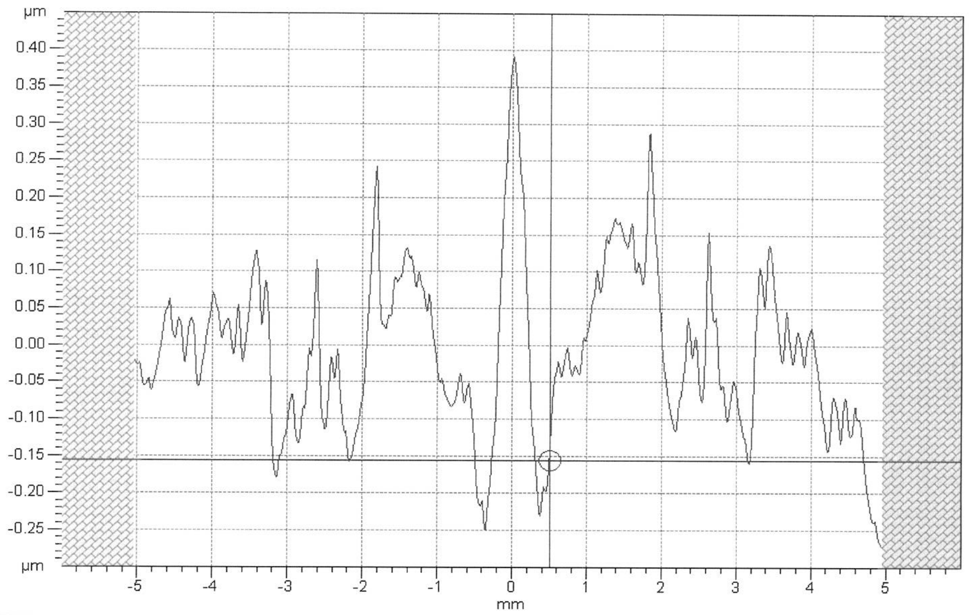

Fig	0.3857	µm	Pa	0.1111	µm	Pt	9.6759	µm
Smn	0.118	°	Smx	18.243	°	Tilt	0.059	°
Xp	5.2360	mm	Xv	5.1241	mm	Xt	5.7890	mm
RMS	0.3436	µm						

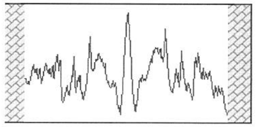

Coefficients	
A01	0.0000000
A02	0.0000000
A03	0.0000000
A04	0.0000000
A05	0.0000000
A06	0.0000000
A07	0.0000000
A08	0.0000000
A09	0.0000000
A10	0.0000000
A11	0.0000000
A12	0.0000000
A13	0.0000000
A14	0.0000000
A15	0.0000000
A16	0.0000000
A17	0.0000000
A18	0.0000000
A19	0.0000000
A20	0.0000000
Conic Form Settings	
Base Radius	7.77233mm
Conic Constant	-180.0000000e-3
Shape	Convex
Manual Scaling	
X-Clear Aperture	0.000mm
Lambda S Filter Settings	
Cut Off	0.08
Radius Optimisation Settings	
Original Radius	7.77000mm

Page 1

10 November 2017 : 11:05

List of Figures

1.1 This graphic depicts the coordinate system for the eye, which is used throughout this thesis: All simulations, models and measurements describe a right eye. The z–axis corresponds to the OA, where the light propagation direction is the $z+$ as defined by DIN 1335 [17]. The x–axis is the left to right coordinate and the y–axis defines the inferior-superior coordinate. φ θ and ψ are the respective right–handed rotations around the $x-$, $y-$ and $z-$axis. Image adapted from [18] 4

2.1 Anatomical structure of the human eye. Image used with permission from [1] 6
2.2 Accurateness of human vision. Thick line depicts the accurateness of vision for photopic vision with respect to the visual field angle. Thin line represents the accurateness for scotopic vision. The plot reveals that the maximal visual accurateness is only possible in bright illumination (photopic view) and in the fovea, the spot on the retina with the highest density of cones. The accuracy quickly drops down in the peripheral field of view. The gray bar represents the location of the blind spot. Data source for image: [22] 7
2.3 Schematic drawing of the model eye according to Liou and Brennan (see Table 2.1 for parameter values) [16]. E is the virtual image of the pupil center through the cornea; E' is the virtual image of the pupil center through the crystalline lens. Note: In contrast to all other simulations and models in this thesis this figure depicts a left eye 8
2.4 IOL haptic types: Three piece IOL are made of three pieces, where the material of the optics and the haptics can be different. Haptics can be L or C -shaped. One–piece IOLs are made of one material, haptics can have fingers. Graphics adapted from [70] 13
2.5 model eyes according to ISO 11979-2:2014 a) "model eye 1"; b) "model eye 2". 1.A model cornea: achromat with a minimal spherical aberration, 1.B model cornea with a known spherical aberration; 2: glass windows, 3: liquid medium in which the IOL is embedded. A refractive index of 1.2336 (refractive index of water) is specified, 4.A spherical IOL which is tested within the model eye. 4.B aspherical IOL which is tested within this model eye should counterbalance the aberrations of the model cornea 1.A, Image source: adapted from [12] 15

3.1 Analogy between ray and wave optics in a simple imaging system: Object point P emits light in all directions, drawn as straight light ray, since the light propagation in all directions in the homogeneous medium with the refractive index n_A is the same, the planes of constant phase (the WF) are concentric around P. When the light hits the lens, which has a higher refractive index n_L, the light rays are refracted. Light propagation is slower in the lens, thus the planes of constant phase are closer to each other. Behind the second lens surface light is refracted again. The rays converge to the image point P', as P' is the geometric intersection of all light rays emerging from the object point P. 22

3.2 Definition of the cardinal points and planes: a) The principal planes H and H' are defined as the planes of effective refraction of an optical system. Between H and H' there is a horizontal ray propagation. b) A point source located in the object sided focal plane F produces parallel rays on the image side of the optical system. c) parallel rays entering the optical system on the object side intersect in a single point in the image sided focal plane F'. 25

3.3 An ideal imaging system focuses incoming parallel rays to a single spot at (location O). If an imaging system is out of focus, the image is either captured too close at H or too far at M, the object point P is not projected to a single point P' but to a blurred spot. The size of the blurred spot is proportional to the amount of defocus and the aperture of the system, the y–axis extension of the light rays. 27

3.4 a) Detail view from Figure 3.3: Light is focused to the point O, which can be seen as the source of a spherical wave. Thus WFs are spheres around O. Since WFs have a constant phase along the WF, theses spheres also have an equal OPL to the object P. At M (red line) the axial rays have not yet traveled the same OPL as the peripheral rays. Compared to the peripheral rays they have a negative phase difference $\Delta\Phi$. b) Phase difference $\Delta\Phi$ as a function of the distance from the OA 27

3.5 Defocused optical system under consideration of an inverse ray direction. In the optical system of Figure 3.3, a point source is placed in the off–focus location M. Compared to a point source in O the spherical WF around M has a bigger radius of curvature at the location of the lens than a spherical wave around O. Thus the wave is divergent in the object space. The WF in the object space (normals to the rays) reveals the same shape as the deliberations in Figure 3.4 28

3.6 SA generated by a spherical lens: The focal length is shorter for rays with wide aperture (W), than for the paraxial rays (P). At an optimal distance, a minimal spot size can be obtained (O). The smaller the aperture the closer the position O is to the paraxial position P. 29

3.7 Positive SA shows a stronger refractive power for peripheral rays than for paraxial rays. If a point source is located in the optimal location O (see Figure 3.6 for explanation) intermediate rays are parallel in the object space. Wide aperture rays are refracted stronger than intermediate rays, resulting in divergent rays as in the case of a defocus. Axial rays are refracted weaker than intermediate rays, which results in convergent rays. The rotationally symmetric shape of the phase difference $\Delta\Phi$ to the ideal plane WF is depicted on the left. 29

3.8 The object point P emits rays in all directions, exemplary a light bundle in the x-z–plane (red) and in the y-z–plane (blue) is drawn. The imaging system has different focal lengths for along the x and y direction. At the location X the x-z bundle is focused to a single spot. y-z ray bundle is defocused. Thus the image of P is a line elongated along the y–axis. At the location O the minimal spot size can be found, but both directions are out of focus. Y is the same systematic as in X but with flipped coordinates. There is no location where a single image point P' can be obtained. 30

3.9 The WF deformation $\Delta\Phi$ is not rotationally symmetric for the astigmatism. It has the shape of a defocus in one direction, and the shape of an inverted (negative) defocus in the orthogonal direction. 30

3.10 An optical system showing comatic aberration has, like a system with SA, different refractive power in the periphery than in the center of the lens. Additionally it induces a deflection of the ray bundle. The second effect also increases for peripheral rays. The figure depicts three parallel ray bundles, red green and blue with increasing distance to the center. The red bundle behaves nearly like an aberration free system. With increasing distance to the center (green and blue), the rays are not focused onto one spot but defocused across a circular area, additionally the blurred circles are shifted off center. 31

3.11 The WF deformation $\Delta\Phi$ is analyzed in in two separate directions for a point source in O. y–z ray fan: The paraxial rays are not aberrated (parallel rays to the OA on the left side). For the positive y–direction the rays show the divergent appearance of the a negative defocus, in the negative y–direction rays are convergent as for the defocus. x–z ray fan: For $y = 0$ the rays are not aberrated. This is the boundary between the segment with positive and the segment with negative defocus. 32

3.12 Diffraction limited image of an ideal lens: An ideal plane wave, which has an infinite extent in the x–y direction propagates towards an ideal lens, which is free from geometric image aberrations. The finite aperture, in this case a circular aperture with the diameter D, reduces the spatial extent of the plane wave – diffraction occurs. Diffraction, see text for the mathematical analysis, results in an electric field distribution which is proportional to the Fourier transform of the aperture (blue). The intensity is proportional to the square (red). The Point image extends over a circle with the radius of $1.22\frac{\lambda f}{D}$ . . 36

3.13 An ideal imaging system focuses incoming parallel rays to a single spot at (location O). If an imaging system is out of focus, the image is either captured too close at H or too far at M, the object point P is not projected to a single point P' but to a blurred spot. The size of the blurred spot is proportional to the amount of defocus and the aperture of the system, the y–axis extension of the light rays. 37

3.14 Example for an image formation from multiple points: a) Exemplary the PSF under presence of defocus and astigmatism is shown. Due to the astigmatism the PSF is broader in x–direction. b) The object consists of three prefect points, having the same distance in x– and y– direction. c) The convolution of PSF and the object results in this image. The points are clearly separable in the y–direction but badly in x–direction. 41

3.15 An object with a single spatial frequency of ξ is imaged with an optical system with the **PSF**, being the system's PSF. image formation can be described with a convolution with the **PSF**. This acts as a low–pass filter. Thus the modulation or contrast of the image is reduced compared to the object. . 42

3.16 Graphical representation of the Zernike polynomials on the unit cycle. m, n in $\mathbf{Z}_n^{\pm m}$ are the angular frequency and the order of the Polynomial; j in $\mathbf{Z}j$ is the Noll index. Detailed explanations on the aberrations Defocus, Astigmatism and Coma and SA are given in Section 3.3. 46

3.17 Summery on the mathematical connections in physical image formation. Left half: describes the diffraction limited image formation; Right half: consideration of diffractive and geometric errors; Top middle: WF decomposition into Zernike polynomials. Incoherent illumination with the wavelength λ is assumed, f is the focal length of the system. Mathematical operations along the errors are the transformations between the different image characterizations. $\odot$ is the autocorrelation, $\otimes$ the convolution, and $\mathcal{F}$ the Fourier Transform (all operations are 2D operations). Fields of complex values are not displayed, as this is impossible in a 2D graph. See text in Chapter 3 for the definitions of the other variables. 48

4.1 Layout for the numerical simulation of the Liou and Brennan Eye. The layout is depicted for a 3 mm iris diameter. In the x–z cross section the 5° tilt between the OA and the visual axis can be seen. Furthermore the iris is shifted 0.5 mm nasally (negative x-direction) corresponding to the Liou and Brennan Model. The eye is symmetric in the y–z cross section. 50

4.2 Modulation values at 100 lp/mm for the Aspira-aXA IOL at the 4.5 mm pupil diameter. The plot depicts the mean modulation (solid line), sagittal modulation (dotted lines) and tangential modulation (dashed lines). The sampling points chosen by the authors of the publication (Eppig et al. [9]) are marked with red lines. The interpolation for the tangential modulation is questionable for the amount of sampling points. Figure is adapted from [9] 52

4.3 3D renderings from the CAD model a) the overall assembly of the mechanical model eye b) tilt and shift unit of the mechanical eye model c) cross section of the mechanical eye model 55
4.4 Photography of the assembled eye model during its use in a measurement. 56
4.5 a) A machine vision setup (telecentric lens and a camera) with an optical resolution of 10 μm per pixel is used to perform absolute measurements of tilt and shift unit's position. b) With a stereo microscope the IOL is observed within the lens holder to check for a correct centered lens placement. . . . 59
4.6 If the IOL is not rotated about its own center, each θ tilt induces a small x shift. This movement is outbalanced by a counter shift with the x–axis shift mechanism. 60
4.7 a)The USAF–target provides patterns of specific spatial frequencies. b) The Siemens star has continuously increasing spacial frequencies from the outer border to center. Both targets can be produced with a sinusoidal intensity pattern which does not include harmonics of the fundamental spatial frequency. 61
4.8 a) A slanted edge target image. b) Due to image aberrations the image of the target is blurred. c) Detail view of b); The green grid depicts the pixel grid from the image acquisition camera sensor with the pixel pitch p. If the pixel intensities are projected along the edge direction, adjacent sensor lines can be used to generate interpolated sub–pixels with higher spatial sampling p_{sub}. 62
4.9 Schematic of the setup for measuring the MTF. A slanted edge target is observed by the model eye. The retina image of the model eye is captured by a camera with a 5x microscope objective. The camera with the microscope objective is mounted on a translation stage, with that the AL of the model eye can be adjusted to different target distances and to the refractive power of the IOL to be tested. Between Model Eye and target optionally color filters for monochromatic measurements can be inserted. 63
4.10 A filter wheel, equipped with three narrow bandpass filters 488 nm, 543.5 nm and 650 nm, all with FWHM 10 nm (Thorlabs FL488–10, FL543.5–10 and FB650–10), can be attached in the front of the eye to measure the optical properties at specific wavelengths. 63
4.11 Working principle of a Hartmann–Shack WFS: The sensor consists of a lenslet array and a CMOS sensor. For a plane WF light focuses on the OA of the microlenses. For the perturbed WF the local WF gradient acts as a WF tilt at the location of a microlens. Thus the individual focuses shift proportional to the local gradient of the WF. By measuring all spot positions behind the lenslets, compared to the reference position the WF can be reconstructed. Image source: [19] 66
4.12 Simplified schematic for the double–pass setup: A laser illuminates the eye via a beam splitter (BS). The diffuse reflection of the illuminated point on the retina propagates through the eye. Telescope optics (L1 and L2) bring the sensor in a conjugate plane to the iris with an appropriate magnification. The deviations from a plane wave are measured by a WFS. Image source: [21] 67

4.13 Simplified schematic for single–pass 1 setup: A laser with a tiny pinhole aperture or alternatively the tip of a mono mode fiber (F1) produces a point source at the location of the retina. The light from the illuminated point on the retina propagates through the eye. L1, L2 and WFS are the same as in Figure 4.12. Image source: adapted from [21] 67

4.14 Photo of the prototype implementation of the single–pass 1 setup: The schematic construction follows Figure 4.13. The tip of a single mode fiber, which acts as a perfect emitter for a spherical wave, is inserted into a rigid brass canula. For a precise adjustment of the AL and point source location on the retina, the canula is mounted on miniature precision translation stages. 68

4.15 Simplified schematic for single–pass 2 setup: A laser is expanded with a beam expander (BE) to a parallel beam with >6 mm diameter having a plane WF to fully illuminate the iris aperture. The eye focuses the beam onto the retina. This aberrated spot image is converted to a parallel beam by lens L1. The WFS measures the deviation from a plane wave. Image source: [21] 68

4.16 Schematic of the setup for measuring the WF. The system is illuminated by a HeNe laser source (not shown), expanded to a diameter bigger than the entrance pupil of the model eye. A compact assembly of a precision aspheric lens and a WFS is mounted on translation stages. With them, the focal point of the aspheric lens can be aligned with the focus of the model eye. 70

4.17 Schematic of the optical projection device. A slanted edge target, or any other object, is mounted on the target screen. The model eye produces an image of the object in the retina plane of the model eye. Compared to Figure 4.9 the retina image is not digitally captured but projected onto the retina of a human investigator by a projection optics. 72

4.18 The optical system consists of three achromatic doublets with a focal length of 25 mm, 75 mm and 50 mm and two diaphragms, the aperture diaphragm (AD) and the field diaphragm (FD). Between the model eye's retina (MR) and the proband's retina (PR) a 1:1 magnification is set up. The ray colors depict four different field heights (0 mm, 0.5 mm, 1 mm and 2.5 mm)calculating the visual performance vs. field height for comparison with Figure 2.2 72

4.19 The breadboard with the projection optics is mechanically compatible to the breadboard of the MTF–setup. They can easily be exchanged by two mounting screws. 73

4.20 Setup of the experiments for this thesis in the photonics laboratory at the UAS Technikum Wien. A) Computer with control and measurement software; B) MTF–setup; C) Camera with telecentric lens for checking the IOL position; D) WF–setup singe–pass 2; E) WF–setup single–pass 1; F) Control electronics for the model eye's stepper motors; G) Different IOLs, IOL–holder and iris holder; H) Optical projection device; I) Target screen of MTF–measurement and demonstration for the visual impression. 74

5.1 Numerical simulation results: Liou and Brennan eye with 3 mm iris diameter. $\mathbf{MTF}_{mean}(100\frac{\text{lp}}{\text{mm}})$=0.62. **Reading the plot:** The MTF depicts the *modulation* or *visibility* vs. spatial frequency ξ. The black line represents the *diffraction limited MTF*, due to diffraction the modulation can not be higher than this limit determined by the iris diameter. Due to additional geometric errors the true modulation of the optical system further drops. Since the WF is not rotational symmetric, the MTF is direction dependent. $\mathbf{MTF}_y$ (dashed blue) and $\mathbf{MTF}_x$ (dotted red) describe MTF in y and x direction. $\mathbf{MTF}_{mean}$ is the mean between those two functions. Corresponding to the ISO–standard the modulation at 100 $\frac{\text{lp}}{\text{mm}}$ is used to quantify the optical performance with a single value. The geometric errors are depicted as WF–map $\mathbf{\Phi}(x, y)$ on the circular pupil. A uniform color would indicate a undistorted WF. The PSF depicts the intensity distribution on the retina plane, when a point–like object is examined. The narrower this function the better the imaging condition is fulfilled. 76

5.2 Numerical simulation results: Liou and Brennan eye with 4.5 mm iris diameter. $\mathbf{MTF}_{mean}(100\frac{\text{lp}}{\text{mm}})$=0.52 76

5.3 Numerical simulation results: Liou and Brennan eye with the PMMA model cornea 3 mm iris diameter. $\mathbf{MTF}_{mean}(100\frac{\text{lp}}{\text{mm}})$=0.62 77

5.4 Numerical simulation results: Liou and Brennan eye with the PMMA model cornea 4.5 mm iris diameter. $\mathbf{MTF}_{mean}(100\frac{\text{lp}}{\text{mm}})$=0.50 77

5.5 Only PMMA model cornea with 3 mm iris diameter. $\mathbf{MTF}_{mean}(100\frac{\text{lp}}{\text{mm}})$=0.47 78

5.6 Numerical simulation results: Only PMMA model cornea with 4.5 mm iris diameter. $\mathbf{MTF}_{mean}(100\frac{\text{lp}}{\text{mm}})$=0.20 78

5.7 Numerical simulation results: Liou and Brennan eye with the MC5812AS IOL and 3 mm iris diameter. $\mathbf{MTF}_{mean}(100\frac{\text{lp}}{\text{mm}})$=0.37 80

5.8 Numerical simulation results: Liou and Brennan eye with the MC5812AS IOL and 4.5 mm iris diameter. $\mathbf{MTF}_{mean}(100\frac{\text{lp}}{\text{mm}})$=0.17 80

5.9 Color map for all plots describing the tilt and shift dependent modulation at $(100\frac{\text{lp}}{\text{mm}})$. On the right side of the figure exemplary images of a sine intensity grating with the modulation or contrast C of 0.6 (map color red), 0.35 (map color green) and 0.1 (map color blue) are depicted, where $C = 0.6$ results in a good visibility and the grating can hardly be resolved at a contrast of $C = 0.1$. 81

5.10 Numerical simulation results: Liou and Brennan eye with the MC5812AS IOL and 3 mm iris diameter. **Reading the plot:** The three subplots depict the modulation, which corresponds to the visibility, at $100\frac{\text{lp}}{\text{mm}}$ for each IOL–position (θ,x). The color map and illustrative examples for the corresponding image contrast is depicted in Figure 5.9. Due to the fact that the MTF is direction dependent, the modulation value is shown for the y–direction ($\mathbf{MTF}_y$), the x–direction ($\mathbf{MTF}_x$) and the mean value between y and x ($\mathbf{MTF}_{mean}$). In this particular example the visibility is best, if the lens is tilted by $\theta = +3.5°$ and shifted by $x = -0.6$ mm, with a mean contrast of approximately 0.5 at $100\frac{\text{lp}}{\text{mm}}$ 82

5.11 Numerical simulation results: Liou and Brennan eye with the MC5812AS IOL and 4.5 mm iris diameter. $\mathbf{MTF}_y$, $\mathbf{MTF}_{mean}$ and $\mathbf{MTF}_x$ at $100\frac{\text{lp}}{\text{mm}}$ is depicted for each IOL–position (θ,x) 82

5.12 Numerical simulation results: Liou and Brennan eye with the MC5812AS IOL and 3 mm iris diameter. The Zernike Coefficients $Z4$ to $Z15$ are depicted for each IOL–position (θ,x) 83

5.13 Numerical simulation results: Liou and Brennan eye with the MC5812AS IOL and 4.5 mm iris diameter. The Zernike Coefficients $Z4$ to $Z15$ are depicted for each IOL–position (θ,x) 83

5.14 Numerical simulation results: Liou and Brennan eye with the MC6125AS IOL and 3 mm iris diameter. $\mathbf{MTF}_{mean}(100\frac{\text{lp}}{\text{mm}})=0.50$ 84

5.15 Numerical simulation results: Liou and Brennan eye with the MC6125AS IOL and 4.5 mm iris diameter. $\mathbf{MTF}_{mean}(100\frac{\text{lp}}{\text{mm}})=0.25$ 84

5.16 Numerical simulation results: Liou and Brennan eye with the MC6125AS IOL and 3 mm iris diameter. $\mathbf{MTF}_y$, $\mathbf{MTF}_{mean}$ and $\mathbf{MTF}_x$ at $100\frac{\text{lp}}{\text{mm}}$ is depicted for each IOL–position (θ,x) 85

5.17 Numerical simulation results: Liou and Brennan eye with the MC6125AS IOL and 4.5 mm iris diameter. $\mathbf{MTF}_y$, $\mathbf{MTF}_{mean}$ and $\mathbf{MTF}_x$ at $100\frac{\text{lp}}{\text{mm}}$ is depicted for each IOL–position (θ,x) 85

5.18 Numerical simulation results: Liou and Brennan eye with the MC6125AS IOL and 3 mm iris diameter. The Zernike Coefficients $Z4$ to $Z15$ are depicted for each IOL–position (θ,x) 86

5.19 Numerical simulation results: Liou and Brennan eye with the MC6125AS IOL and 4.5 mm iris diameter. The Zernike Coefficients $Z4$ to $Z15$ are depicted for each IOL–position (θ,x) 86

5.20 Numerical simulation results: Liou and Brennan eye with the CT LUCIA 611PY IOL and 3 mm iris diameter. $\mathbf{MTF}_{mean}(100\frac{\text{lp}}{\text{mm}})=0.59$ 87

5.21 Numerical simulation results: Liou and Brennan eye with the CT LUCIA 611PY IOL and 4.5 mm iris diameter. $\mathbf{MTF}_{mean}(100\frac{\text{lp}}{\text{mm}})=0.38$ 87

5.22 Numerical simulation results: Liou and Brennan eye with the CT LUCIA 611PY IOL and 3 mm iris diameter. $\mathbf{MTF}_y$, $\mathbf{MTF}_{mean}$ and $\mathbf{MTF}_x$ at $100\frac{\text{lp}}{\text{mm}}$ is depicted for each IOL–position (θ,x) 88

5.23 Numerical simulation results: Liou and Brennan eye with the CT LUCIA 611PY IOL and 4.5 mm iris diameter. $\mathbf{MTF}_y$, $\mathbf{MTF}_{mean}$ and $\mathbf{MTF}_x$ at $100\frac{\mathrm{lp}}{\mathrm{mm}}$ is depicted for each IOL–position (θ,x) 88

5.24 Numerical simulation results: Liou and Brennan eye with the CT LUCIA 611PY D3 IOL and 3 mm iris diameter. The Zernike Coefficients $Z4$ to $Z15$ are depicted for each IOL–position (θ,x) 89

5.25 Numerical simulation results: Liou and Brennan eye with the CT LUCIA 611PY D3 IOL and 4.5 mm iris diameter. The Zernike Coefficients $Z4$ to $Z15$ are depicted for each IOL–position (θ,x) 89

5.26 MTF–measurement of the model cornea C2 with 3 mm iris diameter. $\mathbf{MTF}_x(100\frac{\mathrm{lp}}{\mathrm{mm}})$=0.27 90

5.27 MTF–measurements of three model cornea C1, C2 and C3 with 4.5 mm iris diameter. $\mathbf{MTF}_x(100\frac{\mathrm{lp}}{\mathrm{mm}})$= 0.13 for cornea 2. 90

5.28 WF–measurement of the model cornea C2 with 3 mm iris diameter. The WF is reconstructed from coefficients $Z4$ to $Z15$. MTF and PSF are derived from the WF–data $\mathbf{MTF}_{mean}(100\frac{\mathrm{lp}}{\mathrm{mm}})$=0.35 91

5.29 WF–measurement of the model cornea C2 with 4.5 mm iris diameter. The WF is reconstructed from coefficients $Z4$ to $Z15$. MTF and PSF are derived from the WF–data $\mathbf{MTF}_{mean}(100\frac{\mathrm{lp}}{\mathrm{mm}})$=0.21 91

5.30 Direct $\mathbf{MTF}_x$ measurements: Liou and Brennan eye with MC5812AS IOL and 3 mm iris diameter depicted for a centered IOL. The three functions show the MTF before (pre), during (auto) and after (post) automatically doing all tilts and shifts. 93

5.31 Direct $\mathbf{MTF}_x$ measurements: Liou and Brennan eye with MC6125AS IOL and 4.5 mm iris diameter depicted for a centered IOL. The three functions show the MTF before (pre), during (auto) and after (post) automatically doing all tilts and shifts. 93

5.32 Derived from WF–measurements: Liou and Brennan eye with the MC5812AS IOL and 3 mm iris diameter. $\mathbf{MTF}_{mean}(100\frac{\mathrm{lp}}{\mathrm{mm}})$=0.32 95

5.33 Derived from WF–measurements: Liou and Brennan eye with the MC5812AS IOL and 4.5 mm iris diameter. $\mathbf{MTF}_{mean}(100\frac{\mathrm{lp}}{\mathrm{mm}})$=0.17 95

5.34 Direct $\mathbf{MTF}_x$ measurements: Liou and Brennan eye with the MC5812AS IOL and 3 mm iris diameter. The MTF at $100\frac{\mathrm{lp}}{\mathrm{mm}}$ is depicted for each IOL–position (θ,x) 96

5.35 $\mathbf{MTF}_y$, $\mathbf{MTF}_{mean}$ and $\mathbf{MTF}_x$ derived from WF–measurements: Liou and Brennan eye with the MC5812AS IOL and 3 mm iris diameter. The MTF at $100\frac{\mathrm{lp}}{\mathrm{mm}}$ is depicted for each IOL–position (θ,x) 96

5.36 Direct $\mathbf{MTF}_x$ measurements: Liou and Brennan eye with the MC5812AS IOL and 4.5 mm iris diameter. The MTF at $100\frac{\mathrm{lp}}{\mathrm{mm}}$ is depicted for each IOL–position (θ,x) 97

5.37 $\mathbf{MTF}_y$, $\mathbf{MTF}_{mean}$ and $\mathbf{MTF}_x$ derived from WF–measurements: Liou and Brennan eye with the MC5812AS IOL and 4.5 mm iris diameter. The MTF at $100\frac{\mathrm{lp}}{\mathrm{mm}}$ is depicted for each IOL–position (θ,x) 97

5.38 WF measurement results: Liou and Brennan eye with the MC5812AS IOL and 3 mm iris diameter. The Zernike Coefficients $Z4$ to $Z15$ are depicted for each IOL–position (θ,x) . . . 98

5.39 WF measurement results: Liou and Brennan eye with the MC5812AS IOL and 4.5 mm iris diameter. The Zernike Coefficients $Z4$ to $Z15$ are depicted for each IOL–position (θ,x) . . . 98

5.40 Direct $\mathbf{MTF}_x$ measurements: Liou and Brennan eye with MC6125AS IOL and 3 mm iris diameter depicted for a centered IOL. The three functions show the MTF before (pre), during (auto) and after (post) automatically doing all tilts and shifts. . . . 99

5.41 Direct $\mathbf{MTF}_x$ measurements: Liou and Brennan eye with MC6125AS IOL and 4.5 mm iris diameter depicted for a centered IOL. The three functions show the MTF before (pre), during (auto) and after (post) automatically doing all tilts and shifts. . . . 99

5.42 Derived from WF–measurements: Liou and Brennan eye with the MC6125AS IOL and 3 mm iris diameter. $\mathbf{MTF}_{mean}(100\frac{\text{lp}}{\text{mm}})=0.45$ . . . 101

5.43 Derived from WF–measurements: Liou and Brennan eye with the MC6125AS IOL and 4.5 mm iris diameter. $\mathbf{MTF}_{mean}(100\frac{\text{lp}}{\text{mm}})=0.24$ . . . 101

5.44 Direct $\mathbf{MTF}_x$ measurements: Liou and Brennan eye with the MC6125AS IOL and 3 mm iris diameter. The MTF at $100\frac{\text{lp}}{\text{mm}}$ is depicted for each IOL–position (θ,x) . . . 102

5.45 $\mathbf{MTF}_y$, $\mathbf{MTF}_{mean}$ and $\mathbf{MTF}_x$ derived from WF–measurements: Liou and Brennan eye with the MC6125AS IOL and 3 mm iris diameter. The MTF at $100\frac{\text{lp}}{\text{mm}}$ is depicted for each IOL–position (θ,x) . . . 102

5.46 Direct $\mathbf{MTF}_x$ measurements: Liou and Brennan eye with the MC6125AS IOL and 4.5 mm iris diameter. The MTF at $100\frac{\text{lp}}{\text{mm}}$ is depicted for each IOL–position (θ,x) . . . 103

5.47 $\mathbf{MTF}_y$, $\mathbf{MTF}_{mean}$ and $\mathbf{MTF}_x$ derived from WF–measurements: Liou and Brennan eye with the MC6125AS IOL and 4.5 mm iris diameter. The MTF at $100\frac{\text{lp}}{\text{mm}}$ is depicted for each IOL–position (θ,x) . . . 103

5.48 WF measurement results: Liou and Brennan eye with the MC6125AS IOL and 3 mm iris diameter. The Zernike Coefficients $Z4$ to $Z15$ are depicted for each IOL–position (θ,x) . . . 104

5.49 WF measurement results: Liou and Brennan eye with the MC6125AS IOL and 4.5 mm iris diameter. The Zernike Coefficients $Z4$ to $Z15$ are depicted for each IOL–position (θ,x) . . . 104

5.50 Direct $\mathbf{MTF}_x$ measurements: Liou and Brennan eye with CT611PY IOL and 3 mm iris diameter depicted for a centered IOL. The three functions show the MTF before (pre), during (auto) and after (post) automatically doing all tilts and shifts. . . . 105

5.51 Direct $\mathbf{MTF}_x$ measurements: Liou and Brennan eye with CT611PY IOL and 4.5 mm iris diameter depicted for a centered IOL. The three functions show the MTF before (pre), during (auto) and after (post) automatically doing all tilts and shifts. 105
5.52 Derived from WF–measurements: Liou and Brennan eye with the CT611PY IOL and 3 mm iris diameter. $\mathbf{MTF}_{mean}(100\frac{\text{lp}}{\text{mm}})$=0.50 107
5.53 Derived from WF–measurements: Liou and Brennan eye with the CT611PY IOL and 4.5 mm iris diameter. $\mathbf{MTF}_{mean}(100\frac{\text{lp}}{\text{mm}})$=0.20 107
5.54 Direct $\mathbf{MTF}_x$ measurements: Liou and Brennan eye with the CT611PY IOL and 3 mm iris diameter. The MTF at $100\frac{\text{lp}}{\text{mm}}$ is depicted for each IOL–position (θ,x) 108
5.55 $\mathbf{MTF}_y$, $\mathbf{MTF}_{mean}$ and $\mathbf{MTF}_x$ derived from WF–measurements: Liou and Brennan eye with the CT611PY IOL and 3 mm iris diameter. The MTF at $100\frac{\text{lp}}{\text{mm}}$ is depicted for each IOL–position (θ,x) 108
5.56 Direct $\mathbf{MTF}_x$ measurements: Liou and Brennan eye with the CT611PY IOL and 4.5 mm iris diameter. The MTF at $100\frac{\text{lp}}{\text{mm}}$ is depicted for each IOL–position (θ,x) 109
5.57 $\mathbf{MTF}_y$, $\mathbf{MTF}_{mean}$ and $\mathbf{MTF}_x$ derived from WF–measurements: Liou and Brennan eye with the CT611PY IOL and 4.5 mm iris diameter. The MTF at $100\frac{\text{lp}}{\text{mm}}$ is depicted for each IOL–position (θ,x) 109
5.58 WF measurement results: Liou and Brennan eye with the CT611PY IOL and 3 mm iris diameter. The Zernike Coefficients $Z4$ to $Z15$ are depicted for each IOL–position (θ,x) 110
5.59 WF measurement results: Liou and Brennan eye with the CT611PY IOL and 4.5 mm iris diameter. The Zernike Coefficients $Z4$ to $Z15$ are depicted for each IOL–position (θ,x) 110
5.60 MTF from the projection optics at four different field heights: center = 0 mm (blue), 0.5 mm (green), 1 mm (red) and 2.5 mm (gold). "T" is the MTF in tangential direction "S" is in the sagittal direction. Comparison with Figure 2.2 shows that the optics do not impair the accurateness of vision. 111

6.1 Simulated optical layout for the aberration free IOL at a shift of +0.6 mm. Red circle: The peripheral ray is outside optical diameter of the IOL, vignetting occurs. 116
6.2 Light cone alignment in the MTF–setup. Green: Light cone of the model eye. For constructive reasons the window (W) is tilted with respect to the visual axis and the OA of the microscope lens, thus the output light cone is refracted off axis. Blue: The microscope lens in theory has a sufficient NA, but not aligned with the output light cone. As the output light cone angle changes with IOL tilt and shift, the microscope can not be aligned with the eye for the full measurement sequence. Thus image aberrations are induced by the microscope system. 120

List of Tables

2.1 Structural parameters for the model eye in Figure 2.3. Source: [16]
Gradient refractive indices are calculated with $n(w,z) = n_{00} + n_{01}z + n_{02}z^2 + n_{10}r_{xy}^2$
z ... distance along the OA, r_{xy} ... radius normal to z
Grad A: $n_{00} = 1.368$, $n_{01} = 0.049057$, $n_{02} = -0.015427$, $n_{10} = -0.001978$
Grad B: $n_{00} = 1.407$, $n_{01} = 0.000000$, $n_{02} = -0.006605$, $n_{10} = -0.001978$
r ... radius of surface curvature, c ... asphericity, d ... thickness, n ... refractive index . . . 9

4.1 Refractive indices for two optical media from the Liou and Brennan eye for four different wavelength and the corresponding Abbe Number V_d. 51
4.2 Data of the lenses which were used for simulations and measurements for this thesis. For the CT LUCIA 611PY only basic information is given, since the detailed lens data were provided under a non disclosure agreement. 53
4.3 Parameters for the model cornea.
r ... radius of surface curvature, c ... asphericity, d ... thickness 57

5.1 Comparison of the full Liou and Brennan eye (L&B) and the Liou and Brennan cornea with three different IOLs, when they are centered in the capsular bag. P = photopic vision with 3 mm iris; S = scotopic vision with 4.5 mm iris. Δ AL is the required shortening of the AL to regain optimal contrast at $100\frac{\text{lp}}{\text{mm}}$, when the iris is changed from 3 mm to 4.5 mm. 79
5.2 Zernike coefficients (scaled in λ): Liou and Brennan eye with the MC5812AS 81
5.3 Zernike coefficients (scaled in λ): Liou and Brennan eye with the MC6125AS 85
5.4 Zernike coefficients (scaled in λ): Liou and Brennan eye with the CT LUCIA 611PY 88
5.5 Zernike coefficients (scaled in λ) measured from the model PMMA-Cornea without an IOL are compared with the simulated data for 3 mm iris diameter. Bold marked values reveal that vertical astigmatism $Z6$ and horizontal coma $Z8$ are increased. 92

5.6 Zernike coefficients (scaled in λ) measured from the model PMMA-Cornea without an IOL are compared with the simulated data for 4.5 mm iris diameter. Bold marked values reveal that vertical astigmatism $Z6$ and horizontal coma $Z8$ are increased. 92
5.7 Zernike coefficients (scaled in λ): Liou and Brennan eye with the MC5812AS and 3 mm iris diameter at centered position prior (pre), during (auto) and after (post) the measurement procedure. 94
5.8 Zernike coefficients (scaled in λ): Liou and Brennan eye with the MC5812AS and 4.5 mm iris diameter at centered position prior (pre), during (auto) and after (post) the measurement procedure. 94
5.9 Zernike coefficients (scaled in λ): Liou and Brennan eye with the MC6125AS and 3 mm iris diameter at centered position prior (pre), during (auto) and after (post) the measurement procedure. 100
5.10 Zernike coefficients (scaled in λ): Liou and Brennan eye with the MC6125AS and 4.5 mm iris diameter at centered position prior (pre), during (auto) and after (post) the measurement procedure. 100
5.11 Zernike coefficients (scaled in λ): Liou and Brennan eye with the CT611PY and 3 mm iris diameter at centered position prior (pre), during (auto) and after (post) the measurement procedure. 106
5.12 Zernike coefficients (scaled in λ): Liou and Brennan eye with the CT611PY and 4.5 mm iris diameter at centered position prior (pre), during (auto) and after (post) the measurement procedure. 106
5.13 A weighted cumulative optical performance, see Equation 5.1, is given for all three lenses tested in this thesis. Values are calculated for photopic vision (3 mm iris) and scotopic vision (4.5 mm). The two values are simulation / measurement. Measurement values were deduced from the WF–setup . . 112

6.1 Zernike fit error for the aberration correcting IOL at isotopic illumination. The true RMS value is 0.73λ (see Figure 5.21). 121

List of Acronyms

ACD Anterior Chamber Depth

AL Axial Length

API Application Programming Interface

CA Chromatic Aberration

CS Contrast Sensitivity

DAQ Data Acquisition

ESF Edge Spread Function

FPS Frames Per Second

FWHM Full Width at Half Maximum

HPiAC Hydrophilic Acrylic

HPoAC Hydrophobic Acrylic

IOL Intraocular Lens

ISO International Standards Organization

LCA Longitudinal Chromatic Aberration

LSF Line Spread Function

MP Mega Pixel

MTF Modulation Transfer Function

NA Numerical Aperture

OA Optical Axis

OPL Optical Path Length

OTF Optical Transfer Function

PMMA Polymethylmethacrylate

POM Polyoxymethylene

PSF Point Spread Function

SA Spherical Aberration

TCA Transverse Chromatic Aberration

USAF United States Air Force

VA Visual Acuity

WF Wavefront

WFS Wavefront Sensor

Bibliography

[1] L. Levin, S. Nilsson, J. Hoeve, S. Wu, P. Kaufman, and A. Alm, *Adler's Physiology of the Eye E-Book*. Elsevier Health Sciences, 2011.

[2] D. Pascolini and S. P. Mariotti, "Global estimates of visual impairment: 2010," *British Journal of Ophthalmology*, vol. 96, pp. 614–618, 2012.

[3] World Health Organization, "Visual impairment and blindness." `http://www.who.int/mediacentre/factsheets/fs282/en/`, 2014. Fact Sheet N 282.

[4] D. Allen and A. Vasavada, "Cataract and surgery for cataract," *British Medical Journal*, vol. 333, pp. 128–132, 2006.

[5] E. Baldaszti, *Jahrbuch der Gesundheitsstatistik 2015*. STATISTIK AUSTRIA, 2017.

[6] F. Taketani, E. Yukawa, T. Ueda, Y. Sugie, M. Kojima, and Y. Hara, "Effect of tilt of 2 acrylic intraocular lenses on high-order aberrations.," *Journal of cataract and refractive surgery*, vol. 31, pp. 1182–1186, June 2005.

[7] L. Wang and D. D. Koch, "Effect of decentration of wavefront-corrected intraocular lenses on the higher-order aberrations of the eye.," *Archives of ophthalmology (Chicago, Ill. : 1960)*, vol. 123, pp. 1226–1230, Sept. 2005.

[8] D. L. Guyton, H. Uozato, and H. J. Wisnicki, "Rapid determination of intraocular lens tilt and decentration through the undilated pupil.," *Ophthalmology*, vol. 97, pp. 1259–1264, Oct. 1990.

[9] T. Eppig, K. Scholz, A. Loeffler, A. Messner, and A. Langenbucher, "Effect of decentration and tilt on the image quality of aspheric intraocular lens designs in a model eye.," *JCRS*, vol. 35, pp. 1091–1100, Jun 2009.

[10] A. de Castro, P. Rosales, and S. Marcos, "Tilt and decentration of intraocular lenses in vivo from purkinje and scheimpflug imaging. validation study.," *Journal of cataract and refractive surgery*, vol. 33, pp. 418–429, Mar. 2007.

[11] P. Rosales and S. Marcos, “Phakometry and lens tilt and decentration using a custom-developed purkinje imaging apparatus: validation and measurements.,” *Journal of the Optical Society of America. A, Optics, image science, and vision*, vol. 23, pp. 509–520, Mar. 2006.

[12] International Organization for Standardization ISO Central Secretariat, *International Standard ISO 11979–2:2014: Ophthalmic implants – Intraocular lenses – Part 2: Optical properties and test methods*, iso 11979–2:2014 ed., 2014.

[13] T. Tandogan, G. U. Auffarth, C. Y. Choi, S. Liebing, C. Mayer, and R. Khoramnia, “In vitro comparative optical bench analysis of a spherical and aspheric optic design of the same iol model.,” *BMC ophthalmology*, vol. 17, p. 9, Feb. 2017.

[14] S. Norrby, P. Piers, C. Campbell, and M. van der Mooren, “Model eyes for evaluation of intraocular lenses,” *Applied Optics*, vol. 46, no. 26, pp. 6595–6605, 2007.

[15] S. Norrby, “ISO eye model not valid for assessing aspherical lenses,” *Journal of Cataract & Refractive Surgery*, vol. 34, pp. 1056–1057, jul 2008.

[16] H. Liou and N. Brennan, “Anatomically accurate, finite model eye for optical modelling,” *Journal of the Optical Society of America A*, vol. 14, no. 8, pp. 1684–1695, 1997.

[17] Normenausschuss Feinmechanik und Optik (NAFuO), “Din 1335:2003-12 geometrical optics - nomenclature and definitions,” *DIN Deutsches Institut f. Normung e. V.*, 2003.

[18] S. Maedel, N. Hirnschall, N. Bayer, S. Markovic, J. Tabernero, P. Artal, F. Schaeffel, and O. Findl, “Comparison of intraocular lens decentration and tilt measurements using 2 purkinje meter systems.,” *Journal of cataract and refractive surgery*, vol. 43, pp. 648–655, May 2017.

[19] L. Traxler, N. Bayer, B. Reutterer, and A. Drauschke, “Improvement of optics, mechanics and the usability of a mechanical eye model for vision quality evaluation of iols.,” *IFAC-PapersOnLine*, vol. 48, no. 4, pp. 1 – 18, 2015. 13th {IFAC} and {IEEE} Conference on Programmable Devices and Embedded SystemsPDES 2015.

[20] L. Traxler, B. Reutterer, N. Bayer, E. Rank, S. Krause, E. Beckert, and A. Drauschke, “Tilt and decentration tolerance of intraocular lenses: measurements with an improved mechanical model eye,” in *Ophthalmic Technologies XXVI* (F. Manns, P. G. S"oderberg, and A. Ho, eds.), SPIE-Intl Soc Optical Eng, mar 2016.

[21] L. Traxler, B. Reutterer, N. Bayer, and A. Drauschke, “Comparison of different wavefront measurement setups to judge the position tolerance of intraocular lenses in a model eye,” *Proc. SPIE*, vol. 10251, pp. 1025116–1025116–6, 2017.

[22] R. Schmidt, F. Lang, and M. Heckmann, eds., *Physiologie des Menschen.* Gewerbestrasse 11, 6330 Cham, Switzerland: Springer Berlin Heidelberg, 31. ed., 2011.

[23] R. HUBBARD and G. WALD, “Cis-trans isomers of vitamin a and retinene in vision.,” *Science (New York, N.Y.)*, vol. 115, p. Unknown, Jan. 1952.

[24] I. Escudero-Sanz and R. Navarro, “Off-axis aberrations of a wide-angle schematic eye model.,” *Journal of the Optical Society of America. A, Optics, image science, and vision*, vol. 16, pp. 1881–1891, Aug. 1999.

[25] S. Norrby, “The dubbelman eye model analysed by ray tracing through aspheric surfaces.,” *Ophthalmic & physiological optics : the journal of the British College of Ophthalmic Opticians (Optometrists)*, vol. 25, pp. 153–161, Mar. 2005.

[26] D. A. Atchison, “Optical models for human myopic eyes.,” *Vision research*, vol. 46, pp. 2236–2250, July 2006.

[27] R. Navarro, L. Gonzalez, and J. L. Hernandez-Matamoros, “On the prediction of optical aberrations by personalized eye models.,” *Optometry and vision science : official publication of the American Academy of Optometry*, vol. 83, pp. 371–381, June 2006.

[28] A. V. Goncharov and C. Dainty, “Wide-field schematic eye models with gradient-index lens.,” *Journal of the Optical Society of America. A, Optics, image science, and vision*, vol. 24, pp. 2157–2174, Aug. 2007.

[29] G. Smith, P. Bedggood, R. Ashman, M. Daaboul, and A. Metha, “Exploring ocular aberrations with a schematic human eye model.,” *Optometry and vision science : official publication of the American Academy of Optometry*, vol. 85, pp. 330–340, May 2008.

[30] T. S. de Paula, C. Zilberberg, E. Hajdu, and G. Lobo-Hajdu, “Morphology and molecules on opposite sides of the diversity gradient: four cryptic species of the cliona celata (porifera, demospongiae) complex in south america revealed by mitochondrial and nuclear markers.,” *Molecular phylogenetics and evolution*, vol. 62, pp. 529–541, Jan. 2012.

[31] J. Polans, B. Jaeken, R. P. McNabb, P. Artal, and J. A. Izatt, “Wide-field optical model of the human eye with asymmetrically tilted and decentered lens that reproduces measured ocular aberrations,” *Optica*, vol. 2, no. 2, pp. 124–134, 2015.

[32] D. A. Atchison and L. N. Thibos, “Optical models of the human eye.,” *Clinical & experimental optometry*, vol. 99, pp. 99–106, Mar. 2016.

[33] H. L. Liou and N. A. Brennan, “The prediction of spherical aberration with schematic eyes.,” *Ophthalmic & physiological optics : the journal of the British College of Ophthalmic Opticians (Optometrists)*, vol. 16, pp. 348–354, July 1996.

[34] W. Brezna, N. Dragostinoff, and M. Prinz, “Human eye modeling for intraocular lens design and for calculating intraocular lens power,” *IFAC Proceedings Volumes*, vol. 45, no. 18, pp. 534 – 539, 2012. 8th IFAC Symposium on Biological and Medical Systems.

[35] Y.-C. Chen, C.-J. Jiang, T.-H. Yang, and C.-C. Sun, “Development of a human eye model incorporated with intraocular scattering for visual performance assessment.,” *Journal of biomedical optics*, vol. 17, p. 075009, July 2012.

[36] N. Dragostinoff, W. Brezna, K. Lux, C. Krutzler, and M. Prinz, “Increased quality of vision by innovative intraocular lens and human eye modeling,” *Biomedical Signal Processing and Control*, vol. 12, pp. 62–68, 2014.

[37] W. Brezna, K. Lux, N. Dragostinoff, C. Krutzler, N. Plank, R. Tobisch, A. Boltz, G. Garhofer, R. Told, K. Witkowska, and L. Schmetterer, “Psychophysical vision simulation of diffractive bifocal and trifocal intraocular lenses.,” *Translational vision science & technology*, vol. 5, p. 13, Oct. 2016.

[38] H. Song, X. Yuan, and X. Tang, “Effects of intraocular lenses with different diopters on chromatic aberrations in human eye models.,” *BMC ophthalmology*, vol. 16, p. 9, Jan. 2016.

[39] J. G. Sivak and T. Mandelman, “Chromatic dispersion of the ocular media.,” *Vision research*, vol. 22, pp. 997–1003, 1982.

[40] G. Westheimer, “Image quality in the human eye.,” *Optica acta*, vol. 17, pp. 641–658, Sept. 1970.

[41] M. A. Wilson, M. C. Campbell, and P. Simonet, “change of pupil centration with change of illumination and pupil size.,” *Optometry and vision science : official publication of the American Academy of Optometry*, vol. 69, pp. 129–136, Feb. 1992.

[42] G. Walsh, “The effect of mydriasis on the pupillary centration of the human eye.,” *Ophthalmic & physiological optics : the journal of the British College of Ophthalmic Opticians (Optometrists)*, vol. 8, pp. 178–182, 1988.

[43] G. Walsh and W. N. Charman, “The effect of pupil centration and diameter on ocular performance.,” *Vision research*, vol. 28, pp. 659–665, 1988.

[44] J. T. Schwiegerling, “Eye axes and their relevance to alignment of corneal refractive procedures.,” *Journal of refractive surgery (Thorofare, N.J. : 1995)*, vol. 29, pp. 515–516, Aug. 2013.

[45] H. Shichi, “Cataract formation and prevention,” *Expert Opinion on Investigational Drugs*, vol. 13, no. 6, pp. 691–701, 2004. PMID: 15174955.

[46] D. Raczynska, L. Glasner, E. Serkies-Minuth, M. A. Wujtewicz, and K. Mitrosz, "Eye surgery in the elderly.," *Clinical interventions in aging*, vol. 11, pp. 407–414, 2016.

[47] J. Thompson and N. Lakhani, "Cataracts.," *Primary care*, vol. 42, pp. 409–423, Sept. 2015.

[48] W. S. Kim and K. H. Kim, *Challenges in Cataract Surgery.* Springer-Verlag GmbH, 2016.

[49] A. Agarwal and P. Narang, *Step by Step Phacoemulsification.* Jaypee Brothers Medical Publishers, 2015.

[50] M. J. Tappin and D. F. Larkin, "Factors leading to lens implant decentration and exchange.," *Eye (London, England)*, vol. 14 Pt 5, pp. 773–776, Oct. 2000.

[51] P. Rosales, A. De Castro, I. Jimenez-Alfaro, and S. Marcos, "Intraocular lens alignment from purkinje and scheimpflug imaging.," *Clinical & experimental optometry*, vol. 93, pp. 400–408, Nov. 2010.

[52] J. B. Ale, "Intraocular lens tilt and decentration: a concern for contemporary iol designs.," *Nepalese journal of ophthalmology : a biannual peer-reviewed academic journal of the Nepal Ophthalmic Society : NEPJOPH*, vol. 3, pp. 68–77, 2011.

[53] P.-Y. Chang, C.-Y. Lian, J.-K. Wang, P.-Y. Su, J.-Y. Wang, and S.-W. Chang, "Surgical approach affects intraocular lens decentration.," *Journal of the Formosan Medical Association = Taiwan yi zhi*, vol. 116, pp. 177–184, Mar. 2017.

[54] O. Findl, N. Hirnschall, P. Draschl, and J. Wiesinger, "Effect of manual capsulorhexis size and position on intraocular lens tilt, centration, and axial position.," *Journal of cataract and refractive surgery*, vol. 43, pp. 902–908, July 2017.

[55] J. S. Kim and K. H. Shyn, "Biometry of 3 types of intraocular lenses using scheimpflug photography.," *Journal of cataract and refractive surgery*, vol. 27, pp. 533–536, Apr. 2001.

[56] M. Baumeister, B. Neidhardt, J. Strobel, and T. Kohnen, "Tilt and decentration of three-piece foldable high-refractive silicone and hydrophobic acrylic intraocular lenses with 6-mm optics in an intraindividual comparison.," *American journal of ophthalmology*, vol. 140, pp. 1051–1058, Dec. 2005.

[57] S. Ozates, M. Koc, M. M. Uzel, and P. Yilmazbas, "Comparison of intraocular lens position change following two different implantation techniques.," *Current eye research*, vol. 42, pp. 1235–1239, Sept. 2017.

[58] R. Sheard, "Optimising biometry for best outcomes in cataract surgery.," *Eye (London, England)*, vol. 28, pp. 118–125, Feb. 2014.

[59] S. Norrby, “Sources of error in intraocular lens power calculation,” *Journal of Cataract and Refractive Surgery*, vol. 34, pp. 368–376, 2008.

[60] N. Hirnschall and O. Findl, “Intraocular lens power calculation – still searching for the holy grail,” *European Ophthalmic Review*, vol. 9(1), pp. 13–6, 2015.

[61] J. T. Holladay, T. C. Prager, T. Y. Chandler, K. H. Musgrove, J. W. Lewis, and R. S. Ruiz, “A three-part system for refining intraocular lens power calculations.,” *Journal of cataract and refractive surgery*, vol. 14, pp. 17–24, Jan. 1988.

[62] J. A. Retzlaff, D. R. Sanders, and M. C. Kraff, “Development of the srk/t intraocular lens implant power calculation formula.,” *Journal of cataract and refractive surgery*, vol. 16, pp. 333–340, May 1990.

[63] K. J. Hoffer, “The hoffer q formula: a comparison of theoretic and regression formulas.,” *Journal of cataract and refractive surgery*, vol. 19, pp. 700–712, Nov. 1993.

[64] J. Holladay, “Holladay iol consultant computer program.” Houston, TX, Holladay IOL Consultant, 1996.

[65] T. Olsen, L. Corydon, and H. Gimbel, “Intraocular lens power calculation with an improved anterior chamber depth prediction algorithm.,” *Journal of cataract and refractive surgery*, vol. 21, pp. 313–319, May 1995.

[66] W. Haigis, “Iol power calculations.,” *Ophthalmology*, vol. 117, pp. 400–1; author reply 401, Feb. 2010.

[67] M. Lundstrom, P. Barry, Y. Henry, P. Rosen, and U. Stenevi, “Evidence-based guidelines for cataract surgery: guidelines based on data in the european registry of quality outcomes for cataract and refractive surgery database.,” *Journal of cataract and refractive surgery*, vol. 38, pp. 1086–1093, June 2012.

[68] S. Shah, C. Peris-Martinez, T. Reinhard, and P. Vinciguerra, “Visual outcomes after cataract surgery: Multifocal versus monofocal intraocular lenses.,” *Journal of refractive surgery (Thorofare, N.J. : 1995)*, vol. 31, pp. 658–666, Oct. 2015.

[69] P. Artal, *Handbook of Visual Optics, Volume Two: Instrumentation and Vision Correction.* CRC Press, 2017.

[70] O. Findl, “Intraocular lens materials and design,” in *Achieving Excellence in Cataract Surgery*, Colvard, D. Michael, 2009.

[71] R. Bellucci, “An introduction to intraocular lenses: Material, optics, haptics, design and aberration,” *Cataract. ESASO Course Series*, pp. 38–55, 08 2013.

[72] D. Madrid-Costa, J. Ruiz-Alcocer, T. Ferrer-Blasco, S. Garcia-Lazaro, and R. Montes-Mico, “In vitro optical performance of a new aberration-free intraocular lens.,” *Eye (London, England)*, vol. 28, pp. 614–620, May 2014.

[73] S. Pieh, W. Fiala, A. Malz, and W. Stork, “In Vitro Strehl Ratios with spherical, aberration-free, average, and customized spherical abberation-correcting intraocular lenses,” *Invest Ophthalmol Vis Sci*, vol. 50, no. 3, pp. 1264–1270, 2009.

[74] L. Salerno, M. Tiveron, and A. JL., “Multifocal intraocular lenses: Types, outcomes, complications and how to solve them.,” *Taiwan J Ophthalmol*, 2017.

[75] S. Greenstein and R. Pineda, “The quest for spectacle independence: A comparison of multifocal intraocular lens implants and pseudophakic monovision for patients with presbyopia.,” *Seminars in ophthalmology*, vol. 32, pp. 111–115, 2017.

[76] O. Findl and C. Leydolt, “Meta-analysis of accommodating intraocular lenses.,” *Journal of cataract and refractive surgery*, vol. 33, pp. 522–527, Mar. 2007.

[77] G. Savini, P. Barboni, P. Ducoli, E. Borrelli, and K. J. Hoffer, “Influence of intraocular lens haptic design on refractive error.,” *Journal of cataract and refractive surgery*, vol. 40, pp. 1473–1478, Sept. 2014.

[78] Y.-A. Chen, N. Hirnschall, S. Maedel, and O. Findl, “Misalignment of a novel single-piece acrylic intraocular lens in the first three months after surgery.,” *Ophthalmic research*, vol. 51, pp. 104–108, 2014.

[79] N. E. Norrby, “Standardized methods for assessing the imaging quality of intraocular lenses.,” *Applied optics*, vol. 34, pp. 7327–7333, Nov. 1995.

[80] J. McKelvie, B. McArdle, and C. McGhee, “The influence of tilt, decentration, and pupil size on the higher-order aberration profile of aspheric intraocular lenses.,” *Ophthalmology*, vol. 118, pp. 1724–1731, Sept. 2011.

[81] J. McKelvie, J. Y. Ku, B. McArdle, and C. McGhee, “Wavefront aberrometry: comparing and profiling higher-order aberrations produced by intraocular lenses in vitro using a physical model eye system and hartman-shack aberrometry.,” *Journal of cataract and refractive surgery*, vol. 35, pp. 547–555, Mar. 2009.

[82] M.-J. Kim, Y.-S. Yoo, C.-K. Joo, and G. Yoon, “Evaluation of optical performance of 4 aspheric toric intraocular lenses using an optical bench system: Influence of pupil size, decentration, and rotation.,” *Journal of cataract and refractive surgery*, vol. 41, pp. 2274–2282, Oct. 2015.

[83] S. Bonaque-Gonzalez, P. Bernal-Molina, M. Marcos-Robles, and N. Lopez-Gil, “Optical characterization method for tilted or decentered intraocular lenses.,” *Optometry and vision science : official publication of the American Academy of Optometry*, vol. 93, pp. 705–713, July 2016.

[84] C. Ortiz, J. J. Esteve-Taboada, L. Belda-Salmeron, D. Monsalvez-Romin, and A. Dominguez-Vicent, “Effect of decentration on the optical quality of two intraocular lenses.,” *Optometry and vision science : official publication of the American Academy of Optometry*, vol. 93, pp. 1552–1559, Dec. 2016.

[85] P. Perez-Merino and S. Marcos, “Effect of intraocular lens decentration on image quality tested in a custom model eye,” *Journal of Cataract & Refractive Surgery*, vol. 44, no. 7, pp. 889 – 896, 2018.

[86] W. D. Furlan, L. Remón, C. Llorens, M. Rodriguez-Vallejo, and J. A. Monsoriu, “Comparison of two different devices to assess intraocular lenses,” *Optik*, vol. 127, pp. 10108–10114, Oct. 2016.

[87] J. V. Zudans, N. R. Desai, and W. B. Trattler, “Comparison of prediction error: labeled versus unlabeled intraocular lens manufacturing tolerance.,” *Journal of cataract and refractive surgery*, vol. 38, pp. 394–402, Mar. 2012.

[88] TRIOPTICS, “Quality testing of intraocular lenses.” `https://www.trioptics.com/fileadmin/assets/trioptics/04_Downloads/OptiSpheric/OptiSpheric-WaveMaster-IOL-Brochure-EN.pdf`, 2017. last access 18.11.2017.

[89] P. A. Piers, D. H. Chang, A. Alarcon, and C. Canovas, “Clinically relevant interpretations of optical bench measurement of intraocular lenses.,” *Journal of refractive surgery (Thorofare, N.J. : 1995)*, vol. 33, p. 64, Jan. 2017.

[90] A. Alarcon, C. Canovas, R. Rosen, H. Weeber, L. Tsai, K. Hileman, and P. Piers, “Preclinical metrics to predict through-focus visual acuity for pseudophakic patients.,” *Biomedical optics express*, vol. 7, pp. 1877–1888, May 2016.

[91] H. A. Weeber, C. Canovas, A. Alarcon, and P. A. Piers, “Laboratory-measured mtf of iols and clinical performance.,” *Journal of refractive surgery (Thorofare, N.J. : 1995)*, vol. 32, pp. 211–212, Mar. 2016.

[92] D. D. Koch and L. Wang, “Optical quality of three multifocal lenses.,” *Journal of refractive surgery (Thorofare, N.J. : 1995)*, vol. 32, p. 210, Mar. 2016.

[93] A. Ghatak, *Optics*. McGraw-Hill Education, 2009.

[94] P. Artal, *Handbook of Visual Optics, Volume One: Fundamentals and Eye Optics*. CRC Press, 2017.

[95] W. Demtröder, *Experimentalphysik 2: Elektrizität und Optik*. Springer-Lehrbuch, Springer Berlin Heidelberg, 2014.

[96] O. K. Ersoy, *Diffraction, Fourier optics, and imaging*. Wiley Series in Pure and Applied Optics, Wiley-Interscience, 1 ed., 2007.

[97] E. W. Max Born, *Principles of optics*. Cambridge University Press, 7th ed., 1999.

[98] C. W. Tyler, “Peripheral color demo.,” *i-Perception*, vol. 6, p. 2041669515613671, Dec. 2015.

[99] R. Navarro, "The Optical Design of the Human Eye: a Critical Review," *J Optom,*, vol. 2, no. 1, pp. 3–18, 2009.

[100] L. N. Thibos, M. Ye, X. Zhang, and A. Bradley, "The chromatic eye: a new reduced-eye model of ocular chromatic aberration in humans.," *Applied optics*, vol. 31, pp. 3594–3600, July 1992.

[101] P. Artal, "Image formation in the living human eye.," *Annual review of vision science*, vol. 1, pp. 1–17, Nov. 2015.

[102] M. K. Johnson and H. Farid, "Exposing digital forgeries through chromatic aberration," in *Proceedings of the 8th Workshop on Multimedia and Security*, MM&#38;Sec '06, (New York, NY, USA), pp. 48–55, ACM, 2006.

[103] P. Artal, S. Manzanera, P. Piers, and H. Weeber, "Visual effect of the combined correction of spherical and longitudinal chromatic aberrations.," *Optics express*, vol. 18, pp. 1637–1648, Jan. 2010.

[104] L. N. Thibos, A. Bradley, and X. X. Zhang, "Effect of ocular chromatic aberration on monocular visual performance.," *Optometry and vision science : official publication of the American Academy of Optometry*, vol. 68, pp. 599–607, Aug. 1991.

[105] S. Plainis, D. Petratou, T. Giannakopoulou, D. A. Atchison, and M. K. Tsilimbaris, "Binocular summation improves performance to defocus-induced blur.," *Investigative ophthalmology & visual science*, vol. 52, pp. 2784–2789, Apr. 2011.

[106] R. Schmidt, N. Birbaumer, V. Braitenberg, J. Dudel, U. Eysel, H. Handwerker, H. Hatt, M. Illert, W. Jänig, R. Rüdel, *et al.*, *Neuro- und Sinnesphysiologie.* Springer-Lehrbuch, Springer Berlin Heidelberg, 2013.

[107] S. Ravikumar, L. N. Thibos, and A. Bradley, "Calculation of retinal image quality for polychromatic light.," *Journal of the Optical Society of America. A, Optics, image science, and vision*, vol. 25, pp. 2395–2407, Oct. 2008.

[108] G. D. Boreman, *Modulation Transfer Function in Optical and Electro-Optical Systems,.* SPIE Press, Bellingham, WA, 2001.

[109] International Organization for Standardization ISO Central Secretariat, "International Standard ISO 9334:2012 Optics and photonics – Optical transfer function – Definitions and mathematical relations," 2012.

[110] A. Brahme, *Comprehensive Biomedical Physics.* Elsevier Science, 2014.

[111] Nobelprize.org, "The nobel prize in physics 1953." `https://www.nobelprize.org/nobel_prizes/physics/laureates/1953/`, 2017. last access 27.12.2017.

[112] F. Zernike, “Diffraction theory of the knife-edge test and its improved form, the phase-contrast method,” *Monthly Notices of the Royal Astronomical Society*, vol. Vol. 94, pp. p.377–384, 1934.

[113] H. Nema and N. Nema, *Diagnostic Procedures in Ophthalmology:*. G - Reference,Information and Interdisciplinary Subjects Series, Jaypee Brothers,Medical Publishers Pvt. Limited, 2014.

[114] L. N. Thibos, R. A. Applegate, J. T. Schwiegerling, and R. Webb, “Report from the vsia taskforce on standards for reporting optical aberrations of the eye.,” *Journal of refractive surgery (Thorofare, N.J. : 1995)*, vol. 16, pp. S654–5, Sep-Oct 2000.

[115] R. J. Noll, “Zernike polynomials and atmospheric turbulence,” *J. Opt. Soc. Am.*, vol. 66, pp. 207–211, Mar 1976.

[116] M. Tocci, “How to model the human eye in zemax.” `http://customers.zemax.com/os/resources/learn/knowledgebase/how-to-model-the-human-eye-in-zemax`, 04 2007. last access 19.11.2017.

[117] G. E. Altmann, L. D. Nichamin, S. S. Lane, and J. Pepose, “Optical performance of 3 intraocular lens designs in the presence of decentration.,” *Journal of Cataract and Refractive Surgery*, vol. 31, pp. 574–585, 2005.

[118] Carl Zeiss Meditec AG, “Ct lucia 611p – instructions for use.” `https://kategorizacia.mzsr.sk/Pomocky/Download/RequestAttachment/87399`, 2015. SAP No. 000000-2153-334, Rev C last access: 25.05.2018.

[119] E. Feichtinger, “Monofokale Standard-IOLs,” *MEDICAL NETWORK*, vol. 2017 Special, pp. 104–111, 2017. `http://www.augen.co.at/special_2017/pdf/MNS17_104%E2%80%93111_IOL-Tabellen.pdf`.

[120] refractiveindex.info, “Optical constants of h2o (water).” `https://refractiveindex.info/?shelf=main&book=H2O&page=Hale`, 2017. last access 19.11.2017.

[121] B. N. Walker, R. H. James, D. Calogero, and I. K. Ilev, “Impact of environmental temperature on optical power properties of intraocular lenses.,” *Applied optics*, vol. 53, pp. 453–457, Jan. 2014.

[122] refractiveindex.info, “Optical constants of (c5h8o2)n (poly(methyl methacrylate), pmma).” `https://refractiveindex.info/?shelf=organic&book=poly(methyl_methacrylate)&page=Szczurowski`, 2017. last access 19.11.2017.

[123] B. Reutterer, L. Traxler, N. Bayer, and A. Drauschke, “Further improvement of an intraocular lens holder for more physiological measurements within a mechanical eye model,” *Proc. SPIE*, vol. 10251, pp. 102511Y–102511Y–4, 2017.

[124] International Organization for Standardization ISO Central Secretariat, “International Standard ISO 9335:2012 Optics and photonics – Optical transfer function – Principles and procedures of measurement,” 2012.

[125] J. K. M. Roland, “A study of slanted-edge mtf stability and repeatability,” vol. 9396, pp. 9396 – 9396 – 9, 2015.

[126] International Organization for Standardization, *International Standard ISO 12233:2014, Photography – Electronic still picture imaging – Resolution and spatial frequency responses*, iso12233:2014 ed., 2014.

[127] P. D. Burns, “sfrmat3: SFR evaluation for digital cameras and scanners.” `http://losburns.com/imaging/software/SFRedge/index.htm`, 05 2015. last access 30.11.2017.

[128] E. Moreno-Barriuso and R. Navarro, “Laser ray tracing versus hartmann–shack sensor for measuring optical aberrations in the human eye,” *J. Opt. Soc. Am. A*, vol. 17, pp. 974–985, Jun 2000.

[129] Thorlabs, “Mounted high–precision aspheres: Cnc polished, n–bk7 and s–lah64 substrate.” `https://www.thorlabs.com/newgrouppage9.cfm?objectgroup_id=8402&pn=AL1210M-A#8667`, 2018. last access: 03.01.2018.

[130] P. A. Piers, E. J. Fernandez, S. Manzanera, S. Norrby, and P. Artal, “Adaptive optics simulation of intraocular lenses with modified spherical aberration,” *Investigative Ophthalmology & Visual Science*, vol. 45, no. 12, p. 4601, 2004.

[131] D. Madrid-Costa, J. Ruiz-Alcocer, C. Perez-Vives, T. Ferrer-Blasco, N. Lopez-Gil, and R. Montes-Mico, “Visual simulation through different intraocular lenses using adaptive optics: Effect of tilt and decentration,” *Journal of Cataract & Refractive Surgery*, vol. 38, no. 6, pp. 947 – 958, 2012.

[132] UAS Technikum Wien, “Photonics at UAS Technikum Wien.” `https://www.technikum-wien.at/en/newsroom/news/photonics-at-uas-technikum-wien-fiat-lux/`, 2014. last access 04.01.2018.

[133] A. Crnej, N. Hirnschall, Y. Nishi, V. Gangwani, J. Tabernero, P. Artal, and O. Findl, “Impact of intraocular lens haptic design and orientation on decentration and tilt.,” *Journal of cataract and refractive surgery*, vol. 37, pp. 1768–1774, Oct. 2011.

[134] L. A. Carvalho, “Accuracy of zernike polynomials in characterizing optical aberrations and the corneal surface of the eye,” *Investigative Ophthalmology & Visual Science*, vol. 46, no. 6, p. 1915, 2005.

[135] D. Gatinel, “Limited accuracy of hartmann-shack wavefront sensing in eyes with diffractive multifocal iols,” *Journal of Cataract & Refractive Surgery*, vol. 34, no. 4, p. 528, 2008.

[136] A. Calatayud, L. Remon, J. Martos, W. D. Furlan, and J. A. Monsoriu, "Imaging quality of multifocal intraocular lenses: automated assessment setup.," *Ophthalmic & physiological optics : the journal of the British College of Ophthalmic Opticians (Optometrists)*, vol. 33, pp. 420–426, July 2013.

[137] S. Pieh, P. Marvan, B. Lackner, G. Hanselmayer, G. Schmidinger, R. Leitgeb, M. Sticker, C. Hitzenberger, A. Fercher, and C. Skorpik, "Quantitative performance of bifocal and multifocal intraocular lenses in a model eye: point spread function in multifocal intraocular lenses," *Archives of Ophthalmology*, vol. 120, no. 1, pp. 23–28, 2001.

Dipl.-Ing. Lukas Traxler

Curriculum Vitae

Schirnes 3
3842 Thaya, Austria
☎ *+43 664 4655643*
✉ *traxler@technikum-wien.at*

Info

Born	March 21st, 1988 in Vienna, Austria
Citizenship	Austria

Education

10/2014 – present **Doctoral programme in Engineering Sciences Technical Physics**
Technical University of Vienna

- PhD Thesis: ”Evaluation of the Optical Quality of Intraocular Lenses and their Sensitivity to Misalignment in the Eye”, carried out within the project LOALiS
- Covered skills: technical optics, image processing, ophthalmology
- Degree expected spring 2018

10/2011 – 03/2014 **Master Study Biomedical Engineering**
Technical University of Vienna

- Specialization in medical physics and imaging
- Covered skills: physics, medical imaging, image and signal processing and analysis, machine learning, neurosciences, computer vision, modeling and simulation
- Master thesis ”Identifying and Decoding the Multivariate Brain Activity for Emotional States in Self - and Empathic Perception” carried out at Computational Imaging Research Lab (Medical University of Vienna) under supervision of Prof. Dr. Georg Langs and Prof. Dr. Robert Sablatnig (Computer Vision Lab, TU Vienna)
- Graduation with distinction

09/2008 – 06/2011 **Bachelor of Science in Biomedical Engineering**
University of Applied Sciences Technikum Wien

- Specialization in medical engineering
- Covered skills: anatomy and physiology, electronics, natural sciences, computer science, control engineering, medical engineering in hospitals, radiation physics and radiation medicine, signal analysis; basics of rehabilitation technology, prosthetics, cell culture, tissue engineering, medical informatics and bioinformatics
- Bachelor thesis ”Constrained Independent Component Analysis for Artifact Reduction in CPR Corrupted ECGs” carried out at the Vienna General Hospital under supervision of Dr. Hermann Gilly
- graduation with distinction

09/2002 – 06/2007 **Engineer in Mechatronics**
Secondary College for Mechatronics, HTL Karlstein

- Covered skills: electronics, electrical engineering, measurement and control systems, mechanics, automation and elements of mechatronics, informatics, laboratory (electronics, measurement technology, microprocessor, metal workshop), production engineering, operational technology and quality management, construction and design practice, general education, natural sciences
- graduation with distinction

Work Experience

Teaching

03/2012 – present	**Lector at the University of Applied Sciences Technikum Wien** (03/2012 – 08/2014 Freelance Lector) – Lector for Control Engineering, Physics, Optics, Signal Acquisition and Analysis, – Lector for Control Engineering Laboratory and Physics Laboratory (partly held at the Friedrich Schiller University in Jena, Germany) – Supervision of master thesis, bachelor thesis and student projects – Development of new courses and laboratory infrastructure, study program development – Project supervision at summer school "MedTec Summer Academy"
03/2009 – 06/2011	**Tutor at the University of Applied Sciences Technikum Wien** – Laboratory tutoring: Electronic Laboratory, Control Engineering Laboratory, Biomedical Sensors and Signals Laboratory – Review Courses: Control Engineering, Mathematics, Medical Physics, Basics of Electronics, Basics of Medical Measurement Technology

Research and Development

10/2017 – present	**Scientist at the Austrian Institute of Technology (AIT)** – Freelance Scientist at the Center for Vision, Automation & Control – Competence Unit for High–Performance Vision; Research in Optics and Computer Vision
09/2014 – present	**Project supervisor and Researcher at the UAS Technikum Wien** – Project supervisor for LOALiS (Laser and Optics in Applied Life Sciences) – City of Vienna MA23 funded research project – Researcher for LOALiS with main focus on technical optics, development of courses and teaching materials in the field of optics and photonics, setting up research infrastructure for photonics (new photonics laboratory), scientific publications, conference talks and participation, PhD research – Freelance researcher for "Project Solutions Technikum Wien GmbH" in the field of signal acquisition and analysis
11/2008 – 08/2014	**Laboratory Technician at the UAS Technikum Wien** – Control Engineering Laboratory: devising and maintaining experiments for laboratory tutorials; modelling, simulation and measurement of dynamic control systems – Biomedical Engineering Laboratory: circuit design and PCB design, biological signal analysis – Assistance in research projects on the department of Biomedical Engineering: student projects, lung simulator, development of a mechanical eye model
03/2013 – 01/2014	**Graduand at the Computational Imaging Research Lab (Medical University of Vienna) for research on my master thesis**
06/2014 – 08/2014	**Freelance Developer for SIMCharacters GmbH** – Sensor development for premature birth simulation dummy
04/2011 – 10/2011	**Technical Writer for INSIGHT INSTRUMENTS** – Writing technical documentations for EC–certification of a new biofeedback device
01/2011 – 04/2011	**Bachelor thesis work placement at the Vienna General Hospital**

National Service and Volunatary Work

10/2007 – 08/2008	**Civilian service at the Austrian Red Cross as ambulance man**
09/2008 – 12/2010	**Voluntary work at the Austrian Red Cross**

Scholarships and Awards

2015	”Förderpreis der ÖGBMT in der Kategorie Dissertationen” – 1st place in the student competition at the 2015 annual meeting of the ÖGBMT
2012	Merit scholarship at the Technical University of Vienna, Faculty for Physics
2011	1st place in the IFMBE 2011 Young Investigator Competition at the 5th EMBEC in Budapest, Hungary
2010	Merit scholarship at the University of Applied Sciences Technikum Wien

Computer Skills

Languages	MATLAB (extensive knowledge), C/C++/C#, Visual Basic, PHP, LabVIEW
Documaentation	LaTeX, Microsoft Office
Mathematics	MATLAB, Mathematica, Mathcad, Simulink
Database	Oracle Database
mechanical CAD	PTC Creo Elements(former Pro/E)
electical CAD	Mentor Graphics PADS, EAGLE (PCB design), LTspice for (electronic circuit design)
optical CAD	OpticsStudio (former ZEMAX)
Networks	2 semesters CISCO networking academy
Computer grapics	Adobe Photoshop, Gimp, Inkscape

Languages

German Mother Tongue

		Comprehension		**Speaking**		**Writing**
		Listening	Reading	Interaction	Production	
English	Advanced	*B2*	*C1*	*B2*	*C1*	*C1*

Common European Framework of Reference (CEF) level

Core Competences and Soft Skills

Data Analysis	Signal and image analysis, pattern recognition, multivariate statistics
Mechatonics	Specialized in control systems engineering and automation; combining mechanical engineering, electronics and informatics; integration in optical designs
Natural Sciences	Physics, specialized in optics
Neurosciences	fMRI – data analysis, interdisciplinary work in computer sciences and social sciences
Research	continuous participation in research projects during study and work, participation in acquiring research funding, scientific and administrative supervisor of a research project

Soft Skills

Social

- teamwork skills (teamwork training and work experience)
- project management experience
- collaboration with students (experience education and support of student projects)
- communication skills
- discipline

Organisational

- experience in research project supervision
- training in team organisation and project planning
- autonomous working and self organization
- experience in setting up laboratory facilities

Other Skills

Driving Licence Class B

Special Trainings and Workshops

09–10/2013	6th International Summer School in Biomedical Engineering "Multimodal Integration of Brain Measurements in Research and Clinical Practice" at the Universidad de las Ciencias Informaticas Havana, Cuba
10/2010	ÖGMP Workshop "New Technologies in Radiology" in Vienna, Austria
07/2010	Expertissues Workshop on animal models and in vivo imaging techniques at the Ludwig Boltzmann Institute for Experimental and Clinical Traumatology Vienna, Austria
06–07/2010	Participation at the 60th Meeting of Nobel Laureates in Lindau, Germany. (Yearly meeting of Nobel laureates and invited young researchers)

Interests and Hobbies

culture	music and lindy hop dance, concerts, especially jazz, theater and opera
arts	enthusiastic hobby photographer, playing the accordion
sports	sports climbing, bouldering, dancing (lindy hop), cycling and skiing
craft	DIY'er and amateur craftsman

Talks on Conferences

04/2017	*upcoming* OPTICS & PHOTONICS International 2017 Congress Yokohama, Japan - Presentation of the Publication "Comparison of Different Wavefront Measurement Setups to Judge the Position Tolerance of Intraocular Lenses in a Model Eye"
02/2016	SPIE Photonics West in San Francisco, USA - Poster Presentation of the Publication "Tilt and decentration tolerance of intraocular lenses: measurements with an improved mechanical model eye"
10/2015	ÖGBMT 2015 annual meeting in Vienna, Austria – Paper Presentation of Publication "Prüfung der optischen Qualität von Intraokularlinsen auf Toleranz gegenüber Fehlplatzierungen im Auge" (student competition)
05/2015	13th International IFAC Conference on Programmable Devices and Embedded Systems in Cracow, Poland – Keynote Lecture "Improvement of Optics, Mechanics and the Usability of a Mechanical Eye Model for Vision Quality Evaluation of IOLs"
02/2013	SPIE Photonics West in San Francisco, USA - Poster Presentation of the Publication "Semi-automatic evaluation of intraocular lenses (IOL) using a mechanical eye model"
12/2012	15th Mechatronica in Prague, Czech Republic - Paper Presentation of Publication "Mechanical eye model for comparison of optical and physiological imaging properties"
09/2011	EMBEC 2011 in Budapest, Hungary. Paper Presentation of Publication "Constrained Independent Component Analysis for Artifact reduction in CPR corrupted ECGs"

Publication List

2017	Lukas Traxler, Bernd Reutterer. *Comparison of Different Wavefront Measurement Setups to Judge the Position Tolerance of Intraocular Lenses in a Model Eye* Proc. SPIE 10251, Biomedical Imaging and Sensing Conference 2017
2017	Bernd Reutterer, Lukas Traxler. *Further improvement of an intraocular lens holder for physiological measurements within a mechanical eye model* Proc. SPIE 10251, Biomedical Imaging and Sensing Conference 2017
2016	Lukas Traxler, Bernd Reutterer, Natascha Bayer, Elisabet Rank, Sylvio Krause, Erik Beckert, Andreas Drauschke. *Tilt and decentration tolerance of intraocular lenses: measurements with an improved mechanical model eye.* Proc. SPIE 9693, Ophthalmic Technologies XXVI
2016	Bernd Reutterer, Lukas Traxler, Natascha Bayer, Andreas Drauschke. *Experiments for practical education in process parameter optimization for selective laser sintering to increase workpiece quality* Proc. SPIE 9738, Laser 3D Manufacturing III

2015 Lukas Traxler, Natascha Bayer,Bernd Reutterer, Andreas Drauschke, Wolfgang Husinsky. *Prüfung der optischen Qualität von Intraokularlinsen auf Toleranz gegenüber Fehlplatzierungen im Auge.* Proc. ÖGBMT Jahrestagung 2015

2015 Lukas Traxler, Natascha Bayer, Bernd Reutterer, Andreas Drauschke. *Improvement of Optics, Mechanics and the Usability of a Mechanical Eye Model for Vision Quality Evaluation of IOLs.* IFAC-PapersOnLine, Volume 48, Issue 4, 2015, Pages 1-18, ISSN 2405-8963

2015 Elisabet Rank, Lukas Traxler, Natascha Bayer, Sylvio Krause, Andreas Drauschke, Erik Beckert. *Ein mechanisches Augenmodell zur Simulation eines pseudophaken Auges.* Proc. 28th International Congress of German Ophthalmic Surgeons (DOC)

2014 Elisabet Rank, Lukas Traxler, Natascha Bayer, Bernd Reutterer, Kirsten Lux, Andreas Drauschke. *Reproducibility analysis of measurements with a mechanical semiautomatic eye model for evaluation of intraocular lenses.* Proc. SPIE 8936, Design and Quality for Biomedical Technologies VII 1 - 18

2014 Lukas Traxler. *Identifying and Decoding the Multivariate Brain Activity for Emotional States in Self - and Empathic Perception.* Master Thesis TU Vienna, Supervisors: Prof. DI Dr. Robert Sablatnig, Prof. DI Dr. Georg Langs, Prof. Dr. Claus Lamm

2013 Andreas Drauschke, Elisabet Rank, Mathias Forjan, Lukas Traxler. *Semi-automatic evaluation of intraocular lenses (IOL) using a mechanical eye model.* Proc. SPIE 8567, Ophthalmic Technologies XXIII

2013 Lukas Traxler. *Mechanisches Augenmodell zum Vergleich der physiologischen und physikalischen optischen Bildqualitï£¡t.* compulsory project to Medical Physics and Imaging in the study course Biomedical Engineering TU Vienna, March, Supervisors: Prof. DI Dr. Wolfgang Husinsky, Dr. Andreas Drauschke

2012 Andreas Drauschke, Elisabet Rank, Lukas Traxler, and Mathias Forjan. *Mechanical eye model for comparison of optical and physiological imaging properties.* Proceedings of International Conference on Mechatronics, 15th Mechatronika 2012 (IEEE Catalog Number: CFP1257K-CDR):291-296. ISBN: 978-80-01-04985-3

2012 Theresa Steiner, Mathias Forjan, Lukas Traxler, Zbynek Bures, Andreas Drauschke. *Development of a Negative Pressure Based Active Lung Simulato.* Proceedings of International Conference on Mechatronics, 15th Mechatronika 2012 (IEEE Catalog Number: CFP1257K-CDR):318-323, 2012. ISBN: 978-80-01-04985-3

2011 Lukas Traxler, Marcus Granegger and Hermann Gilly. *CPR Artifact Reduction in the Human ECG by Using Constrained Independent Component Analysis.* Proceedings of 5th European Conference of theInternational Federation for Medical And Biological Engineering / Budapest, Hungary / ISBN 978-3-642-23508-5

2011 Lukas Traxler. *Constrained Idependent Component Analysis for Artifact Reduction in CPR Corrupted ECGs.* 2nd Bachelor Thesis UAS Technikum Wien, May 2011, Supervisors: Dr. Hermann Gilly, Marcus Granegger MSc

2010 Lukas Traxler. *Independent Component Analysis for Artifact Detection, Reduction and Elimination in Biological Signals.* 1st Bachelor Thesis UAS Technikum Wien, December 2010, Supervisor: Dr. Hermann Gilly

2010 Ferenc Gerbovics, Michael Haller, Lukas Traxler, Philipp Urbauer, Matthias Frohner, Stefan Sauermann, Alexander Mense. *Implementation of a wrist wearable Health Data Hub-prototype for context based telemonitoring of elderly people using standardized data transfer methods.* Proceedings of the 15th International Conference of the International Society for Telemedicine and eHealth (GT2010) 2010 / Australia / ISBN: 978-1-60750-658-4